Modification of K^0_S and $\Lambda(\overline{\Lambda})$ transverse momentum spectra in Pb–Pb collisions at $\sqrt{s_\mathrm{NN}} = 2.76$ TeV with ALICE

Dissertation
zur Erlangung des Doktorgrades
der Naturwissenschaften

vorgelegt beim Fachbereich Physik
der Goethe-Universität Frankfurt am Main
in Frankfurt am Main

von
Simone Schuchmann
aus Frankfurt am Main

Frankfurt (2015)
(D 30)

vom Fachbereich Physik der
Goethe-Universität Frankfurt am Main als Dissertation angenommen.

Dekan: Prof. Dr. René Reifarth

Gutachter: Prof. Dr. Harald Appelshäuser, Prof. Dr. Reinhard Stock

Datum der Disputation: 22.07.2015

"In den Experimenten über Atomvorgänge haben wir mit Dingen und Tatsachen zu tun, mit Erscheinungen, die ebenso wirklich sind wie irgendwelche Erscheinungen im täglichen Leben. Aber die Atome oder die Elementarteilchen sind nicht ebenso wirklich. Sie bilden eher eine Welt von Tendenzen und Möglichkeiten als eine von Dingen und Tatsachen."

Werner Heisenberg: Physik und Philosophie 1959

Zusammenfassung

10^{-6} Sekunden nach dem Urknall. Elementare Materie unter hohem Druck und hoher Temperatur. Ihr Zustand, ein Plasma aus stark wechselwirkenden Elementarteilchen - ein Quark-Gluon-Plasma (QGP), das am Large Hadron Collider (LHC) des Kern- und Teilchenforschungszentrum CERN[1] in Genf erforscht wird. Allerdings werden die Erkenntnisse dort nicht durch Himmelsbeobachtungen gewonnen. Vielmehr wird dieser spezielle Materiezustand künstlich zu erzeugen versucht: Der LHC beschleunigt Blei-Kerne (Pb-Kerne) auf (fast) Lichtgeschwindigkeit und lässt sie kollidieren, wodurch sehr viel Energie auf sehr kleinem Raum konzentriert wird. Somit werden ähnliche energetische Bedingungen wie wenige Mikrosekunden nach dem Urknall (Big-Bang) hergestellt, in sogenannten "Little-Bangs". Da das Kollisionssystem innerhalb von 10^{-23} s in viele Teilchen zerfällt, ist jedoch eine direkte Verfolgung der verschiedenen Systemstadien, die Ausbildung des Plasmas und seine Expansion mit anschließendem Erkalten und Bildung von neuen Teilchen (in Analogie zur Expansion des Universums nach dem Urknall), experimentell nicht möglich. Die Detektoren, die das Kollisionszentrum umgeben und beobachten, nehmen lediglich die Signale auf, die von den Produkten der Kollision generiert werden. Die Untersuchung der Little-Bangs ist daher ein komplexer Prozess bestehend aus der Auswertung der Detektor-Signale, ausgelöst durch die erzeugten Teilchen, der darauf aufbauenden Rekonstruktion der Teilchenspuren und der abschließenden Analyse der Teilcheneigenschaften. Die vorliegende Arbeit dokumentiert die Auswertung von Messungen der Teilchen K_s^0 und $\Lambda(\overline{\Lambda})$ in Pb–Pb und Proton-Proton Kollisionen bei einer Schwerpunktenergie von $\sqrt{s_{NN}}$ = 2.76 TeV, die von der ALICE Kollaboration am CERN aufgezeichnet wurden.

Einleitung

Das QGP besteht aus nicht gebundenen, quasi-freien[2] Quarks und Gluonen (Partonen). Letztere sind die elementaren Bausteine unserer Materie - von Protonen, Neutronen -, aber auch von vielen anderen, wenn auch kurzlebigen Teilchen. Um einen solchen Zustand von elementarer Materie in Teilchenkollisionen zu erzeugen, wird eine hohe Anzahl an Protonen und Neutronen (Nukleonen) auf engstem Raum benötigt, was bei der Kollision von Pb-Kernen mit 208 Nukleonen erfüllt ist.

Während die Gluonen die bindende Kraft zwischen den Quarks vermitteln, sind die Quark-Typen entscheidend für die Teilchensorte. Bisher sind sechs verschiedene Quarks bekannt und gemessen, die sich in ihrer Masse und Ladung unterscheiden. Protonen und Neutronen bestehen aus u- und d-Quarks. Die in Kollisionsexperimenten erzeugten Teilchen können auch die schwereren s-, c- und b-Quarks enthalten. Das zusätzliche t-Quark ist das schwerste aller Quarks und das d-Quark das leichteste. Schwerere Quarks können sich in leichtere umwandeln, was erklärt, warum unsere stabile Materie aus Teilchen geformt ist, die ausschließlich u- und d-Quarks enthalten. Die elektrische Ladung der Quarks ist drittelzahlig. Hinzu kommt noch

---

[1]Conseil Européen pour la Recherche Nucléaire
[2]Obwohl sie nicht gebunden sind, unterliegen sie dennoch einer Wechselwirkung.

die sogenannte Farbladung, die dazu führt, dass immer jeweils drei Quarks oder ein Quark und ein Anti-Quark miteinander gebunden sein müssen. Diese Zustände aus gebundenen (Anti-)Quarks nennt man allgemein Hadronen. Teilchen, die wie Protonen aus drei Quarks bestehen, werden als Baryonen bezeichnet, Quark-Anti-Quark-Paare heißen Mesonen.

In einer Pb–Pb Kollision werden demnach die Bindungen zwischen den Quarks der Nukleonen durch die hohe Temperatur und Dichte aufgelöst und ein Plasma formt sich - so die Idee. Allerdings ist das QGP nicht wechselwirkungsfrei. Die sogenannte starke Kraft - eine der vier Naturkräfte neben der Gravitationskraft, der elektromagnetischen und der schwachen Kraft -, die mit Hilfe der Quantenchromodynamik (QCD) beschrieben wird, ist trotz der aufgelösten Bindungen zwischen den Quarks präsent. Um nun Prozesse im QGP, die Effekte während der Expansion und der anschließenden Abkühlungsphase berechnen zu können, müssen komplexe mathematische Zusammenhänge gelöst werden, die sich aus der QCD herleiten. Da dies analytisch nicht möglich ist, gibt es prinzipiell zwei Berechnungsansätze. Erstens, die sogenannte Gittertheorie, die sich semi-analytisch mit dem Niederenergie-Bereich der Prozesse beschäftigt und zweitens die Störungstheorie der QCD (pQCD), wobei hochenergetische Prozesse behandelt werden. Die Methode der Störungstheorie kann dort eingesetzt werden, wo die Kopplung der starken Kraft kleiner als 1 wird. Neben der Trennung in hoch- und niederenergetische Prozesse spielt die Komplexität des Kollisionssystems bei der Lösbarkeit- und Vorhersagbarkeit von theoretischer Seite eine entscheidende Rolle.

Für Kernmaterie kann ein Phasendiagramm konstruiert werden, dessen genaue Erforschung das Hauptanliegen der Schwerionenphysik darstellt. Dazu zählen insbesondere die Lokalisierung der QGP-Phase, die Bestimmung ihrer thermodynamischen Eigenschaften (Zustandsgleichung) sowie die Charakterisierung der Ordnung ihrer Übergänge zu anderen Formen der Materie. Ein umfassendes Verständnis des QGP würde bedeuten, dass sowohl das Phasendiagramm als auch die Impulsspektren, die Häufigkeitsverteilungen und die Korrelationen der erzeugten Teilchen theoretisch beschreibbar wären. Dafür müssten allerdings die verschiedenen Stadien des Kollisionssystems verstanden sein, was deren Lebensdauer, Zustandsgleichung und Transportkoeffizienten beinhaltet. Allgemein wird unterschieden zwischen Anfangseffekten und deren Fluktuationen, die durch die Geometrie der Kollision und der Struktur der Kollisionspartner festgelegt werden, sowie Endzustandseffekten, die nach der Ausbildung des QGP auftreten und die Teilchenspektren festlegen. Erst wenn diese Effekte verstanden sind, können sie von den Messungen der Teilchenspektren "abgezogen" werden, um die Eigenschaften des QGP zu studieren, denn die Teilchenspektren stellen eine Integration über die gesamte Entwicklung der Kollision dar. Direkte Fragen, wie zum Beispiel nach der Temperatur des QGP, lassen sich bisher nicht mit direkten Messungen klären. In der Praxis beinhalten Modellrechnungen bereits die Anfangs- und Endzustandseffekte zusätzlich zu den Annahmen über das QGP. Allerdings stellt sich hier das Problem, dass die Effekte möglichst gut beschrieben werden müssen, damit durch Vergleich von Daten und Modell, die Eigenschaften des QGP extrahiert werden können.

Problemstellung

Um theoretische Vorhersagen zu bestätigen, zu verwerfen oder freie Parameter eines Modells festzulegen, sind experimentelle Messungen notwendig. Die Berechnungen auf Grundlage der pQCD sind in der Regel mit großen systematischen Unsicherheiten be-

haftet, so dass nur Messungen helfen können, die Anzahl und die Variation der freien Parameter weiter einzugrenzen. Aufgrund der Komplexität der Prozesse in Schwerionenkollisionen werden als Referenzprozesse elementare Kollisionen, d.h. Elektron-Positron (e^-e^+) oder Proton-Proton (pp) Kollisionen, betrachtet. Diese lassen sich für hohe Impulse einfacher berechnen, da weniger freie Parameter vorhanden sind und der direkte Vergleich mit Messungen möglich ist. In Kombination mit den Besonderheiten in Schwerionenkollisionen, wie das Entstehen eines Mediums und seiner Expansion, ergibt sich mit Hilfe der Referenzprozesse ein Modell, womit sich entsprechende Teilchenspektren berechnen lassen. Dafür ist es erforderlich, die Besonderheiten einer Schwerionenkollision zu kennen und zu quantifizieren. Eine einfache Möglichkeit zur Quantifizierung des Unterschieds in pp und Kern-Kern (AA) Kollisionen stellt der sogenannte nukleare Modifikationsfaktor R_{AA} dar. Zur Berechnung dieses Faktors wird ein Transversalimpulsspektrum (p_T-Spektrum) in AA Kollisionen auf die Anzahl der binären Kollisionen der Target- und Projektilnukleonen normiert und anschließend durch das p_T-Spektrum in pp Kollisionen dividiert. Falls $R_{AA}= 1$, würden AA Kollisionen der Superposition von einzelnen Kollisionen der Nukleonen entsprechen. Bisherige Beobachtungen haben ergeben, dass R_{AA} bei hohen Impulsen Werte kleiner als eins annimmt, wenn es sich um Spektren von Hadronen handelt, die der starken Wechselwirkung unterliegen. Für elektromagnetisch oder schwach wechselwirkende Teilchen wird keine Modifikation beobachtet, was darauf schließen lässt, dass das Medium in AA Kollisionen stark wechselwirkend ist und die Produktion dieser Teilchen mit der Anzahl der binären Kollisionen skaliert.

Das Medium beeinflusst somit die Hadronenproduktion im Vergleich zu pp und/oder verändert das p_T-Spektrum derart, dass eine Unterdrückung für hohe Impulsbereiche entsteht. Diese Beeinflussung durch das Medium bzw. das QGP wird hauptsächlich dem Energieverlust der Partonen zugeschrieben, die das heiße System durchqueren. Dabei handelt es sich um Partonen mit hohen Impulsen, die am Anfang der Kollision in harten Stoßprozessen entstehen. Das Medium selbst besteht aus Quarks und Gluonen mit niedrigen Impulsen. Nach Verlassen des Mediums oder sogar noch im Medium fragmentieren die harten Partonen und bilden hochenergetische Hadronen. Somit reflektiert die Unterdrückung in AA Kollisionen gegenüber pp bei hohen p_T den Energieverlust der Partonen im Medium. Bei niedrigeren Impulsen wird ebenfalls ein Unterschied zwischen den beiden Kollisionssystemen erwartet, der insbesondere in zentralen AA Kollisionen durch den kollektiven radialen Fluss des thermalisierten Mediums hervorgerufen wird.

Es schließt sich die Frage an, ob der vom Medium induzierte Energieverlust für alle Quarksorten gleich ist. Um diese Frage zu klären, wird R_{AA} für Hadronen mit unterschiedlichem Quarkinhalt bestimmt. Die Aufgabenstellung dieser Arbeit enthält die Bestimmung von R_{AA} von K_s^0 und $\Lambda(\overline{\Lambda})$, die zusätzlich zu u- und d-Quarks, d.h. zu "normaler" Materie, auch s-Quarks enthalten. Daneben soll die Produktionshäufigkeit (Rapiditätsdichte) dieser Teilchen sowohl in Pb–Pb als auch in pp Kollisionen bestimmt und verglichen werden. Alle Ergebnisse werden auch im Vergleich mit denen anderer Hadronen bei gleicher Schwerpunktsenergie sowie mit den Resultaten bei einer niedrigeren Kollisionsenergie betrachtet.

ALICE am LHC

Der ALICE-Detektor befindet sich am Interaktionspunkt 2 (Point 2) des LHC am CERN. Er ist speziell für die Messungen von Pb–Pb Kollisionen konstruiert worden,

in denen etwa 100-mal mehr Teilchen entstehen als in pp Kollisionen. Daher ist das konzeptionelle Design von ALICE unterschiedlich zu dem der beiden anderen großen Experimente ATLAS und CMS, die hauptsächlich pp Kollisionen untersuchen. Eminent wichtig ist die Bestimmung des Kollisionsvertex, um die Bruchstücke der Teilchenspuren in den verschiedenen Detektor-Subsystemen richtig zusammenzufügen und Teilchen aus Zerfällen, d.h. solche mit einem Sekundärvertex, herauszufiltern. Insbesondere in Pb–Pb Kollisionen ist die Vertex-Rekonstruktion eine anspruchsvolle Aufgabe, da durch die vielen Spuren die Auflösung negativ beeinflusst wird. Durch ein hochauflösendes Tracking-System kann dem jedoch entgegengewirkt werden, was bei ALICE mit einem 6-lagigen System von Silizumdetektoren (ITS) erreicht wird. Zur Teilchenidentifikation wird eine Spurendriftkammer (TPC) eingesetzt. Letztere ist ein großvolumiger, gasbetriebener Spurdetektor, worin geladene Teilchen mit unterschiedlicher Geschwindigkeit unterschiedlich viel Energie durch Ionisation verlieren. Über diesen Energieverlust und die Spurkrümmung im Magnetfeld, das parallel zur Strahlachse die zentralen Spurdetektoren durchdringt, können Masse, Ladung und Impuls der Teilchen bestimmt werden.

Die Zentralität einer Pb-Pb Kollision gibt an, wie groß der geometrische Überlappbereich der beiden Kerne bei der Kollision ist. Sie kann weder experimentell eingestellt noch direkt gemessen werden. Daher muss die Zentralität einer Kollision durch die Messung der Kollisionsprodukte erfolgen, denn je nach Zentralität werden mehr oder weniger Teilchen produziert. Für die vorliegende Arbeit wurden p_T-Spektren in pp Kollisionen sowie in sechs Zentralitätsklassen in Pb–Pb Kollisionen gemessen und analysiert.

Analyse

K_s^0 und $\Lambda(\overline{\Lambda})$ werden auch als sogenannte V^0-Teilchen bezeichnet, bezugnehmend auf die Topologie ihres Zerfalls und ihrer Beobachtung im Detektor. Das "V" deutet auf die V-förmig angeordneten Spuren der Tochterteilchen hin und die "0" auf die elektromagnetische Neutralität des Mutterteilchens, das aufgrund dessen nicht vom Detektor "gesehen" wird. Das Messprinzip für diese V^0-Teilchen basiert auf der Rekonstruktion der invarianten Masse. Hierbei werden jeweils zwei entgegengesetzt geladenen, im Detektor gemessenen Teilchen, die Massen der Tochterteilchen eines V^0 zugeordnet und damit die invariante Masse berechnet. Nur wenn die geladenen Teilchen wirklich die angenommene Masse haben und aus einem Zerfall des V^0 stammen, ergibt sich eine Überhöhung (Peak) im Spektrum der invarianten Masse. Solche Messungen wurden für alle Impulsbereiche mit ausreichender Statistik wiederholt und die entsprechenden Peaks extrahiert. Anschließend wurden die daraus resultierenden Transversalimpulsspektren auf die Anzahl der analysierten Kollisionen normiert und auf Detektorineffizienzen korrigiert. Im Fall von Λ und $\overline{\Lambda}$ sind zusätzlich die sogenannte Feed-Down-Korrektur und die Absorptionskorrektur notwendig. Erstere ergibt sich aus dem Beitrag zum gemessenen Spektrum von hauptsächlich Ξ^-, die zu 99% in Λ (Ξ^+ in $\overline{\Lambda}$) zerfallen. Dieser p_T-abhängige Beitrag wurde mit Hilfe der bereits publizierten Resultate von Ξ^- p_T-Spektren und unter der Verwendung von Simulationen berechnet. Die Absorptionskorrektur war erforderlich, um die in der verwendeten Simulation berechnete Absorptionsrate von Anti-Protonen aus dem $\overline{\Lambda}$-Zerfall zu korrigieren, da diese dort nicht richtig bestimmt wird. Abschließend wurden die systematischen Unsicherheiten der Analyse durch umfangreiche Studien abgeschätzt.

Ergebnisse

Die Ergebnisse dieser Arbeit sind die Transversalimpulsspektren von K_s^0 und $\Lambda(\overline{\Lambda})$ in Pb–Pb und pp Kollisionen bei einer Schwerpunktsenergie von $\sqrt{s_{NN}} = 2.76\,\text{TeV}$ für Impulsbereiche von $0.3 \leq p_T \leq 20\,\text{GeV}/c$ für K_s^0 sowie $0.6\ (0.5) \leq p_T \leq 16\,\text{GeV}/c$ (pp) für Λ und $\overline{\Lambda}$.

Die Spektren verschiedener Zentralitätsklassen in Pb–Pb Kollisionen unterscheiden sich nicht nur in der Amplitude sondern auch in ihrer Form. Mit zunehmender Zentralität entsteht eine größer werdende Überhöhung im Niedrigimpulsbereich bis zu $p_T < 5\,\text{GeV}/c$, die hauptsächlich mit dem eingangs erwähnten radialen Fluss zusammenhängt. Letzterer ist auch dafür verantwortlich, dass der mittlere Transversalimpuls in zentralen Kollisionen am größten ist. In pp Kollisionen dagegen wird eine solche Überhöhung, wie erwartet, nicht beobachtet. Stattdessen wurde ab $p_T = 3\,\text{GeV}/c$ für K_s^0 bereits eine Spektrenform festgestellt, die mit einem Potenzgesetz beschrieben werden kann, was auch für das Spektrum der fragmentierenden Partonen zutrifft. Für die Berechnung des nuklearen Modifikationsfaktors R_{AA} wurden die Spektren in pp Kollisionen mit Hilfe eines Fits mit einem Potenzgesetz extrapoliert, um sie dem Impulsbereich der Spektren in Pb–Pb Kollisionen anzupassen. Der nukleare Modifikationsfaktor zeigt in zentralen Pb–Pb Kollisionen im Vergleich mit pp Kollisionen eine starke Unterdrückung von K_s^0 und Λ bei hohen p_T. Diese Unterdrückung entspricht der von geladenen Hadronen, die hauptsächlich aus Pionen bestehen, die aus "normaler" Materie aufgebaut sind. Da K_s^0 und $\Lambda(\overline{\Lambda})$ jedoch s-Quarks enthalten, scheint diese Modifikation in Pb–Pb Kollisionen vom Quark-Typ unabhängig zu sein. Bei niedrigeren p_T wurde eine starke Unterdrückung von K_s^0, nicht jedoch von Λ festgestellt. Im Vergleich der p_T-Spektren von Λ mit denen von K_s^0 wurde eine Überhöhung in zentralen Pb–Pb Kollisionen gegenüber peripheren Pb–Pb und pp Kollisionen gefunden. Gegenwärtig wird diese Beobachtung mit dem sogenannten Rekombinationsmechanismus erklärt, der durch den Einfluss des radialen Flusses Baryonen, in diesem Fall Λ, relativ gesehen häufiger bei einem bestimmten p_T produziert als Mesonen. Da in pp Kollisionen kein radialer Fluss erwartet wird, ist die Unterdrückung von K_s^0 bei niedrigeren p_T größer als die von Λ.

Neben R_{AA} wurden auch die Rapiditätsdichten, d.h. die Teilchen-Häufigkeiten integriert über p_T, für mittlere Rapiditäten extrahiert. Es konnte ein linearer Anstieg der Rapiditätsdichten von K_s^0 und Λ mit der Zentralität, ausgedrückt durch die mittlere Anzahl der Partizipanten der Kollision, beobachtet werden. Das Häufigkeitsverhältnis von Λ/K_s^0 ändert sich nicht mit der Zentralität und hat in pp Kollisionen den gleichen Wert innerhalb der Unsicherheiten. Die Werte für $\overline{\Lambda}$ entsprechen denen für Λ sowohl in Pb–Pb als auch in pp Kollisionen, was auf Grund des sehr kleinen baryochemischen Potentials (ca. 1 MeV in Pb–Pb) - einem Maß der Balance zwischen Baryonen und Anti-Baryonen - am LHC erwartet wurde.

Diskussion und Zusammenfassung

Der Vergleich von R_{AA} der hier untersuchten Hadronen K_s^0 und Λ mit Modellrechnungen von BAMPS (Boltzmann Approach to Multi-Parton Scatterings) hat gezeigt, dass auch von theoretischer Seite die Annahme des gleichen Energieverlustes von u-, d- und s-Quarks, den sogenannten leichten Quarks, zuzutreffen scheint. Da allerdings auch die von ALICE gemessenen D-Mesonen, die ein viel schwereres c-Quark enthalten, mit der gleichen Stärke in Pb–Pb Kollisionen unterdrückt sind, kann zu dem Schluss gelangt werden, dass der Energieverlust vom Quark-Typ unabhängig ist.

Die Messung von B-Mesonen durch die CMS Kollaboration widerlegt diese Schlussfolgerung, denn dort wurde eine geringere Modifikation für die b-Quarks enthaltenden Mesonen festgestellt. Die Masse des b-Quarks ist jedoch nur drei Mal größer als die des c-Quarks. Aus Sicht der betrachteten Modelle (BAMPS, MC@sHQ + EPOS2) ist allerdings die erhöhte Masse dafür verantwortlich, dass QCD-Strahlungsprozesse (analog der Bremsstrahlung in der Quantenelektrodynamik) für b-Quarks etwas mehr unterdrückt werden als für die leichteren Quarks, wodurch der Energieverlust im Medium reduziert wird.

Bezüglich der Teilchenhäufigkeiten wurde im Vergleich mit Messungen am Relativistic Heavy Ion Collider (RHIC) (USA) bei einer kleineren Schwerpunktsenergie von $\sqrt{s_{\mathrm{NN}}} = 0.2\,\mathrm{TeV}$ festgestellt, dass sich die Produktion von Hadronen, bestehend aus leichten Quarks, d.h. von Protonen, Pionen und K_s^0 und Λ, am LHC sowohl in pp als auch in Pb–Pb Kollisionen etwas mehr als verdoppelt. Jedoch trifft dies nicht ganz zu für Hadronen, die mehr als ein s-Quark enthalten, wie z.B. Ξ^-, denn trotz der großen Messunsicherheiten zeigt sich ein Trend zu einer zusätzlich erhöhten Produktion dieser Teilchen in pp Kollisionen. Diese Beobachtung wird derzeit im Sinne einer Annäherung der Eigenschaften des pp Systems an AA bei hohen Energien diskutiert. Somit stellt sich die Frage, ob bei LHC Energien pp Kollisionen eine optimale "medium-freie" Referenz für die Teilchenproduktion, bei der hauptsächlich die Häufigkeiten bei niedrigen Impulsen eingehen, darstellen, um die Eigenschaften von Pb–Pb-Kollisionen zu studieren und zu quantifizieren.

Zusammenfassend kann festgestellt werden, dass sich bei LHC Energien die Eigenschaften von K_s^0 und $\Lambda(\overline{\Lambda})$ und von Hadronen bestehend aus u- und d-Quarks im Vergleich zu pp Kollisionen weder bei hohen Transversalimpulsen, im Hinblick auf die Modifikation der p_{T}-Spektren in Pb–Pb Kollisionen, noch bei niedrigen Impulsen, im Bezug auf die Teilchenproduktion, unterscheiden.

Abstract

Measurements of the transverse momentum (p_T) spectra of K^0_s and $\Lambda(\overline{\Lambda})$ in Pb–Pb and pp collisions at $\sqrt{s_{NN}} = 2.76$ TeV with the ALICE detector at the LHC at CERN up to $p_T = 20$ GeV/c and $p_T = 16$ GeV/c, respectively, are presented in this thesis. In addition, the particle rapidity densities at mid-rapidity and nuclear modification factors of K^0_s and $\Lambda(\overline{\Lambda})$ are shown and discussed.

The analysis was performed using the Pb–Pb data set from 2010 and the pp data set from 2011. For the identification of K^0_s and $\Lambda(\overline{\Lambda})$, the on-the-fly V0 finder was employed on tracking information from the TPC and ITS detectors. The Λ and $\overline{\Lambda}$ spectra were feed-down corrected using the measured published Ξ^- spectra as input.

Regarding the rapidity density at mid-rapidity, a suppression of the strange particle production in pp as compared to Pb–Pb collisions is observed at all centralities, whereas the production per pion rapidity density stays constant as a function of $dN_{ch}/d\eta$ including both systems. Furthermore, the relative increase of the individual particle species in pp and AA collisions is compatible for non- and single-strange particles when going from RHIC ($\sqrt{s_{NN}} = 0.2$ TeV) to LHC energies. On the other hand, in case of multi-strange baryons, a stronger increase in the particle production in pp is seen. The $\overline{\Lambda}$ and Λ production in Pb–Pb and pp collisions was found to be equal. Concerning the nuclear modification factors, at lower p_T ($p_T < 5$ GeV/c), an enhancement of the R_{AA} of Λ with respect to that of K^0_s and charged hadrons is observed. This baryon-to-meson enhancement appearing in central Pb–Pb collisions at RHIC and LHC is currently explained by the interplay of the radial flow and recombination as the dominant particle production mechanism in this p_T sector. The effect of radial flow is thus also seen in the low and intermediate p_T region of R_{AA}, where a mass hierarchy is discovered among the baryons and mesons, respectively, with the heaviest particle being least suppressed. When comparing the results from RHIC and LHC, the R_{CP} is found to be similar at low-to-intermediate p_T, while a significantly smaller R_{AA} of K^0_s and Λ in central and peripheral events at the LHC is observed in this p_T region as compared to the RHIC results. This can be attributed to the larger radial flow in AA collisions and to the harder spectra at the LHC. At high p_T ($p_T > 8$ GeV/c), a strong suppression in central Pb–Pb collisions with respect to pp collisions is found for K^0_s and $\Lambda(\overline{\Lambda})$. A significant high-$p_T$ suppression of these hadrons is also observed in the ratio of central-to-peripheral collisions. The nuclear modification of K^0_s and $\Lambda(\overline{\Lambda})$ is compatible with the modification of charged hadrons at high p_T. The calculations with the transport model BAMPS agree with these results suggesting a similar energy loss for all light quarks, i.e. u, d and s. Moreover, a compatible suppression for c-quarks appears in the ALICE measurements via the D meson R_{AA} as well as in the BAMPS calculations, which hints to a flavour-independent suppression if light- and c-quarks are regarded. Within this consideration, no indication for a medium-modified fragmentation is found yet.

To summarize, for the particle production in Pb–Pb collisions at the LHC relative to pp neither at lower p_T (rapidity density) nor at higher p_T (nuclear modification factor) a significant difference of K^0_s and $\Lambda(\overline{\Lambda})$ carrying strangeness to hadrons made of u- and d-quarks was found.

Contents

"Six quarks, six leptons, together with the gluons of QCD and the photon and the weak bosons [and the Higgs boson], are enough to describe the tangible world and more, with remarkable economy."

Robert Cahn and Gerson Goldhaber (2009)

1

Introduction

The Large Hadron Collider (LHC) at CERN[1] is currently the most powerful particle accelerator. Since the start of data taking in 2009, the LHC achieved collision energies ranging from 900 GeV up to 8 TeV for protons (pp) and 2.76 TeV for lead ions (Pb–Pb). These energies outreach those of earlier built machines as for example the Tevatron at FermiLab (USA) or the Relativistic Heavy Ion Collider (RHIC) at Brookhaven National Laboratory (BNL) (USA) by a factor 4 to 10. In 2015, the design collision energies of 13 TeV for protons and 5.1 TeV per nucleon for lead ion collisions (Pb–Pb) are planned to be realized [1].

The spurring scientific motivations of the four main LHC experiments, ATLAS, CMS, LHCb and ALICE are very different. Though these experiments all look forward to testing and expanding the understanding of the Standard Model of particle physics, a wide spectrum of physics topics is covered by the individual collaborations. This spectrum contains the following research questions:

- Where does the mass of particles originate from?

- What is the origin of the invisible matter in our universe, called dark matter? Is super-symmetry an explanation? What does dark energy consist of?

- Why is matter preferred to anti-matter in the universe, although it should have been produced in equal amounts from the available energy after the big-bang?

- What were the properties of matter a few microseconds after the big-bang when neither nucleons nor atoms had yet been formed?

While ATLAS and CMS address the first two research problems by the investigation of the famous Higgs boson[2] and the search for super-symmetry particle candidates, LHCb is dedicated to the study of a potential matter-antimatter asymmetry via the determination of the mixing relation of particles and anti-particles [5]. These phenomena are expected to be best visible in pp collisions, because in this case the background is much smaller as compared to Pb–Pb and the feasible collision energies are larger by

---

[1]Conseil Européen pour la Recherche Nucléaire

[2]The Higgs boson or more precisely its Higgs field is supposed to give mass to the particles, which makes them distinguishable. It was recently discovered by ATLAS and CMS at the LHC, see [2–4].

a factor of three. Furthermore, for pp, a sufficiently high luminosity for high enough statistics in the data can be provided. To summarise, the main task of these three experiments is to measure the reaction products of pp collisions.

The ALICE (A Large Ion Collider Experiment) apparatus, however, was principally designed for the investigation of relativistic Pb–Pb collisions. There, the particle multiplicity is around 100 times larger than in pp collisions. Not only the observables to be measured but also the detector structure/set-up, which is discussed in chapter 3, differs strongly from that of ATLAS or CMS. By the means of heavy-ion collisions, ALICE addresses questions about the state of dissolved nuclear matter during the first microseconds of the big-bang and the characteristics of matter under extreme conditions. In the following, the motivations and goals for the analysis of heavy-ion collisions are reviewed.

1.1 Heavy-ion collisions

The LHC is capable of accelerating protons as well as lead ions to velocities exceedingly close to the speed of light. The apparent difference between the two collision systems pp and Pb–Pb is the fact that a lead nucleus consists of 82 protons and 126 neutrons (= 208 nucleons). Hence, whereas during a Pb–Pb collision the nucleons of the accelerated lead nuclei are surrounded by other nucleons, the collision of two single protons can be regarded as a collision in the vacuum, not only for the protons but also for the elementary constituents of the protons, the quarks and gluons. While pp collisions are studied in order to acquire knowledge about specific particle production mechanisms from elementary reactions, heavy-ion collisions are the tool for investigating the nature of nuclear matter at high temperatures as well as high energy densities. At very high energies or densities, a transformation of nuclear matter to a dissolved state of its elementary constituents is expected. This state of quasi-free quarks and gluons is called quark gluon plasma (QGP). In fact, the QGP first postulated in 1975 by Collins and Perry, is a hot and dense state that presumably occurred during the evolution of the universe a few microseconds after the big bang before nuclei were formed [6]. Thus, the relativistic heavy-ion collisions at LHC can be regarded as little bangs, which allow to study the nature of elementary matter and the natural forces acting on them in the laboratory.

The QGP is not a stationary medium but subjected to dynamical evolution. The expansion of the system leads to a cooling followed by the final formation of hadrons, which are particles built from the available quarks and gluons. These newly created particles, consisting either of three quarks (baryons) or of a quark and an anti-quark (mesons) are eventually measured by a detector. In addition to the hadrons, leptons (i.e. electrons, photons) are produced, which will be further discussed in the following section. Since the whole collision evolution with a duration of 10^{-23} s is technically not possible to be followed, observables are vital that reveal the characteristics of the medium and the underlying processes during the different evolution phases.

The evolution of the QGP in the laboratory is thought to be similar to its evolution in the big bang model [6]. Whereas in collider experiments, the story ends with the measurement of the newly created particles by the detectors, the evolution of the universe continued - as we obviously can assume. Of the created particles mainly protons and neutrons (nucleons) survived while the others decayed after their creation.
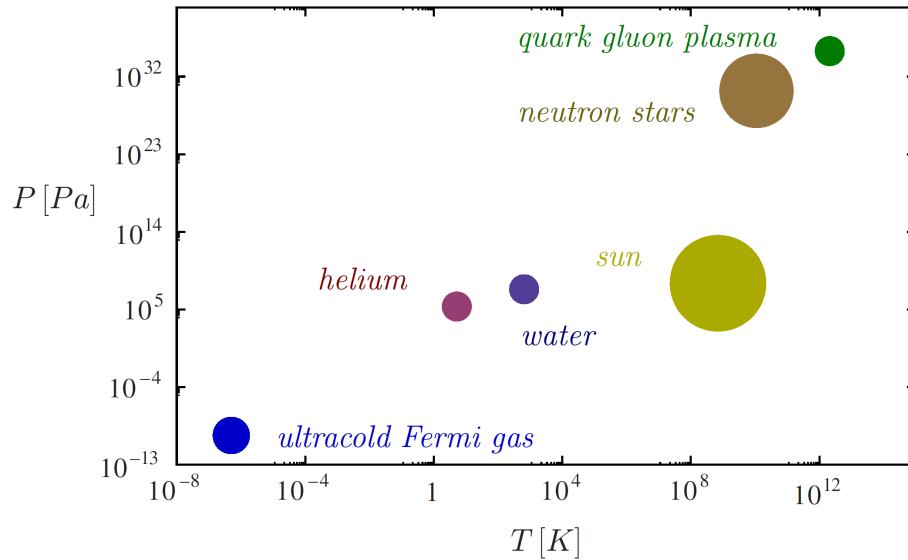
Figure 1.1: Temperature and pressure scales of extreme quantum matter. Ultra-cold quantum gases are the coldest matter produced to date, while the QGP is the hottest, together spanning about 19 orders of magnitude in temperature and about 44 orders of magnitude in pressure. [...] We include two other well-known quantum fluids, liquid helium and hot proto-neutron star matter, as well as a classical fluid, water and a classical plasma, the Coulomb plasma in the sun. Figure and caption taken from [8].

During the continuing expansion and cooling of the system, the nucleons gathered and formed atomic nuclei (nucleosynthesis). When the temperature was decreasing further, the nuclei eventually caught electrons (also created during the big bang evolution) and finally atoms were formed. Afterwards, blocks of matter were accumulated and finally stars were created. The whole process lasted nearly 400 million years [7]. The clustering of matter of any kind (subatomic, atomic, molecules) is driven by the natural principle of energy minimization or by populating the energetically lowest state respectively.

In order to shed light on the characteristics of matter in a QGP state, a lot of energy is needed to crack the nuclei and their nucleons into their elementary particles, the quarks and gluons. Until now, the critical temperature of the phase transition to the QGP has not yet been determined exactly. Nonetheless temperature estimates yield values of 100 - 200 MeV (see section 1.2), roughly corresponding to 10^{12} K, which is a hundred thousand times hotter than the core of the sun. Moreover, the spatial scale of a heavy-ion collision is about a few femtometer leading to extremely high energy densities (pressures) as compared to ground state nuclear matter. Figure 1.1 summarizes the temperatures and pressures of different matter systems ranging from ultra-cold quantum gases over sun to the QGP. After these considerations, the usage of the phrase "nuclear matter exposed to extreme conditions" seems to be appropriate, putting the research subject in a nutshell.

1.2 Nuclear matter

From experimental observations at RHIC, where the QGP "was created well above the transition temperature for the first time [...] in 2000" [9], it is known, that if

force or interaction	relative strength	range (m)	exchange particle / gauge boson	Higgs boson
gravitation	10^{-39}	∞	graviton ?	
weak	10^{-7}	$< 10^{-15}$	$W^{+,-}, Z^0$	H
electromagnetic	10^{-2}	∞	γ	
strong	1	$\approx 10^{-15}$	gluon	

Table 1.1: The four natural forces. The last three of them are the basis of the Standard Model of particle physics [10] extended with the recently discovered Higgs boson [2].

nuclear matter is exposed to extreme conditions such as extremely high temperatures in this case, a strongly interacting medium is created. The underlying interactions are mediated by the so-called strong force, one of the four natural forces listed in table 1.1. The weak force, the electromagnetic and the strong force form the basis of the so-called Standard Model of particle physics.

Whereas the electromagnetic and gravitational force are commonly well known from daily life due to their infinite range, the weak and the strong force are part of the atomic and subatomic world. Radioactive decays of nuclei as well as changes of elementary particle types are caused by the weak interaction. The strong force confines the quarks in hadrons and basically holds together the nucleons in nuclei. The following paragraph illustrates the properties of the strong force acting between the quarks and gluons.

The bricks of hadronic matter: the quarks

According to the Standard Model of particle physics all hadronic matter is built from six fundamental quarks. The quark type is referred to as "flavour". These six different quarks listed in table 1.2 are grouped in three generations containing one quark of electrical charge $+2/3$ and one of charge $-1/3$. The first generation forms the basis of the "common material of the present universe"[10]: the protons and neutrons. They are built from the lightest quarks u and d. Hadrons containing heavier quarks are unstable and decay to particles made from u and d. In order to study the characteristics of matter containing quarks of the 2nd or 3rd generation, they need to be produced. This can happen either naturally in cosmic ray events or artificially by the utilisation of particle accelerators. The heavier the hadron or the heavier the quarks it consists of, the higher the energy of the colliding particles must be according to $E = m c^2$. The top quark, for example, was discovered in $p\bar{p}$ (proton - anti-proton) collisions at a centre of mass energy of 1.8 TeV at Fermilab (USA) in 1995 [11, 12]. The generations are completed by the same amount of leptons - elementary particles, that only interact via the electromagnetic (if they carry electrical charge) and the weak force. The corresponding lepton pairs in each generation are the electron e^- and the electron neutrino ν_e (1st generation), the muon μ^- and its neutrino (2nd generation) and finally the tau τ^- and its neutrino (3rd generation). Whereas the neutrinos seem

1.	m (GeV/c^2)	2.	m (GeV/c^2)	3.	m (GeV/c^2)	electr. charge
u	$2.3 \pm_{0.5}^{0.7} 10^{-3}$	c	1.275 ± 0.025	t	$173.21 \pm 0.51 \pm 0.71$	$+2/3$
d	$4.8 \pm_{0.3}^{0.5} 10^{-3}$	s	$95 \pm 5\, 10^{-3}$	b	4.18 ± 0.03	$-1/3$

Table 1.2: The three quark generations represented by quarks of six different flavours of mass m grouped to pairs. The u-, d-, and s-quark masses are estimates of so-called current-quark masses, the c- and b-quark masses are the "running" masses [13]. In case of the t-quark, the mass was directly measured.

to have either no or a vanishing low mass, the electron, the muon and the tau can be ordered according to their mass with the electron being the lightest particle. Also here, transitions from the heavier leptons to the lighter ones are possible. In case of the neutrinos, a change of type is possible for all generations. Latest results have shown, that neutrinos even change their type many times while moving distances of kilometres [14].

As a final remark to the particle "zoo" it is necessary to allude that the above-mentioned quarks and leptons are categorized as fermions whereas the gauge particles as bosons. The difference between fermions and bosons is given by the special characteristic called spin, which is an additive quantity either being of integer value in case of bosons or of n times $1/2$, with $|n| > 0$, in case of fermions. Consequently, combinations of three quarks, i.e. baryons, are thus fermions $(3 \cdot 1/2)$ and bound states of a quark and an anti-quark, i.e. mesons, form bosons.

Characteristics of the strong force

Regarding the theoretical perspective, the interactions between the quarks and the exchange particles of the strong force, the massless gluons (see table 1.1), are described by Quantum Chromo Dynamics (QCD) [15], which represents a relativistic gauge field theory [16]. In analogy to the electric charge as conserved quantity in the corresponding gauge theory of Quantum Electro Dynamics (QED), QCD also contains a charge, the so-called colour charge. This is not only carried by the quarks but also by the gluons that can thus self-interact, contrary to the photons in QED. The colour charge appears in three charge states[3], red, green and blue for quarks as well as in their opposite states, anti-red, anti-green and anti-blue for anti-quarks. A colour neutral state is given, if all three colours are present or if a colour and its anti-colour are combined. In contrast to a quark, a gluon is charged with a colour and an anti-colour; the latter's opposite charge must be different to the colour charge in order to cause the interaction to be colour independent and ensure that the gluons couple only to colour charged objects. If a gluon was neutral, it would couple to colour neutral objects which would cause an infinite range of the strong force that is against observation.

---

[3]The existence of three colour charges as internal degrees of freedom defines the symmetry group of QCD, which is the special unitary group SU(3). From its dimension definition $n^2 - 1 = 8$ eight coloured gluons can be derived. As a guidance, the QED symmetry group is the unitary group U(1) with dimension 1, which is inherited from the single electrical charge.
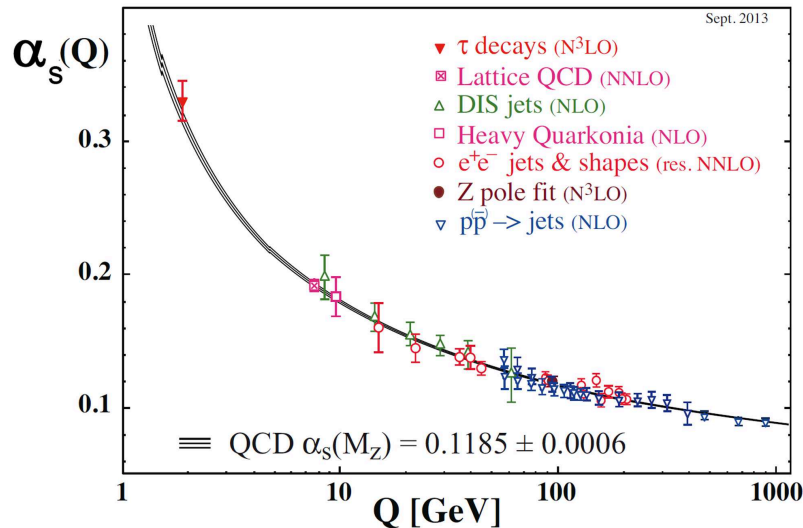
Figure 1.2: Summary of measurements of α_s as a function of the energy scale Q. The respective degree of QCD perturbation theory used in the extraction of α_s is indicated in brackets (NLO: next-to-leading order; NNLO: next-to-next-to leading order; res. NNLO: NNLO matched with re-summed next-to-leading logs; N3LO: next-to-NNLO). Figure and caption taken from [13].

The strong force: qualitative and a quantitative consideration

Though being the strongest force in respect to its strength, the range of the strong force is limited to subatomic length scales which is a consequence of the distance dependence of its potential [17]. The phenomenological description of this potential,

$$V = -\frac{4}{3} \cdot \frac{\alpha_s}{r} + k \cdot r, \tag{1.1}$$

with α_s as the coupling factor of the strong force, the linear string strength k and r as the distance of two sources of the strong force, is referred to as the Cornell potential [17]. In fact, this is a simplified and qualitative description of the potential of a (static) quark-anti-quark ($q\bar{q}$) pair.

Though being of phenomenological nature, this formula serves as a starting point for the calculation of quantum states: The potential shows a Coulomb like behaviour for short distances but asymptotically approaches infinity for infinite distances. The latter leads to a confinement of the quarks in a colour neutral state as for example in a $q\bar{q}$ pair. An increase of the distance between the quark and the anti-quark increases the energy between them, which finally causes the production of a new quark-anti-quark pair from the vacuum. The initial quark and anti-quark together with those newly created form again colour neutral hadrons. Totally free quarks have not yet been observed [13]. On the other hand, at small distances the potential is a result of the single gluon exchange resulting into a similar potential as between elementary charges [10].

Leaving behind phenomenology, measurements of α_s revealed that the coupling of the strong force is not constant but strongly depending on the momentum transfer Q^2 or on the distance[4] r, i.e. the coupling is a so-called running coupling. Figure 1.2 shows

---

[4]The momentum can be translated into a minimal distance and vice versa via Heisenberg's uncertainty principle $\Delta p \Delta r \geq \hbar$, with $\hbar$ as the Planck constant divided by 2π.

$\alpha_s(Q^2)$ as measured by different experiments. These results are not only extremely important for revealing the nature of the strong coupling but also for determining its values at different energies, because "QCD does not predict the actual value of $\alpha_s(Q^2)$, however it definitely predicts the functional form of the energy dependence of α_s. [...] The value of $\alpha_s(Q^2)$, at a given energy or momentum transfer scale Q^2, must be obtained from experiment."[18] The coupling becomes large at small energy scales but small at high energies:

$$\alpha_s(Q^2) \rightarrow \infty \qquad \text{for} \quad Q^2 \rightarrow 0 \qquad\qquad \text{confinement,} \qquad (1.2)$$
$$\alpha_s(Q^2) \rightarrow 0 \qquad \text{for} \quad Q^2 \rightarrow \infty \qquad\qquad \text{asymptotic freedom,} \qquad (1.3)$$

leading to confinement in the first case and to the so-called asymptotic freedom in the second case, which is discussed in the following paragraph.

Asymptotic freedom

As seen in figure 1.2, at high momentum transfers the strength of the coupling decreases with Q and reaches values smaller than unity. This allows the application of the mathematical technique called perturbation theory[5], which facilitates theoretical predictions when analytical calculations are not feasible as it is discussed later. Applying this to the mathematical formulation of QCD, the QCD Lagrangian (see eq. 1.7), the perturbative QCD (pQCD) formulation is obtained from which a description of the running coupling α_s in the given energy regime can be derived [10, 19]:

$$\alpha_s(Q^2) = \frac{\alpha_s(\mu^2)}{1 + \alpha_s(\mu^2)\beta_0 \ln\left(Q^2/\mu^2\right)} \qquad (1.4)$$

with β_0 containing N_f, the number of active quark flavours at the energy scale Q (active means $m_q < Q$). If a renormalisation scale μ is chosen, α_s can be calculated analytically at any energy scale $Q^2 > 1\,\text{GeV}$. At energies below this threshold, perturbative methods are not applicable any more.

This description of α_s in the perturbative limit is a leading order calculation, where only the first part of the series expansion of α_s is considered. Equation 1.4 extended with higher order corrections describes very well the various measurements for the mass of the neutral gauge boson of the electroweak interaction Z^0 with $m = 91\,\text{GeV}$ [13] as energy scale, which can be seen in figure 1.2. Politzer [20], Gross and Wilzcek [21] were awarded with the Nobel prize 2004 for this derivation of the asymptotic freedom from QCD. The current world average value is $\alpha_s(M_{Z^0}) = 0.1185 \pm 0.0006$ [13].

Introducing the parameter Λ with

$$\Lambda^2 = \frac{\mu^2}{e^{1/(\beta_0\alpha_s(\mu^2))}}, \qquad (1.5)$$

which has the dimension of energy and is technically identical to the energy scale Q, where $\alpha_s(Q^2)$ diverges to infinity, the coupling can be written as

$$\alpha_s(Q^2) = \frac{1}{\beta_0 \ln\left(Q^2/\Lambda^2_{\text{QCD}}\right)}, \qquad Q^2 \gg \Lambda^2_{\text{QCD}}, \qquad (1.6)$$

---

[5]"In quantum field theories like QCD and QED, physical quantities R can be expressed by a perturbation series in powers of the coupling parameter α_s or α, respectively. If these couplings are sufficiently small, i.e. if $\alpha_s \ll 1$, the series may converge sufficiently quickly such that it provides a realistic prediction of R even if only a limited number of perturbative orders will be known."[18]

with $\Lambda = \Lambda_{\mathrm{QCD}}$. The latter sets the fundamental scale of QCD, where hadronisation, the transition to confinement, sets in. In fact, this parameter is the only free parameter of QCD in this energy regime. Including higher order corrections in the perturbative calculation, the value of the Λ_{QCD} parameter is

$$\Lambda_{\mathrm{QCD}} = 213 \pm 8 \, \mathrm{MeV} \approx \frac{\hbar c}{1 \, \mathrm{fm}} = \frac{197 \, \mathrm{MeV \, fm}}{1 \, \mathrm{fm}},$$

in case of five flavours (u, d, s, c, b) entering in the determination of Λ. This is appropriate if hadronisation processes are considered, since the top quark decays before it has time to hadronise [13].

Confinement

Processes at low Q^2, where α_s is larger than unity, are not analytically calculable, because there, QCD represents a complicated non-linear theory (see next paragraph). As a consequence, up to now no analytic ab-initio derivation exists for the confinement at $Q < \Lambda_{\mathrm{QCD}}$. In this case, special numerical techniques or approximations need to be applied. An example performed in a fundamental manner is given by the lattice QCD (LQCD) approach, which includes in first principles calculations of discrete space-time [22].

The QCD Lagrangian

Finally, for completeness, a formulation of the QCD Lagrangian is presented here [13]:

$$\mathcal{L}_{\mathrm{QCD}} = \sum_f^{N_f} \bar{\psi}_{f,a} \left(i\gamma^\mu \partial_\mu \delta_{ab} - g_s \gamma^\mu t_{ab}^C A_\mu^C \frac{\lambda^a}{2} - m_f \delta_{ab} \right) \psi_{f,b} - \frac{1}{4} F_{\mu\nu}^A F^{A\mu\nu}, \qquad (1.7)$$

with ψ_f the quark field spinors, a the colour-index (from $a = 1$ to $N_c = 3$, i.e. quarks can have one of three colours), f the quark flavour index (from $f = 1$ to $N_f = 6$), γ^μ the Dirac matrices, m the quark mass and $F_{\mu\nu}^A$ the gluon field tensor, A_μ^C the gluon fields or colour four potential with C running from 1 to $N_C^2 - 1 = 8$ yielding eight kinds of gluons, $g_s = \alpha_s \cdot 4\pi$ the strong coupling. t_{ab}^C are the eight 3×3 matrices, the generators of SU(3). The part between the quark fields is analogously constructed to the well understood Lagrangian of QED. The major difference however appears in the field $F_{\mu\nu}^A$ which is given by

$$F_{\mu\nu}^A = \partial_\mu A_\nu^A - \partial_\nu A_\mu^A - g f_{ABC} A_\mu^B A_\nu^C, \qquad (1.8)$$

with f_{ABC} being the structure constants of SU3. This field tensor is similar to that from QED except the self-interaction term of the gluon fields, which is represented by the last term in equation 1.8. This leads to non-Abelian or non-commutative behaviour[6] causing the confinement as well as the asymptotic freedom. Albeit screening effects, as for example the virtual screening of the electrical charge by an electron-positron pair, are present in any Abelian and non-Abelian theory, the anti-screening effect due to gluons carrying colour and anti-colour is solely a feature of non-Abelian gauge theory. If the anti-screening prevails, asymptotic freedom is reached [23].

---

[6]The order of a group operation depends on the order of the groups, i.e. interactions cannot be exchanged: $AB \neq BA$.

QGP and QCD

The main message of this section to be conveyed is, that within QCD, there are two inherent extreme states for elementary nuclear matter: either the quarks are confined in hadrons or they are deconfined as a result of the asymptotic freedom. From the latter, the contingency of a QGP can be derived albeit its characteristics are not given by QCD and hence need to be modelled. Competing scenarios are an ideal gas of weakly coupled quarks and gluons or a hadron resonance gas and a strongly interacting system showing a fluid like behaviour. At RHIC energies, the system seems to be strongly interacting, almost a perfect liquid [9]. At higher temperatures at LHC, a weaker coupled fluid could be expected due to the dependence of α_s on the energy scale [24]. For further proof and for revealing more characteristics of the QGP, the research work is lively ongoing as elaborated in the following sections.

1.3 "Little bangs in the laboratory": Motivations and goals

"Little Bangs in the laboratory - or how to cook a QGP"

Figure 1.2 contains all information needed for two basic recipes for the creation of the QGP:

- compressing via reducing $r \Rightarrow Q \uparrow$, i.e. low collision energies

- heating via increasing $Q \Rightarrow r \downarrow$, i.e. high collision energies.

The compression of two nuclei leads to a high density in a small volume, which causes small interaction ranges. The latter can be translated into large momentum transfers via the uncertainty principle, which are accompanied by a small coupling as seen in figure 1.2. In a simple picture of the bag model, the protons and neutrons of finite size start to overlap and finally to dissolve into quarks and gluons at certain critical density ρ_c. On the other hand, large momentum transfers can be achieved via high temperatures - the temperature serves a measure of energy and especially of kinetic energy. At a critical temperature T_c, the baryons of the nuclei start to overlap causing a system of deconfined quark matter.

These two methods of creating a QGP artificially are realized at different accelerator facilities. Whereas at LHC and RHIC the heating method is pursued with the help of high collision energies, smaller accelerators as the Super Proton Synchrotron (SPS) at CERN or the future Facility of Antiproton and Ion Research (FAIR) at GSI (Germany) operate at lower collision energies (factor 100-1000) in order to compress the nuclear matter.

Qualitative picture of phase diagram

The given recipes mark two regions in the so-called phase diagram of QCD, which relates the temperature to the pressure of nuclear matter expressed by the baryo-chemical potential μ_{B}. The latter describes the excess of baryons to anti-baryons, i.e. if $\mu_{\mathrm{B}} > 0$, the system is baryon dominated. For grond-state nuclear matter μ_{B} is close to 1 GeV [9].

A sketch of the phase diagram is displayed in figure 1.3. At LHC energies, $\mu_{\mathrm{B}} \approx 0$, which was also the case during the evolution of the early universe. This again motivates research projects in the field of heavy-ion physics since realizing $\mu_{\mathrm{B}} \approx 0$ means

scientifically going backwards in the cosmic evolution. From astrophysics it is expected, that cold nuclear matter, which can be created by compressing with $\mu_{\mathrm{B}} > 1\,\mathrm{GeV}$, is present in neutron stars [25].

"The coupling constant runs towards a smaller value with increasing energy scale. It is hence a natural anticipation that QCD matter at high energy densities undergoes a phase transition from a state with confined hadrons into a new state of matter with on-shell (real) quarks and gluons." [26] The critical energy density for the transition to a QGP is according to LQCD calculations around $1\,\mathrm{GeV/fm^3}$ [27], which is about an order of magnitude larger than that inside the nuclei, where $\varepsilon_{\mathrm{nm}} \approx 0.15\,\mathrm{GeV/fm^3}$ [6]. Experimentally, the estimation of the achieved initial energy density is obtained with the Bjorken formula [28]:

$$\varepsilon_B = \frac{1}{\pi R^2 \tau_0} \cdot \left. \frac{\mathrm{d}E}{\mathrm{d}\eta} \right|_{\eta=0}, \tag{1.9}$$

with R as the initial radius of the collision system, τ_0 as the formation time and $\mathrm{d}E/\mathrm{d}\eta$ as the measured energy per unit rapidity $\mathrm{d}\eta$. In the transverse plane this is $\mathrm{d}E/\mathrm{d}\eta/\mathrm{GeV} = \mathrm{d}E_{\mathrm{T}}/\mathrm{d}\eta/\mathrm{GeV} \approx 1.25 \cdot \mathrm{d}N_{\mathrm{ch}}/\mathrm{d}\eta$ [29]. Using the value for $\mathrm{d}N_{\mathrm{ch}}/\mathrm{d}\eta = 1601 \pm 60$ as measured by ALICE [30], $R = 6.62\,\mathrm{fm}$ for $^{208}\mathrm{Pb}$ [31] and τ_0 assumed to be maximal $1\,\mathrm{fm}/c$ (with $c = 1$), one can calculate the energy density at $\sqrt{s_{\mathrm{NN}}} = 2.76\,\mathrm{TeV}$:

$$\varepsilon_B = 14.53 \, \frac{\mathrm{GeV}}{\mathrm{fm^3}}. \tag{1.10}$$

This value is a conservative estimate of the energy density, which grows with decreasing formation time. Already with an assumed formation time of $1\,\mathrm{fm}/c$, the energy density exceeds the critical density from the LQCD calculations, showing the capability of the LHC experiments to produce a QGP, if the theoretical estimates are correct.

The current estimates of the critical temperature given by the LQCD groups are $150\,\mathrm{MeV}$ (depending on the normalisation) [27] and $154 \pm 9\,\mathrm{MeV}$ [32]. In [33] it is however stated, that there is no unique T_{c} expected, because the phase transition is a non-singular cross-over. The maximum temperatures reached at LHC are estimated via hydrodynamic calculations to be around $470\,\mathrm{MeV}$ [34], which is three times larger than the given estimate for T_{c}. Hence, it can be expected that a phase transition is realised in heavy-ion collisions at $\sqrt{s_{\mathrm{NN}}} = 2.76\,\mathrm{TeV}$.

Another feature of nuclear matter as shown in figure 1.3 is the strong increase of the energy density over a narrow range of temperature. The "energy density, pressure and entropy are all roughly proportional to the number of degrees of freedom" [35], hence the drastic change in degrees of freedom seems to cause rapid changes in these parameters. Whereas well below T_c, the active hadronic degrees of freedom are limited to three (dilute gas of three charge states of pions[7]), above T_c there are 40 - 50 internal degrees of freedom activated, which is mainly influenced by the additional 8 gluon degrees of freedom.

Besides the determination of T_{c}, the order of the phase transition is another open issue: Is it a first or second order phase transition[8]? Does a cross-over phase exist at

---

[7]Pions: π^+, π^0, π^- are mesons consisting of $u\bar{d}$, $u\bar{u} + d\bar{d}$, $d\bar{u}$

[8]A first order phase transition is characterised by a discontinuity of the first derivative of an EoS, a second order phase transition is given in case of a discontinuity of a second derivative. Typical for
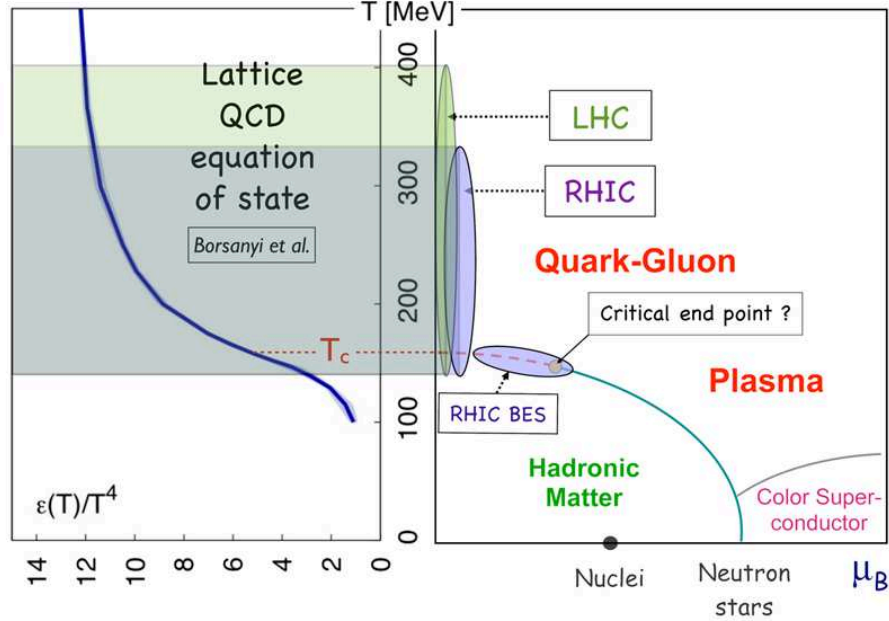
Figure 1.3: Phase diagram of QCD matter (right panel) overlaid with regions covered by LHC and RHIC. The experimentally covered ranges are projected onto the energy density versus temperature at $\mu_B = 0$ curve calculated by lattice QCD (left panel). Figure and caption taken from [37]. The energy density is calculated in [27].

small μ_B instead of a phase transition? Is there a critical point marking the limiting point of a phase transition region and if so, at which (μ_B, T)? Vital for answering these questions is the profound understanding of the QGP properties. More specifically, it is necessary to clarify, if the medium really behaves like a fluid and if so, is it an ideal or viscous fluid? Which viscosity can be expected and how dense is the medium? And subsequently: When and how does the system freeze out[9]? Which kind of stages are present between the initial collision and final freeze-out? What are the matter properties during these stages? Could early thermalisation be assumed?

Due to the difficulty to calculate heavy-ion collisions with QCD, many theoretical models or numerical techniques have been established to explain the measurements and make predictions to motivate further measurements. Since from QCD itself neither a phase transition region from the confinement to the asymptotic freedom nor a coexistence of the two states are deducible [6], many models are dedicated to the description of the phase diagram of nuclear matter and to the Equation of State (EoS) in particular. The determination of the critical temperature for a given baryo-chemical potential, where a phase transition of first or second order could happen, is among the main goals.

Concluding this section, the motivation of ALICE is to measure observables that reveal the properties of the medium created during heavy-ion collisions as well as the collision system evolution.

the latter is a continuous behaviour of the order parameter of interest, whereas a step is seen in the first case. This classification of phase transitions is also referred to as Ehrenfest classification [36].

[9]A common, simplified definition of the freeze-out says, that the newly created hadrons decouple when the mean free path of the particles in the system is larger than the system size. The mean free path is given by $\Lambda = 1/n\sigma$ where σ is the cross section of elastic collisions between the particles.

1.4 Research approach

The collision evolution with a duration of 10^{-23} s is technically not possible to be followed. Thus, observables are vital that reveal the characteristics of the medium and the underlying processes during the different evolution phases. Observables serve as a connection of measurements to theory, which is needed in order to extract information from experimental results. On the other hand, the measurements are crucial for the constraint of models, which are usually restricted in their predictive power without experimental input - otherwise, analytical calculations would have already replaced the models.

Concerning the experimental approach, two main strategies are listed in the following, that will be further elaborated in the later text; the last two additional methods are added for completeness:

- Study of processes at high momentum transfer, where the running coupling α_s is smaller than unity and hence the QCD calculations can be performed in a pertubative manner.

- Investigation of particles which contain in- or exclusively quarks that are not the constituents of the colliding nuclei, i.e. no u and d quarks.

- Quantification of collective effects via correlation analyses in order to shed light on the system propagation/dissipation, which serves as input for the EoS.

- Measurement of global event properties such as temperatures of different phases of the system evolution, e.g. initial stage, chemical or kinetic freeze-out, energy and entropy distribution via particle spectra, mean p_T and particle abundances or multiplicities.

In general, the experimental method of extracting information from a hadron collision perused by all experiments in the field of high energy physics is to analyse the properties of the particles created in the collisions regarding their mass, abundance, momentum and spatial distribution, providing various levels of complexity and differential formats. From the particle emission pattern, it is principally feasible to trace back the processes during the collision, provided that the theoretical assumptions for the measurements are correct. The latter is important since most of the measured distributions represent integrals over the whole system evolution.

Stable particles, which are (nearly) directly seen by the detector are for example protons, deuterons, charged pions, charged kaons, electrons, muons, photons. An experimental challenge is however given by the early decay of some produced particles, which do not reach the detector, but their decay daughters do. The particle decays can be driven by the strong or the (electro-)weak force. Strong decays can happen even within the final phase of the system evolution resulting in extremely small decay lengths of fm, which might never be possible to resolve technically. Decays by reason of the weak force however have mean life times or to be more descriptive, decay lengths of the order of μm to m, which are to a certain extent properly measurable via the detection of their stable decay products or even stable secondary decay products. Vital for this is an appropriate space resolution of the particle tracks in the detector as well as a sufficiently good momentum resolution.

The theoretical research means are summed up in [37]: "The theory tool-kit in relativistic heavy-ion physics is quite diverse. It includes QCD perturbation theory in the vacuum and in a thermal medium (especially for the description of jets and heavy quarkonia); semi-classical gauge theory (for the description of the initial conditions reached in the nuclear collision); lattice gauge theory (for static thermodynamic properties of QCD matter, such as its equation of state and colour screening); holographic methods mapping strongly coupled gauge theories on their gravity duals (for transport properties and the dynamics of thermalization); and transport theory, especially viscous hydrodynamics (for the evolution of the bulk matter)." In the adjacent chapter, more details about some of these models will follow.

The bridge between the theoretical and experimental research field is built by the Monte Carlo (MC) event generators. The Monte Carlo method as invented in 1949 [38] is used within event generators [39] in order to numerically calculate the output of a particle collision under predetermined conditions, for example the evolution time, the viscosity, parton spectra etc. Whereas in theory the generators are predominantly used to make predictions and to develop techniques to propose to the experiments [39], experimentalists utilize it mainly in combination with a detector simulation in order to obtain corrections for the data and to test the data analysis procedure (in absence of measured data).

1.5 A brief history of heavy-ion collision research

The introductory chapter is closed by a brief review of the history of heavy-ion collisions in order to emphasise the complexity of the field and to document the developing capabilities of accelerator facilities.

"The research field of Relativistic Heavy Ion Collisions was born in the late 1960s, from a coincidence of questions arising in astrophysics (neutron star interior matter, supernova dynamics, early stages in the cosmological evolution) and in fundamental nuclear/hadronic physics (extended nuclear matter and its collective properties, excited hadronic matter and its limits of existence)." [40]. The quest for the phase diagram of extended QCD matter and the EoS has coined the research field since the first experiments were performed at the BEVALAC of the Laurence Berkeley National Laboratory (LBNL) (USA) at centre of mass (c.m.) energies per nucleon-nucleon pair of $\sqrt{s_{NN}} = 1$ - $2\,\mathrm{GeV}$ and at the Joint Institute for Nuclear Research (JINR) in Russia in the 1970ies. The main discovery was the observation of compressed nuclear matter. These studies were followed by intensive and comprehensive measurements at the Brookhaven Alternating Gradient Synchrotron (AGS) energies up to $\sqrt{s_{NN}} = 5.4\,\mathrm{GeV}$ from 1986 until 1991 and at the SIS 18 at GSI up to $\sqrt{s_{NN}} = 8\,\mathrm{GeV}$ from 1990 till present. These research activities were extended by measurements at the SPS at CERN with heavy-ion collision energies up to $\sqrt{s_{NN}} = 19.4\,\mathrm{GeV}$ from 1986 to 2000. The outcome of these experiments was that "compelling evidence has been found for a new state of matter, featuring many of the characteristics expected for a Quark-Gluon Plasma" [41]. All experiments at the above-mentioned accelerator laboratories have in common, that they have been fixed-target experiments, where a beam of ions or protons hits a fixed target. In the c.m. system, this is a symmetric collision at an energy of $E_{cm} = 1.37 \cdot \sqrt{E_{beam} \cdot \mathrm{GeV}}$, which is much smaller than the initial beam energy. However, the collision of two particle beams supplies twice the beam energy in the c.m. system. This advantage was made use of during the planning of accelerators for

experiments requiring higher c.m. energies. The RHIC at BNL was the first collider in the heavy-ion research history offering a maximum energy of $\sqrt{s_{NN}}$ = 200 GeV. Currently, energies from $\sqrt{s_{NN}}$ = 19.4 - 200 GeV are investigated there within a beam energy scan programme. The results from RHIC have led to the discovery that the partonic matter, the QGP, behaves rather like a strongly coupled perfect liquid than like a weakly coupled plasma or ideal gas of quarks and gluons in the vicinity of the phase boundary. In terms of collision energy, the RHIC programme is followed by heavy ion collision measurements at LHC, providing energies of $\sqrt{s_{NN}}$ = 2.76 - 5.1 TeV. According to the huge increase in beam energy as compared to RHIC, the associated cross sections for the production of jets and heavy quarks as well as the particle density are much larger, hence more precise investigations of the QGP can be performed. At LHC, the QGP is expected to be hotter, larger, and longer living.

1.6   Organization of this thesis

The remainder of this thesis is organized as follows: the next chapter discusses the motivation and research objectives of the thesis subject. Afterwards, the experimental conditions are reviewed in chapter 3. In chapter 4 follows the description of the analysis concepts and methods. Finally, the results are presented in chapter 5 and discussed in the adjacent and last chapter 6 .

<div style="text-align: right; font-size: 4em; color: #1a5fb4; font-weight: bold;">2</div>

Problem statement: Modification of p_{T} spectra in AA collisions

Could a heavy-ion collision be described by a superposition of individual nucleon-nucleon collisions? If not, which mechanisms are responsible for a deviating behaviour? How could this deviation be quantified and how could it be related to the properties of the created matter?

Experimentally, as an entrée to the unfolding of the peculiarities of heavy ion collisions, differential analyses of particle abundances as a function of the transverse momentum (p_{T}) are commonly performed. The advantage of the analysis of p_{T} distributions over those of longitudinal momentum p_{L} is given by the fact that the initial parton p_{T} is negligibly small as compared to p_{L} and thus the final p_{T} of the produced hadrons is predominantly created during the collision process. Therefore, the p_{T} spectra of the measured hadrons provide a link to the underlying processes of the reaction and the system evolution. Performing this for different collision centralities in nucleus-nucleus (AA) collisions, i.e. for different overlap areas of the colliding nuclei, the changes of the p_{T} distribution for different amounts of participating[1] or colliding[2] nucleons can be studied: Do the features of the medium change with the number of colliding nucleons? Is it possible that a Pb–Pb collision is similar to a pp collision if peripheral enough? These questions lead to the comparison of p_{T} distributions from Pb–Pb collisions to those from pp. Since the underlying theory to describe the reactions in pp at high p_{T} is pQCD (for the vacuum case), the p_{T} spectra in pp provide a reference for understanding the QCD processes embedded in a medium created in Pb–Pb collisions. A common quantitative measure of the difference of pp and Pb–Pb collisions is the nuclear modification factor

$$R_{\mathrm{AA}} = \frac{1}{\sigma_{\mathrm{INEL}}^{\mathrm{pp}} \ \langle T_{\mathrm{AA}} \rangle} \cdot \frac{(\mathrm{d}N/\mathrm{d}p_{\mathrm{T}})_{\mathrm{AA}}}{(\mathrm{d}N/\mathrm{d}p_{\mathrm{T}})_{\mathrm{pp}}} \qquad (2.1)$$

as introduced in [42] with $\sigma_{\mathrm{INEL}}^{\mathrm{pp}}$ as the total inelastic hadronic cross section in pp collisions and $\langle T_{\mathrm{AA}} \rangle$ as the nuclear thickness function. Since $\sigma_{\mathrm{INEL}}^{\mathrm{pp}} \cdot \langle T_{\mathrm{AA}} \rangle = \langle N_{\mathrm{coll}} \rangle$, the

---

[1]Participating nucleons are those nucleons, which suffered at least one inelastic interaction.

[2]The number of colliding nucleons or the number of average binary collisions describes the total number of inelastic nucleon-nucleon collisions.
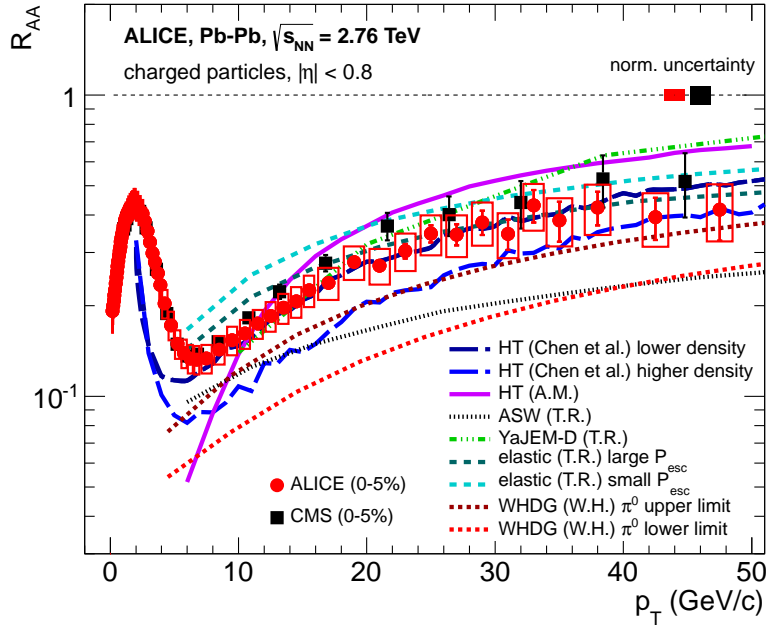
Figure 2.1: Nuclear modification factor R_{AA} of charged particles measured by ALICE in the most central Pb–Pb collisions (0 - 5%) at $\sqrt{s_{NN}} = 2.76\,\text{TeV}$ in comparison to results from CMS and different model calculations [47].

total number of binary nucleon-nucleon (NN) collisions in AA collisions, the following equation is frequently used:

$$R_{AA} = \frac{1}{\langle N_{coll} \rangle} \cdot \frac{(dN/dp_T)_{AA}}{(dN/dp_T)_{pp}}. \tag{2.2}$$

The result from pp collisions is scaled p_T-independently by the number of possible binary NN collisions in a Pb–Pb collision. A deviation of R_{AA} from unity hence reveals, that the Pb–Pb collisions are not simple super-positions of individual nucleon-nucleon collisions. It should be noted, that the assumed binary collision scaling applies only to hard processes, i.e. to processes that contribute predominately to the high-p_T region [43]. At low p_T, the particle production scales with the number of participants (N_{part}) [30], which means that only the number of nucleons taking part in the reaction are relevant but not the individual nucleon-nucleon collisions. Thus, a deviation of R_{AA} from unity at low p_T can be expected, if N_{coll} is used for the R_{AA} calculation. Alternatively, R_{AA} scaled with N_{part}, as it was performed in [44], can be studied to investigate the low p_T region and the transition to a probable N_{coll} scaling.

Typically, for hadrons, consisting of strongly interacting partons, this parameter is smaller than unity, disclosing that the medium is strongly interacting. If so, one speaks about a suppression of the particle yields as a function of p_T or centrality in Pb–Pb as compared to pp. In 1982 Bjorken already predicted such a suppression for hadrons at high p_T [45], which was later referred to as jet quenching in [46] (see section 2.1). An example for R_{AA} of charged particles (mainly hadrons: pions, kaons and protons) is shown in figure 2.1, where the results published by the ALICE collaboration [47] are displayed. In contrast to hadrons, there is no suppression visible for electromagnetic and/or weakly interacting particles (see figure 2.2), such as photons, $W^{+,-}$ and Z^0 bosons respectively, which underlines the dominance of the strong interaction in the
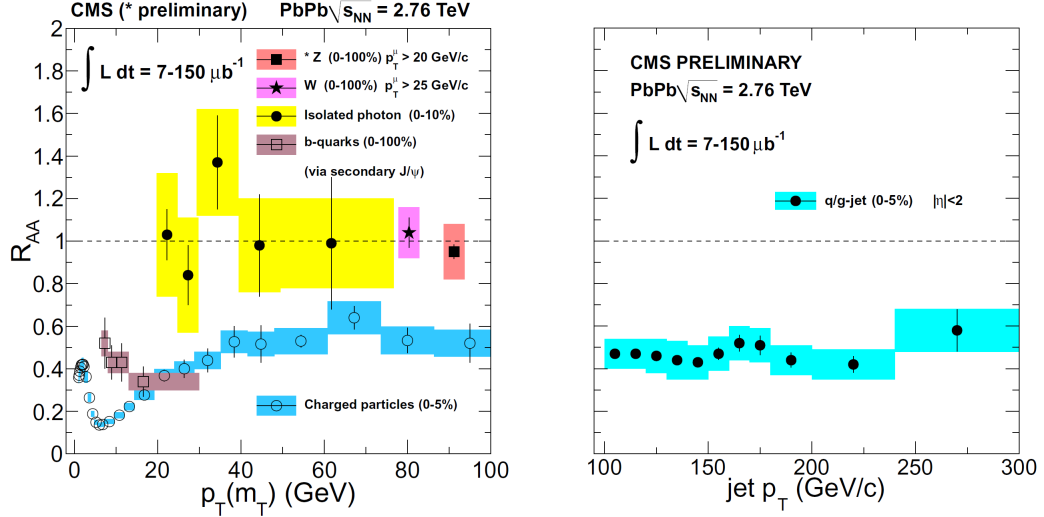
Figure 2.2: Nuclear modification factor R_{AA} of different particles measured by CMS [48].

medium. Moreover, the binary collision scaling shows that their production rates are not modified by the presence of a medium.

The interpretation of the observed hadron suppression in AA collisions is that an elementary reaction between two colliding partons - including their scattering as well as their properties after the scattering and their fragmentation into hadrons - is modified by the surrounding medium. This modification could possibly be driven by

- absorption

- energy loss

in the medium, which are currently considered as the dominant effects. While the first effect would lower the p_T spectrum due to a decrease of the abundance (downward shift), the latter could cause a shift of the spectrum to lower p_T values (shift to the left) [49]. For the high p_T region, one would expect that the energy loss dominates as a function of the length traversed by the parton in the medium, since the momentum is still large enough for escaping the medium and fragmenting outside into hadrons before being absorbed. Whether fragmentation inside the medium needs to be taken into account and if this process is modified is currently under investigation.
Two momentum regions can roughly be distinguished in the R_{AA} distribution in figure 2.1: the low-to-intermediate-p_T region from $0 < p_T < 6\,\text{GeV}/c$, where a local maximum is observed, and the high-p_T region for $p_T > 6\,\text{GeV}/c$, which is characterized by a strong rise and a subsequent saturation region. The following sections discuss these two momentum regimes separately.

2.1 High p_T: Fragmentation, jets and in-medium energy loss

The high transverse momentum region of particle spectra is of special interest, since partons with high p_T are predominantly produced in scattering processes with high momentum transfer at the initial stage of the collision ($Q \gg \Lambda_{QCD}$). In case of a pp

collision, the underlying processes is possible to be calculated via pQCD, because a pp collision can be rather regarded as a collision of the partons in the vacuum. In case of heavy-ion collisions though, the hard scattering processes are embedded in the partonic medium, which builds up at the same time as the scattering takes place. The following interactions with the medium complicate the prediction of final hadron p_T spectra as compared to pp.

Nevertheless, the calculations of hard processes in pp serve as basic input for heavy-ion collision models. Therefore, the following paragraph is dedicated to the pQCD approach of calculating identified hadron high-p_T spectra in pp collisions.

Hard scatterings in elementary reactions

On the basis of Feynman's parton model of hadrons [50, 51], in which the hadron consists of three point-like constituents, the partons, Bjorken has first described the hard scattering cross section of two hadrons (e.g. pp) for the inclusive reaction $A + B \rightarrow h + X$ [52]: "Choose a collinear frame of reference in which the initial projectiles move relativistically and in opposite directions. Replace each projectile A, B by a beam of massless, non-interacting partons (a, b) ... Regard the collision as a 2-body collision of a parton from each beam, the cross section depending only on [the momenta] of the interacting parton pair and independent of the rest of the environment of 'spectator' partons". In fact, the hadron reaction $A + B \rightarrow h + X$ is regarded as if it was an inelastic parton scattering process $a + b \rightarrow c + d$. The successive formulation in [53] is completed with the convolution of the fragmentation function (FF), that describes the probability of the creation of a hadron h from a parton (c in this case) carrying away a fraction z of the parton momentum. The creation process is referred to as fragmentation, where the coloured parton fragments into colour neutral objects. In detail, the fragmentation of a parton implies the creation of q$\bar{\text{q}}$ pairs via g $\rightarrow$ q$\bar{\text{q}}$, gluon radiation (q $\rightarrow$ qg) or splitting (g $\rightarrow$ gg). The coloured remnants with distinctly lower momentum than that of the initial parton finally form colour neutral hadrons. The invariant cross section of identified hadrons as expressed in [53] is given here:

$$E_h \frac{\text{d}^3\sigma}{\text{d}p_h^3}(A + B \rightarrow h + X) = \sum_{\text{abcd}} \int \text{d}x_\text{a}\,\text{d}x_\text{b}\,\text{d}z_\text{c}\, G_{\text{a/A}}(x_\text{a})\, G_{\text{b/B}}(x_\text{b})\cdot$$

$$D_{h/\text{c}}(z_\text{c}) \frac{\hat{s}}{z_\text{c}^2 \pi} \frac{\text{d}\sigma}{\text{d}\hat{t}}(\text{ab} \rightarrow \text{cd})\, \delta(\hat{s} + \hat{t} + \hat{u}),$$

(2.3)

$$\text{with} \quad \left.\frac{\text{d}\sigma}{\text{d}\hat{t}}\right|_{\hat{s}} = \frac{\pi\,\alpha_s(Q^2)}{\hat{s}^2} \sum^{\text{ab}}(\cos\theta^*) \qquad (2.4)$$

as the fundamental sub-process cross section, $x_\text{a} = p_\text{a}/p_\text{A}$ as the momentum fraction of parton a from hadron A, $G_{\text{a/A}}(x_\text{a})$ as the probability of finding parton a in hadron A (parton distribution function PDF), $D_{h/\text{c}}(z_\text{c})$ as the FF of parton c into hadron h with the momentum fraction $z_\text{c} = p_h/p_\text{c}$. σ denotes the inelastic cross section of the interaction of parton a and b resulting in partons c and d. Finally, the delta function describes the two-body scattering of massless partons. In more detail, it describes the two-body phase space under the assumption that the initial and final partons are collinear with the initial and final hadrons, i.e. no transverse (k_T) smearing is included
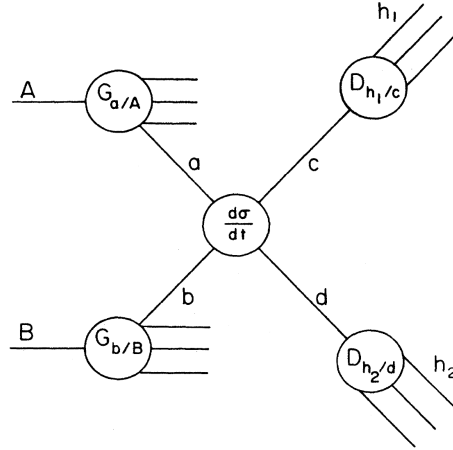
Figure 2.3: Schematic representation of a high p_T reaction factorized into parton distribution functions (G), parton fragmentation functions (D), and a hard scattering process. Figure and caption taken from [53].

[53]. The variables $\hat{s}, \hat{t}, \hat{u}$ represent the so-called Mandelstam variables[3]. A sketch of the scattering process is shown in figure 2.3.

Although the parton model is based on pQCD, it assumes scale invariance of the PDFs and the FFs, which means that they are independent of Q^2; only the scattering cross section has a scale dependence. This assumption originates from the so-called Bjorken scaling, where the structure functions, which describe the internal structure of the proton by combinations of different PDFs, are independent of Q^2 for large parton momentum fractions,

$$x = \frac{Q^2}{2\,M\,\nu} = \frac{Q^2}{2\,\mathbf{P}\mathbf{q}} \quad \text{[13]}, \tag{2.5}$$

with M as the mass of the proton, $\mathbf{P}$ as the proton four-momentum and the momentum transfer $Q^2 = -\mathbf{q^2}$ or ν as the energy loss of the scattering lepton, which is collided with the proton in order to reveal the internal structure of the proton. "This property is related to the assumption that the transverse momentum of the partons in the infinite-momentum frame of the proton is small. In QCD, however, the radiation of hard gluons from the quarks violates this assumption, leading to logarithmic scaling violations, which are particularly large at small x. The radiation of gluons produces the evolution of the structure functions."[13] In order to introduce a scale dependence, which would allow the description of the cross section in a perturbative way, a so-called factorization procedure is applied. Consequently, the scale dependent FFs and PDFs can be related to measurements of identified hadron spectra, e.g. in e^+e^- collisions, and of the hadron structure functions from Deep Inelastic Scattering (DIS) of leptons with protons at a given Q^2. In case of the structure functions this yields:

$$F_2(x) \to F_2(x, Q^2) = \frac{1}{2}\,x \sum_q e_a^2\, f_q(x, Q^2), \tag{2.6}$$

$$\text{where } f_q(x, Q^2) = q(x, Q^2) + \bar{q}(x, Q^2) \tag{2.7}$$

are the PDFs and e_a^2 the electric charge of the quark with flavour q [13].

---

[3]They are a different Lorentz-invariant formulation of the four momenta of the scattering particles with $\hat{s} + \hat{t} + \hat{u} = 0$ for massless particles.

With regard to figure 2.3, on the one hand, the given process can be separated into a hard scattering that takes place between the interacting partons and that can be calculated perturbatively. On the other hand, in the assumed collinear configuration, the interacting quarks have a small relative momentum, which translates into a very strong interaction between them. Hence, pQCD is not applicable until a factorisation scale dependence is introduced, which separates for example the structure function into a part, that is calculable, depending only on Q^2, and into another part, which is not calculable but can be constrained by measurements. "The [factorisation] scale [μ_F] can be thought as one which separates the perturbative short-distance physics from the non-perturbative long-distance physics. Thus partons emitted at small transverse momenta $< \mu_F$ (i.e. approximately collinear processes) should be considered as part of the hadron structure. Partons emitted at large transverse momenta contribute to the short-distance part of the cross section which can be calculated."[54].

The structure functions measured by experiments, however, must be independent of the choice of μ_F. Requiring the derivative of the structure function with respect to the scale μ_F to be zero, the so-called DGLAP equation is obtained: Dokshitzer, Gribov and Lipatov, Altarelli and Parisi showed, that the structure function itself is not calculable but its changes with the factorisation scale are [55–58]. Despite the fact that the PDFs cannot be fully calculated via pQCD, the latter can predict how the distribution evolves as the scale varies via the DGLAP evolution. The DGLAP evolution hence allows that the structure function at the scale Q can be expressed by the structure functions measured for example in DIS at a given scale Q_0, which can be lower than Q. Usually the factorization scale is chosen to be $\mu_F = Q$.

The cross section from equation 2.4 for partons $a + b \rightarrow c + d$ can be calculated in a perturbative manner from the incoherent summation over all possible constituent scatterings above the given momentum transfer limit. Similarly to the PDFs, the FFs are obtained from fits of theoretical calculations to identified hadron spectra from e^+e^- collisions in this case. However, the calculation of the FFs is accompanied by additional difficulties as compared to the PDFs, because the hadronisation process is sensitive to physics happening at long distances, where pQCD starts not to be applicable any more. Moreover, the kinematic reach of data by which the FF can be constrained, is more limited as it is the case for the PDFs [24]. On the other hand, the FF for the vacuum are expected to be universal and hence independent of the collision system [13].

Hadrons produced from hard-scattered partons follow a power-law function,

$$E_h \frac{\mathrm{d}^3\sigma}{\mathrm{d}p_h^3} \propto p_T^{-n}\, F(x_T), \tag{2.8}$$

where $x_T = 2p_T/\sqrt{s}$. A power-law behaviour was first proposed by BBK [59] and is still confirmed by recent measurements [60]. The power-law shape of the hadrons is a result of the power-law shaped distributions of the scattered partons, where the power n from the parton spectrum is maintained [24].

The NLO calculations for jet and particle spectra in pp are well advanced. Recent calculations are able to describe jet spectra for a wide range of energies, ranging from $\sqrt{s}$ = 0.2 - 7 TeV, with reasonable accuracy and moderate systematic uncertainties [13, 60]. In case of pp p_T spectra though, NLO does not agree well with the data, but is able to reproduce the relative dependence on p_T of cross sections of two collision energies [60]. A profound understanding of processes and their description with
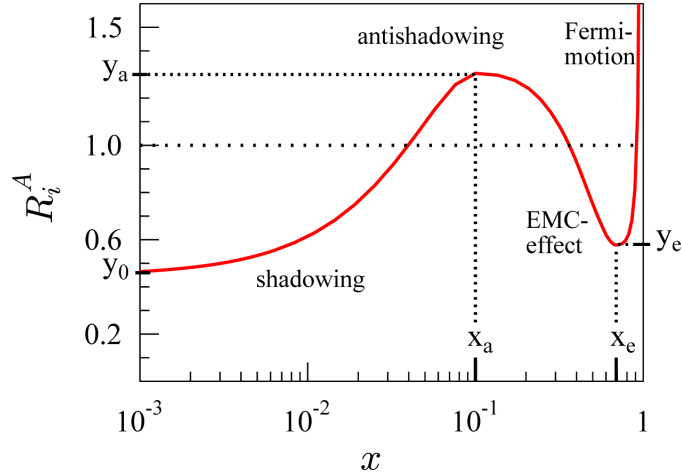
Figure 2.4: A sketch of the EPS09 fit functions $R_i^A(x)$ [with i as the parton flavour] and the role of certain fit parameters. Figure and caption taken from [61].

pQCD, respectively, is however an important ingredient for the investigation of AA collisions.

Nuclear parton distribution function

For the calculation of AA collisions, instead of the PDFs, the nuclear parton distribution functions (nPDF) are needed as input. They are related to the hadron PDFs via a scaling factor, that is also depending on x and Q^2:

$$f_i^{\mathrm{A}}(x, Q^2) \equiv R_i^{\mathrm{A}}(x, Q^2)\, f_i(x, Q^2) \tag{2.9}$$

with i the quark flavour and A the mass number of the nucleus. Figure 2.4 shows a sketch of the evolution of $R_i^{\mathrm{A}}(x)$ with x. At values of $x \ll 0.1$ a depletion or "shadowing" is observed, which evolves to a "anti-shadowing" around $x \approx 0.1$. This is followed by the "EMC-effect[4]" in the range of $0.2 < x < 0.7$ causing a depletion. The final rise is generated by the "Fermi motion" leading to an excess at $x = 1$. The shadowing at low x is also referred to as one of the cold nuclear matter effects, that modify the initial parton distributions as compared to pp. This modification is distinguished from the modification due to the presence of a hot medium. The invariant cross section in p–A collisions, which could be regarded as a "cold" collision, would scale linearly with the cross section in pp $\sigma_{pA} = \sigma_{pp}\,A$ if no nuclear matter effects were expected. As far as figure 2.4 is concerned, this is clearly not the case; in fact, the relation is rather given by $\sigma_{pA} \propto \sigma_{pp}^A$. Another definition of $x = p_{\mathrm{T}}/\sqrt{s} \cdot e^{-y}$ (y is the rapidity) shows, that at the LHC lower values of x are probed as at RHIC or at the SPS if the same p_{T} is regarded and thus different nuclear matter effects become important.

Recent calculations of the $R_i^A(x, Q^2)$ parameter are delivered by the EPS09 collaboration [62], who work with results from DIS and measurements from d–Au collisions at RHIC. The calculations are based on a NLO global DGLAP analysis of nPDFs. "In the lack of sufficient data constraints, we are forced to start with only three different modification ratios: $R_G^A(x, Q^2)$, $R_V^A(x, Q^2)$, and $R_S^A(x, Q^2)$ for gluons, valence quarks and sea quarks, correspondingly. The A dependence is embedded in the A dependence of the parameters." [61] Despite the fact that the recent results of the nPDFs

---

[4]European Muon Collaboration

are in good agreement with measurements, the nPDFs are not yet available for all centralities, which is essential for describing the QGP evolution and properties. Concerning the FF from nuclei (nFF), no significant theoretical output is available yet. Instead of nFF, the FF from the vacuum are used and folded with a medium influence in order to describe AA collisions. Vital for the determination of nPDFs and nFFs is the distinction of effects that originate from processes in the vacuum and from the influence of cold or hot nuclear matter, which can only be sorted out by future measurements.

Hard scatterings and energy loss in heavy-ion collisions

Resuming the discussion above, the basic ingredients for the calculation of the particle production in Pb–Pb collision seem to be available, if no effects introduced by the hot medium, e.g. the QGP, are expected. That the latter is not the case was already explained in the context of the above-mentioned energy-loss scenarios.

High-p_{T} partons are predominantly created in hard scatterings at the initial stage of the collision. The recipe for the invariant cross section of particle production at high p_{T} in Pb–Pb collisions thus contains a hard scattering pQCD process as discussed in the previous section and the influence of the QCD medium in which the process is embedded. A simplified description of the invariant cross section for the creation of a hadron h under the assumption that the initial parton fragmentation is modified by the medium via the energy loss $P(\Delta E(Q^2, E))$ approximation,

$$\mathrm{FF}_{h/c}^{\mathrm{med}}(z_{\mathrm{c}}, Q^2, E_{\mathrm{c}}) \approx \int_0^E \mathrm{d}(\Delta E)\, P(\Delta E(Q^2, E_{\mathrm{c}}))\, \mathrm{FF}_{h/c}^{\mathrm{vac}}\left(z_{\mathrm{c}} - \frac{\Delta E}{E_{\mathrm{c}}}, Q^2\right), \qquad (2.10)$$

is presented here:

$$E_h \frac{\mathrm{d}^3\sigma}{\mathrm{d}p_h^3}(\mathrm{A} + \mathrm{B} \to h + \mathrm{X}) \approx \sum_{\mathrm{abcd}} \int \mathrm{d}x_{\mathrm{a}}\, \mathrm{d}x_{\mathrm{b}}\, \mathrm{d}x_{\mathrm{c}}\, \mathrm{nPDF}_{\mathrm{a}}(x_{\mathrm{a}}, Q^2)\, \mathrm{nPDF}_{\mathrm{b}}(x_{\mathrm{b}}, Q^2) \cdot$$

$$\mathrm{FF}_{h/c}^{\mathrm{med}}(z_{\mathrm{c}}, Q^2, E_{\mathrm{c}})\, \sigma(Q^2)(\mathrm{ab} \to \mathrm{cd}). \qquad (2.11)$$

Within this approximation, the fragmentation process is not modified, but the parton momentum is changed by the energy loss. The FF obtained from fits to measured results from elementary collisions, i.e. e^+e^-, as for example by AKK [63], are used instead of the nFF due to large uncertainties of the latter as explained earlier. The parameter, which shows the largest uncertainty, is the medium-induced energy loss $P(\Delta E(Q^2, E))$. Understanding and quantifying this medium property as well as the applicability of pQCD for the given process are among the major challenges in the field.

In order to quantify the medium-induced energy loss, two effects are commonly considered [64]:

- incoherent collisional energy loss ($\sim$ elastic scattering)

- coherent radiative energy loss ($\sim$ inelastic scattering),

which are sketched in figure 2.5. Whereas the collisional energy loss from elastic scatterings with thermal partons, i.e. partons not stemming from hard scatterings, affects mainly partons at lower momenta [45], the radiative energy loss is commonly thought

Figure 2.5: Diagrams for collisional (left) and radiative (right) energy losses of a quark of energy E traversing a quark-gluon medium. Figures and caption from [64].

to be dominant for high-p_T partons with $p_T > 5\,\text{GeV}/c$. Gluons and light quarks, such as u, d, s, are expected to lose energy rather via bremsstrahlung (quarks) or medium-induced gluon radiation (both), respectively, than from elastic scatterings. This is opposite to heavy quarks (c, b), where the radiative loss is supposed to be reduced by the so-called dead-cone effect [65] and thus collisional effects could dominate, which are mass dependent [66].

The inelastic radiation process induced by multiple scatterings involves gluons, that are coherently radiated in a bremsstrahlung-like interaction. This is expressed in pQCD for a large medium as compared to the mean free path λ ($L \gg \lambda$) via the Landau-Pomeranchuk-Migdal (LPM) formalism [67, 68]. The LPM effect is expected to cause a quadratic path or formation length (L) dependence of the mean radiative energy loss [64]:

$$\left\langle \Delta E_{\text{med}}^{\text{LPM}} \right\rangle \approx \alpha_s \hat{q} L^2 \quad \left(\sim L^2 T^3 \quad [69] \right), \tag{2.12}$$

with the transport coefficient, governing the transverse momentum diffusion of a fast parton per unit path length,

$$\hat{q} = \frac{\langle q_\perp \rangle^2}{\lambda}, \tag{2.13}$$

where λ is the mean free path given by $1/(\sigma\rho)$, with ρ as the density, and $\langle q_\perp \rangle$ as the mean transverse momentum transferred from the medium to the parton per collision. $\langle q_\perp \rangle$ characterizes the typical momentum exchange with the plasma. However, it has not been clarified yet, if the total radiative energy loss really depends on L^2 or on another power of the path length. The additional power of L as compared to the collisional energy loss is one of the main reasons why the radiative energy loss is considered to dominate [69]. According to [70], $\hat{q}$ could be thought to be energy-dependent, although it appeared to describe the measurement only for very high p_T. Consequently, the gluon radiation needs to be tracked through the medium in order to reveal the medium density and transport properties, that are both linked to L. For the experimental realization, observables of the radiative energy loss are vital and have to be defined. This leads to the definition of "jets", which will be explained in the following section.

Summarizing this paragraph, for the understanding of the medium properties, the following aspects of partonic energy loss need to be understood: path length dependence, space time evolution and geometry, which influence the path length, quark-gluon difference, difference of vacuum and in-medium radiation and the contributions of the collisional and radiative energy loss to the total energy loss.

Jets and radiative energy loss

A jet originates from a hard scattering parton, which produces a collimated parton shower via the fragmentation process finally creating colour neutral particles with subsequently lower momenta than the original parton momentum. The jet is defined by a certain angular region, recovering the parton energy by the summation over all produced particles in this region. The jet cone is determined by the distance parameter R. The collimation into a jet-like shape is caused by the strong scale dependence of the coupling, which leads to a suppression of large-angle radiation. In reality, however, the full reconstruction of the parton energy is only possible in pp collisions, because in heavy-ion collisions, the radiative energy loss of the parton in the medium plays a major role.

The effect of radiative energy loss on a hard scattered parton can be visualised by the measurement of the jet R_AA. Basically, there are two scenarios:

- **$R_\mathrm{AA} = 1$** as a result of jet broadening in transverse direction caused by in-cone radiation in the medium. From these radiated gluons fragmenting outside the medium (as the leading parton), the initial leading parton spectrum can still be recovered.

- **$R_\mathrm{AA} < 1$** due to out-of-cone radiation, which results into a modified jet p_T spectrum and finally to a suppression of the yield in a given p_T range as compared to pp.

As figure 2.2 shows, the jet R_AA at the LHC is compatible with that of inclusive charged particles. In detail, the jet suppression is also around 0.5, hinting to out-of-cone radiation. This could also include the absorption of the radiated gluons by the medium. The saturation of the jet and hadron spectra R_AA at very hight p_T is not yet fully understood and currently under investigation [70].

Apart from the nuclear modification factor as a function of p_T, there is the so-called I_AA parameter used for di-jet studies. Also here, a strong suppression is observed: Di-jets are two jets which are assumed to originate from the same scattering process wherein they were produced with opposite transverse momenta. Hence, their constituents are correlated not only within one jet but also between the two jets. A correlation analysis (di-hadron analysis) is usually performed by selecting a trigger particle with a given (high) momentum and calculating the angular difference in azimuthal direction between this particle and all others of lower momenta, $\Delta\phi = \phi_\mathrm{trig} - \phi_\mathrm{assoc}$. From this angular difference, two regions in $\Delta\phi$ can be distinguished: the near-side peak around zero and the away-side peak around π. If the integrated yield at the near or away side in AA collisions is divided by that in pp collisions, the parameter I_AA is obtained, in analogy to R_AA for the p_T spectra. I_AA is commonly studied as function of the trigger particle's p_T or of centrality. In pp collisions, the amplitude of both peaks is of the same order, whereas in Au–Au collisions, the away-side peak is suppressed by a factor of 3 - 5 at RHIC [72, 73]. The unmodified near-side peak is a result of the trigger particle procedure, where with the trigger particle selection, partons from or close to the surface are selected, which did not encounter energy loss. Their path length is hence much smaller than that of the recoiled parton, which had to travel basically through the whole medium and suffered strong energy loss. Therefore, one could think of the sensitivity of this measurement to the path length dependence of the energy loss. Though, during
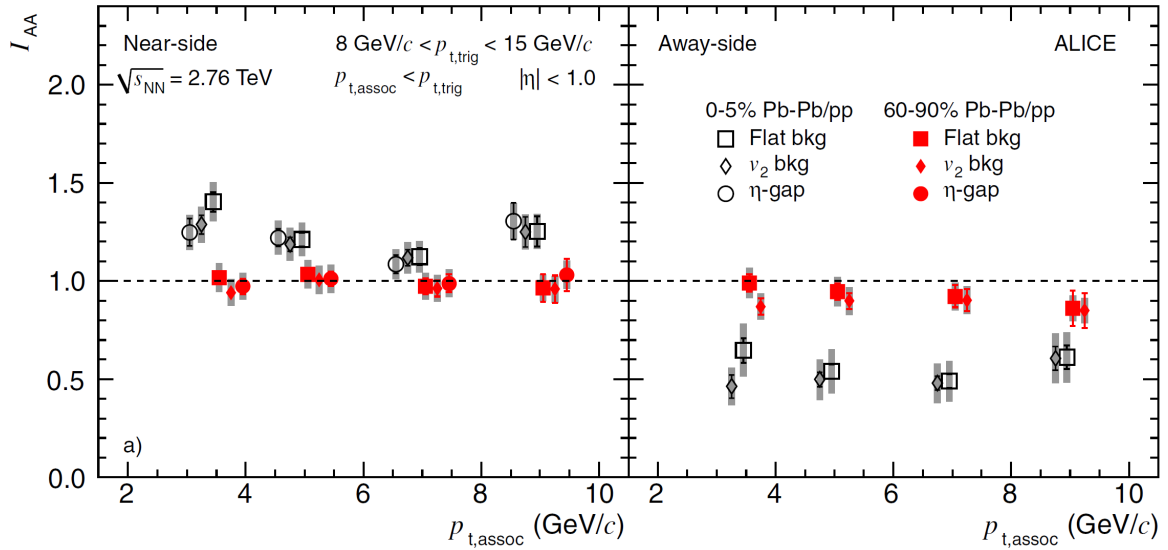
Figure 2.6: I_{AA} for central (0 - 5% Pb–Pb/pp, open black symbols) and peripheral (60 - 90% Pb–Pb/pp, filled red symbols) collisions. Results using different background subtraction schemes are presented: using a flat pedestal (squares), using v2 subtraction (diamonds) and subtracting the large $|\Delta\eta|$-region (circles, only on the near-side). For clarity, the data points are slightly displaced on the $p_{T,assoc}$-axis. The shaded bands denote systematic uncertainties. Figure and caption taken from [71].

the long travel through the medium, the medium properties, i.e. its density, could have already changed due to the rapid expansion. Interestingly, the shape of the away side peak equals that in pp for trigger particles with $p_T \gtrsim 7\,\mathrm{GeV}/c$.

In case of LHC, a suppression of 0.6 for the away side and a slight enhancement of 1.2 for the near side in central collisions has been reported by ALICE as seen in figure 2.6. The latter feature is observed for the first time [71] and could hint to a higher Q^2 in the medium than in vacuum. For peripheral collisions, no suppression for the near-side peak and only a small suppression (~ 0.9) is found for the away-side peak indicating that this system is either smaller or less dense than in central collisions. Remarkable is, that the I_{AA} is much smaller in central collisions at RHIC than at the LHC, while this is not the case for R_{AA}. The lower away-side I_{AA} suggests that the medium is more opaque or stronger coupled at RHIC [74]. Since the R_{AA} represents a less differential observable, which integrates over the near- and away-side, the rather similar R_{AA} at both energies hints to a larger contribution from partons closer to the surface (for which the loss of energy is generally less) to the R_{AA} than to the away-side I_{AA}.

Attempts of basic R_{AA} interpretation

For a basic understanding of the influence of the energy loss on the spectra and thus on R_{AA}, two simplified energy loss scenarios are considered in the following[5]. The nuclear modification factors are calculated assuming a power-law behaviour of the parton and consequently also of the hadron spectrum with $Ed^3\sigma/d^3p_T \propto p_T^{-n}$, which corresponds to $dN/dp_T \propto p_T^{-(n-1)}$:

---

[5]This discussion is inspired by Macro van Leeuwen's lectures within the Helmholtz Research School for Quark Matter Studies in Heavy Ion Collisions (HQM) lecture week series [75].

1. **Constant energy loss**

$$p'_\mathrm{T} = p_\mathrm{T} + \Delta E/c$$

$$\Rightarrow \quad R_\mathrm{AA} = C + \left(\frac{1}{1 + \Delta E/p_\mathrm{T}\, c}\right)^{(n-1)}. \tag{2.14}$$

After the energy loss, the yield at a given p_T in AA corresponds to the yield in pp at a higher p'_T, which is lower than that at p_T in pp. The constant C accounts for the relative amount of partons very close to the surface, that could escape without being affected by the medium [49].

2. **Constant fractional energy loss** [76]

$$p'_\mathrm{T} = p_\mathrm{T} + S(p_\mathrm{T}) \quad \text{with} \quad \mathrm{d}S/\mathrm{d}p_\mathrm{T} = S_0$$

$$\Rightarrow \quad R_\mathrm{AA} = C + \left(\frac{1}{1 + S_0}\right)^{(n-2)} \tag{2.15}$$

The constant fractional energy loss S_0 can be substituted by an effective fractional energy loss S_{loss} via the relation $S_\mathrm{loss} = S_0/(1 + S_0)$, leading to

$$R_\mathrm{AA} = C + (1 - S_\mathrm{loss})^{(n-2)} \tag{2.16}$$

$$\Rightarrow \quad S_\mathrm{loss} = 1 - (R_\mathrm{AA} - C)^{\frac{1}{n-2}}. \tag{2.17}$$

In the first case, the constant energy loss leads to a p_T-dependent suppression. Since $\Delta E/p_\mathrm{T}$ decreases with larger p_T, R_AA is expected to increase and to finally approach unity [42] depending on n. In the second case of constant fractional energy loss, the measured spectrum shifts towards lower p_T. For a pure power-law spectrum this yields a constant R_AA, which is indeed observed at $p_\mathrm{T} > 30\,\mathrm{GeV}/c$ (see fig. 2.2). For a growing fractional energy loss with p_T, the slope of R_AA is softer than for the case of constant energy loss. Consequently, the slope of R_AA contains valuable information about the momentum (energy) dependence of the energy loss. The sensitivity to the details of parton energy loss is strongly correlated with the power n of the parton spectrum, therefore the extraction of the energy loss from measurements is not straightforward. It has to be clarified if the observed R_AA is a result from a combination of both discussed scenarios and if the assumption of a pure power-law with the same n for all p_T is correct [70]. In case of ALICE jet measurements, a slightly smaller exponent is observed for $p_\mathrm{T} = 20$ - $125\,\mathrm{GeV}/c$ than for the charged particle spectra with $p_\mathrm{T} < 30\,\mathrm{GeV}/c$ [60, 77].

Figure 2.7 shows the R_AA of charged particles measured by ALICE [47] together with the neutral pion[6] R_AA in Au-Au collisions at $\sqrt{s_\mathrm{NN}} = 200\,\mathrm{GeV}$ published by PHENIX [78]. Both R_AA are fitted with the function of equation 2.14 in order to extract the constant energy loss ΔE and the fraction C of partons with unmodified p_T. At RHIC, $n = 8.1$ [76], while at the LHC $n = 6.47$ is measured [60] for $p_\mathrm{T} < 30\,\mathrm{GeV}/c$. The results for $C \approx 0.12$ seem to be similar for RHIC and LHC energies for both centralities within the uncertainties. However, the value of C in central collisions increases for peripheral collisions by a factor 4 - 5. Since a smaller, less dense medium (if at all) is

---

[6]A neutral pion, π^0, consists of a mixture of $\mathrm{d\bar{d}}+\mathrm{u\bar{u}}$ quarks. Its R_AA is hence comparable to the charged particle R_AA.
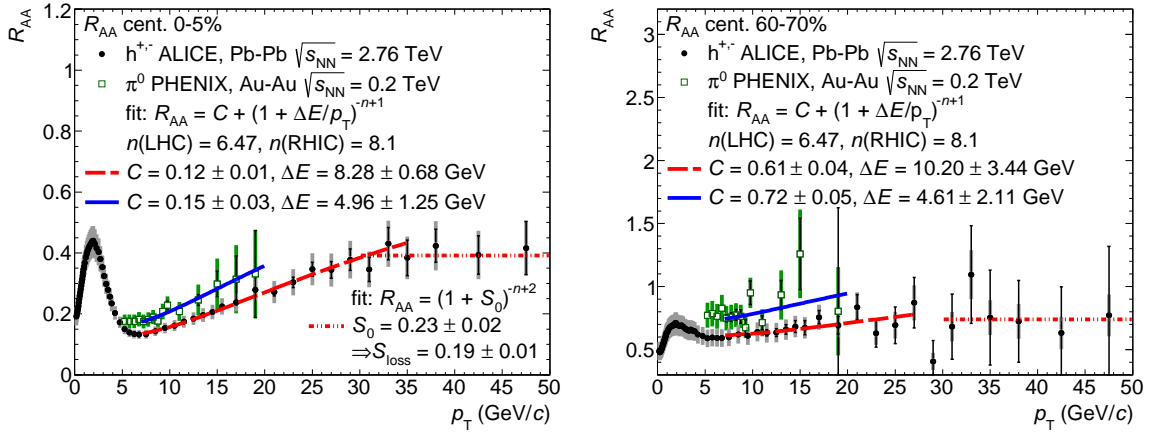
Figure 2.7: Nuclear modification factor of charged particles measured by ALICE [47] and of neutral pions measured by PHENIX [78] fitted with equation 2.14 for the case of constant energy loss (full, dashed line) and with equation 2.15 (dashed-dotted line).

expected for peripheral collisions, more partons could fragment outside the medium and/or stem from parts, where they suffered no energy loss. The energy loss at RHIC and the LHC remains rather constant for both centralities, whereas at the LHC ΔE is almost twice as large as at RHIC, where $\Delta E \approx 5\,\mathrm{GeV}$. If C is neglected in the fit, the energy loss reduces from $5\,\mathrm{GeV}$ to $2.3\,\mathrm{GeV}$ at RHIC and from $8.3\,\mathrm{GeV}$ to $5\,\mathrm{GeV}$ at the LHC. Due to the large uncertainties of RHIC measurements, it is not yet possible to conclude, if the R_{AA} becomes similar to the LHC R_{AA} above $12\,\mathrm{GeV}/c$, which would influence the slope of the fit and hence the extracted energy loss. In case of the ALICE measurement in figure 2.7, the plateau above $p_T = 30\,\mathrm{GeV}/c$ was additionally fitted with equation 2.15. For central collisions $S_{\mathrm{loss}} = 0.2$ and for peripheral $S_{\mathrm{loss}} = 0.07$ was extracted with $C = 0$. Thus, if all partons lost energy in the medium, the mean fractional energy loss would be 20% (7%) as compared to the original p_T in pp collisions. If 88% (39%) of the partons were affected in central (peripheral) collisions, the fractional loss would be 25% (40%) instead. These simple considerations show the need for further investigations concerning the disentanglement of the different modification options and the contribution of unmodified partons to the observables.

The energy loss can also be considered to be a p_T-dependent momentum loss. This is expressed by the p_T-dependent momentum difference in AA and pp collisions $\delta p_T = p_T(\mathrm{pp}) - p_T(\mathrm{AA})$ as suggested in [78]. In figure 2.8, the comparison of $S_{\mathrm{loss}} = \delta p_T/p_T(\mathrm{pp})$ in central and peripheral collisions measured by PHENIX for π^0 at $\sqrt{s_{NN}} = 0.2\,\mathrm{TeV}$ and by ALICE for charged particles at $\sqrt{s_{NN}} = 2.76\,\mathrm{TeV}$ is shown as a function of the p_T in pp collisions. S_{loss} was extracted by employing a fit with a power-law function to the $\langle T_{AA}\rangle$ scaled spectrum in pp collisions and by calculating the horizontal shift to the spectrum in Au–Au at each p_T in pp collisions. The relative momentum change is constant below $12\,\mathrm{GeV}/c$ for all centralities and collision energies. Only in central events a slight decrease is observed above this p_T, which is consistent with the slow rise of R_{AA}. Although the R_{AA} is similar above $10\,\mathrm{GeV}/c$ for LHC and RHIC energies, S_{loss} is 30% lower at RHIC, which could be a result of the different n of the power-laws. Assuming that the fragmentation of the initial parton remains unchanged after the energy loss, the fractional momentum loss can be interpreted as average fractional energy loss of the initial parton [78].
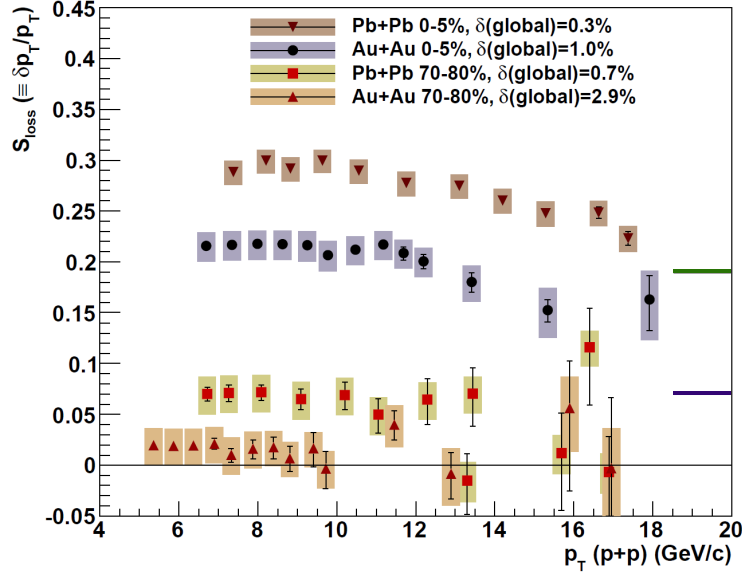
Figure 2.8: $S_{\mathrm{loss}} = \delta p_T/p_T$ for charged particles from ALICE [79] and for π^0 measured by PHENIX [78]. The error bars are statistical, the boxes around the points indicate systematic uncertainties. Figure taken from [78]. The coloured lines at high p_T mark the results from fits with equation 2.15 with $C = 0$ to the ALICE R_{AA} in central (green) and peripheral (blue) collisions.

In [80], an estimation procedure for the lower limit of R_{AA} is introduced, which can be regarded as a geometrical limit of R_{AA}. This universal bound model considers hadrons above $p_T = 5\,\mathrm{GeV}/c$, where the collective flow effects (see section 2.2) are no longer expected to contribute. The lower bound of R_{AA} is given by

$$R_{\mathrm{AA}}^{\mathrm{geom}} = k\,\frac{N_{\mathrm{part}}}{2\,N_{\mathrm{coll}}} \propto N_{\mathrm{part}}^{-1/3}, \tag{2.18}$$

where the constant factor k "is an adjustable parameter of order unity; its numerical value is universal for all particles (except perhaps for hadrons containing b quarks at moderate p_T) and is determined by the thickness of low-density 'corona'."[80]. In order to obtain $R_{\mathrm{pp}} = k$, the factor 2 in the denominator is inserted. Since R_{pp} is expected to be 1, k should also be of the order of 1.

$R_{\mathrm{AA}}^{\mathrm{geom}}$ is based on the following dependences given by the Glauber model, which is referred to again in section 3.5: The volume R^3 is proportional to N_{part} and thus the surface to volume ratio is $\propto N_{\mathrm{part}}^{-1/3}$. Taking into account that $N_{\mathrm{coll}} \propto N_{\mathrm{part}}^{4/3}$, one obtains $N_{\mathrm{part}}^{-1/3} = N_{\mathrm{part}}/N_{\mathrm{coll}}$. The model describes the lower bound of the data at high p_T quite well with $k = 1.0$, as shown in figure 2.9. A question arising from this is, if this is also true for other particle species than those containing u and d quarks and if this limit is universal.

The findings with regard to the nuclear modification factor at high p_T from RHIC and the LHC are summarized in the following:

- **RHIC:** R_{AA} seems to slightly rise with p_T, following the lower bound (see figure 2.9) given by the geometric limit from 5 - 12 GeV/c, which hints to surface emission, i.e. only particles stemming from partons produced close to the surface of the medium contribute to the particle yield at these p_T. The remaining partons
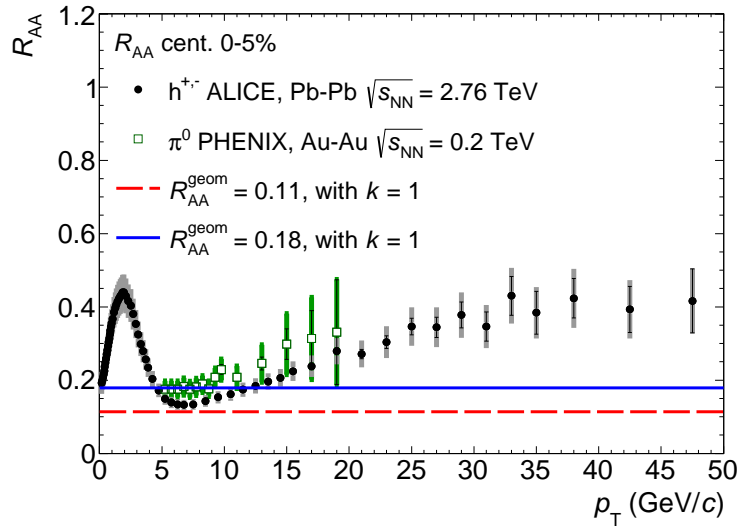
Figure 2.9: Nuclear modification factor of charged particles from ALICE [47] and of π^0 measured by PHENIX [78]. The error bars are statistical, the boxes around the points indicate systematic uncertainties. The lines marks the geometrical limit as calculated in [80] with $k = 1$.

are absorbed such, that their energy is shifted to lower momenta contributing to the thermal background. The approximate flatness of R_{AA} with p_T could also be the result from a spectrum shift by fractional energy loss. However, within the present uncertainties, this remains a guess. At $p_T > 12\,\mathrm{GeV}/c$, the suppression is similar to that at the LHC within the uncertainties. Nonetheless, the modification in central events for both energies is strong ($R_{AA} \approx 0.2$ - 0.4), indicating that the medium is almost opaque and absorbs a lot of the energy of a fast trespassing parton. The fit to the R_{AA} assuming a constant parton energy loss yields $\Delta E \approx 5\,\mathrm{GeV}/c$ ($2.3\,\mathrm{GeV}/c$) for $C = 0.15$ (0), the fraction of partons fragmented outside the medium or unaffected by energy loss, which corresponds to the estimate of the lower bound of R_{AA} within the systematics.

- **LHC:** R_{AA} of unidentified charged particles is significantly p_T-dependent, the geometrical limit is only touched at $p_T = 6$ - $7\,\mathrm{GeV}/c$ (see figure 2.1). The deviation from the constant geometrical limit at lower p_T could be a result of the steeper slope parameter of the assumed power-law shaped spectrum. A constant behaviour is observed for $p_T \gtrsim 30\,\mathrm{GeV}/c$ at a suppression of $R_{AA} \approx 0.4$ - 0.5 [81], as seen in figure 2.2. According to [42], "at hypothetically large p_T when the total energy loss is negligible compared to the initial jet energy, the ratio should approach to one". This still needs to be clarified by measurements at $p_T > 300\,\mathrm{GeV}/c$, which is expected to be the case during the data recording period starting in 2015. The fit to the R_{AA} assuming a constant parton energy loss yields $\Delta E \approx 8\,\mathrm{GeV}/c$, which is almost twice as much as at RHIC indicating a more opaque medium at the LHC. Also at the LHC, the estimate of the lower bound of R_{AA} corresponds to the fraction $C = 0.12$.

Summarizing the models for parton energy loss contained in figure 2.1, such as models based on a leading-parton energy loss description for elastic energy loss ($\propto L$, e.g. [82]), radiative energy loss ($\propto T^3 L^2$, e.g. (D)GLV [83, 84], ASW [85], AMY [86], HT [87–89], YaJEM [90]), both mechanisms (WHDG [68]) and strong coupling ($\propto T^4 L^3$ in AdS/CFT [7] [91]), the resulting p_T dependence of R_{AA} in these models from intermediate to high p_T is comparable. Concerning the charged particle R_{AA} at the LHC in figure 2.1, most of the mentioned models are able to reproduce the shape but not the overall magnitude of the modification. Whereas the values obtained by the elastic energy loss models are above the data at low p_T, the radiative and strong coupling models overestimate the suppression.

Taking into account the results from RHIC and the LHC at the same time, it seems that the favoured power of L is $1 < n \leq 2$ [69], which would mean that the radiative energy loss dominates over the other energy loss processes depending on higher orders of L. The dominance of elastic energy loss however is thought to be possible for heavy quarks [92]. A clear distinction between the parton distribution modified by the path length depended energy loss, a possibly modified fragmentation and the contribution from partons fragmenting in- and outside the medium is difficult [42]. Therefore it is questionable if the path length and temperature dependence can be extracted at all from R_{AA}. Concerning the radiative energy loss in the above-mentioned models, "in addition to the microscopic model of the medium, a realistic calculation of energy loss in heavy-ion collisions also requires a macroscopic model of the medium, specifying the space-time dependence of the local properties of the plasma."[93] For the same parameters, the radiation formalisms yield different modified fragmentation functions as it can be seen in figure 2.10, which demonstrates the difficulty of modelling the plasma properties, as for example the medium response to a trespassing parton, and the need for constraints from reliable measurements. It should be kept in mind that the description of R_{AA} by models is not enough, a complete understanding is only possible if all observables can be described simultaneously. This includes R_{AA} and I_{AA} as well as the hadron p_T spectra, the flow (see next chapter), the (relative) particle abundances and particle correlations.

Energy loss and flavour dependence

Until now, no distinction with regard to the particle flavour was made. However, the investigation of flavour dependent energy loss and the dependence on the number of constituent quarks is important as well. Are the above-mentioned observations universal in this respect?

The colour coupling factor for gluons given by QCD is larger by 9/4 as compared to quarks. Thus, the QCD medium induced energy loss should consequently be smaller for quarks than for gluons resulting in a smaller suppression for quarks. Moreover, "the gluon density inside nucleons at small x is larger than for quarks; the gluon-gluon scattering cross section is larger than the quark-quark; and a gluon jet produces more [soft] particles than a quark jet."[42] In addition, the fragmentation functions by AKK and KKP show, that for baryons the contribution of gluon fragmentation is larger than for mesons.

The following research questions can be deduced from this discussion: Is the energy loss independent of the quark mass and thus of the quark flavour? Is the suppression

---

[7]anti de-Sitter conformal field theory (string theory)
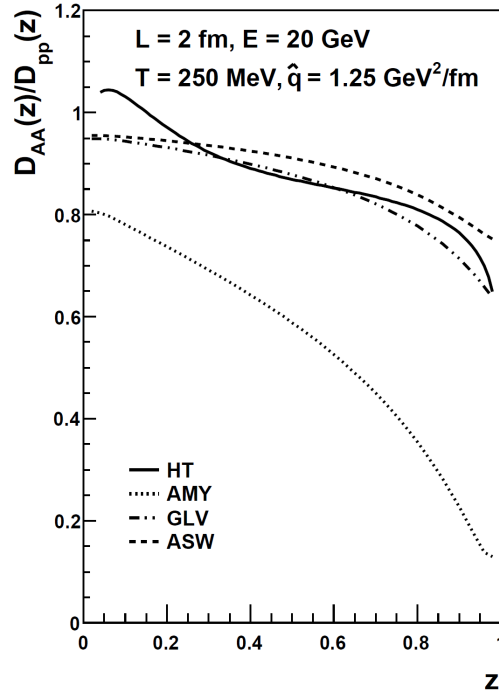
Figure 2.10: Comparison of quark fragmentation function ratios using four different formalisms for a uniform medium with $L = 2\,\mathrm{fm}$ and $T = 250\,\mathrm{MeV}$. Figure and caption taken from [93].

different for hadrons predominantly stemming from quark fragmentation to those from gluon fragmentation, i.e. is there a difference in the modification for baryons and mesons? Is a flavour or parton type dependent energy loss possible to be translated into the suppression measured from identified hadrons?

Referring to the first question, in case of heavy quarks the energy loss is expected to be even smaller than for light quarks due to the dead-cone effect [65]. This is supposed to reduce small-angle gluon radiation for heavy quarks (already in the vacuum). The medium influence is consequently smaller and thus decreasing the suppression. A competing effect is the in-medium hadron formation and dissociation or melting [94], which takes place at later stages as the initial scattering processes but being faster than the light-flavour formation times. Which mechanism dominates is left to be clarified. Concerning the second and third question, the particle production mechanisms need to be considered: Either the constituent quarks of the hadron could have lost energy before forming the hadron (recombination picture, see section 2.2) or the parton fragmenting into the hadron could have suffered energy loss. The translation of the observed identified hadron suppression to the energy loss is hence only possible, if the production mechanisms of the hadrons are definite. In case of fragmentation, the fraction of gluon and quark fragmentation leading to the hadron production as well as the momentum distribution of the partons contributing to the hadron formation need to be known. As explained earlier, this knowledge is available from the fragmentation functions as determined by various groups [63, 95]. Since the fragmentation process does not link a hadron p_T directly with the parton p_T it is created from - an integration over the parton p_T is needed (see equation 2.4) - the energy loss cannot be extracted from the R_{AA} if it is parton energy dependent. Consequently, the trial and error principle perhaps seems to be the best opportunity, which means in detail, that the

energy loss needs to be modelled by theory and the resulting R_AA eventually to be compared to measurements.

First it has to be clarified if $R_\mathrm{AA}(h(\mathrm{u,d})) = R_\mathrm{AA}(h(\mathrm{s}))$ and whether this implies $\Delta E(\mathrm{u,d}) = \Delta E(\mathrm{s})$. Additionally the question could be raised if the baryon and the meson R_AA are equal at high p_T. In [96], for example, the proton R_AA was calculated to be smaller than the pion R_AA at RHIC, which was mainly caused by the different fragmentation functions. Moreover, at present it is not clear, whether the energy loss of light quarks is larger than that of heavy quarks and if this furthermore results into

$$R_\mathrm{AA}(h(\text{light quarks})) < R_\mathrm{AA}(h(\mathrm{c})) < R_\mathrm{AA}(h(\mathrm{b})) \tag{2.19}$$

above $p_\mathrm{T} = 10\,\mathrm{GeV}/c$. One idea behind is that at high momenta ($p_\mathrm{T} \geq 10\,\mathrm{GeV}/c$), the heavy-quark masses contribute more to the total hadron p_T than light quark masses at the same p_T. Thus, if the energy loss increases with the velocity as it could be the case for the collisional energy loss [66], the heavy-quark hadron suppression can be thought be smaller than that of light-quark hadrons. On the other hand, in addition, the above-mentioned dead-cone effect, reducing the contribution from radiative energy loss for heavy quarks plays a role for this ordering. However, recent calculations [97] weaken the importance of the dead-cone effect by showing that the radiative gluon emission does play a significant role for heavy quarks from intermediate to high p_T. Moreover, it is stated that the dead-cone effect is only predominantly present at lower p_T though being much "less important than originally advocated". On these grounds, the measurement and comparison of the mentioned differently flavoured particles R_AA is expected to provide a test of the colour-charge and mass dependence of parton energy loss and may help to constrain model calculations on fragmentation mechanisms in the system evolution of hot and dense nuclear matter. This implies the path length dependence inside the created medium, the flavour and colour charge dependence of the energy loss of the interacting partons surrounded by the medium. From this, with the help of models it could be possible to constrain the medium density and transport parameters. And finally it has to be clarified if also the fragmentation is modified by the medium besides the parton spectrum or if the fragmentation happens exclusively outside the medium. Important for that is the understanding of the dynamical evolution of the system and the complete picture of the partonic final-state interactions.

2.2   Low p_T: Initial state effects and bulk

In the lower momentum region, the application of pQCD as well as the description of the hadronisation process via the fragmentation functions is no longer valid. The so-called bulk medium consisting of partons with mean p_T or a temperature, respectively, of around $200\,\mathrm{MeV}/c$ (at RHIC and LHC energies) is created at the early stage of heavy-ion collisions, right after the initial hard scatterings. The bulk is considered to be strongly gluon dominated as a result of the nPDFs. The measured hadron spectra at low p_T ($p_\mathrm{T} \lesssim 2\,\mathrm{GeV}/c$) reflect the properties of the bulk at the so-called kinetic freeze-out, when the momentum distributions are fixed and elastic collisions stopped to occur. The shape of the hadron spectra can be described by an exponential function,

$$E\frac{\mathrm{d}^3\sigma}{\mathrm{d}^3 p_\mathrm{T}} \propto e^{-a\,p_\mathrm{T}}, \tag{2.20}$$

where the slope parameter $a \approx 6\,(\mathrm{GeV}/c)^{-1}$ [59] varies only little with the collision energy. This functional form represents a Boltzmann spectrum of an equilibrated thermal system. Via a more sophisticated model, the so-called Blast-Wave formalism [98], the effective temperature

$$T_{\mathrm{eff}} = T_{\mathrm{kin}} \cdot \sqrt{\frac{1 + \beta_{\mathrm{R}}}{1 - \beta_{\mathrm{R}}}} \tag{2.21}$$

can be extracted, with T_{kin} as the kinetic freeze-out temperature and β_{R} as the radial flow velocity. In this model, a superposition of thermal sources is assumed, which are boosted in longitudinal and transverse direction. Hence, the model can be regarded as a simplified version of the hydrodynamical approach to describe the collision evolution. The Blast-Wave function and the effective temperature, the latter is deduced in the limit $m_T/p_T \to 1$, contains the kinetic freeze-out temperature and the radial flow velocity, which describes the boost of the thermal source resulting in a blue-shifted temperature. The functional form of the spectra in this model is given by

$$\frac{\mathrm{d}N}{m_T \, \mathrm{d}m_T} \propto \int_0^R r \, \mathrm{d}r \, m_T \, I_0 \left(\frac{p_T \sinh \rho}{T_{\mathrm{kin}}} \right) K_1 \left(\frac{m_T \cosh \rho}{T_{\mathrm{kin}}} \right), \tag{2.22}$$

where $m_T = \sqrt{m_0^2 + p_T^2}$ is the transverse mass, $\rho = \tanh^{-1}(\beta_{\mathrm{R}})$ denotes the boost angle or rapidity, I_0 and K_1 represent modified Bessel functions[8]. If no radial expansion is present, the formula reduces to

$$\frac{\mathrm{d}N}{m_T \, \mathrm{d}m_T} \propto e^{-m_T/T_{\mathrm{kin}}} \qquad \text{for} \quad m_T \gg T_{\mathrm{kin}}. \tag{2.23}$$

The impact of the boost is visible in the rise of R_{AA} at $p_T \approx 2\,\mathrm{GeV}/c$. If the flow effect was mass (constituent quark number) dependent, one would expect a mass (constituent quark number) dependent enhancement of R_{AA}. At RHIC, such a mass ordering was indeed observed [99]. To show this at LHC energies is one motivation for this thesis besides the investigation of the high p_T region.

In addition to the radial flow, which is triggered by the expansion of the source, the so-called elliptic flow acts on the parton momenta in non-central AA collisions. The elliptic flow is a result of a initial spatial azimuthal asymmetry (initial elliptic shape of the over-lap region) relative to the reaction plane resulting in a pressure gradient, which finally causes an anisotropic particle production. The elliptic flow is quantified by the parameter[9] v_2 and usually measured as a function of p_T for different centrality classes and particle species. The largest elliptic flow is observed in mid-central collisions, because here, as compared to peripheral collisions with the strongest asymmetry, the amount of partons is still large enough to transport the pressure. The pressure transport is only possible if a collective behaviour of the medium constituents is given, allowing that the momentum kick from the pressure gradient caused by the spatial anisotropy is imparted among the partons. The fact, that elliptic flow is observed for the final state hadrons, shows, that the thermalisation of the system

---

[8]Solution of the Bessel linear differential equation of second order. Modified means here, that the behaviour is exponential instead of oscillating.

[9]Second component of the Fourier expansion of the azimuthal dependence of the invariant yield [100, 101].

happens rapidly, i.e. a hydrodynamical system is established before the anisotropy vanishes [24, 102]. Rapid means in this case that $\tau \lesssim 1\,\text{fm}/c$, which is much smaller than the system life time of $\tau \approx 10\,\text{fm}/c$ [103].

The discovery of collectivity and fast thermalisation at RHIC and at the LHC are important findings and an essential input for the EoS. From this review here, flow seems not to be expected in pp collisions - currently it is heavily discussed if pp collisions at LHC energies could built up flow after all. This discussion is triggered by the results of di-hadron correlations in pp, which show as a function of the azimuthal and polar angular difference a similar background profile (a ridge structure on the near-side) as it is observed in Pb–Pb collisions [104]. In the latter system, this structure is thought to be caused by flow. Since in pp collisions at LHC, multiplicities are measured, which are comparable to that of semi-central Pb–Pb collisions, the question of a spacious system in pp - a core -, where collectivity can occur, is reasonable. In [105] a collective hadronisation is suggested and the inclusion of radial flow seems to improve the description of identified hadron spectra in pp [106]. Whether this is the whole answer, remains to be validated within the field.

The above-mentioned Blast-Wave model as a simplified hydrodynamic description is usually used in order to extract the total yield of a particle species since most measured spectra are restricted to a limited p_T range. For a more system evolution oriented consideration, though, the full hydrodynamic formulation is employed. Within the discussed p_T range of $0 \leq p_T \lesssim 3\,\text{GeV}/c$, the description of the hadron spectra via pure hydrodynamics works reasonably well at RHIC as well as at LHC energies [107, 108].

The hydrodynamical formulation of the system evolution, of the deconfined phase and of the resulting formation of hadron spectra is based on the conservation of the energy-momentum tensor

$$T^{\mu\nu} = (\epsilon + P)\, u^\mu u^\nu + P\, \eta^{\mu\nu}, \tag{2.24}$$

with $P = P(\epsilon)$ as the EoS, u^μ the fluid velocity, $\eta^{\mu\nu}$ the metric tensor, and the baryon number B via

$$\partial_\mu \langle T^{\mu\nu} \rangle = 0, \qquad \partial_\mu \langle j_B^\mu \rangle = 0, \tag{2.25}$$

assuming local thermal equilibrium [6]. The latter though, takes a short time to evolve ($\tau \approx 0.2$ - $0.4\,\text{fm}/c$ [102]), which allows the description of the system via a hydro-approach only after the earliest moments of the collision. Hence, the initial conditions (energy density, entropy, net baryon density), as an essential input for the calculations, need to be constrained by measurements, as for example particle multiplicities and transverse energy. From the experimental results for the above-mentioned flow components and those of higher order, matter properties such as the velocity of sound and the viscosity (or shear viscosity, describing the dissipation due to internal friction, over entropy density η/s) can be extracted. This extraction however is strongly model dependent, since some features, e.g. the energy density profile, do need to be modelled and hence bear a source of systematic uncertainties. From the simulated time evolution, a lower limit of the initial temperature can be deduced, when comparing the calculations to data [37]. Generally it is stated, that the EoS is well constrained by LQCD. The remaining open aspects including the energy density profile, equilibration times, possible pre-equilibrium processes and a
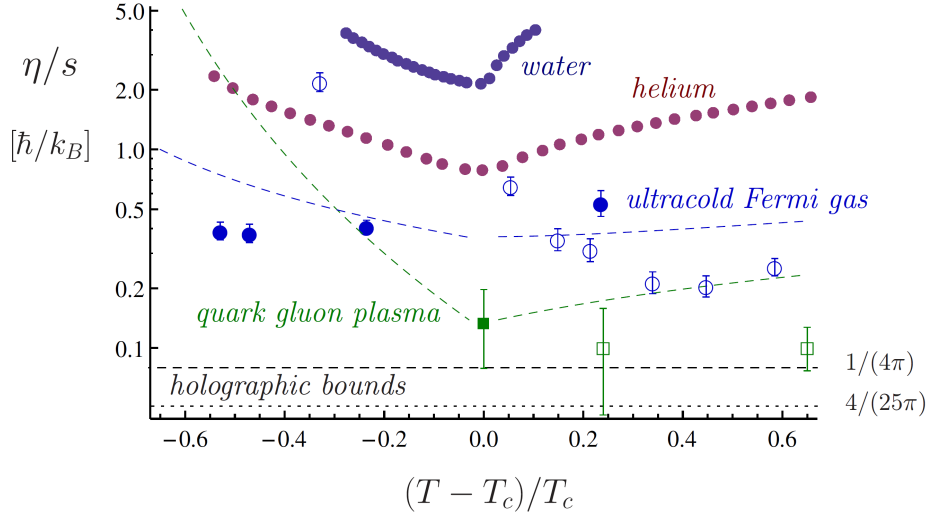
Figure 2.11: Transport properties of strongly correlated fluids. The ratio of shear viscosity to entropy density s as a function of $(T - T_c)/T_c$, where T_c is the super-fluid transition temperature in the case of ultra-cold Fermi gases, the deconfinement temperature in the case of QCD and the critical temperature at the endpoint of the liquid gas transition in the case of water and helium. The QGP point (square) is taken from the analysis of viscous hydrodynamics, the open squares show lattice QCD data and the lattice data for the ultracold Fermi gas are displayed by the open circles. The dashed curves are theory curves. The theories are scaled by overall factors to match the data near T_c. The lines labelled "holographic bound" correspond to the Kovtun, Son and Starinets (KSS) bound and the Gauss-Bonnet bound. (Figure and caption taken from [8].)

possible core-corona separation as well as the exact hadronisation process, though, reflect the uncertainties of the hydrodynamical approach [37, 109].

If a perfect fluid, i.e. a fluid with vanishing viscosity, is considered, the expectation values can be parametrized only by the local energy density, ϵ, and the local pressure, P [6]. The success of viscous hydrodynamical calculations in describing the p_T spectra as well as the flow components at RHIC and LHC energies has however shown that the medium behaves only approximately as a perfect fluid, approaching closely the lower bound of $\eta/s = 1/(4\pi) \approx 0.08$ (in units of $\hbar/k_B$) as given by AdS/CFT [110]. This finding adds the viscosity to the parametrisation. For comparison, in case of strongly correlated classical fluids the value is much bigger than $\hbar/k_B$, in case of strongly correlated quantum fields however, it is of the order of $\hbar/k_B$, "indicating that dissipation is governed by quantum effects" [8] as it is also the case for ultra-cold Fermi gases, which is shown in figure 2.11.

That the viscosity indeed matters is shown by the authors of [111], from which figure 2.12 is taken. In this figure, the initial energy density as well as the energy density after a system evolution time of 6 fm/c in case of an ideal and a viscous fluid, respectively, are illustrated. Whereas in the ideal case, the initial fluctuations are still somewhat recognizable, the viscosity leads to a significant effect of dissipation. Translating this effect into the calculation of the elliptic flow, it turns out that viscosity reduces the flow effect as compared to the ideal case. This reduction of the flow, which is needed to reproduce the measurements, can be tuned by the value of the viscosity.
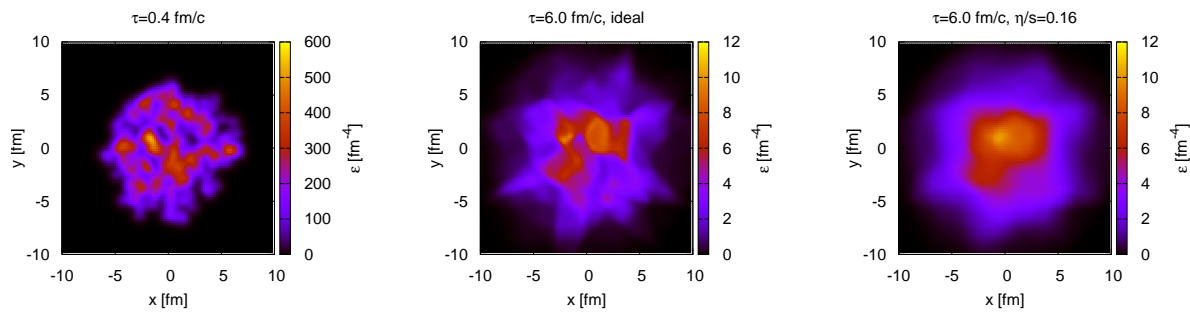
Figure 2.12: Energy density distribution in the transverse plane for one event with $b = 2.4\,\mathrm{fm}$ at the initial time (left), and after $\tau = 6\,\mathrm{fm}/c$ for the ideal case (middle) and with $\eta/s = 0.16$ (right). Figure and caption taken from [111]. Calculations from the viscous fluid-dynamic simulation MUSIC.

Recent calculations indicate, that the system at the LHC seems to be "less ideal" than at RHIC [102], where $\eta/s \approx 0.12$ is 40% smaller than at LHC energies. Since "a small η/s is generally considered to be evidence for the on-set of a strongly-coupled deconfined plasma early in the evolution of the collision"[112], does a larger value hint to a "weaklier" coupled system as it could be expected due to the dependence of α_s on the energy scale?

Baryon-to-meson-enhancement

In figure 2.13, the proton-to-pion-ratio measured by ALICE is shown for different centralities. In central collisions the ratio exhibits a baryon-to-meson enhancement compared to more peripheral collisions. This enhancement is well described by viscous hydrodynamics for $p_\mathrm{T} \lesssim 3\,\mathrm{GeV}/c$. Since within the hydrodynamic picture, the collectivity and the flow respectively are the main ingredients, the proton-to-pion ratio can be understood as a result of the mass ordering induced by the radial flow, pushing heavier particles to higher p_T. In contrast to the anisotropic elliptic flow, the radial flow is strongest in central collisions and increases with collision energy if the same centralities are considered [107].

  Leaving the hydro-regime and regarding now the momentum region above, another hadron production mechanism or the hadron production influencing mechanism may come into effect. The authors of [115] propose "that hadron production at momenta of a few GeV/c in an environment with a high density of partons occurs by recombination, rather than fragmentation, of partons." It is shown "that recombination always dominates over fragmentation for an exponentially falling parton spectrum, but that fragmentation wins out eventually, when the spectrum takes the form of a power-law." Recombination means in this case that baryons and mesons are formed within a densely populated phase space from combinations of the available quarks and anti-quarks during the hadronisation process, i.e. at a late stage of the system evolution. Since the population in the lower p_T region is much larger than at higher p_T due to the steeply falling parton spectrum, the recombination is expected to appear mainly at low p_T. The low phase space density at high p_T seems to suppress the recombination, although it is principally much easier to build a high p_T hadron from three quarks with momenta of $p_\mathrm{T}/3$ than from a fragmenting parton which needs to have a much
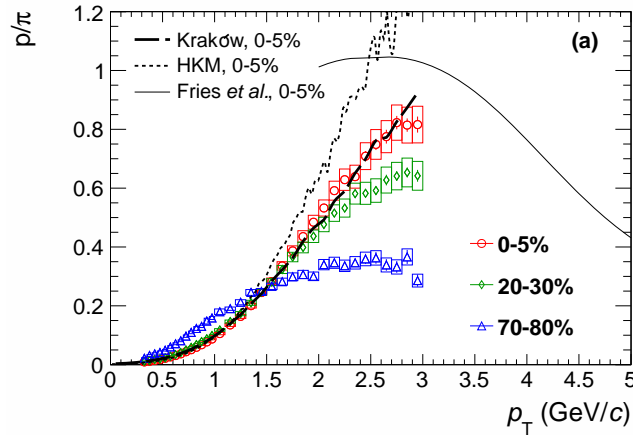
Figure 2.13: $\mathrm{p}/\pi = (\mathrm{p} + \bar{\mathrm{p}})/(\pi^+ + \pi^-)$ as a function of p_T for different centrality bins compared to ratios from the Kraków [113] and HKM [114] hydrodynamic models and to a recombination model [115]. Figure and caption taken from [107].

higher p_T than the resulting hadron. Two basic features characterize the recombination model: "the probability for the emission of a meson (baryon) is proportional to the single parton distribution squared (cubed), and the parton momenta sum up to the hadron momentum."[115]

Concerning the elliptic flow v_2, in the recombination picture this quantity should not scale with the particle mass but rather obey the quark number scaling. The latter is given if the v_2 distributions of different particles fall on a single curve when v_2 and the corresponding p_T are divided by the number of constituent quarks. At RHIC, such a scaling was indeed observed, though at the LHC, it is violated by $\approx 20\%$ [116]. As a remark, in case of RHIC, the key measurement for the idea of constituent quark number scaling was the v_2 and the R_{AA} of the ϕ meson, which has a slightly larger mass than a proton but shows a similar v_2 and suppression as the pions [99]. Regarding the particle production in central collisions, baryons should hence profit more from the radial partonic flow than mesons, because baryons consist of three quarks whose p_T were shifted to higher values. Consequently, in the recombination picture, an enhancement of the baryon-to-meson ratio could be expected for central collisions, where the radial flow is largest. Therefore, the observed baryon-to-meson enhancement in central collisions at RHIC [99, 117, 118] could be interpreted in terms of recombination at intermediate p_T. Comparisons of model calculations with data from RHIC show an agreement up to $p_T \approx 5\,\mathrm{GeV}/c$ [118].

Is recombination also given at the LHC? When does fragmentation take over? This discussion is left to the last chapter of this document.

2.3 Modification of K_s^0 and $\Lambda(\overline{\Lambda})$ p_T spectra in Pb–Pb collisions

The K_s^0 meson and the $\Lambda(\overline{\Lambda})$ baryon are particles containing strange quarks. Prior to the review of the thesis title and its motivation, the role of strangeness in heavy-ion collisions is discussed in the following.

particle	mass (GeV/c^2)	quark content	decay channel	BR (%)	$c\tau$ (cm)
baryons					
Λ	1.115	uds	$p + \pi^-$	63.9	7.89
Ξ^-	1.321	dss	$\Lambda + \pi^-$	99.9	4.91
Ξ^0	1.314	uss	$\Lambda + \pi^0$	99.5	8.7
Ω^-	1.672	sss	$\Lambda + K^-$	67.8	2.46
mesons					
K_s^0	0.498	$\frac{1}{\sqrt{2}}(\mathrm{d\bar{s}}+\mathrm{\bar{d}s})$	$\pi^+ + \pi^-$	69.2	2.68
K^+	0.494	$\mathrm{u\bar{s}}$	$\mu^+ + \nu_\mu$	63.6	371
K^-	0.494	$\mathrm{\bar{u}s}$	$\mu^- + \nu_{\bar{\mu}}$	69.2	371

Table 2.1: Strange particles analysed or regarded in this work. BR: branching ratio, $c\tau$: mean proper decay length. Values from [13].

2.3.1 What a strange particle! - Strangeness in AA collisions

"The very high abundance of strange particles, in particular of hyperons (the Omega-to-pion ratio increases by up to a factor 20 from pp to Pb–Pb), was predicted as a consequence of QGP formation. Today it is interpreted more generally as a manifestation of statistical hadronisation from a thermalised medium, where most hadrons, not only those containing strange quarks, are created in thermal equilibrium ratios."[119]

Strange particles are those particles, which consist of at least one s (s̄) quark. In case of strange baryons, one also speaks about hyperons. The particles analysed (Λ, K_s^0) or regarded in this work are listed in table 2.1. In case of the baryons, also the anti-particles with opposite charge as well as the corresponding anti-quark content and the anti-decay-particles are considered, which are not included in the table.

The occurrence of strangeness is dominated by the production from fragmentation and string breaking as compared to the availability as sea-quarks in the nucleons determined by the PDFs. Simply speaking, strangeness needs to be produced during the collision in contrast to u and d quarks, which are present as valence quarks at the initial state. The dominant mechanism is the gluon fusion with $gg \to s\bar{s}$. Quark-antiquark annihilation is suppressed, because the time scale is too long as compared to the QGP equilibrium and to the gluon fusion.

In central AA collisions, where a thermal equilibrated state is likely to be formed, also statistical equilibration is thought to be reached. Statistical equilibration is produced in a "system of hadrons of given energy, baryon number and strangeness from some non-hadronic state by a statistical process, which fills hadronic phase-space in the statistically most probable configuration."[120] Since strangeness is conserved by the strong interaction, s and s̄ quarks have to be produced by the same amount. Hence, in small systems, together with one strange hadron, another hadron with opposite strangeness has to be created inside the small volume at the same time. The latter requires more energy as compared to heavy-ion collisions, limiting the production rate: In AA collisions, the strangeness conservation needs to be fulfilled only globally, because the production of a strange hadron can be compensated by the production of an anti-strange hadron on the other side of the nuclear fireball [120] - the larger phase space relaxes the local strangeness conservation. Whereas pp and peripheral AA
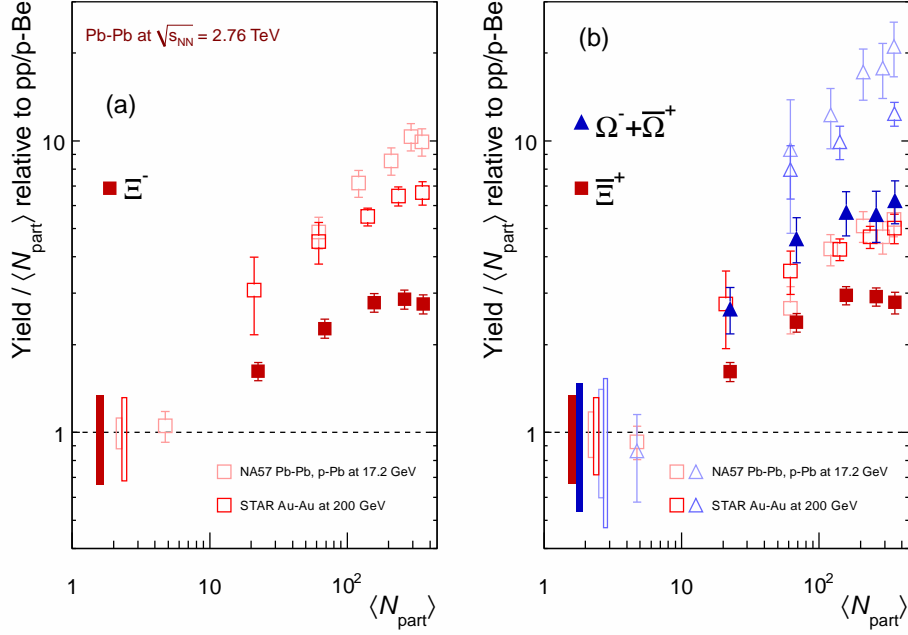
Figure 2.14: Enhancements in the rapidity range $|y| < 0.5$ as a function of the mean number of participants $\langle N_{part} \rangle$, showing LHC (ALICE, full symbols), RHIC and SPS (open symbols) data. The LHC data use interpolated pp values (see text). Boxes on the dashed line at unity indicate statistical and systematic uncertainties on the pp or pBe reference. Error bars on the data points represent the corresponding uncertainties for all the heavy-ion measurements and those for p–Pb at the SPS. Figure and caption taken from [108].

collisions can be regarded as canonical systems, central AA collisions rather represent a grand canonical ensemble [121]. Consequently, one speaks about canonical suppression of strangeness in pp collisions as compared to AA collisions.

The strange hadrons profiting most from the strangeness re-distribution within the system are the multi-strange hadrons such as Ξ and Ω. In figure 2.14 (a,b), the ratio of the abundances of these particles from pp to central heavy-ion collisions are shown as a function of N_{part} for SPS, RHIC and LHC energies. The ratios are normalised to N_{part} in order to account for the system size. The observed strangeness suppression, represented by the ratios all exceeding unity, is increasing with decreasing collision energies. In case of the Ω^-, the values are larger than for Ξ^- at all energies, which could be a result of the triple s quark content of the Ω^- reflecting the enhanced $s\bar{s}$ in a hot and extended medium.

Apart from the multi-strange baryon production, also the abundances of single strange particles are of interest. Within this work, additionally the production of single strange particles as compared to pp and to pions is addressed.

As soon as the mean free path of the elastic reactions becomes larger than the system size as a consequence of the expansion, the thermal equilibrium collapses and the system freezes out. This freeze-out reflects the already mentioned kinetic freeze-out. Prior to that, the system is anticipated to freeze-out chemically, i.e. the thermal equilibrium is maintained, but the hadron abundances are fixed due to the vanishing inelastic reactions [6]. Thus, the chemical freeze-out is expected to occur at a higher temperature T_{ch} than the kinetic freeze-out. Therefore, in order to obtain a

full description of the particle production from a hydrodynamical consideration, the calculation of the hydrodynamical phase must be followed by a hadronic freeze-out formalism including the freeze-out stage(s). The assumption of their duration as well as of the chemical freeze-out existence and its temperature are the main source of large systematic uncertainties of the calculations.

The following parameters mainly describing the particle production in equilibrium are T_ch, μ_B via the ratio of the $\overline{\mathrm{p}}/\mathrm{p}$ yield,

$$\frac{\overline{\mathrm{p}}}{\mathrm{p}} = \exp^{\frac{-2\mu_\mathrm{B}}{T_\mathrm{ch}}}, \tag{2.26}$$

and the volume V, that is typically constrained by the pion production, as a normalization parameter [122]. Statistical hadronisation models (SHM) are relatively successful in describing particle abundances and the corresponding particle ratios. The chemical freeze-out temperature is obtained from a global fit to a large number of different particle yields. Current estimates are $T_\mathrm{ch} = 156\,\mathrm{MeV}$ ($\mu_\mathrm{B} = 0$) in [123] and T_ch $170\,\mathrm{MeV}$ ($\mu_\mathrm{B} = 1\,\mathrm{MeV}$) in [124]. These models, as mentioned at the beginning of this section, assume a thermally equilibrated, grand-canonical system, that finally freezes out after the creation of hadrons. The hadronisation process is described by the formation of massive colourless objects such as clusters. "Each cluster gives rise to multi-hadronic states in a purely statistical fashion,"[125] which means that the formalism for statistical ensembles are used to extract information, such as the chemical freeze-out temperature, from the clusters. Most of the SHM models additionally contain the so-called strangeness suppression factor γ_s, which is 0.5 - 0.7 in elementary collisions and ≈ 1 in non-peripheral heavy-ion collisions.

Closing questions are: How is the thermal equilibrium established? How is the chemical and the kinetic freeze-out reached; are they universal? Does a chemical freeze-out exist or is there only one freeze-out stage? These aspects are still under investigation. Two competing scenarios for the equilibrium are discussed in [119]: The system is either evolving into (thermal) equilibrium or the partons are born into (phase-space) equilibrium [126]. It has to be clarified, "whether it is a proper thermal-statistical equilibrium in a finite volume or rather a phase space dominance effect."[127] The authors of [128] argue that the chemical freeze-out is indeed given by a universal statistical hadronisation. While the latest temperature of chemical equilibrium is expected to be universal and to coincide with the critical (cross-over) temperature from LQCD, T_ch is found to be centrality-dependent. On the other hand, since the chemical freeze-out temperature resembles the QCD temperature, doubts exist, that the chemical freeze-out takes place at all or at least appears as a separate stage of the collision.

2.3.2 R_AA of $\mathrm{K^0_s}$ and $\Lambda(\overline{\Lambda})$

Summarising this chapter, the working title of this thesis, "Modification of $\mathrm{K^0_s}$ and $\Lambda(\overline{\Lambda})$ p_T spectra in Pb–Pb collisions with ALICE", adds two further dimensions to the initial problem statement as discussed at the beginning: Could an AA collision be understood as a superposition of single pp collisions?

During the last sections it was argued that AA collisions are not comparable with a pp superposition picture, neither at high nor at low p_T. At high p_T, the fragmentation and/or the energy loss in the medium cause the difference, while at low p_T, different

strangeness production mechanisms are at work. In case of flow, the situation in pp seems to be less clear, but flow is in fact considered to be strongest in Pb–Pb collisions. The additional dimensions as further means for exploring possible differences of the two collision systems, here, are the strangeness on the one hand and the baryon-versus-meson comparison on the other. The advantage of K_s^0 and $\Lambda(\overline{\Lambda})$ as compared to the multi-strange particles is given by their larger p_T reach, enabling the study of the high p_T region, where the fragmentation and the parton energy loss are the aspects of interest. The low p_T region is investigated in order to quantify the strangeness production and to investigate the balance of different particle production mechanisms in the two collision systems. The main research questions of this work are:

- How does the R_{AA} of K_s^0 and $\Lambda(\overline{\Lambda})$ compare to that of unidentified charged particles?

- Is the modification different for different flavours?

- Are there divergences for baryons and mesons?

- Is the modification different for particles and anti-particles?

- How does the modification change, when comparing to lower collision energies?

- How much strangeness is produced in pp at the LHC?

For addressing these questions, the p_T spectra of K_s^0 and $\Lambda(\overline{\Lambda})$ are determined in pp collisions as well as for different centralities in Pb–Pb collisions. The adjacent chapter reviews the experimental conditions, the data analysis is then discussed in the subsequent chapter.

"ALICE (A Large Ion Collider Experiment) is a general-purpose, heavy-ion detector at the CERN LHC which focuses on QCD, the strong-interaction sector of the Standard Model. It is designed to address the physics of strongly interacting matter and the quark-gluon plasma at extreme values of energy density and temperature in nucleus-nucleus collisions. Besides running with Pb ions, the physics programme includes collisions with lighter ions, lower energy running and dedicated proton-nucleus runs."

ALICE Collaboration [129]

3

The ALICExperiment

At the research centre for nuclear and particle physics CERN in Geneva (Switzerland) the currently largest and most powerful particle accelerator is in operation, the Large Hadron Collider (LHC). The ALICE apparatus, as one of the main LHC particle detectors, is located at the interaction Point 2 of the LHC ring. In figure 3.1 the LHC complex, the location of the LHC experiments and the different accelerator components used for the pre-acceleration are sketched. The LHC is capable of colliding protons with protons (pp), lead with lead nuclei (Pb–Pb) as well as protons with lead nuclei (p–Pb).
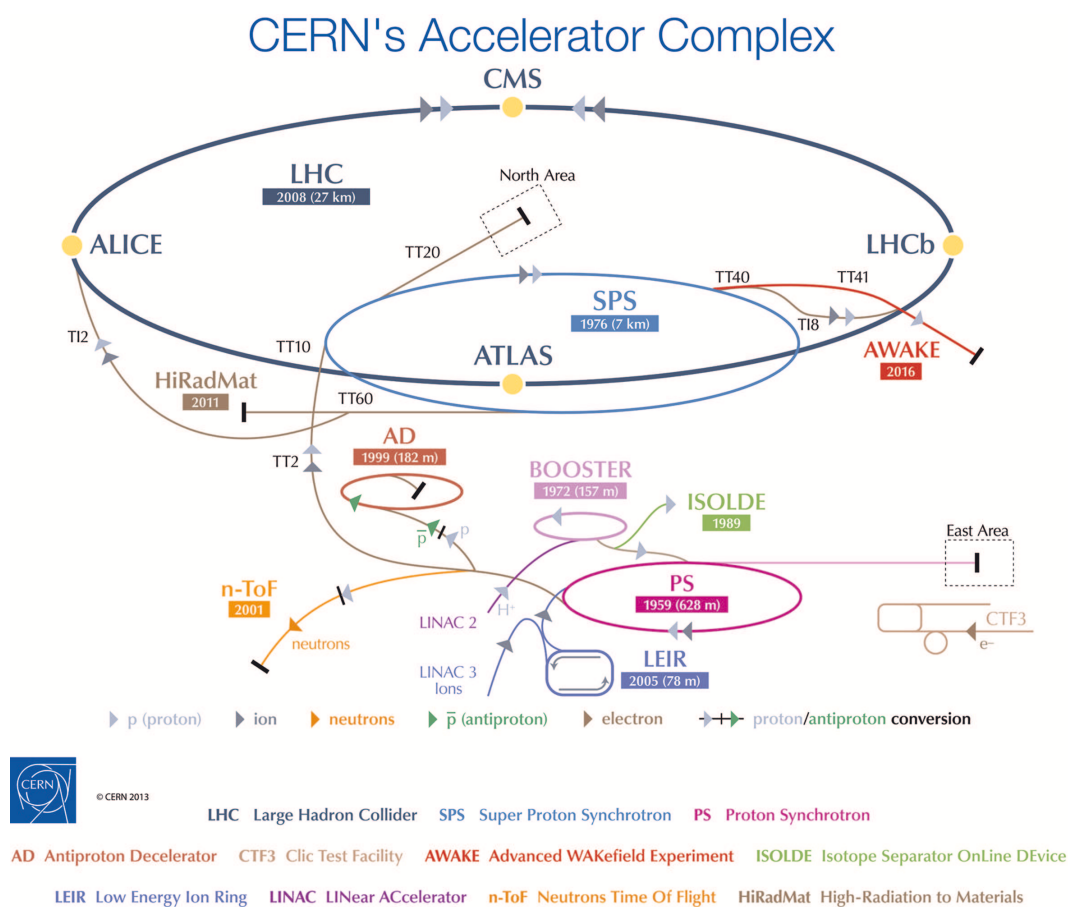
Figure 3.1: A sketch of the CERN accelerator complex [130].
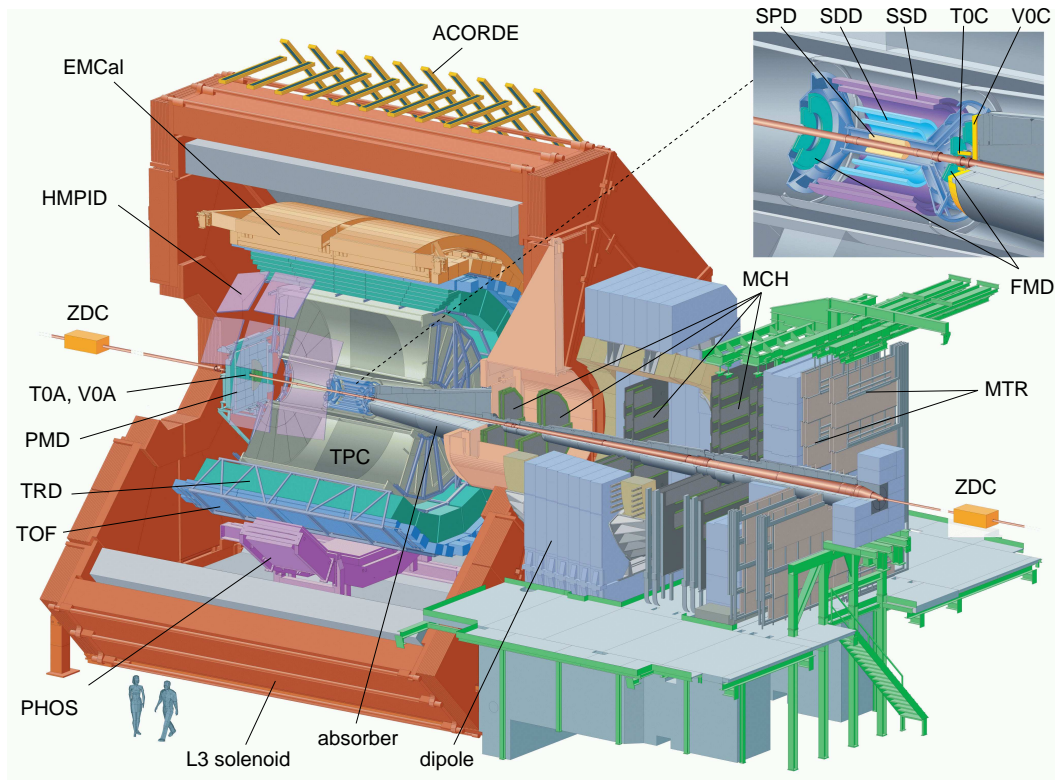
Figure 3.2: A schematic drawing of the ALICE detector set-up with abbreviations of the sub-detectors [131].

3.1 The detector set-up

The ALICE apparatus is designed for the measurements of high energy Pb–Pb collisions. The challenge to cope with is the large particle multiplicity, which is 100 - 1000 times larger than the multiplicity in pp collisions. Whereas CMS and ATLAS are intendedly constructed to track special particles (mainly muons and electrons) from pp collisions at large transverse momenta, ALICE has its strength in measuring all kinds of charged particles with low as well as high momenta and accomplishing the large track density in central Pb–Pb collisions at the same time thanks to the high detector granularity. An example for a high multiplicity Pb–Pb collision as seen by the Time Projection Chamber (TPC) of ALICE is shown in figure 3.3. The low momentum threshold is around $p_T^{\min} = 0.15\,\mathrm{GeV}/c$ with a relative momentum resolution of 3.5% (10% at $p_T = 50\,\mathrm{GeV}/c$). The particle identification (PID) capability covers a p_T range from 0.15 - 20 GeV/c.

The detector layout is mainly based on the so-called onion layer model. In the central-barrel, defined as the volume inside the L3 solenoid magnet with a B-field of 0.5 T longitudinal to the beam axis, detectors for vertex finding, tracking and PID are installed. Their order is chosen such, that they meet the requirements of coping with the local track density and simultaneously ensuring a sufficiently high vertex and momentum resolution.
The determination of the collision vertex is the fundamental task in collider experiments, since the vertex marks the reference point for the track finding and reconstruction. Hence, a high granularity of the vertex detector system, a fast detector response
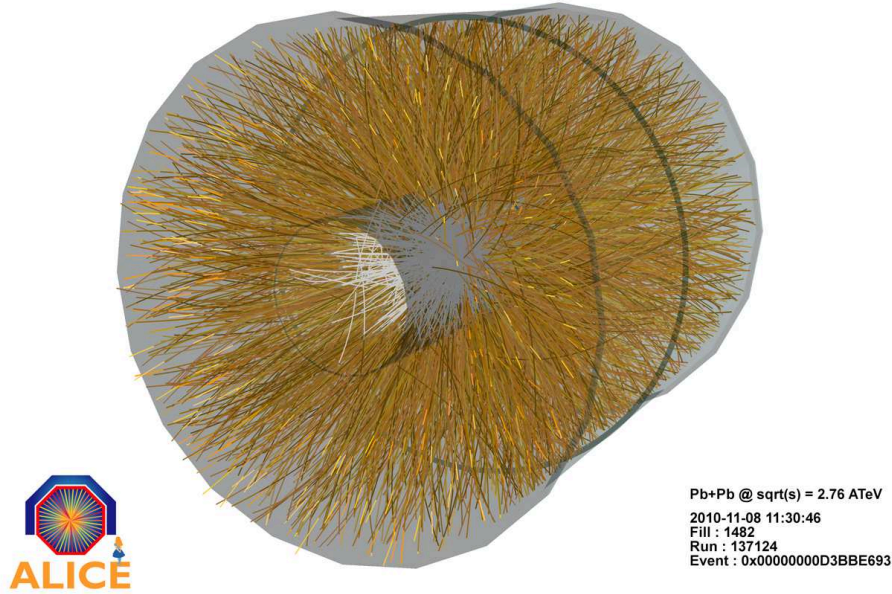
Figure 3.3: An event display of a Pb–Pb collision recorded in 2010 as seen by the central barrel detectors of ALICE.

as well as a short distance to the interaction point are important. For this reason, most vertex detectors are pixel detectors surrounding the interaction point. The track density decreases with the growing distance to the collision vertex. Therefore, the high granularity required of the innermost detector for the vertex reconstruction can be reduced at some distance, which marks the transition from one to another detector system. In case of ALICE, the central-barrel detectors covering the full azimuth[1] are the Inner Tracking System (ITS), the TPC, the Transition Radiation Detector (TRD) and the Time Of Flight detector (TOF) (see figure 3.2). Each detector has its own strengths and capabilities, which are discussed in the following section for some of the detectors that are important for the present analysis.

In order to enlarge the precision in the high momentum region as well as on the identification of selected particles such as photons, the Photon Spectrometer (PHOS), the Electromagnetic Calorimeter (EMCal), and the High Momentum Particle Identification Detector (HMPID) were added to the detector system covering around 100° degrees in azimuth. Common to all mentioned detectors is the symmetric polar acceptance coverage around the origin of the coordinate system. The individual acceptance, however, is different for each system. Usually, the polar acceptance is expressed in terms of the pseudo-rapidity[2] η, for example $|\eta| < 0.9$ in case of the TPC. Furthermore, forward detectors (non-symmetric coverage in η) were installed to perform the triggering, the event characterization as well as the multiplicity measurement (see section 3.5) and the muon identification. The majority of these systems, such as the plastic scintillator detector VZERO, the quartz Cherenkov detector T0, the Photon Multiplicity Detector (PMD) and the silicon-based Forward Multiplicity Detector (FMD)

---

[1] "The ALICE Coordinate System is a right-handed orthogonal Cartesian system defined as follows. The origin is at the LHC Interaction Point 2 (IP2). The z axis is parallel to the mean beam direction at IP2 and points along the LHC Beam 2 (i.e. LHC anticlockwise). The x axis is horizontal and points approximately towards the centre of the LHC. The y axis, consequently, is approximately vertical and points upwards."[131]

[2] $\eta = -\ln \tan\left(\frac{\theta}{2}\right)$, with θ representing the polar angle.

are installed inside the L3 magnet. Only the Zero Degree Calorimeter (ZDC) and the Muon spectrometer, the latter is operated with an additional dipole magnet, are placed outside symmetrically in azimuth around the beam line. The polar acceptance coverages of all referred detectors can be found in [131].

The following sections describe in more detail the ITS as well as the TPC specifications and capabilities as both are the main detector systems used within this analysis. These systems are also the main charged-particle tracking detectors of ALICE. Furthermore, a section is dedicated to the VZERO detector of/from which the multiplicity information for the event characterization is extracted.

3.1.1 Central barrel: ITS and TPC

The ITS is the innermost layer of the detectors in the central barrel and surrounds the beam pipe. The system itself consists of three layers, each of them employing a different detection technique. The detector sub-system with the smallest radius (3.9 cm, $|\eta| < 2.0$) is constructed by two layers of Silicon Pixel Detectors (SPD), which can be also used for triggering. The second system is given by two layers the Silicon Drift Detectors (SDD), that can be also used for a specific energy loss measurement (dE/dx) thanks to its analogue readout to measure the deposited charge. This is also true for the third system, consisting of three layers of Silicon Strip Detectors (SSD) with an outer radius of 43 cm ($|\eta| < 1.0$). It is important to mention here that the dE/dx measurement is only used for tracks at very low p_T (p_T <0.15 - 0.7 GeV/c depending on the particle species).

The TPC is a gas detector used for tracking as well as for PID by the principle of the specific ionisation energy loss of charged particles traversing the gas. This cylindric detector, surrounding the ITS covers an acceptance of $|\eta| < 0.9$, which is a result of its dimensions that are 5 m in beam direction and a radius of 2.5 m. The active volume ranges from 85 cm $< r <$ 247 cm and is filled with a gas mixture of Ne-CO_2. The read-out is placed perpendicular to the beam axis at the opposite end-caps, and is segmented into 18 individual read-out sectors. Each of them consists of 159 pad-rows for measuring the charge deposit caused by the trespassing charged particles ionising the gas.

The connection between the PID and the dE/dx measurement is given by the Bethe-Bloch formula [132]:

$$\left\langle \frac{dE}{dx} \right\rangle = \frac{4\pi\, N\, e^4}{m_e\, c^2} \frac{z^2}{\beta^2} \left(\ln \frac{2\, m\, c^2\, \beta^2\, \gamma^2}{I^2} - \beta^2 - \frac{\delta\left(\beta\right)}{2} \right), \qquad (3.1)$$

where N is the number density of electrons in the matter traversed, e is the elementary charge, $m_e\, c^2$ is the rest energy of the electron, z the charge of the particle and β its velocity. I represents the mean excitation energy of the gas atom. With $p/(m\, c) = \beta\gamma$, the energy loss can be formulated as function of the particle momentum. In turn, for a given momentum, dE/dx depends only on the charge and mass of the particle. Each particle mass yields a different Bethe-Bloch curve according to which a probability of having found a particle of this specific mass is calculable. The complication of this method lies in the fact that the curves for some particles cross or have the same shape in some momentum regions. Figure 3.4 displays this description by showing the specific energy deposit versus the particle momentum together with ALEPH parametrisations of the Bethe-Bloch formula. Concerning the PID performance, "a truncated
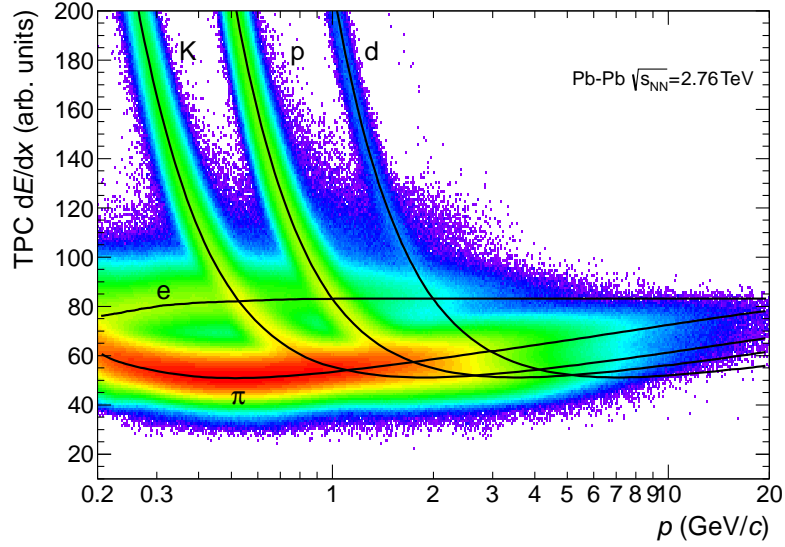
Figure 3.4: Specific energy deposit $(\mathrm{d}E/\mathrm{d}x)$ in the ALICE TPC vs. particle momentum in Pb–Pb collisions at $\sqrt{s_{\mathrm{NN}}} = 2.76\,\mathrm{TeV}$. The lines show the parametrizations of the expected mean energy loss. Figure and caption taken from [131].

mean $\mathrm{d}E/\mathrm{d}x$ (40% highest-charge clusters discarded) is calculated and used for a wide range of momenta. The largest separation is achieved at low p_{T} ($p_{\mathrm{T}} < 0.7\,\mathrm{GeV}/c$) but a good separation is also present in the relativistic rise region ($p_{\mathrm{T}} > 2.0\,\mathrm{GeV}/c$) up to $20\,\mathrm{GeV}/c$."[131]

3.1.2 VZERO detectors

The major tasks of the VZERO system are to provide triggers (see section 3.2.1) and to separate beam-beam interactions from accelerator background events, e.g. beam-gas interactions. In addition, the measurement of the luminosity[3], needed for the determination of the absolute cross-section of the collision, as well as the measurement of the charged particle multiplicity for the centrality determination are performed by the system [133].

The VZERO system consists of two parts in opposite forward direction, the VZERO-A detector at $2.8 < \eta < 5.1$ and the VZERO-C detector at $-3.7 < \eta < -1.7$. In figure 3.5 their position along the beam axis relative to the interaction point (IP) is sketched. Both detectors are built from plastic scintillating material connected to photo multiplier tubes for read-out. The sensitive surface perpendicular to the beam line is segmented into rings, that are read out independently.

---

[3]The luminosity is defined via the beam interaction rate $R = \sigma L$, where σ is the interaction cross-section and the luminosity $L = f\,n\frac{N_1 N_2}{A}$. The latter is determined by the revolution frequency f of the accelerated particle bunches, N is the number of particles in each bunch, n is the number of bunches and A is the cross-sectional area of the beams [10].
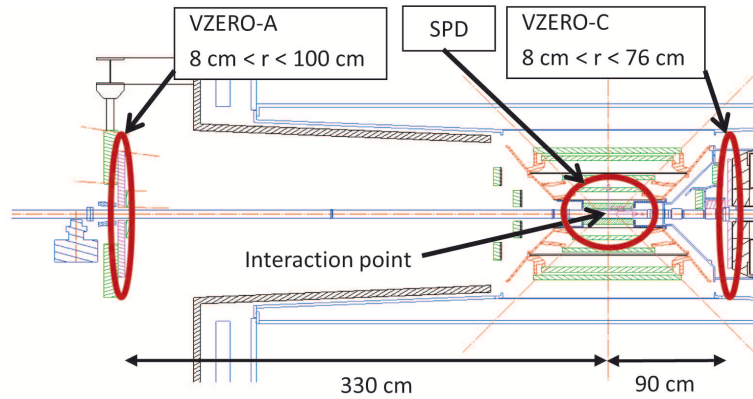
Figure 3.5: A sketch of the VZERO system component positions along the beam line [134].

3.2 Data taking and analysis environment

3.2.1 Trigger

A very important step in the data taking procedure is the selection of events to be recorded. Not every detector signal is connected to a real hadron collision and not every hadron collision is of interest in the given research programme. Already during signal collection the so-called trigger system is capable of selecting certain event classes, which are meant to be stored.

Besides beam-gas collisions, the machine background originating from beam machine material interaction (e.g. material knock-out) need to be separated from the intended beam-beam collisions. If these satellite events are recognized early enough by, for example, the VZERO detector system, the other central barrel detectors do not need to be switched to the read-out mode. This selection of events and the communication among the different detector systems is called triggering. In addition, the trigger is responsible for checking if some detectors are in a busy state, i.e. if they are currently not available for data taking, and for providing a past-future protection[4]. The latter is important since some detectors as the TPC have long sensitive times ($88\,\mu$s as compared to $25\,\mu$s between the bunch crossings (machine clock cycle)) during which they register tracks from already passed and recent collisions [135].

The ALICE trigger system is subdivided into three levels: L0, L1, L2. In addition there is the so-called High Level Trigger (HLT), which filters events that passed L2 and hence, allows to trigger on special physics cases such as jets or high momentum electrons. "The trigger decision is generated by the Central Trigger Processor (CTP) of ALICE based on detector signals and information about the LHC bunch filling scheme."[131] Afterwards, the CTP sends the correct sequence of trigger signals to all detectors [135].

The Level 0 trigger collects information from the VZERO system, T0, SPD, EMCAL, PHOS and MTR. Already at this level beam-gas events are rejected. The time between a collision and a L0 decision is about $\sim 0.9\,\mu$s. The L1 trigger decision relies on informations from the ZDC, EMCAL and TRD, which takes an additional time of $\sim 6.5\,\mu$s. Both, the L0 and the L1 trigger the buffering of the event data in the

---

[4]i.e. veto those interactions wherein pileup of more than one interaction is contained.

front-end electronics. Only on L2 it is decided whether the data are sent to the Data Acquisition (DAQ) as well as to the HLT. The whole decision process from L0 to L2 takes about $\sim 107.4\,\mu$s.

3.2.2 Computing

Due to petabites of data, the processing of the tracking as well as the analysis requires an appropriate environment offering high enough computation speed and adequate disk space. In view of these requirements, the GRID computing was accomplished, which aims at providing resources e.g. computing power, storage, software. In detail the GRID coordinates and integrates these resources that are not subject to centralized control [136]. This means that the storage and the computing are hosted in different control domains, which can be the user's desktop or the CERN computing facility. The GRID can be regarded as a virtual organization, that shares its resources with others [137]. Service level agreements define how a member of a virtual organization can access the resources. Due to the necessity for dynamic resource allocation, grid computing enhances the previous distributed computing paradigms in various ways. Current GRID systems expose local computing resources to a larger number of users via the Internet, using GRID middle-wares such as Globus [138], gLite [139], Unicore [140] or ALIEN [141] in case of ALICE.

In addition to the GRID, analyses are also performed on local computing farms as for example "Prometheus" at GSI. There, the main parts of this analysis were carried out via the so-called analysis train. An adapted version of the latter is also run on the GRID by the ALICE collaboration.

Apart from the computing resources, a coding environment is vital for a well structured and organised data analysis. All individual data analyses as well as the event and particle track reconstruction are employing the coding framework of ROOT, the particle physics analysis tool invented at CERN [142]. Each experiment has established its own specific programming environment on the basis of C++ and ROOT. In case of ALICE, the corresponding software is named AliRoot. Each piece of code to be added or changed needs to fulfil the coding rules of ALICE, before being committed to AliRoot.

3.3 Event and track reconstruction

The detector information stored during the read-out need to be translated into particle track information such as charge of the particle, the track curvature, the track momentum, the track position and length, the specific energy loss in the detector material. The detector information is available as digits or cluster of digits, which are digitised signals (ADC counts) from the sensitive readout parts of the detector components. By the help of the `AliReconstructor` (see figure 3.6) taking into account the track bending due to the magnetic field as well as the material budget, this information from the several clusters is combined in order to reconstruct the particle track and the collision vertex. During the reconstruction procedure of the raw data containing the cluster information, the so-called offline (i.e. after the data taking) detector calibration is performed. This procedure is repeated up to three times in order
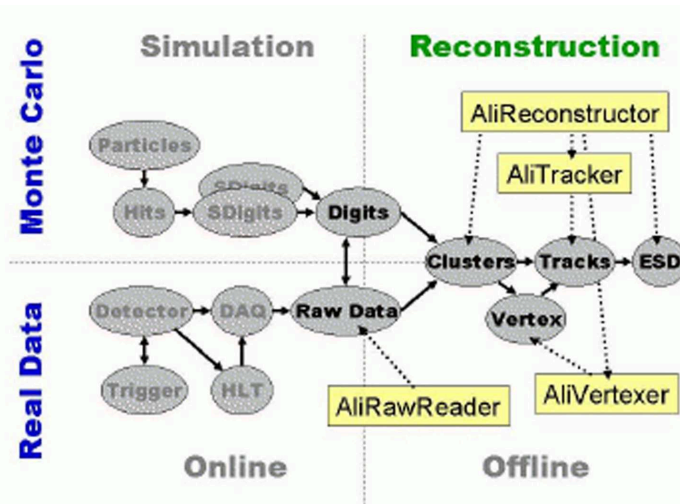
Figure 3.6: The ALICE data and track reconstruction framework for MC and data [143].

to improve the quality of the calibration iteratively and to reduce the uncertainties on the track information. The final data format of the output of the reconstruction is called Event Summary Data (ESD). It contains lists of reconstructed tracks, i.e their properties as well as global event properties like the collision centrality and the vertex position.

A more detailed description of the tracking procedure in ALICE is given by the sketch in figure 3.7. Directly after the clusterisation, the preliminary primary collision vertex finding is started using information of the SPD, the innermost layer of the ITS. The primary vertex position serves as input for the next tracking step, the track finding in the TPC. There, the preliminary tracks are calculated under the assumption to originate from the primary vertex and to stem from pions, i.e. the pion mass is associated with each track in order to calculate the momentum from the track curvature. This step is followed by a matching procedure, which tries to find the corresponding track parts in the ITS. Only if a match is found, the track finding in the ITS is performed. The tracks are successively propagated in outward direction to find matches in the other detector systems such as the TRD, TOF, EMCAL, PHOS and the HMPID. Finally, the tracks are propagated in the inward direction trough the whole apparatus. At this moment, the vertex reconstruction is revisited and finalized with the fully propagated tracks. The assumption, that all tracks originate from the primary vertex, however, is not true. Therefore, subsequently a decay vertex (secondary vertex) finding is performed before the reconstruction procedure is finalized.

The reviewed reconstruction procedure is also followed in case of simulated collisions. Here, the collision is obtained from event generators such as HIJING [144] in case of Pb–Pb, PYTHIA [145] or PHOJET [146] in case of pp and DPMJET [147] or EPOS [148] for all collision systems. These generators are based on or use in some way pQCD calculations as mentioned in chapter 2 and constraints provided by measurements. The particles created in the generated collision are then propagated through a detector simulation yielding the digits and clusters needed as input for the reconstruction scheme (see figure 3.6). The detector simulation is currently performed with the GEANT3 software package [149].

```
┌ ─ ─ ─ ─ ─ ─ ─ ┐     ┌──────────────┐     ┌──────────────┐     ┌──────────────┐
│ Clusterization │────▶│ Preliminary (SPD) │──▶│ TPC track    │────▶│ TPC track    │
│ (all detectors)│     │ interaction      │   │ finding      │     │ matching in ITS │
└ ─ ─ ─ ─ ─ ─ ─ ┘     │ vertex finding   │   └──────────────┘     └──────────────┘
                      └──────────────┘

┌──────────────┐     ┌────────────────────────────┐     ┌──────────────┐
│ Track inward │◀────│ Track outward propagation, length │◀──│ Standalone ITS │
│ propagation  │     │ integration for PID. Matching to TRD, │   │ track finding │
│ with final refit │  │ TOF, EMCAL, PHOS, and HMPID │     └──────────────┘
└──────────────┘     └────────────────────────────┘

┌──────────────┐     ┌──────────────┐     ┌──────────────┐
│ Final interaction │──▶│ Secondary vertex │──▶│ Cascade      │
│ vertex finding │     │ (V⁰) finding │     │ finding      │
└──────────────┘     └──────────────┘     └──────────────┘
```

Figure 3.7: The ALICE track reconstruction scheme [131].

3.3.1 Calibration

The calibration strategy includes the online calibration, i.e. a calibration already applied during data recording, and the offline calibration, which is performed during the event and track reconstruction process.

Important for the online calibration is information about the conditions, as for example the temperature and pressure conditions for each detector system, because they affect the detector response and operation. These data are continuously monitored by the detector control system (DCS) and are processed by the DAQ system. Finally the calibration data are stored in the online calibration data base (OCDB) for each run. A run is defined by the events continuously recorded until the data acquisition is stopped.

The offline calibration is performed during the reconstruction process, which is executed after the data acquisition. During cpass0, only a few events of each run are reconstructed in order to obtain input for the following calibration process. "The complete calibration reconstruction sequence is thus: cpass0, calibration, cpass1, quality assurance and calibration, manual multi-run calibration, validation pass, quality assurance, physics reconstruction pass, quality assurance." [131] The complete calibration, however, is finalized after the data taking period. The reason for this is the quality assurance process including run-wise checking, which needs to be manually performed.

3.4 Secondary vertex reconstruction

Two procedures for secondary vertex reconstruction are implemented in AliRoot. Figure 3.8 depicts the track topology of the daughter particles from K_s^0 ($K_s^0 \rightarrow \pi^+ + \pi^-$) and Ξ^- ($\Xi^- \rightarrow \Lambda + \pi^-$) decays. The basic principle of finding a secondary vertex is the combination of two tracks from particles of opposite signed tracks, which are close in 3D and which are presumably originating from the decay of one mother particle. At this stage, no mass for the daughters is assumed, the secondary vertex is reconstructed via geometrical considerations and only a 3D momentum vector is calculated from the daughter tracks. The properties of the combined tracks as well as of the resulting mother momentum are requested to pass some quality selection criteria before being
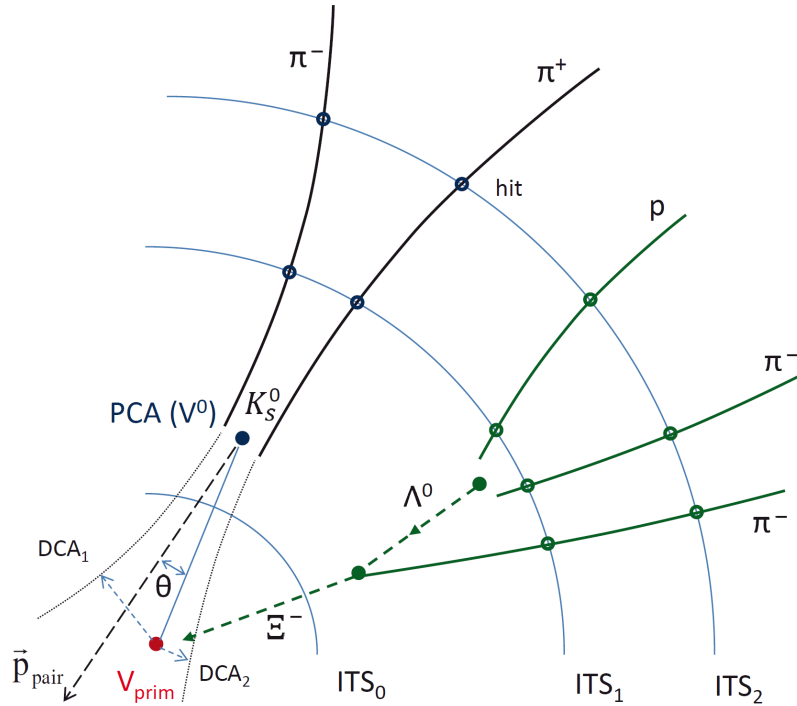
Figure 3.8: Secondary vertex reconstruction principle, with K_s^0 and Ξ^- decays shown as an example. For clarity, the decay points were placed between the first two ITS layers (radii are not to scale). The solid lines represent the reconstructed charged particle tracks, extrapolated to the secondary vertex candidates. Extrapolations to the primary vertex and auxiliary vectors are shown with dashed lines. Figure and caption taken from [131]. Λ^0 means in this case Λ.

stored as secondary vertex and as a so called V^0 candidate respectively. The term V^0 accounts for the V-shaped track topology of the daughters and 0 stands for the decay of neutral particles. The identification of a V^0 candidate with a specific particle species, i.e. with a specific mass, is performed at the analysis level via an invariant mass analysis assuming specific masses of the daughter particles. This analysis technique is explained in more detail in chapter 4.

 Whereas the so-called offline V^0 finder is executed after the tracks were reconstructed, the so-called on-the-fly V^0 finder is already operated during the track fitting. The on-the-fly V^0 finder checks if the χ^2 for a track matching with the primary vertex is above a minimal value. In case of a large χ^2, the track is assumed to originate from a secondary vertex and is combined with a candidate of opposite charge from the so-called track hypothesis tree (a virtual intermediate storage system during the reconstruction process). The tracks are re-fitted under the assumption to stem from this secondary vertex candidate taking into account the material budget[5]. The latter can be different for the re-fitted track as compared to the first reconstruction due to a possibly changed track position and curvature. Nevertheless, the track information from the global fitting are kept and stored for further usage. The V^0 track candidates and the secondary vertex candidate, i.e. the mother particle, need to fulfil a number of conditions, which are similar to the offline V^0 finder but less restrictive. In case of the

---

[5]The detector material causes an energy loss of the particles while traversing the detectors and needs hence to be carefully taken into account.

offline V^0 finder, due to the larger amount of combinatorial background from random track combinations, the storage and the computing time would be too large if there were no tight selections. The on-the-fly finder reduces the combinatorial background via the causality selection. This selection minimizes the impact of falsely associated clusters. In detail, the absence of space points in ITS layers which lie between the primary vertex and the decay vertex can be required. Hence, in comparison to the offline V^0 finder, the on-the-fly finder procedure strongly relies on the quality of the performance of both, TPC and ITS, as well as on the detector geometry and material budget description. The following selections (cuts) are applied during the V^0 reconstruction process:

- **DCA/σ**: The Distance of Closest Approach (DCA) of the V^0 candidate momentum vector to the primary vertex is required to be below a given threshold in order to increase the probability of finding a primary V^0 particle and to reduce the combinatorial background (BG). Within the V^0 finder algorithm this variable is scaled by the error σ of the DCA determination, since this quantity forms a Gaussian shape, where the width is independent of the particle momentum. It also takes into account the possible difference in the reconstructed track position in the transverse plane and along the beam direction [150].

- **DCA$_\mathbf{d}$/σ**: The normalized DCA between a daughter track of a V^0 candidate to the secondary vertex (DCA$_1$ and DCA$_3$ in figure 3.8). Also here, the DCA$_\mathrm{d}$/σ is expected to be below a given value in order to reject false V^0 candidates or reduce the number of candidates with an insufficient vertex resolution. Indeed, this selection reduces the BG as well. In addition, a minimal DCA of a daughter track to the primary vertex can be required in order to ensure that the track does not origin from the primary vertex and hence does not belong to a V^0.

- **cos(PA)**: The cosine of the Pointing Angle (PA), which is represented by θ in 3.8, is a comparable variable to the DCA. However it offers a higher granularity and the effect of a cut in cos(PA) is stronger than a cut on DCA thus reducing also more BG.

- **mass hypothesis:** If the daughter tracks of a V^0 candidate are associated with the masses of the decay products of an assumed mother particle, it is not clear whether the assumption represents the truth even if the mass of the mother of interest is reproduced from the 4-momenta of the daughter tracks. If at the same time the same daughter tracks are associated with the masses of the decay products of another particle and if the mass of the latter particle is reproduced as well, then the V^0 candidate is rejected. This selection represents a cut on the mass hypothesis.

3.5 Centrality determination in Pb–Pb collisions

Collisions or events, respectively, can be characterised and identified via trigger schemes. Such schemes do not only contain selections on real collisions or on the incidence of a special particle type above a momentum threshold, also a classification in terms of the collision centrality can be performed, either at the trigger level or at a later stage of the analysis.
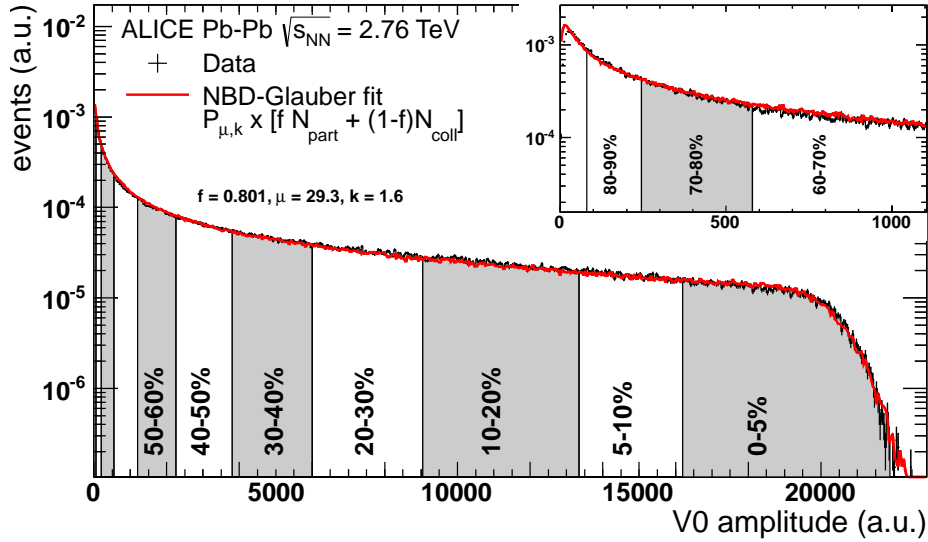
Figure 3.9: Fit of a Glauber model calculation to the VZERO amplitude representing the charged particle multiplicity at mid-rapidity measured by ALICE in Pb–Pb collisions at $\sqrt{s_{\mathrm{NN}}}$ = 2.76 TeV. The area is split into the centrality classes (see text). Figure taken from [31].

The impact parameter of two colliding extended objects describes the distance of closest approach in the transverse plane to the collision axis between the centres during the reaction. In order to study changes of the system behaviour with the impact parameter, the determination of the latter of each collision is necessary since it cannot be induced from outside i.e. it is not possible to control the overlap with the help of the accelerator system. Technically, it is impossible to collide two single Pb ions or protons at these high energies due to their dimensions of femtometer. Therefore, in order to enhance the success rate of a collision, bunches of 10^{10} densely packed Pb ions are collided instead; this underlines again the necessity of triggering on interesting events.

Furthermore, the impact parameter is also not directly accessible via detector information. The key observable for its extraction from data is the charged particle multiplicity for each collision (or the corresponding detector amplitudes), which is sampled for all recorded events yielding the distribution in figure 3.9. The frequency distribution of the amplitude in the VZERO detector is shown, which is proportional to the charged particle multiplicity in the given acceptance. This distribution is overlaid with a calculated curve obtained from the Glauber model [151] for the given experimental conditions. The connection between the multiplicity and the impact parameter is established by the model linking the multiplicity of a collision with a minimal and maximal impact parameter via the so-called nuclear thickness function T_{AA}. Consequently, the relation between the impact parameter and the multiplicity is not unique due to the fact that only the probability of a certain multiplicity at a given impact parameter is predicted by the model.

A common method in the field is to determine the centrality of a collision in percent of the overall hadronic cross section σ_{AA} or of the total number of hadronic interactions N_{ev}, respectively. The total hadronic cross section is given by the integral of the measured particle multiplicity distribution for a given collision energy and system. In figure 3.9 the centrality classes are indicated by the areas between the vertical lines. A

centrality class is fixed by a minimal and maximal multiplicity and can thus be related to a certain range of the impact parameter. "In ALICE, the centrality is defined as the percentile c of the hadronic cross section σ_{AA} corresponding to a particle multiplicity N_{ch} above a given threshold (N_{ch}^{tr}):

$$c \approx \frac{1}{\sigma_{AA}} \int_{N_{ch}^{tr}}^{\infty} \frac{d\sigma}{dN_{ch}} dN_{ch}. \tag{3.2}$$

The percentile of the hadronic cross section is determined for any value of the VZERO amplitude by integrating the measured VZERO amplitude distribution normalized at the anchor point V0AP, it is necessary to know the particle multiplicity at which the purity of the event sample and the efficiency of the event selection becomes 100%. We define the Anchor Point (AP) as the amplitude of the VZERO detector equivalent to 90% of the hadronic cross section. For example, if we define V as the VZERO amplitude, the top 10% central class is defined by the boundary V010, which satisfies 3.3

$$\frac{\int_{V010}^{\infty} (dN_{ev}/dV)dV}{\int_{V0AP}^{\infty} (dN_{ev}/dV)dV} = \frac{1}{9} \quad ." \; [31] \tag{3.3}$$

Although the Glauber model is not directly needed for the centrality class determination, it is vital for the calculation of the total cross section, which is the input for the centrality class definition (equation 3.2): At low multiplicities (amplitudes), the trigger efficiency decreases and the collisions are dominated/influenced by electromagnetic and other background processes. Hence, the measurement yields larger values at low multiplicities that need to be corrected by the Glauber fit to the higher multiplicities in order to determine the unbiased number of events at low multiplicities. The centrality for each event can then be independently calculated from the multiplicities detected by VZERO-A, VZERO-C, ZDC, SPD, and TPC. The total hadronic cross section in Pb–Pb events at $\sqrt{s_{NN}} = 2.76\,\text{TeV}$ is

$$\sigma_{PbPb} = 7.7 \pm 0.1(\text{stat.})^{+0.6}_{-0.5}(\text{syst.})\,\text{b} \quad [131]. \tag{3.4}$$

Another advantage of the Glauber model fit is that variables as the number of participating nucleons in the collision N_{part}, the number of colliding nucleons N_{coll} and the nuclear thickness T_{AA} are accessible for each centrality class as average values over the corresponding impact parameter range. Table 3.1 provides a compilation of these values for the centrality classes studied in this work.

3.6 Cross sections in pp

A centrality classification of pp events is not adequate due to the elementary character of the reaction. Thus, analyses for multiplicity classes are commonly performed instead. Although this is not the case in this work, the determination of the total inelastic cross section is reviewed in the following, because the normalisation of the particle spectra to this cross section is needed as it is explained later.

centrality class	$\langle N_{\mathrm{coll}}\rangle$	$\langle N_{\mathrm{part}}\rangle$	$\langle T_{\mathrm{AA}}\rangle$ (mbarn^{-1})
0 - 5 %	1685	382.7	26.32
5 - 10 %	1316	329.4	20.56
10 - 20 %	921.2	260.1	14.39
20 - 40 %	438.4	157.2	6.85
40 - 60 %	127.7	68.56	1.996
60 - 80 %	26.71	22.52	0.417

Table 3.1: Mean number of binary collisions $\langle N_{\mathrm{coll}}\rangle$, mean number of participants $\langle N_{\mathrm{part}}\rangle$ and the mean nuclear thickness $\langle T_{\mathrm{AA}}\rangle$ for different centrality classes. Compilation of values from [31].

In Pb–Pb collisions, the total inelastic cross section is basically given by the total hadronic cross section. Inelastic, non-hadronic processes, such as diffraction and electromagnetic reactions only contribute at very low multiplicities. Due to the triggering, these kind of events are mostly rejected, for which reason the measured cross section needs to be corrected. The resulting uncertainty in Pb–Pb is small since the major part of the distribution at higher multiplicities is fully given by measurements. As pp collisions show similar multiplicities as low multiplicity Pb–Pb events, the effect of missed events is much larger, resulting in a larger correction of the hadronic cross section to the total number of inelastic events. Furthermore, the correction procedure is more complex, because the Glauber model is not applicable here.

The fraction of missed inelastic events in pp is extracted from the so-called van der Meer scan[6] of events triggered as VZEROand or MBand. The chosen reference process for all of these scans is the coincidence of hits in the VZERO detectors on the A and C sides (MBand). The resulting cross section of this process is $\sigma_{\mathrm{MBand}} = 47.4 \pm 0.9\,\mathrm{mb}$ [131]. For MBor events, a cross section of $\sigma_{\mathrm{MBor}} = 55.5 \pm 1.0\,\mathrm{mb}$ was obtained [60, 153] at a trigger efficiency of 88.1% [153]. Concerning the procedure for extracting the total inelastic cross section, "a Monte Carlo simulation, tuned so as to reproduce the fractions of diffractive events observed in data, was used to determine the efficiency of the MBand trigger for inelastic pp interactions. The MBand cross sections were then corrected for this efficiency"[131], which yields

$$\sigma_{\mathrm{INEL}} = 62.8^{+2.4}_{-4.0}\,(\mathrm{MC}) \ \pm 1.2(\mathrm{vdM})\,\mathrm{mb} \tag{3.5}$$

for $\sqrt{s} = 2.76\,\mathrm{TeV}$ [153].

---

[6]Further details can be found in [152].

4

Analysis: Reconstruction of K^0_S and $\Lambda(\overline{\Lambda})$ transverse momentum spectra

4.1 Transverse Momentum spectra

The transverse momentum spectra determined and analysed in this work for K^0_s and $\Lambda(\overline{\Lambda})$ are represented by the following relation:

$$\frac{1}{N_\mathrm{ev}}\frac{\mathrm{d}^2 N}{\mathrm{d}p_\mathrm{T}\,\mathrm{d}y} = \frac{1}{N_\mathrm{ev(\pm 10cm)}}\frac{\mathrm{d}N}{\Delta p_\mathrm{T}} \cdot \frac{1}{\Delta y} \cdot \frac{1}{\mathrm{eff.}} \cdot \frac{1}{\mathrm{BR}} \cdot \mathrm{FD}_\mathrm{corr}(p_\mathrm{T})\,\mathrm{norm}_\mathrm{abc}, \tag{4.1}$$

where N_ev is the number of analysed events, Δy is the rapidity window, "eff." means efficiency, BR denotes the branching ratio of the selected decay channel, $\mathrm{FD}_\mathrm{corr}(p_\mathrm{T})$ the feed-down correction and $\mathrm{norm}_\mathrm{abc}$ represents some additional normalisation abc. The invariant yield, i.e. the yield being invariant under Lorentz transformation[1] and describing the total cross section of the V^0 production, can be calculated by dividing each yield for a given p_T by $2\pi p_\mathrm{T}$:

$$E\frac{\mathrm{d}^3\sigma}{\mathrm{d}p^3} = E\frac{\mathrm{d}^3\sigma}{\mathrm{d}\phi\, p_\mathrm{T}\,\mathrm{d}p_z\,\mathrm{d}p_\mathrm{T}} = \frac{\mathrm{d}^3\sigma}{\mathrm{d}\phi\, p_\mathrm{T}\,\mathrm{d}y\,\mathrm{d}p_\mathrm{T}} \implies \frac{\mathrm{d}^2\sigma}{2\pi\, p_\mathrm{T}\,\mathrm{d}y\,\mathrm{d}p_\mathrm{T}} = \frac{\sigma\,\mathrm{d}^2 N}{2\pi\, p_\mathrm{T}\,\mathrm{d}y\,\mathrm{d}p_\mathrm{T}} \tag{4.2}$$

The normalisations and corrections in equation 4.1 are elucidated in the following.

- **N_ev:** The spectrum is normalized to the number of analysed collisions (events). These events have to be selected according to defined quality criteria such as the performance of the detectors, the trigger scheme and the vertex position as well as reconstruction quality. Concerning the detector performance, the so-called run condition table can be considered in order to select the runs corresponding to the required detector criteria. If an event passes these selections, the event is investigated further according to its vertex properties. The standard vertex position window along the beam axis (z) is $|z_{vertex}| < 10\,\mathrm{cm}$. If an event is finally excepted, it counts as analysed event and the p_T spectra analysis is processed subsequently.

---

[1]Shift of the 4-D (time, 3D space) reference frame in one direction with a constant velocity. This is the case if a steady observer watches a moving system with a constant velocity. In the latter system, the physics and the velocity of light in particular must be the same as for the observer.

- **Δy:** The rapidity window represents a selection in longitudinal direction. The rapidity itself is a relativistic representation of the longitudinal velocity of a particle with energy E and longitudinal momentum p_L:

$$y = \frac{1}{2} \ln \left(\frac{E + p_\mathrm{L}}{E - p_\mathrm{L}} \right) = \tanh^{-1}\left(\frac{p_\mathrm{L}}{E} \right), \tag{4.3}$$

  where $p_\mathrm{L}/E = \beta_\mathrm{L} = v_\mathrm{L}/c$. Contrary to p_T, p_L is not invariant under Lorentz transformation in z-direction. Therefore, the choice of the rapidity instead of p_L for the definition of the yield is a must. Usually, a rapidity window around mid-rapidity is selected since the spectra, i.e. the particle production, are considered to be independent of the rapidity or at most weakly dependent there. Most theoretical models also restrict the calculations to this window in order to facilitate the modelling, because boost-invariance can be assumed. Moreover, at mid-rapidity, the particle production is largest, allowing a large variety of studies.

- **$\Delta p_\mathbf{T}$:** denotes the width of the p_T bin, i.e. the p_T range of a given data point.

- **efficiency:** The efficiency correction is important due to imperfections of the detector and the reconstruction procedure. In addition, selections on the particle track qualities and variables reduce the measured yield, which needs to be corrected for. In the following, the efficiency includes also the acceptance correction accounting for the limited apparatus size and coverage.

- **BR:** The branching ratio is included in order to scale the V^0s to the total yield, which is expected, if all decay channels were measured. Usually, the analyses of decay particles are restricted to a certain decay channel either for feasibility reasons or due to the very small BR of the other channels permitting a thorough study.

- **$\mathbf{FD_{corr}}(p_\mathbf{T})$:** The so-called feed-down correction is needed in case particles of the same species not originating from the collision process itself but from a particle decay contribute to the yield. This is important for $\Lambda(\overline{\Lambda})$ but negligible for K_s^0.

- **$\mathbf{norm_{abc}}$:** In case of pp, some additional normalizations are needed, which was already mentioned in section 3.6.

If there is no difference in the treatment of Λ and $\overline{\Lambda}$, the symbol Λ refers to both particles.

Invariant mass analysis

The yield per p_T bin of a V^0 particle is extracted via the invariant mass analysis. For each p_T bin, the invariant mass,

$$M_{V^0}^2 = \mathbf{P^2} = (\mathbf{P_1} + \mathbf{P_2})^2 = (E_1 + E_2)^2 - (\vec{p_1} + \vec{p_2})^2 \tag{4.4}$$

is calculated for each available V^0 candidate, where $\mathbf{P} = (\mathrm{E}, \vec{p})$ is the four-momentum (Lorentz vector) of the mother particle and $\mathbf{P_i}$ are the four-momenta of the daughter particles. Associating the daughter 3D momenta ($\vec{p_1}$ and $\vec{p_1}$) with the masses of the
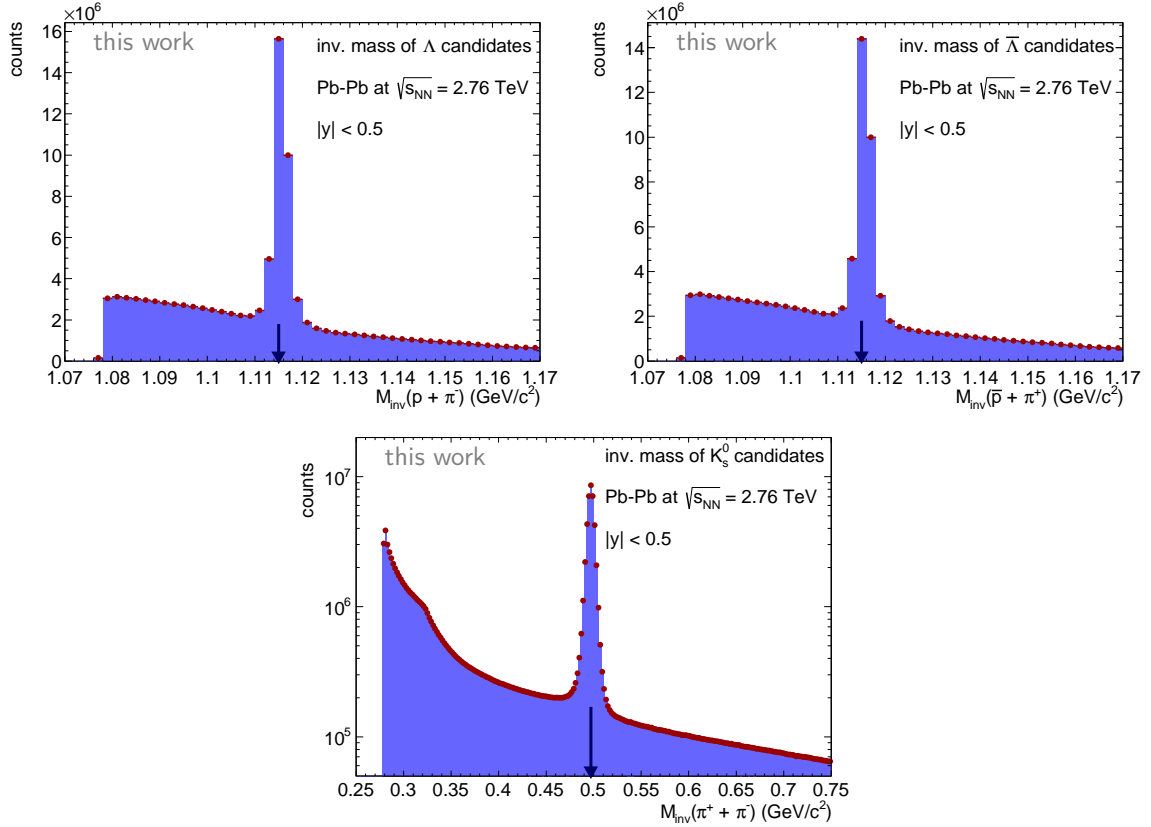
Figure 4.1: Invariant mass distributions of Λ (top left), $\overline{\Lambda}$ (top right) and K_s^0 (bottom) candidates measured in Pb–Pb events integrated over all p_T. The arrows indicate the value of the literature mass of the particles.

decay particles in a specific decay channel of the considered V^0 particle yields E_1 and E_2 via $E_i^2 = m_i^2 + \overrightarrow{p_i}^2$. Only if the V^0 candidates represent the V^0 particle of interest, the invariant mass distribution exhibits an enhancement around the given mass value. Figure 4.1 shows such an invariant mass distribution for $K_s^0 \rightarrow \pi^+ + \pi^-$ in the lower panel, for $\Lambda \rightarrow p + \pi^-$ in the left and for $\overline{\Lambda} \rightarrow \bar{p} + \pi^+$ in the right panel.

The fact that a mass peak with a non-vanishing width is observed in the measurement instead of a delta function, has two reasons: First, a definite peak width is given for quantum mechanical reasons reflecting the mean lifetime τ of a particle, whereby the width is given by $\Gamma = \hbar/\tau$. This width is however of the order of eV to keV, which is very small as compared to the second effect: the momentum resolution is limited due to limitations of the detector as well as due to the measurement itself affecting the tracks, as for example the material budget, causing an energy loss of the particles. The momentum resolution ranges from 1.5 - 10% within the momentum range considered in this work. Hence, widths of a few MeV can be expected. Actually, through the measurement of the peak width, the resolution of the detector can be cross-checked. Finally, the enhancement of the invariant mass distribution needs to be quantified, which is performed via the subtraction of the background (BG). This background mainly consists of V^0 candidates, whose daughters were obviously associated with incorrect masses, or of the combination of tracks, which do not stem from any V^0 decay. These candidates are summarized as combinatorial BG.

The following section documents the run and event selection for Pb–Pb and pp, respectively. In addition, the Monte-Carlo (MC) simulation samples used for the cor-

Data set or sub-set	no. of events
minimum bias	17 M
cent. 0 - 5%	849 k
cent. 5 - 10%	850 k
cent. 10 - 20%	1688 k
cent. 20 - 40%	3397 k
cent. 40 - 60%	3394 k
cent. 60 - 80%	3397 k

Table 4.1: Number of events of the Pb–Pb 2010 data set (minimum bias) and the sub-sets according to the centrality selection.

rections of the spectra are specified. In section 4.3 the track selection for V^0 candidates is discussed, which is followed by the review of the yield extraction procedure and a short detailed discussion of the peculiarities of the pp reference. After the presentation of the raw spectra in Pb–Pb and pp, the previously introduced corrections to the spectra are explained and documented. Before the final results are presented, the systematic uncertainties are reviewed and discussed.

4.2 Data selection

Pb–Pb collisions at $\sqrt{s_{NN}}$ = 2.76 TeV

Data

For this analysis, the Pb–Pb data at $\sqrt{s_{NN}}$ = 2.76 TeV recorded in 2010 was analysed. The corresponding data sample was processed in the ESD format. The run selection was based on their quality labels: A "good" run is given if all main tracking detectors (ITS and TPC) were sending signals and were performing in the expected manner during the data recording. Moreover, the calibration of these runs must have had to be properly executed before the reconstruction. The selected runs are listed in the appendix B.1.

The number of events before event selection is 46.5 M. After the selection of collision candidates and the vertex selection this number reduces to 17 M. In table 4.1, the numbers of events for the different centrality classes are collected. The following listing summarizes the event selections for Pb–Pb collisions:

1. **Physics selection:** Collision candidates

2. **Trigger class selection**

3. **Vertex position:** The vertex determined by all global tracks was used. The z-vertex position was required to be within $+/-$ 10 cm on the z-axis.

MC

The MC productions used for this analysis are minimum bias samples containing events simulated with the HIJING event generator. Only the runs of the MC sample, which correspond to those used in the data analysis, were taken. In two of these

samples, additional particles were generated on top of the underlying HIJING event in order to increase the statistics of high-momentum particles. These injected particles are

- 4 Λ and $\overline{\Lambda}$ with an m_{T}-scaled p_{T} spectrum

- 1 K_s^0 and 1 Λ with a flat p_{T} spectrum from 1 - 10 GeV/c and from 1 - 20 GeV/c, respectively

- 3 Ξ^- and Ξ^0 with a flat p_{T} spectrum from 1 - 15 GeV/c.

These particles were injected with a flat θ distribution, which implies a different rapidity distribution as compared to the data.

In order to determine the systematic uncertainty due to the material budget estimation, two additional the MC productions were studied. In one sample the material budget is enhanced by 7%, whereas in the other it is reduced by 7%. The findings from this study can also be used for the pp analysis since the material budget uncertainty is not expected to be strongly multiplicity dependent.

pp collisions at $\sqrt{s} = 2.76$ TeV

Data

In case of pp at $\sqrt{s} = 2.76$ TeV, the data from 2011 was analysed. Two data sets with different reconstruction schemes are available. The data sample was reconstructed once with and once without SDD information. The corresponding names of the resulting two data sets used in this text are wSDD and nSDD, respectively. The selected runs, which are the same for both reconstructions, are listed in the appendix B.1.

The total number of analysed events before the physics selection is 75 M for wSDD and 80.2 M for nSDD. After all event cuts, the remaining statistics is 24.5 M for wSDD and 52 M for nSDD. The difference in the final statistics is owing the fact that the readout time of the SDD is twice as slow as that of the TPC ($500\,\mu$s busy time). Therefore, if the data taking rate is adapted to the TPC readout time, only each second event contains information from the SDD. Thus, if the SDD is required in the reconstruction scheme, each second event, the one without SDD information, is not considered. As a result, the final statistics of the wSDD sample is half the statistics in nSDD. In order to take advantage of both the larger statistics in nSDD and the additional detector information for the tracking in wSDD, both samples were studied. In the next chapter the impact of the SDD in- and excluded, respectively, during the reconstruction is discussed in more detail.

Contrary to Pb–Pb, the primary vertex selections become very important in pp due to the lower number of produced particles, which complicates the vertex determination but enlarges the vertex resolution if a vertex is found. The number of particle tracks, which contribute to the primary vertex determination, was required to be larger than one in order to ensure that a real vertex for the triggered event was measured. In summary, these event selections were applied:

1. **Physics selection:** Collision candidates

2. **Trigger class selection**

3. **Existence of a vertex:** Requirement of more than one particle track contributing to the vertex position measured by the SPD or TPC.

4. **Vertex position:** The vertex determined by all global tracks is used. The z-vertex position was required to be within $+/- 10$ cm on the z-axis.

MC

The MC productions were specifically produced for this analysis. Only events which contained at least one Λ, $\overline{\Lambda}$ or K_s^0 with $p_T > 2\,\mathrm{GeV}/c$ were accepted during the simulation. For systematic studies especially of the low p_T region, also the default minimum bias samples and one sample with different injected particles were studied.

4.3 Track selection

The event selection is followed by the selections on the V^0 candidates as well as on the V^0 daughter track properties. The V^0 finder employed in this work is the on-the-fly V^0 finder.

In section 3.4, the default selection criteria for on-the-fly V^0 candidates and their daughters were already discussed. These selections enhance the probability of obtaining a real V^0 among the fakes as well as the amount of secondary vertices with a reconstruction of good quality in the sample. However, they do neither guarantee a high quality of the daughter tracks nor a specification of the mass of the daughters and thus of the mass of the mother. Therefore, in addition to the internal cuts of the V^0 on-the-fly finder, cuts on the daughter tracks regarding their pseudo-rapidity (to be within the TPC acceptance), their measured space points in the TPC and the specific energy deposit were introduced. In order to further reduce the BG, the selections on the DCA_{xy} of the mother to the primary vertex[2], on the cosine of pointing angle $(\cos(\mathrm{PA}))$ of the mother and the DCA between the daughters $(\mathrm{DCA_d})$ were tightened. Additionally, a cut on the transverse decay vertex R_{xy} was introduced, which is discussed later.

In case of K_s^0, a cut in the Armenteros-Podolanski diagram[3] was applied in order to smooth the BG. The latter has initially a very irregular shape due to the internal on-the-fly V^0 finder selections. In figure 4.2, this diagram is shown, relating q_T, the relative transverse momentum of the positive daughter to the mother, to α, which basically describes the decay asymmetry in longitudinal direction. The ellipse spanning the whole diagram represents the K_s^0, whereas the smaller ellipses on the left and right hand side mark the $\overline{\Lambda}$ and Λ, respectively. The intended cut, which is applied for the figure, removes the contributions by Λ and $\overline{\Lambda}$ from the K_s^0 distribution via requiring the K_s^0 values for q_T to be above an α-dependent limit represented by the lines perpendicular to the K_s^0 ellipse in the diagram. Hence, this cut removes BG contributions as well as those V^0, which could either yield a K_s^0 or a Λ. In case of Λ, no such cut was used since it introduces an irregular BG shape.

For the proton identification in case of Λ, the specific energy loss information from the TPC was used. In order to select protons, the cut of $\mathrm{n}\sigma_{\mathrm{proton,TPC}} < 3.0\sigma$ was

---

[2]Since the vertex resolution in z-direction is worse than in xy and a cut in xy imposes a constraint in z as well, the cut in the xy-plane was chosen.

[3]For details see appendix A.1.

selection criterion	V^0	value (Pb–Pb) or applied or p_T range		value (pp) or applied or p_T range	
daughter track variables					
$|\eta|$		<	0.8	<	0.8
χ^2 per cluster		<	4	<	4
TPC crossed rows		>	70	>	70
TPC refit			yes		yes
found/findable TPC cluster		>	0.5	>	0.5
DCA between	K_s^0	<	0.23 cm	<	0.4 cm
daughters	Λ	<	0.35 cm	<	0.4 cm
PID TPC dE/dx for p($\overline{p}$): $n\sigma$	Λ	<	3 σ	<	3 σ
V^0 candidate variables					
rapidity $|y|$		<	0.5	<	0.5
DCA_{xy}	K_s^0	<	0.4 cm	<	0.4 cm
DCA_{xy}	Λ	<	1.2 cm	<	1.2 cm
cos(PA)	K_s^0	>	0.99	>	0.99
cos(PA)	Λ	>	0.998	>	0.998
decay radius R_{xy}		>	5 cm	>	5 cm
Armenteros-Podolanski:					
$q_\perp > 0.2 \cdot |\alpha|$	K_s^0	all	GeV/c	<	6 GeV/c

Table 4.2: Selections on the V^0 candidate and its daughters in addition to the on-the-fly V^0 finder cuts. Explanations see text.

applied in the full momentum range. In case of the pions from the Λ, no such cut was introduced, since the correlation between the proton and the pion momentum resulting in the correct Λ mass already works as a quite good selection on the pions. For the pions of K_s^0, no dE/dx selection is needed, since the applied topological cuts are much stronger. In addition, roughly 90% of the measured charged particles are pions, hence the effect of a dE/dx cut is small as compared to protons.

All cuts presented in table 4.2 were balanced such that they optimize the background (BG) shape for fitting as well as the signal-to-background ratio or the significance, respectively, and impose only a relatively small amount of signal loss. Corresponding figures showing the impact of these cuts are presented in section 4.4.3.

As compared to the offline V^0 finder, the background shape for V^0s from the on-the-fly finder is more difficult to describe. However, the efficiency at low and high p_T is larger for the on-the-fly V^0 finder and thus allows to extend the p_T reach with the same statistics by one to two additional bins at high p_T, increasing the p_T range by 70% (K_s^0) and 35% (Λ) from 12 to 20 and to 16 GeV/c, respectively.

4.4 Yield extraction procedure

In the following, the yield extraction from the invariant mass distributions of K_s^0 and $\Lambda(\overline{\Lambda})$ is described: First, the BG underneath the mass peak needs to be deter-
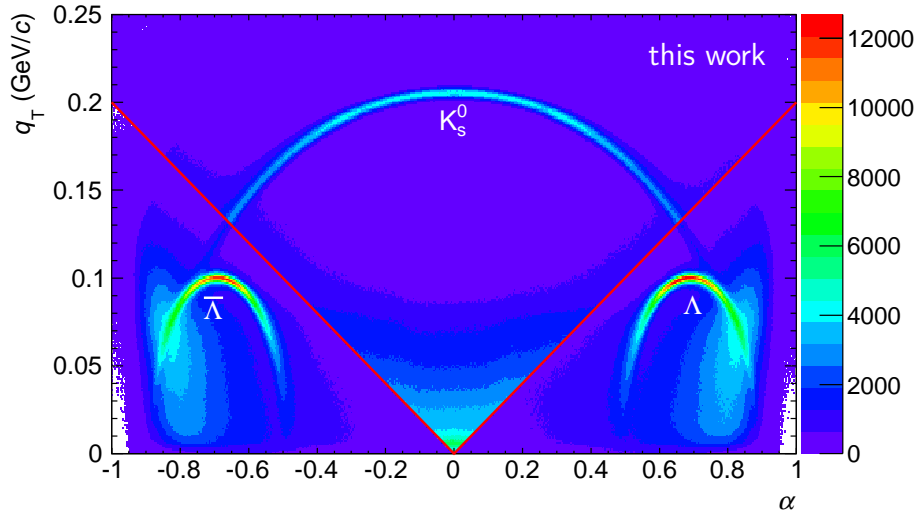
Figure 4.2: Armenteros-Podolanski diagram in Pb–Pb collisions at $\sqrt{s_{NN}} = 2.76\,\text{TeV}$. The red lines mark the cut applied for K_s^0. Only K_s^0 with q_T values above the lines were accepted.

mined. This can be achieved via the mixed-event method[4], the like-sign method[5] or via a fit considering the regions on the left and right hand side of the peak at the same time. Since the V^0 candidates are already built during the reconstruction, where the daughter momenta are refitted to match the secondary vertex, neither the mixed-event nor like-sign method is applicable for the on-the-fly V^0s. Second, the estimated BG is subtracted from the invariant mass distribution leaving basically only the peak. The yield corresponds to the amount of entries in this remaining peak. This procedure is depicted in figure 4.3, where an invariant mass distribution for Λ is shown together with the BG fit. The BG subtracted peak is shown in addition.

4.4.1 Background fit for background subtraction

For the determination of the BG underneath the mass peak, a fit of the BG excluding the peak region was performed. The fit range and the size of the peak window was varied with p_T according to the change of the peak width and the background shape. For the fit function, a polynomial was chosen. Its order was changed with p_T from 5th to second or first order at high p_T. The order dependence on p_T is documented in table 4.3 for K_s^0 and 4.4 for Λ, respectively. When the statistical error and the statistical fluctuations became large at the same time, the fit method of χ^2 minimization was changed to the likelihood method (see table 4.5). Contrary to the first method, the latter takes empty bins into account, which becomes important in case of low statistics. The quality of the BG fit was checked via monitoring the χ^2 for each p_T bin and in addition by eye. In case of a large χ^2, the fit range was iteratively varied during the fitting procedure.

---

[4]Combination of a daughter track from one event with another from another event.

[5]Combination of two particle tracks in the same event with the same sign.
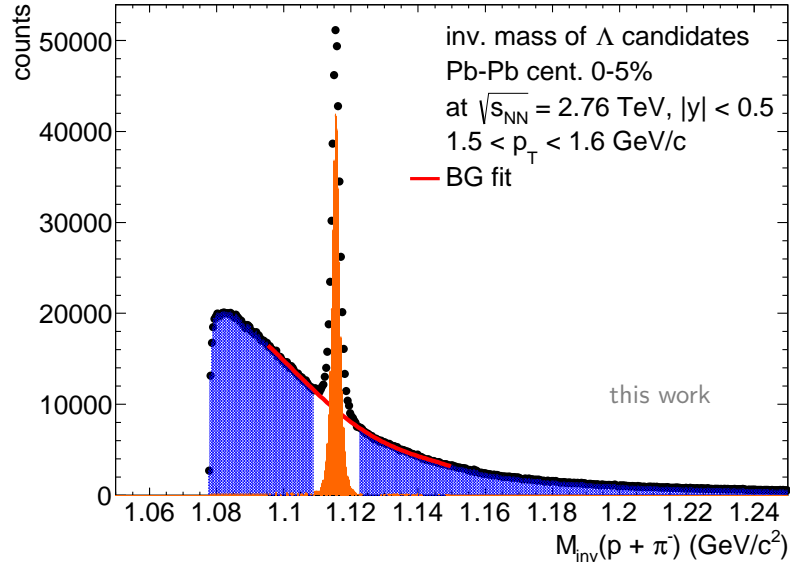
Figure 4.3: Example of an invariant mass distribution of Λ candidates in central Pb–Pb events for $1.5 < p_{\mathrm{T}} < 1.6\,\mathrm{GeV}/c$. The red line is a fit to the BG excluding the mass peak region and the orange area marks the remaining peak after the BG subtraction.

order	Pb–Pb cent. 0 - 20%	Pb–Pb cent. 20 - 60%	Pb–Pb cent. 60 - 80%	pp MB
5		$0.5{\leq}p_{\mathrm{T}}{<}3.4$	$0.6{\leq}p_{\mathrm{T}}{<}3.4$	$0.6{\leq}p_{\mathrm{T}}{<}2.6$
3	$0.1{\leq}p_{\mathrm{T}}{<}6.0$	$0.1{\leq}p_{\mathrm{T}}{<}0.5$ $3.4{\leq}p_{\mathrm{T}}{<}6.0$	$0.1{\leq}p_{\mathrm{T}}{<}0.6$	$0.1{\leq}p_{\mathrm{T}}{<}0.6$
2	$6.0{\leq}p_{\mathrm{T}}{<}12.0$	$6.0{\leq}p_{\mathrm{T}}{<}12.0$	$3.4{\leq}p_{\mathrm{T}}{<}6.0$	$2.6{\leq}p_{\mathrm{T}}{<}5.5$
1	$12.0{\leq}p_{\mathrm{T}}$	$12.0{\leq}p_{\mathrm{T}}$	$6.0{\leq}p_{\mathrm{T}}$	$5.5{\leq}p_{\mathrm{T}}$

Table 4.3: p_{T} regions in GeV/c for the usage of a given order of the polynomial for the BG fit of $\mathrm{K}^0_{\mathrm{s}}$.

4.4.2 Signal extraction

The signal was extracted by subtracting a histogram filled partially with the values of the fit function and partially with those from the BG from the invariant mass distribution. The mass window, where the fit function was used instead of the true BG distribution, corresponds to the mass peak range from the aforementioned fit procedure. Afterwards, the remaining distribution consisting of the mass peak and few remnants from BG subtraction was fitted with a Gaussian[6] to determine the mass (i.e. the mean) and the peak width (σ). The peak width serves as input for the mass window determination used for the subsequent signal extraction, which was performed by bin counting. The mass range was about 4σ for all studied particles. At high p_{T} ($p_{\mathrm{T}} > 6$ - $7\,\mathrm{GeV}/c$), this was changed to 3.5 due to the larger binning in the invariant mass distribution. The values of the windows in each p_{T} bin were used again during

---

[6]The p_{T} smearing caused by detector effects has a Gaussian shape. Therefore, the peak structure can also be assumed to be Gaussian in first order. However, due to the interplay of different detector systems with different p_{T} smearing, the peak may be a superposition of several Gaussians with different widths.

order	Pb–Pb cent. 0 - 40%	Pb–Pb cent. 40 - 60%	Pb–Pb cent. 60 - 80%	pp MB
5	$0.6 \leq p_T < 0.8$	$0.6 \leq p_T < 0.8$		
4	$0.8 \leq p_T < 5.0$	$0.8 \leq p_T < 5.0$	$1.5 \leq p_T < 3.0$	$1.5 \leq p_T < 3.0$
3	$5.0 \leq p_T < 6.0$	$5.0 \leq p_T < 5.5$	$0.6 \leq p_T < 1.5$ $3.0 \leq p_T < 3.6$	$0.5 \leq p_T < 1.5$
2	$6.0 \leq p_T$	$5.5 \leq p_T$	$3.6 \leq p_T < 6.5$	$3.6 \leq p_T < 7.0$
1			$6.5 \leq p_T$	$7.0 \leq p_T$

Table 4.4: p_T regions in GeV/c for the usage of a given order of the polynomial for the BG fit of Λ.

collision class		$p_T(K_s^0)$	$p_T(\Lambda)$
Pb–Pb cent.	0 - 60 %	$> 8.0\ \mathrm{GeV}/c$	$> 3.6\ \mathrm{GeV}/c$
Pb–Pb cent.	60 - 80 %	$> 3.2\ \mathrm{GeV}/c$	$> 3.2\ \mathrm{GeV}/c$
pp		$> 3.2\ \mathrm{GeV}/c$	$> 2.6\ \mathrm{GeV}/c$

Table 4.5: p_T threshold for the usage of the likelihood minimization method instead of the χ^2 method for the BG fit.

the efficiency extraction. In figures B.11 and B.12 in the appendix the edges of the signal extraction windows are shown for Λ and K_s^0 in Pb–Pb and pp collisions.

The error of the remaining signal yield S after the BG (B) subtraction $N - B = S$ is given by

$$\Delta S^2 = \Delta N^2 + \Delta BG_{fit}^2 \qquad \text{with} \tag{4.5}$$
$$\Delta N^2 = N = S + B \tag{4.6}$$

and with BG_{fit} as some statistical error due to BG subtraction if independent error propagation is applied. The latter is however not allowed to be assumed, because the BG and the signal are statistically not independent. Therefore, no statistical errors were assumed neither for the values of the BG nor of the BG fit function here. Moreover, the statistical error extracted from the fit was found to be negligibly small as compared to the statistical error of N. Thus, the statistical error squared is given by the yield of the peak S plus that of the BG only. Uncertainties due to the BG fit and the BG subtraction, respectively, were addressed by a systematic study using a linear fit function in a tight window around the peak (see section 4.7) - a linear fit is the simplest ansatz for a BG shape estimation - and by varying the fit range at high p_T, where the statistics is lower.

4.4.3 Systematic cut studies

In order to optimize the V^0 candidate and the daughter track selection, the impact of the cuts was studied. Helpful in this case is the comparison of the cut value distribution in data and in MC reconstructed as data (MC_{reco}) and the monitoring of the change of the BG as well as of the significance, $s = S/\sqrt{S+B}$, induced by the cuts. The former is of importance, because the amount of V^0, which are rejected due to not passing the selections, needs to be quantified in order to correct for the loss. This quantification is performed via the efficiency determination with the help
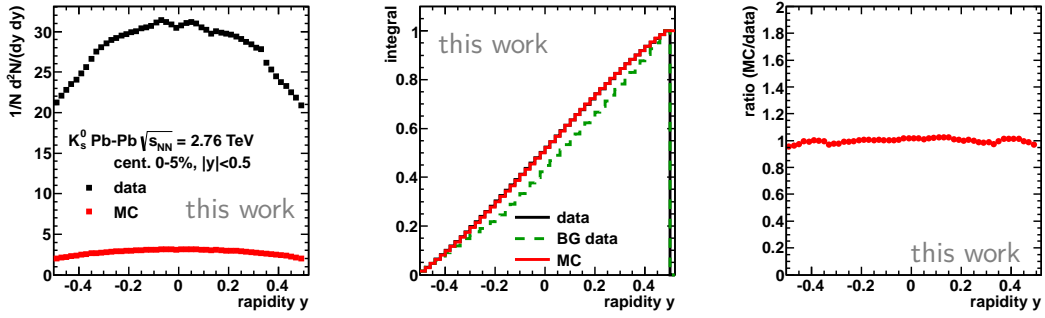
Figure 4.4: Comparison of the rapidity of K_s^0 in data with that in MC rescaled with the data p_T distribution in central Pb–Pb collisions. The ratio of MC and data is normalized to the ratio of the distribution integrals.

of MC simulations. The amount of the BG reduction and significance enhancement is discussed later.

MC to data comparison

The following figures 4.4-4.7 and the figures in appendix B.4 show the distributions of the cut variables in MC_{reco} (MC reconstructed as data) compared to those from data in central Pb–Pb collisions. Since neither the p_T distribution nor the particle (secondary) abundances in MC_{reco} correspond to reality, the variables as a function of p_T need to be scaled to the data p_T distributions before dividing by the corresponding variable distributions from data. In case of Λ, also the secondary Λ contribution in MC_{reco} was rescaled by the p_T distribution of the raw secondary Λ spectrum (see section 4.6). Afterwards, the primary Λ spectrum from MC_{reco} was rescaled with the feed-down corrected raw Λ spectrum and added to the secondary Λ distribution in MC_{reco}. As a result, the inclusive Λ distribution as it is experimentally measured is obtained for MC_{reco} in that way.

For the rescaling procedure a two dimensional histogram with the variable of interest versus p_T was filled for MC_{reco}. The latter was treated as data but requiring the V^0 candidate to be a K_s^0 or Λ (this is not possible in data), respectively, and to have decayed via the channel investigated in data. According to the V^0 PDG code[7] as well as to the identifying numbers for the daughters from MC_{truth}, i.e from the collision simulation before the propagation through the detector simulation, the intended V^0 candidates can be selected in MC_{reco}, since the numbers are preserved. Before filling the histogram, the mass range of Λ and K_s^0 was restricted to a window of 4σ of their peak width integrated over p_T. The final 2D histogram, which represents the analogue to the raw data case (but without BG), was sliced in p_T using the p_T bin width of the raw data p_T spectrum. Each slice was divided by the integral of this p_T slice and multiplied with the corresponding value from the raw data p_T spectrum. Afterwards, all p_T slices were added up finally yielding the variable of interest distribution rescaled to data p_T.

---

[7]The Particle Data Group (PDG) code is also called the MC numbering scheme as defined by the PDG. Each elementary particle as well as all hadrons are assigned to an individual number. The distinction between a particle and its anti-particle is made via assigning the same number with a minus sign to the anti-particle.
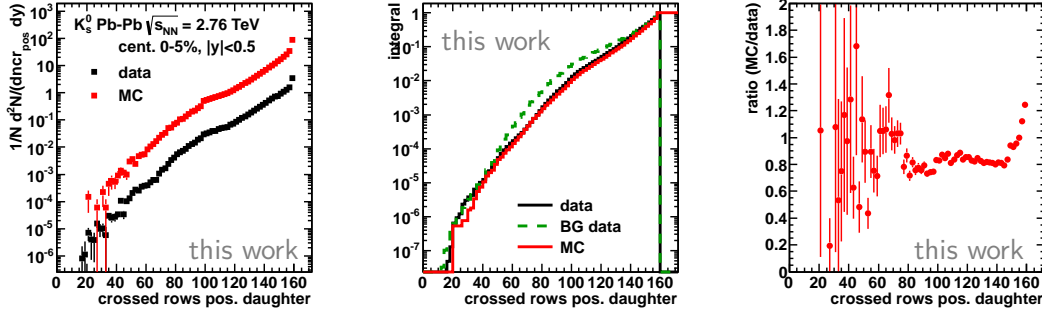
Figure 4.5: Comparison of the number of crossed rows in the TPC for the positive K_s^0 daughter in data with that in MC rescaled with the data p_T distribution in central Pb–Pb collisions. The ratio of MC and data is normalized to the ratio of the distribution integrals.
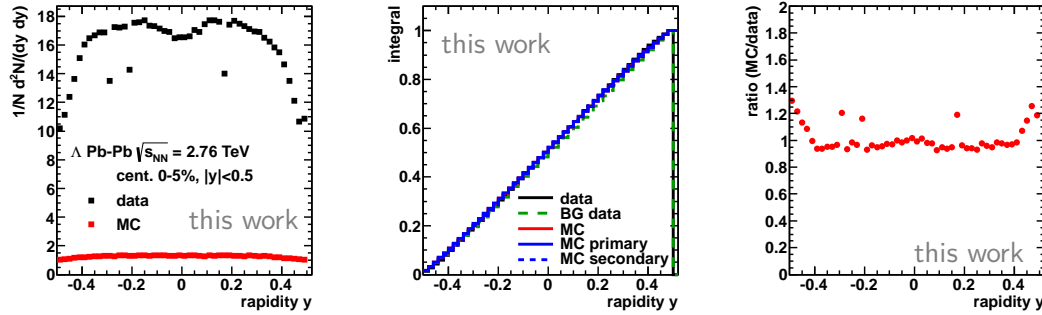
Figure 4.6: Comparison of the rapidity of Λ in data with that in MC rescaled with the data p_T distribution in central Pb–Pb collisions. The ratio of MC and data is normalized to the ratio of the distribution integrals.

Concerning the resulting figures for the MC-to-data ratios of the number of TPC clusters and of the TPC found-over-findable clusters, only a cut on the the (pseudo-) rapidity as well as the Armenteros-Podolanksi diagram for K_s^0 and the dE/dx cut for Λ, respectively, were applied. In all other cases, the cut on crossed rows and on found-over-findable clusters were applied in addition.

Impact of the cuts

The impact of the cuts applied for K_s^0 and Λ as function of p_T is demonstrated in figures 4.8, 4.9, 4.10, 4.13, B.51, B.52, 4.14 for Pb–Pb central collisions. The equivalent figures for pp collisions are 4.16, 4.17, 4.18. The markers represent the ratios of spectra with cuts to those without cuts, whereas the lines show the ratio of the BG for the corresponding spectra. In figures 4.11, 4.12, 4.15, 4.16, 4.17, the ratio of the significance for the cut to no cut scenario is presented in addition.

For Λ, the raw distributions contain all Λ, i.e. primary and secondary Λ. The cuts were also selected such, that they reduce the secondary contamination. Therefore a 20% signal loss due to a cut, for example, does not necessarily mean a 20% loss of primary Λ.
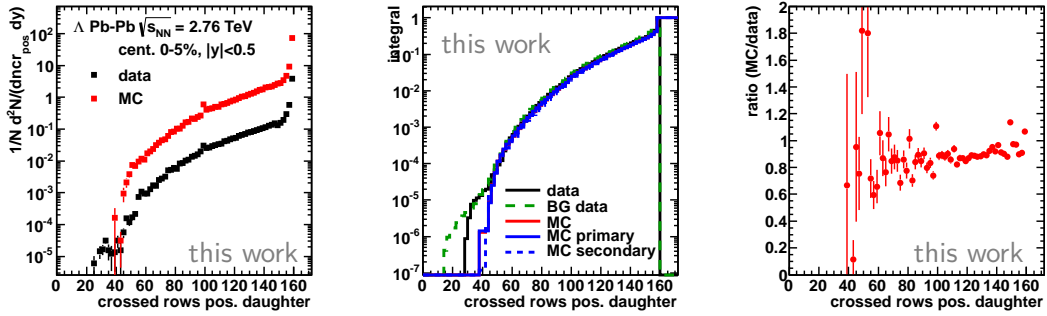
Figure 4.7: Comparison of the number of crossed rows in the TPC for the positive Λ daughter in data with that in MC rescaled with the data p_T distribution in central Pb–Pb collisions. The ratio of MC and data is normalized to the ratio of the distribution integrals.
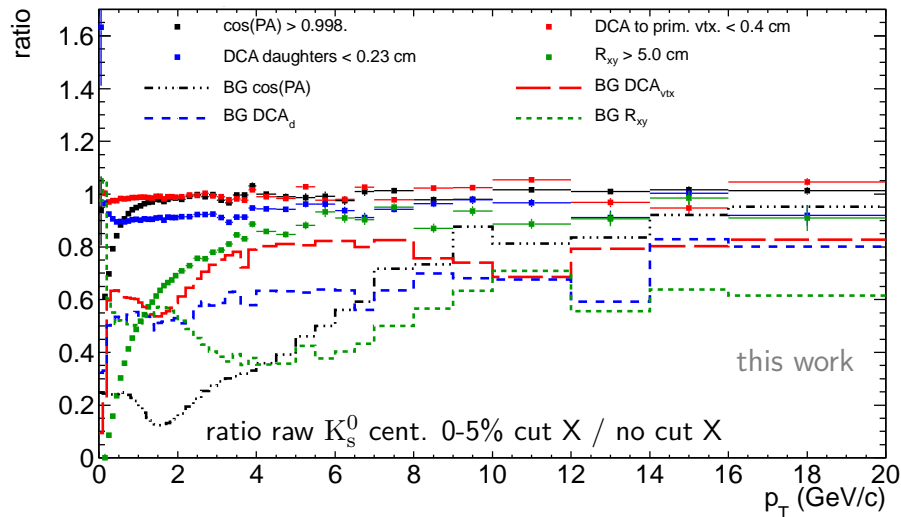
Figure 4.8: Ratio of raw K_s^0 spectra in central Pb–Pb collisions with the cuts indicated in the legend applied over those spectra without these cuts applied.

Results of the cut studies and MC-to-data comparison

In the following list, the details and results of the MC_{reco} to data comparison and the cut studies can be found for each cut variable. In general, the variables of K_s^0 are rather well described by MC_{reco}, which is however not always the case for Λ.

- **rapidity:** If a rapidity window of $|y| < 0.5$ for K_s^0 and Λ is selected, the data is best reproduced by MC_{reco}. Figures 4.4, B.22 and 4.6, B.41 show a flat MC_{reco}-to-data ratio in the selected rapidity range. For larger rapidities, the MC deviates from the data due to a strongly differing η distribution. The latter is a result of the flat θ distribution of the injected particles in the MC_{reco}.

- **pseudo-rapidity:** Figures B.14, B.15 and B.32, B.33 show a flat MC_{reco}-to-data ratio in the selected rapidity range.

- **crossed rows TPC:** A minimum of 70 crossed (read-out) pad rows was required, which removes only a small fraction of V^0 ($< 1\%$) and is rather well
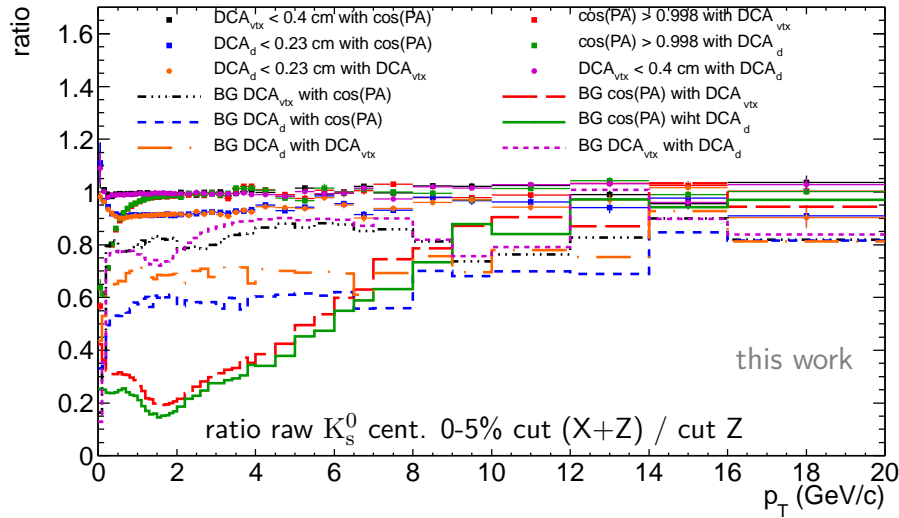
Figure 4.9: Ratio of raw K_s^0 spectra in central Pb–Pb collisions with the cut indicated in the legend applied (X) over those spectra without this cut applied. "With cut" refers to cut (Z), which was applied for the spectrum in the numerator as well as for that in the denominator in order to compare the impact of another cut X.
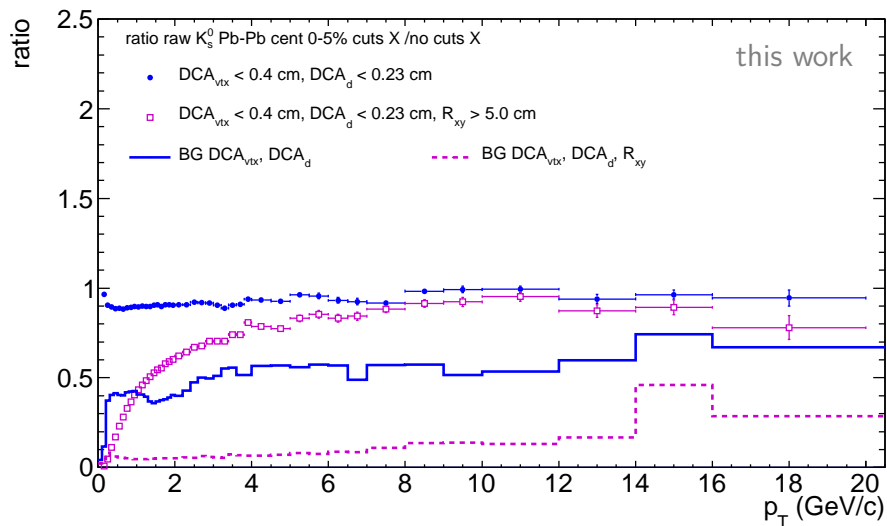
Figure 4.10: Ratio of raw K_s^0 spectra in central Pb–Pb collisions with the final cuts to the case without the indicated cuts. In addition, the BG ratio is shown.

described by MC_{reco}, as it can be seen in figures 4.5, B.23, B.31, 4.7, B.43 and B.42.

- **found-over-findable clusters TPC:** Concerning the cut on found-over-findable TPC clusters, a minimal value of 0.5 was required. A stronger cut was not introduced, since at larger values the deviation between data and MC_{reco} becomes too strong or the shape differs too much, i.e. there, the ratio MC_{reco} to data is not flat (see figures B.16, B.24 and B.35, B.34, B.45, B.44). The requirement of the found-over-findable ratio of TPC clusters being smaller than 1 has only a small effect as well, since after the cut on 70 crossed rows, most of the tracks with the ratio larger than 1 are removed already.
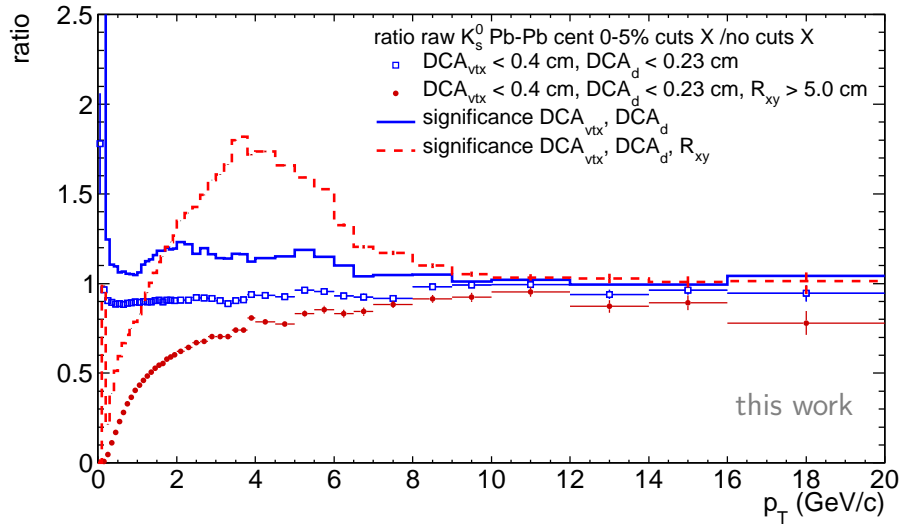
Figure 4.11: Ratio of raw K_s^0 spectra in central Pb–Pb collisions with the final cuts to the case without the indicated cuts. In addition, the significance ratio is shown.
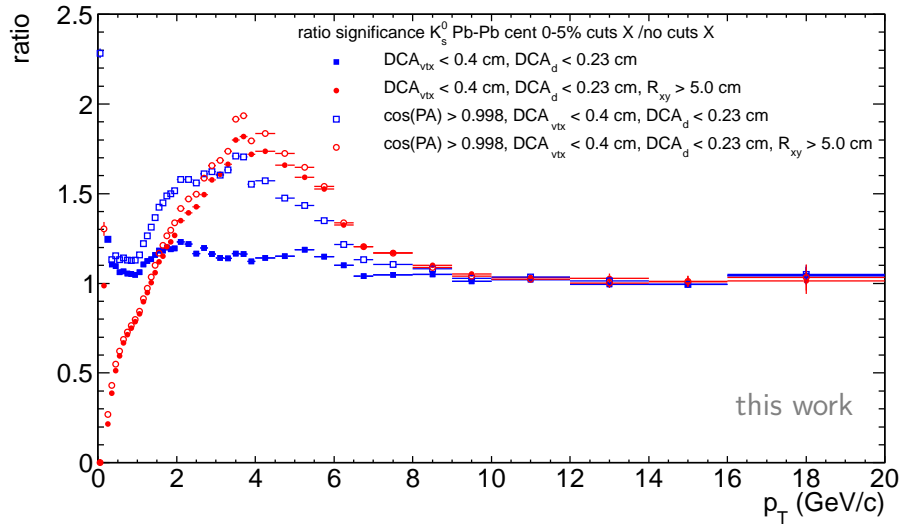
Figure 4.12: Ratio of raw K_s^0 significance in central Pb–Pb collisions for cuts applied over no cuts applied. The effect of the cos(PA) cut is shown here in particular.

- **cos(PA):** In case of K_s^0, if the significance ratios in figure 4.12 are considered, this cut is only causing an increase of the significance and a reduction of the BG if no cut on the decay radius is applied. Since the decay radius cut was introduced for the offline V^0 finder analysis [154], it was also applied here in order to obtain a comparable sample of V^0 to that of the published analysis. In pp it is questionable if the cos(PA) cut shall be used at all since it is not well reproduced in MC_{reco} (see figures B.17, B.25), which is also seen in the spectra comparison figures.

  In case of Λ, the distribution is rather well reproduced by MC_{reco} (see figures B.36, B.46), and was hence applied in order to also decrease the secondary Λ contribution.
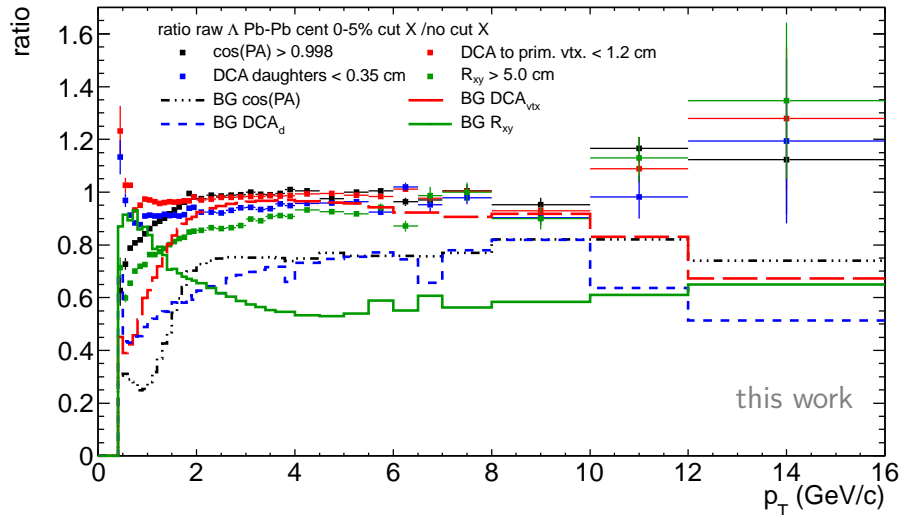
Figure 4.13: Ratio of raw Λ spectra in central Pb–Pb collisions with the cuts indicated in the legend applied over those spectra without these cuts applied. In addition, the BG ratio is shown. The signal loss also contains the reduction of secondary Λ.
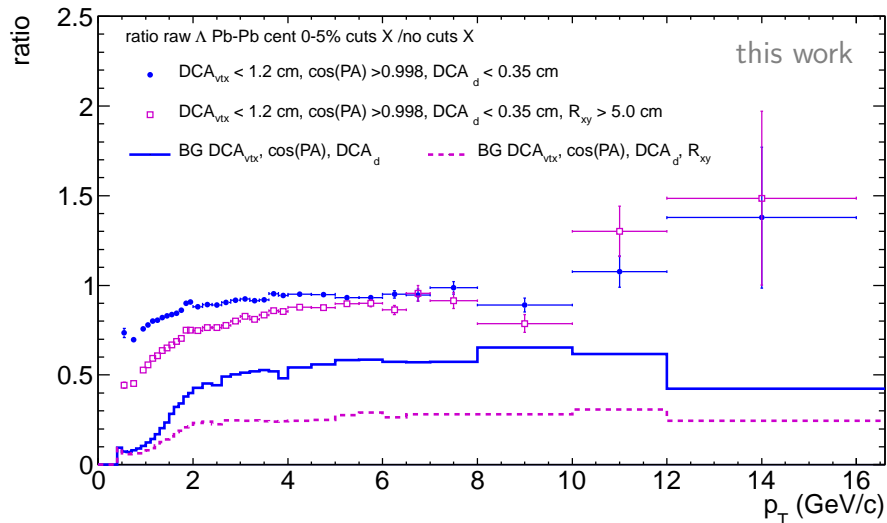
Figure 4.14: Ratio of raw Λ spectra in central Pb–Pb collisions with the final cuts to the case without the indicated cuts. In addition, the BG ratio is shown. The signal loss also contains the reduction of secondary Λ.

- **decay radius:** Regarding the decay radius, it was found in the offline V^0 analysis of Pb–Pb data [154], that below 5 cm in the 2D radial direction, the decay radius distribution in data at low p_T is not described by MC_{reco}. This becomes obvious in the corresponding $c\tau$ analysis. Thus, a cut on the 2D decay radius removing the decays from 0 - 5 cm was introduced. This cut rejects secondary vertices that appear before the second layer of the SPD. In addition, this cut reduces the centrality dependence of the efficiencies, which can be seen in figure 4.19. Since the mean lifetime of the K_s^0 is below 5 cm, this cut removes a huge fraction of K_s^0 at low to intermediate p_T (see figure 4.10).

  In case of Λ, it is questionable if the decay radius selection is needed. First, the mean life time of Λ is 7.89 cm, which is beyond the cut value and therefore, the
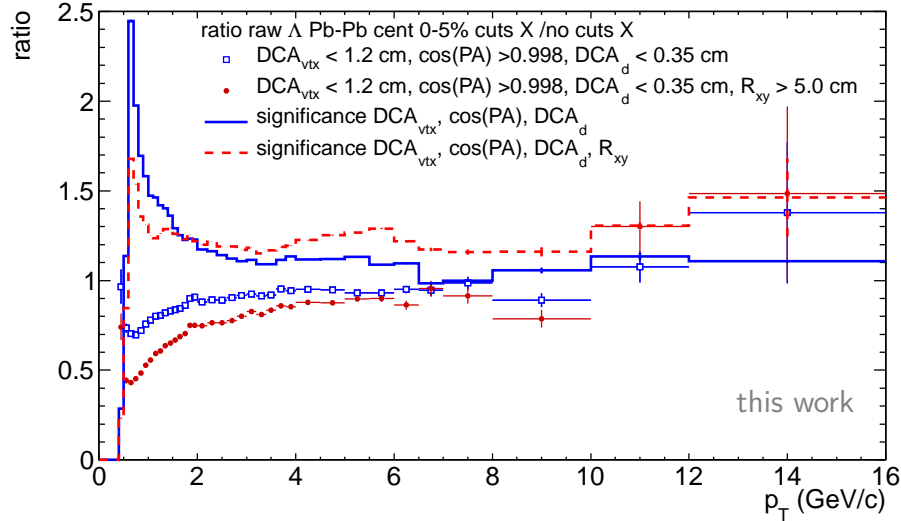
Figure 4.15: Ratio of raw Λ spectra in central Pb–Pb collisions with the final cuts to the case without the indicated cuts. In addition, the significance ratio is shown. The signal loss also contains the reduction of secondary Λ.
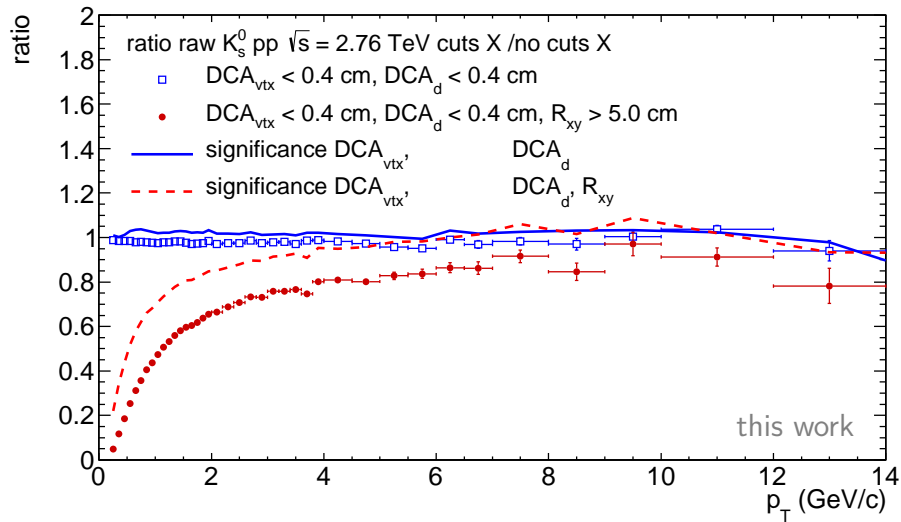
Figure 4.16: Ratio of raw K_s^0 spectra in pp collisions with the final cuts to the case without the indicated cuts. In addition, the significance ratio is shown.

contribution of Λ with smaller decay radii is much lower than for K_s^0. On the other hand, considering figures 4.14 and 4.15, the BG reduction and the significance are consequently improved by the cut, except for $p_T < 1.5\,\mathrm{GeV}/c$. Second, the radius distribution is rather badly reproduced by $\mathrm{MC}_{\mathrm{reco}}$. At the moment, the cut is applied in order to maintain consistency between the analyses.

In pp collisions, the radius cut was introduced in order to maintain consistency between the analyses of the data from the two collision systems. The effect in of this cut turned out to be very small for K_s^0, as it can be seen in figure 4.18. Since only values above $p_T = 0.3\,\mathrm{GeV}/c$ were used for the spectrum, no significant difference was found. For Λ, deviations from 8-5% from $0.6 < 1.5\,\mathrm{GeV}/c$
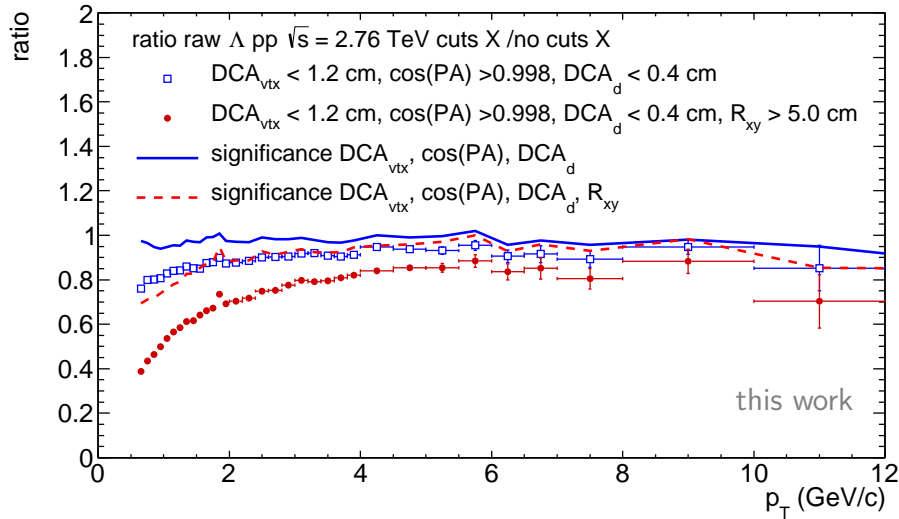
Figure 4.17: Ratio of raw Λ spectra in pp collisions with the final cuts to the case without the indicated cuts. In addition, the significance ratio is shown. The signal loss also contains the reduction of secondary Λ.
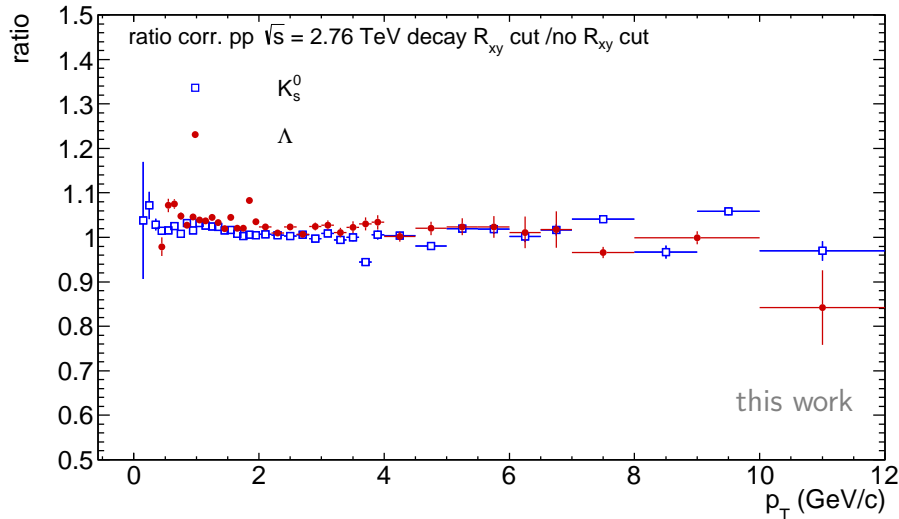
Figure 4.18: Ratio of the corrected K_s^0 (Λ) spectrum in pp collisions with a decay radius to the spectrum without this cut.

are visible. This difference was added to the systematic uncertainties.

Compared to Pb–Pb, the significance is strongly reduced by the radius cut, which is about 80% for K_s^0 and 35% for Λ at low p_T, which is shown in figures 4.16 and 4.17.

- **DCA_d:** The distribution of the DCA between the daughters is rather well described by MC_{reco} if the integral of the distribution is considered. For K_s^0 the MC_{reco}-to-data ratio is flat above 0.4 cm in pp and for all values in Pb–Pb. Therefore, cutting at 0.4 cm in pp (fig. B.26) and 0.23 cm in Pb–Pb (fig. B.18) is appropriate. In case of Λ, the ratio is flat above 0.4 cm in pp (fig. B.47) and 0.3 cm in Pb–Pb (fig. B.37), which allows to cut at 0.4 cm in pp and 0.35 cm in Pb–Pb. The data above 1.0 cm are neglected due to the low statistics. The DCA_d cut in Pb–Pb removes 10% of the K_s^0 signal at $p_T < 4\,\mathrm{GeV}/c$ and
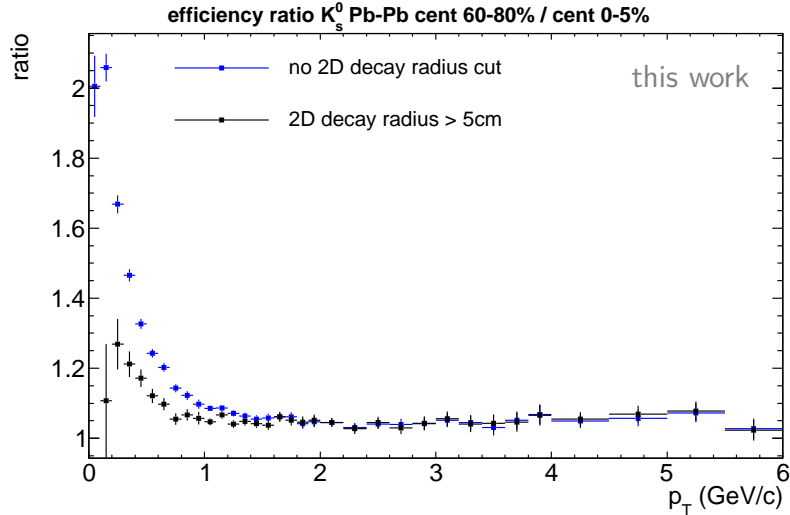
Figure 4.19: Ratio of the K_s^0 efficiency in peripheral to central events. The black rectangles show the case with the 2D decay radius cut whereas the blue rectangles represent the case without this cut.

roughly 5% above this range. The BG reduction is about 50% and in addition with the cut on DCA_{xy}, still 35% are removed in addition (see figure 4.9). In pp collisions, there is nearly no signal loss and no change of the significance for this cut combination (see figure 4.16). The Λ signal in Pb–Pb is reduced by about 10% at $p_T < 4\,\mathrm{GeV}/c$, while the BG is reduced by about 60-30% depending on p_T (see figure 4.13). In combination with the cut on DCA_{xy}, the impact is similar. The same is true in pp, although the BG reduction is about 10%.

- **DCA_{xy}:** Whereas the MC_{reco}-to-data ratio shows a flat behaviour in Pb–Pb for K_s^0 (fig. B.19), this is the case for Λ only above 1.0 cm in pp (fig. B.48) and in Pb–Pb (fig. B.38). In pp however, this is limited for K_s^0 to values above 0.3 cm (fig. B.27). The chosen cuts of 1.2 cm for Λ and 0.4 cm for K_s^0 in pp as well as in Pb–Pb are within this flat region.

- **Armenteros-Podolanski variables:** A cut in the Armenteros-Podolanski variables can be corrected with MC, since the distribution is purely based on kinematics.

4.4.4 Raw spectra in Pb–Pb collisions at $\sqrt{s_{NN}} = 2.76\,\text{TeV}$

The raw p_T spectra in Pb–Pb collisions for all measured centralities after cuts are shown in figures 4.20. The data points were calculated by dividing the bin content by the bin width. The spectra were normalized to the number of analysed events (vertex position within $|z_{vertex}| < 10\,\text{cm}$), to the rapidity window and to the branching ratio. Furthermore, the mass peak properties, such as peak position, which corresponds to the mean V^0 mass and the peak width σ are extracted for each particle and p_T bin. The values for K_s^0 and Λ, shown in figures 4.21 and 4.22, are obtained from a fit with a Gaussian to the BG-subtracted peak in the invariant mass spectrum[8]. Although the peak shape is not perfectly described by a Gaussian distribution, the fit results give a good estimate of the p_T-dependent trend of the masses and peak widths, which reflect the detector calibration quality and the momentum resolution/smearing, respectively. The mass difference of $\overline{\Lambda}$ and Λ as shown in figure 4.23 can reveal a shift in the momentum times particle-charge distribution, since the masses should be ideally exactly the same for each p_T bin.

Within the uncertainties, no centrality dependence of all discussed quantities is observed (see additional figures in appendix B.3). The mass difference to the literature value, taking the uncertainties into account, is at maximum $2\,\text{GeV}/c$ for K_s^0 and $0.5\,\text{GeV}/c$ for Λ. Concerning the mass difference of $\overline{\Lambda}$ and Λ, a negligible shift of $0.1\,\text{GeV}/c$ is observed below $p_T = 6\,\text{GeV}/c$. Above this p_T, except some statistical fluctuations, which are in the range of $\pm1\,\text{MeV}$, no significant mis-calibration is found. The peak width and mass differences are all well reproduced by MC_{reco} for most p_T bins and within $\pm1\,\text{MeV}$ at maximum outside the statistical uncertainties for a few p_T bins.

4.5 pp reference at $\sqrt{s} = 2.76\,\text{TeV}$

The pp reference spectra are accompanied by an extra dimension of complication due to the two reconstruction schemes in- and excluding SDD information. As only each second event contains SDD information, the data set wSDD consists only of half of the statistics recorded. In order to extract the maximal p_T reach, a strategy for combining the advantages of both data sets was needed. The reason why not only the nSDD data set with twice the statistics was used is based on the working principle of the on-the-fly V0 finder, which relies strongly on the full ITS information. Due to the lack of measured SDD hits in the nSDD sample, one third of possible ITS information is not available. This information, however, is important for the track refitting and re-calculation of the momenta of the daughters with respect to a possible secondary vertex, taking into account the material budget. As shown in figure 4.24, the loss of K_s^0 for the case without SDD is up to 80% at low p_T. This loss is unfortunately not reproduced by MC_{reco}. On the other hand, for $p_T > 6\,\text{GeV}/c$, this difference vanishes for K_s^0 as well as for Λ. Therefore, the nSDD sample was taken for the high p_T region in order to profit from the two times larger with respect to the wSDD sample. The final spectra were extracted from the wSDD sample for $p_T < 6\,\text{GeV}/c$ and those from nSDD for $p_T \geq 6\,\text{GeV}/c$.

---

[8]These plots are limited to the most central, most peripheral and pp collisions. For all centralities, see the following figures in the appendix B.3.
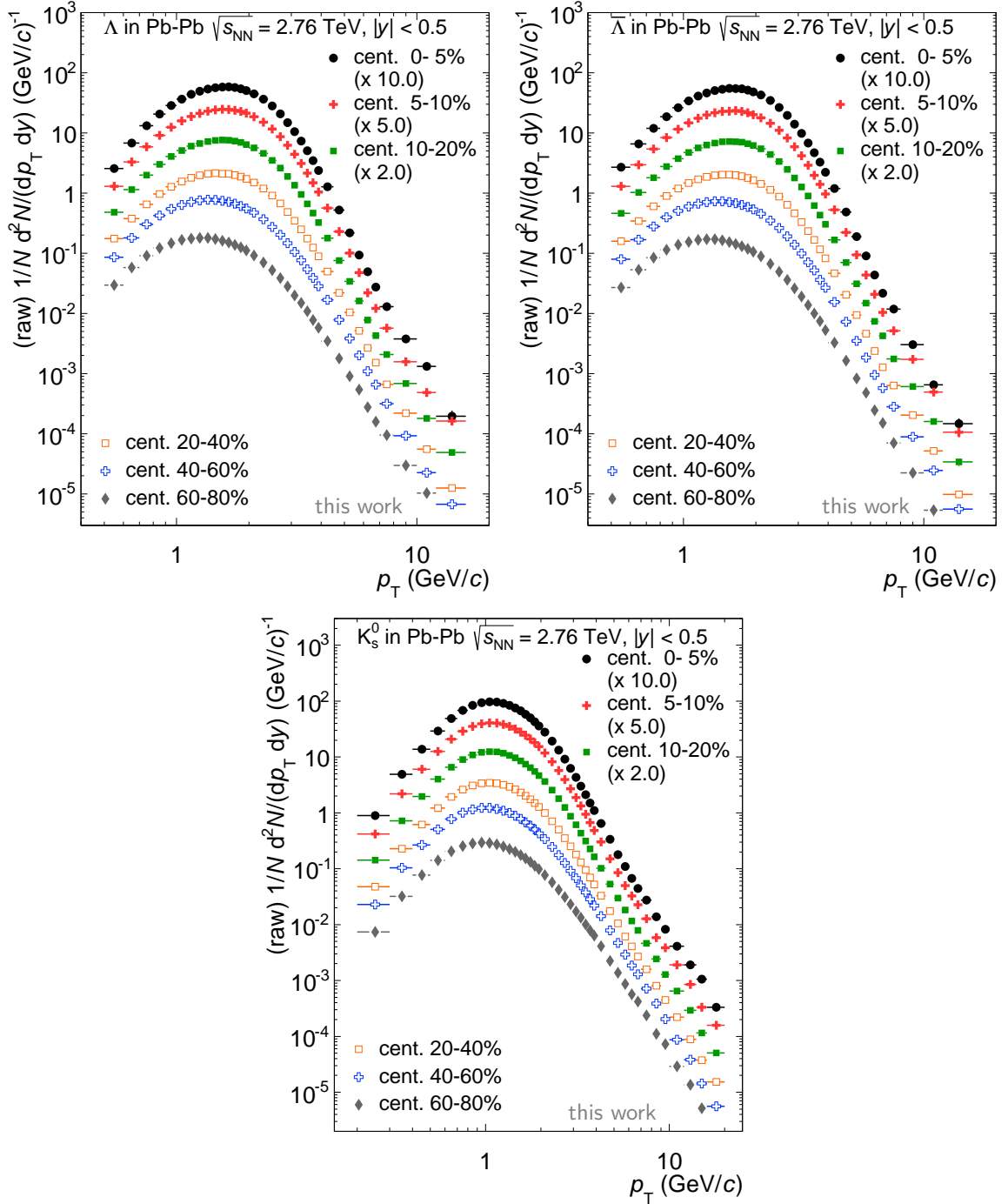
Figure 4.20: Raw p_T spectra of Λ (upper left), $\overline{\Lambda}$ (upper right) and K_s^0 (bottom) in Pb–Pb collisions.

Raw spectra pp

The raw p_T spectra of Λ and K_s^0 were calculated by dividing the yield per p_T bin by the bin width. The spectra were then normalized to the number of analysed events (vertex position within $|z_{vertex}| < 10$ cm) and to the rapidity window. The results from pp shown in figure 4.25 were additionally normalized to minimum bias and inelastic collisions.

The kink at $p_T = 6$ GeV/c for K_s^0 is a result from the cut in the Armenteros-Podolanski
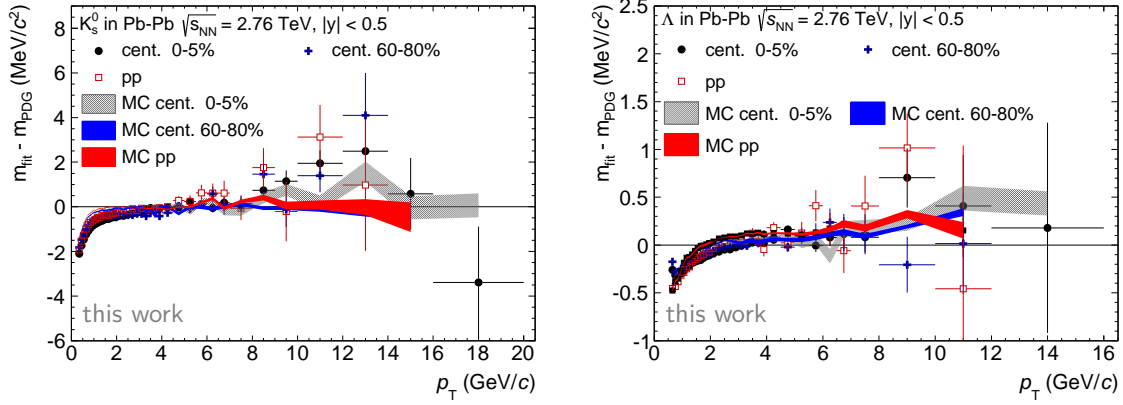
Figure 4.21: Difference of the mass obtained from a Gaussian fit of the K_s^0 (left) and Λ (right) peak after BG subtraction to the nominal mass as function of p_T for data and MC_{reco} in Pb–Pb and pp collisions.
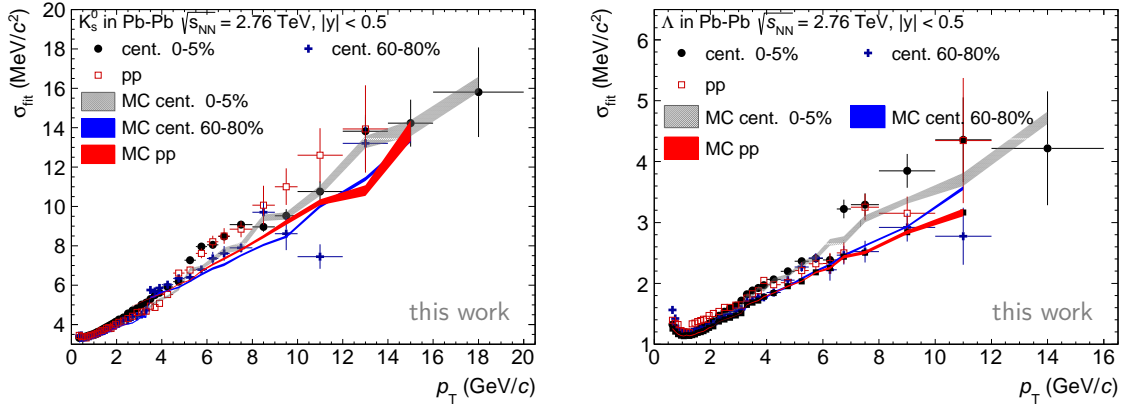
Figure 4.22: Peak width obtained from a Gaussian fit to the K_s^0 (left) and Λ (right) invariant mass peak after BG subtraction as function of p_T for data and MC_{reco} in Pb–Pb and pp collisions.
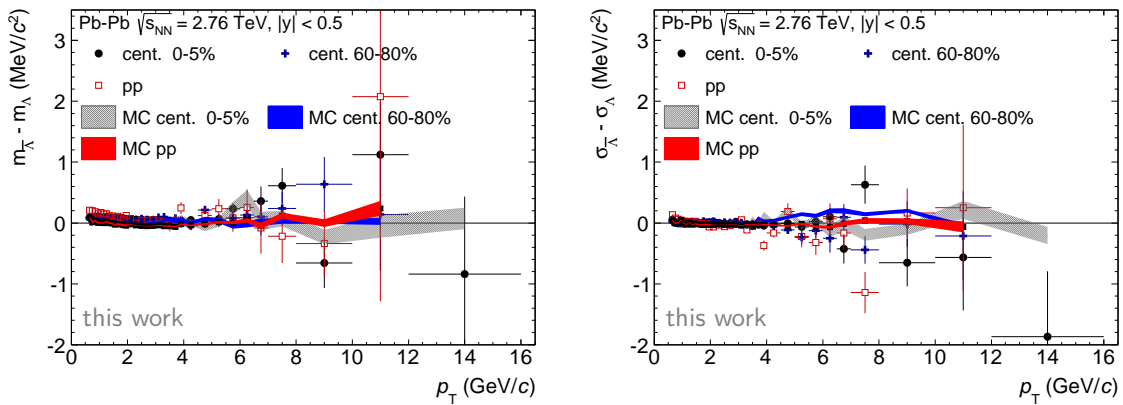
Figure 4.23: Difference of the mass (left) as well as of the peak width (right) of $\overline{\Lambda}$ and Λ as function of p_T in data and MC_{reco} in Pb–Pb and pp collisions.
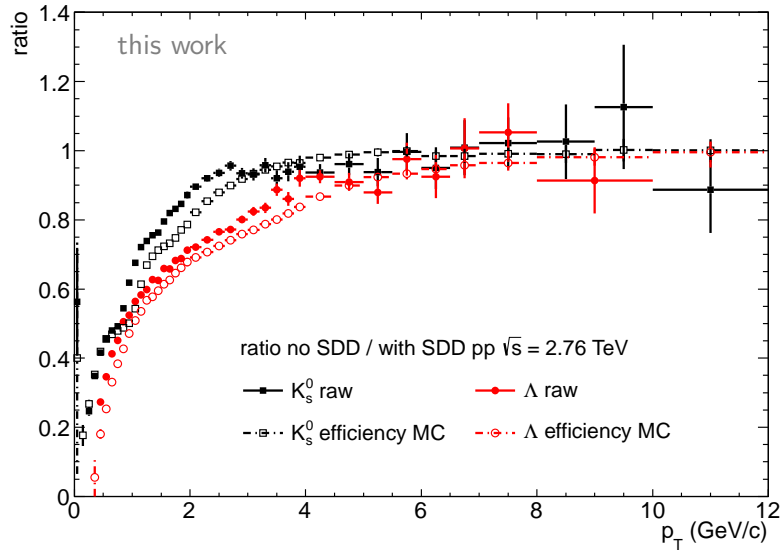
Figure 4.24: Ratios of K_s^0 and Λ raw spectra in pp at $\sqrt{s} = 2.76\,\mathrm{TeV}$ between nSDD and wSDD (filled symbols) compared to the corresponding MC efficiency ratio (hollow symbols).

space, which was not applied for the nSDD sample, i.e. above this p_T threshold, for reasons of statistics.

The binning was chosen to be the same as for the Pb–Pb spectra. Nevertheless, an alternative binning, especially at high p_T was tested and found to impose no effect on the results. Therefore, for simplification in view of the calculation of R_{AA}, the binning from Pb–Pb was kept. Since the p_T reach in pp is smaller than in Pb–Pb, the final spectra need to be extrapolated, which is discussed later.

The extracted values for the masses and peak widths can be found in figures 4.21, 4.22 and 4.23. Within the uncertainties, no difference to the values obtained for Pb–Pb is observed.

4.6 Corrections and normalisations

4.6.1 Efficiency correction

The efficiency and the acceptance correction as function of p_T was determined with the help of MC simulations. After the review of the efficiency calculation procedure, the MC samples are discussed.

Efficiency calculation

The efficiency correction is needed in order to recover the lost V^0s, which can either happen due to not reconstructing them (loss of one or more daughters) or due to a rejection according the selection scheme for quality insurance. The ideal case (MC_{truth}) is represented by the output of a suitable event generator, in this case PYTHIA for pp and HIJING for Pb-Pb. In order to estimate the detector effects on the track measurement, the simulation of the collision is followed by the propagation of the particles
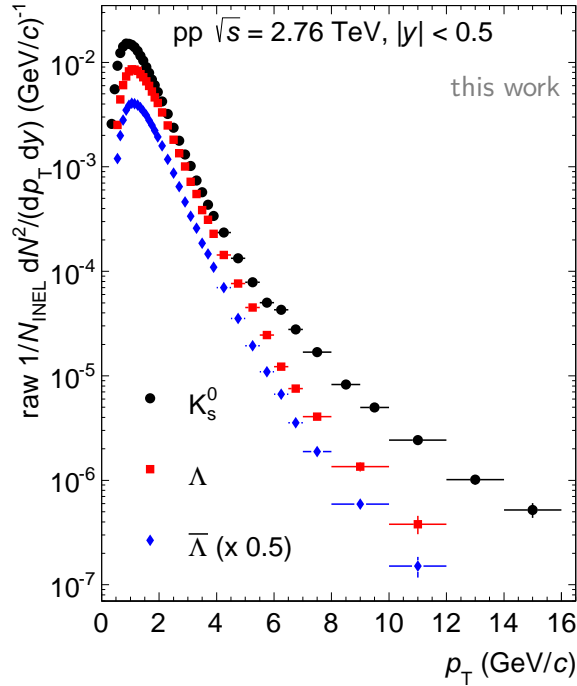
Figure 4.25: Raw p_T spectra of K_s^0, Λ and $\overline{\Lambda}$ in pp $\sqrt{s}$ = 2.76 TeV. Data points at $p_T < 6$ GeV/c are from the wSDD sample and at $p_T \geq 6$ GeV/c from the nSDD sample.

through a the experimental set-up, where the detector response is modelled and raw data information is generated. In the next step, the simulated data are reconstructed in an analogous way as real data, yielding the set of reconstructed tracks (MC_{reco}). The efficiency is given by the ratio of MC_{reco} to MC_{truth}, while the efficiency correction is defined by the inverse ratio.

The physics and vertex selections were applied for both MC_{reco} and MC_{truth}. The p_T distribution in MC_{truth} was constructed such that only Λ and K_s^0 from MC_{truth} in the rapidity window of $|y| < 0.5$ (as in data) were considered. Furthermore, only those Λ and K_s^0 were accepted, which stem directly from the collision, i.e. which are primary particles. Moreover, only those V^0s entered in the calculation, that decayed into the channel investigated in data. In other words, those Λ and K_s^0 were selected, that decayed into $p + \pi^-$ and $\pi^+ + \pi-$, respectively.

The p_T distribution in MC_{reco} consists of the yield of Λ and K_s^0 in MC_{reco} per generated (simulated) p_T bin. The generated p_T was preferred to the reconstructed p_T, because the p_T-smearing is not correctly treated in MC_{reco}. Although the smearing is nearly negligible, using the generated p_T helps to avoid binning effects due to the non-physical p_T distribution in MC. If a V^0 was accepted in MC_{truth}, the daughter identifying numbers (IDs) were used to find the corresponding V^0 in MC_{reco}. The latter was searched by looping over all available V^0s in MC_{reco}. Since, as in data, in MC_{reco} the species of the V^0 is not known, it needs to be identified by its daughters, which are linked to MC_{truth}. In case of secondary Λ, the procedure is similar, but instead of requiring a primary Λ in MC_{truth}, only secondary Λ stemming from the Ξ family were accepted (more on this in the following section 4.6.3). The subsequent procedure for calculating the different particle variables and for applying the cuts was
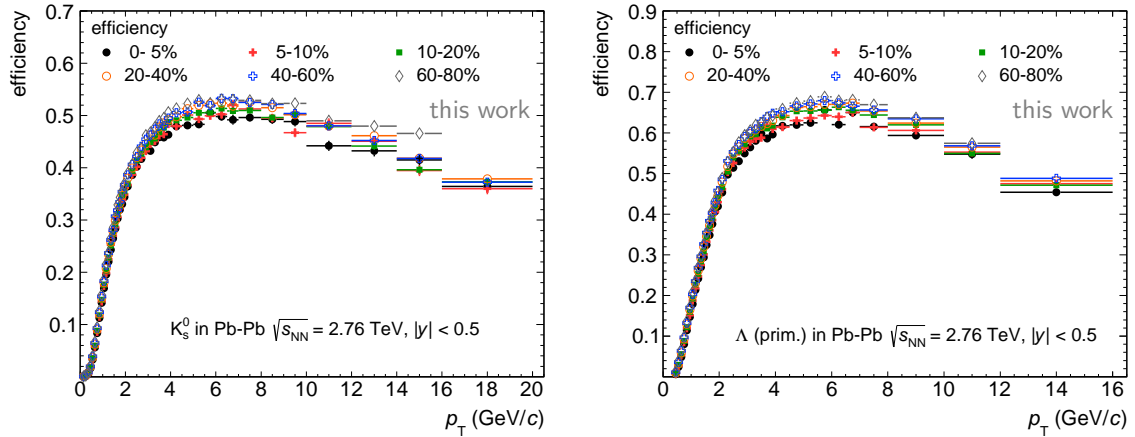
Figure 4.26: Efficiencies of K_s^0 (left) and Λ (right) in Pb–Pb collisions.

exactly the same as for data. The final invariant mass distributions of MC_{reco} do not contain BG as it is the case in data, due to the requirement of the correct PDG code for the mother. Although this requirement only yields real V^0s, the mass peak window for the signal extraction from data was used p_T bin-dependent here as well. This is important in order to avoid that Λ and K_s^0 enter in the efficiency calculation, which are outside the peak region considered in data. If the values outside mass peak region were taken into account, this would bias the efficiency by up to 10% at high p_T. A compilation of the K_s^0 and primary Λ efficiencies in Pb–Pb is shown in figure 4.26. In case of $\overline{\Lambda}$, the ratio of the Λ efficiency to the $\overline{\Lambda}$ efficiency is shown in figure 4.27, in order to demonstrate the effect of the anti-proton absorption, which is addressed in the next subsection. The secondary Λ efficiencies in Pb–Pb are presented in the right panel of figure 4.29 and all efficiencies in pp are displayed in the left panel of this figure. Concerning the secondary $\overline{\Lambda}$ efficiency, more information can be found in the next paragraph.

The statistical error of the efficiency was calculated using the binomial error calculation. However, the statistical errors seem not to account for the bin-by-bin fluctuations at higher p_T. Hence, several efficiency distributions were fitted with a polynomial and/or a distribution as in [155],

$$\text{eff.} = a \cdot e^{(p_T - b)^2/d} f \cdot \log(\sqrt{p_T} - g) \cdot (1 - \exp(k - p_T) + l \cdot p_T + n \, (p_T - r)^2), \quad (4.7)$$

where a, b, d, f, g, k, l, n, r are free parameters, in order to obtain a smooth distribution, which should ideally be the case. The ratio of the parametrized efficiency to the original efficiency can be seen in figure 4.28 for K_s^0, Λ and $\overline{\Lambda}$ for the cases, where the parametrization was used. The fit was not performed for the whole p_T range, since the fluctuations mainly occur at intermediate to high p_T. For the correction of data, the resulting parametrization in the given p_T range was used instead of the efficiency points. For $\overline{\Lambda}$ in Pb–Pb, the efficiency of primary and secondary particles was parametrized, while for Λ a fit to the primary efficiency only was used. In case of pp, fits were performed for K_s^0, secondary Λ and secondary $\overline{\Lambda}$.

MC productions

In Pb–Pb, due to the p_T cut-off of the injected K_s^0 at $p_T = 20\,\text{GeV}/c$ the LHC11a10b_plus sample was used only up to $p_T = 19\,\text{GeV}/c$. In order to enlarge
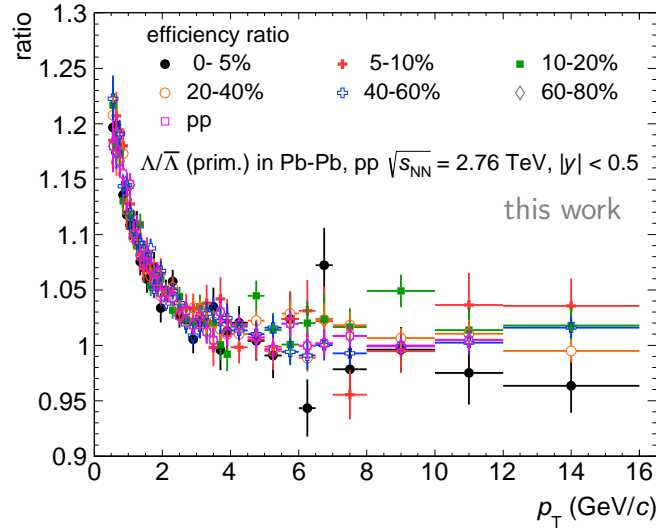
Figure 4.27: Ratio of the Λ efficiency to the $\overline{\Lambda}$ efficiency in Pb–Pb and pp collisions at $\sqrt{s_{\mathrm{NN}}} = 2.76\,\mathrm{TeV}$.

the p_{T} reach of the K^0_s efficiency up to $p_{\mathrm{T}} = 20\,\mathrm{GeV}/c$ corresponding to the reach of the data spectrum, the efficiency was linearly extrapolated taking into account the last three bins. In case of Λ_{sec}, the efficiency needed to be extrapolated from $p_{\mathrm{T}} = 14.0$ - $16.0\,\mathrm{GeV}/c$, which was also performed with a linear fit function.

For $\overline{\Lambda}$, the secondary efficiency does not compare to the Λ secondary efficiency in the same way as for the primary particles. Therefore, the ratio of the primary $\overline{\Lambda}$ to Λ efficiency was used in order to obtain the secondary $\overline{\Lambda}$ efficiency: the secondary Λ efficiency was scaled with the inverse of the primary $\overline{\Lambda}$ to Λ efficiency ratio.

In pp, additionally a minimum bias MC sample was investigated, where neither particles were injected nor a triggering on special particles was performed. This sample provides a reference for all other MC samples with special configurations. It was found, that the K^0_s efficiency from the triggered samples deviates from that of the minimum bias sample by 5 - 8% for $p_{\mathrm{T}} = 1.5\,\mathrm{GeV}/c$. As a consequence, the efficiency of the latter was used for the given p_{T} range.

4.6.2 Absorption correction

The detector simulation package GEANT3, which is employed for the MC samples in this study, reproduces the majority the detector effects. Concerning the absorption rate of particles in the detector material, however, the programme fails to calculate the particle losses correctly. Hence, an additional detector simulation programme, Fluka [156], is usually invoked, in order to obtain a p_{T}-dependent correction for the wrongly calculated absorption rate affecting the efficiencies. This correction is strongest for anti-particles, which are in this case anti-protons.

For this work, an MC sample using the standard version of GEANT3 in ALICE and a sample with a newer version of GEANT3 including an absorption correction were produced. This correction is based on a parametrisation of an optical model for particle absorption. The parametrisation is derived from low-energy measurements within the research field of astrophysics. It is assumed that this correction is collision system independent. Finally, the ratio of the resulting efficiencies of both samples was
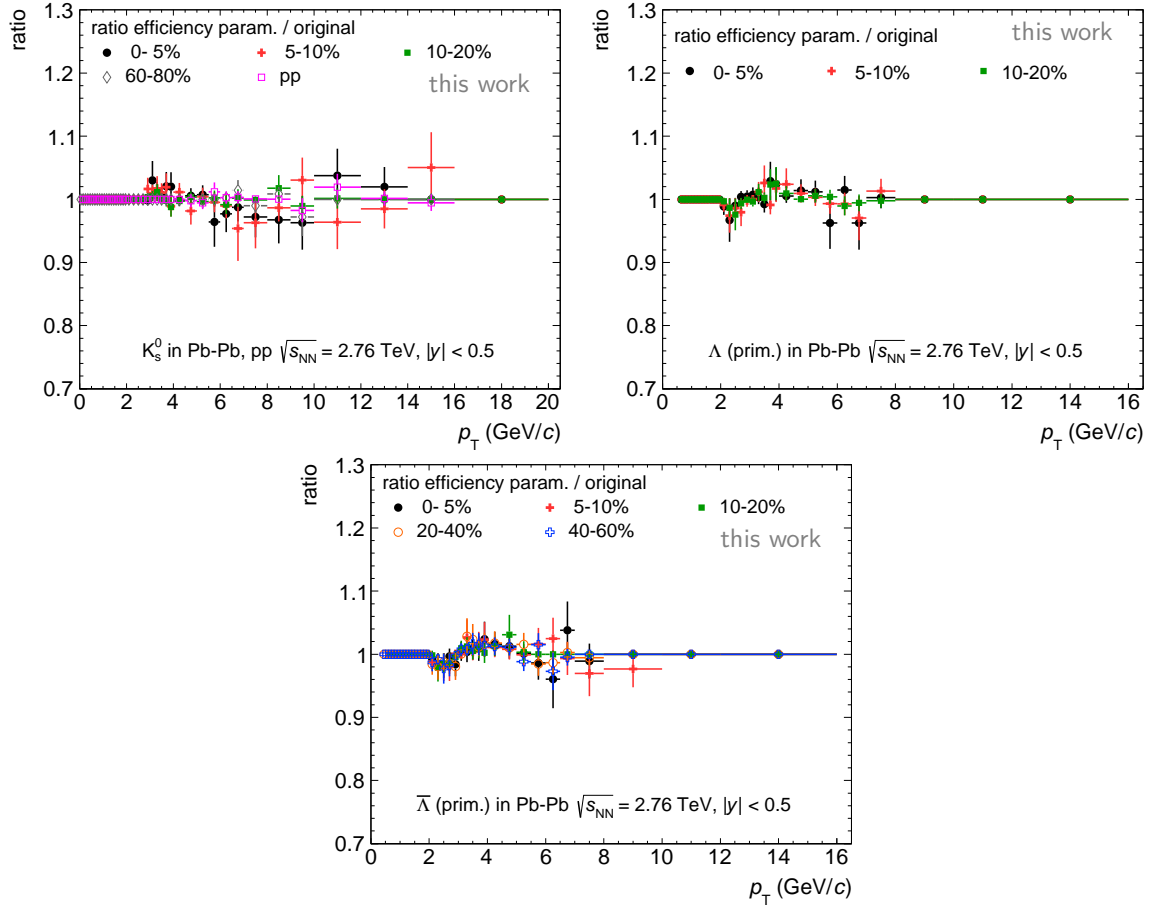
Figure 4.28: Ratio of the fit to the efficiencies over the efficiency for K_s^0 (upper left), Λ (upper right) and $\overline{\Lambda}$ (bottom) in Pb–Pb and pp collisions.

used as the correction for $\overline{\Lambda}$. Figure 4.30 shows the $\overline{\Lambda}$ efficiency ratio as a function of p_T. In addition, the GEANT/Fluka correction applied in ALICE for the low p_T analyses is shown. The deviation between these two corrections enters into the systematic uncertainty estimation. In case of K_s^0 and Λ, the correction was found to be negligible.

4.6.3 Feed-down estimation for Λ

The measured Λ spectrum is a sum of Λ originating from different sources. On the one hand, there are primary Λ produced during the collisions and on the other hand there are secondary Λ, which origin from the decay of particles, Λ_{sec} in the following. The main particles which have a Λ in their most probable decay channel are the those of the Ξ family, the Σ^0 and the $\Omega^{-,+}$.

The main contribution to the primary Λ spectrum is the feed-down (FD) from Ξ^- (Ξ^+ for $\overline{\Lambda}$) decaying into Λ and π^- with a probability of 99.89%. There is also a contribution from the decay of Ξ^0, which is usually not reconstructed, because the dominant decay mode is $\Xi^0 \to \Lambda + \pi^0$, with the π^0 mainly decaying into two photons and hence complicating the analysis. The feed-down from Ξ^- was therefore multiplied by two in order to account for Ξ^0, whose p_T spectrum is similar to that of Ξ^-. In case of Ω^-, the Λ is the most probable decay product but with the yield being 6 - 10 times smaller than for Ξ^-, it can be neglected as a secondary Λ source. The Σ^0
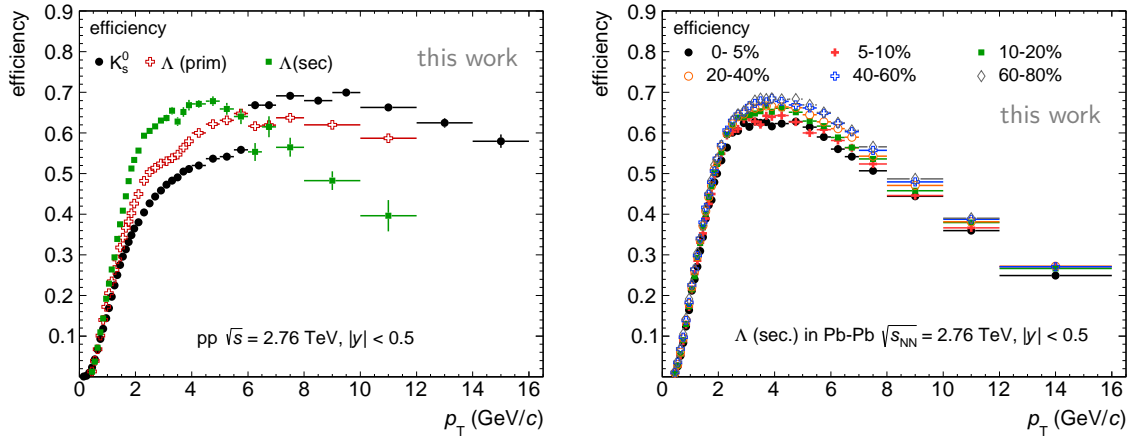
Figure 4.29: Left panel: Efficiency of K_s^0 primary and secondary Λ in pp at 2.76 TeV. For $p_T < 6$ GeV/c the sample with SDD (wSDD) is used, above this p_T the sample without SDD (nSDD). Right panel: Efficiency of secondary Λ in Pb–Pb collisions.
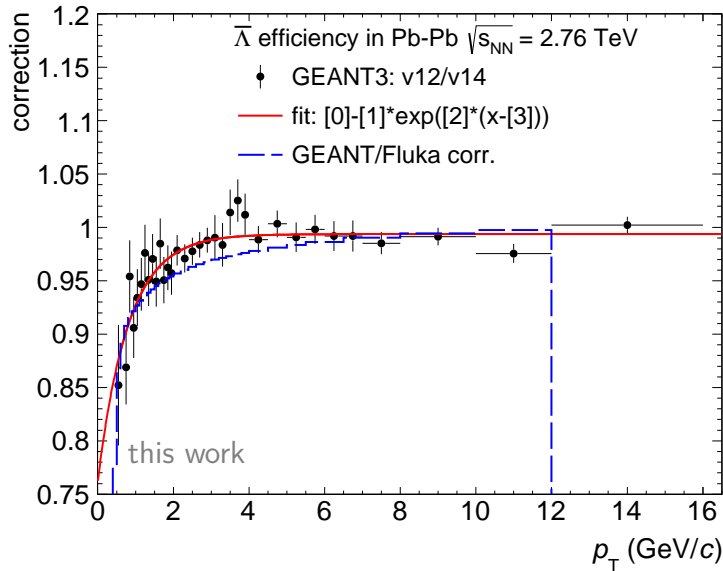
Figure 4.30: Absorption correction as a function of p_T for $\overline{\Lambda}$. The red line shows the fit to the $\overline{\Lambda}$ efficiency ratio for an MC production using GEANT3.v12 to that employing GEANT3.v14. The blue line represents the standard GEANT/Fluka correction.

contributes to the feed-down by an electromagnetic decay into Λ. However the decays driven by the electromagnetic interaction take place at much shorter time scales than those due to weak interaction (factor 10^9), such as the Ξ and the $\Omega^{-,+}$, which makes it impossible to resolve the decay vertex. Therefore, the feed-down from Σ^0 was not subtracted here.

In the following, the method of subtracting the feed-down contributions is explained. The general idea is to use the measured Ξ^-, Ξ^+ spectra as input and to translate the p_T of the mother particle into the p_T of its decay product Λ_{sec}. Figure 4.31 shows the correlation of connecting both momenta via pure decay kinematics (see further details in appendix A.2). The p_T of Ξ^- is drawn versus the p_T of Λ_{sec} in central (0 - 5%) Pb–Pb events generated with a stand-alone toy MC simulation of 100 M events. This correlation was compared to that obtained from the MC produc-
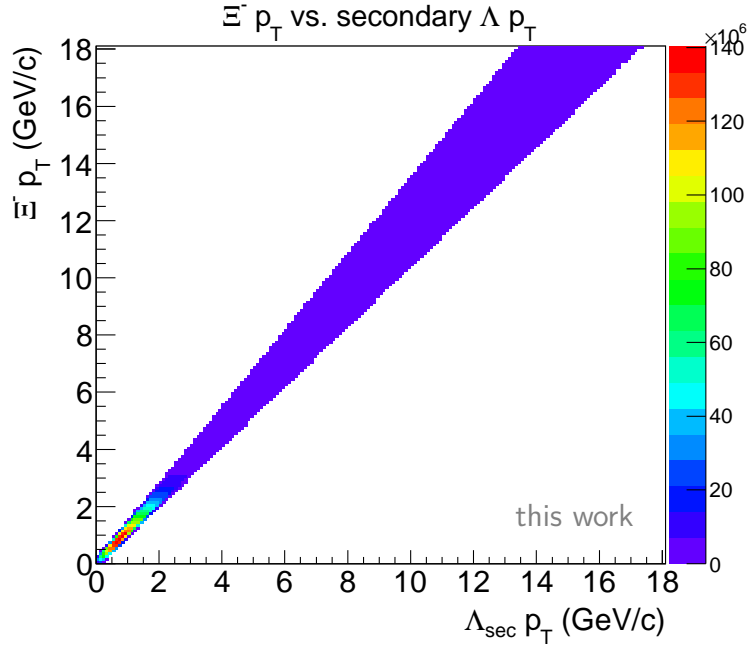
Figure 4.31: Ξ^- p_T versus p_T of the secondary Λ (daughter) from toy MC using pure decay kinematics.

tions and found to be equal. The matrix generation was needed, since the statistics available from the standard MC productions is too low. In [157], the Ξ^- transverse momentum spectra in Pb–Pb collisions measured by the ALICE collaboration are published which serve as input for the generation of this matrix. In case of pp, the preliminary spectra from [158] were used. The projection onto the x-axis of the matrix yields the p_T spectrum of Λ_{sec}. In Figure 4.32, the ratio of Λ_{sec} to the Ξ^- spectra is shown for different centralities and pp. A shift of the maximum to lower p_T values is clearly visible. At large p_T, the shape of the Λ distribution is similar to that of its mother because the Λ with $m_\Lambda \approx 8 \cdot m_\pi$ carries away the largest fraction of the momentum.

Since the input to the calculation was a fully corrected Ξ^- spectrum, the resulting Λ_{sec} spectra is in that sense also fully corrected and therefore cannot directly be subtracted from a measured raw Λ spectrum. In order estimate the feed-down contribution to the raw Λ spectra, these "corrected" Λ_{sec} spectra were multiplied with their efficiency (under the cut conditions applied for all measured Λ) extracted from MC. After the subtraction of these "raw" Λ_{sec} from the raw Λ in each p_T bin, the primary raw Λ spectrum was corrected with the efficiency of primary Λ. The procedure reads mathematically as follows:

$$
\begin{aligned}
\Lambda(p_T)_{sec}^{raw} &= \Lambda(p_T)_{sec}^{corr} \cdot \mathrm{eff}(p_T)_{sec} \cdot \frac{1}{\mathrm{GA}} \\
\Lambda(p_T)_{prim}^{raw} &= \Lambda(p_T)_{all}^{raw} - \Lambda(p_T)_{sec}^{raw} \\
\Lambda(p_T)_{prim}^{corr} &= \frac{\Lambda(p_T)_{prim}^{raw}}{\mathrm{eff}(p_T)_{prim}} \cdot \mathrm{GA},
\end{aligned}
\tag{4.8}
$$

with GA as the GEANT absorption correction. Since this correction is of 15 - 1% at $p_T \lesssim 2\,\mathrm{GeV}/c$ for $\overline{\Lambda}$ and only of $<1\%$ for Λ, it is neglected for secondary Λ.
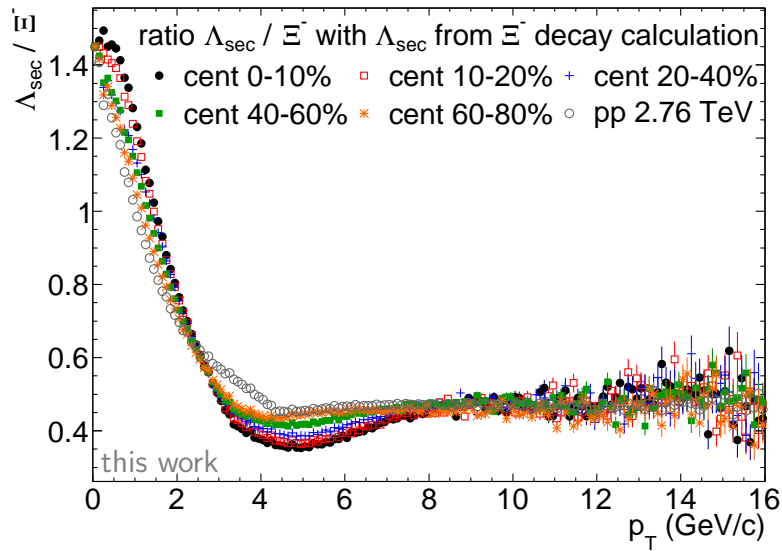
Figure 4.32: Ratio of secondary Λ from Ξ^- decay kinematics calculation to Ξ^- for different centralities in Pb–Pb and for pp collisions at $\sqrt{s_{\mathrm{NN}}} = 2.76$ TeV.

If MC represented the reality for both the yield and the p_{T} shape for Ξ^- and Λ the procedure of feed-down correction could have been simplified to:

$$\Lambda(p_{\mathrm{T}})^{\mathrm{corr}}_{\mathrm{all}} = \frac{\Lambda(p_{\mathrm{T}})^{\mathrm{raw}}_{\mathrm{all}}}{\mathrm{eff}(p_{\mathrm{T}})_{\mathrm{all}}}$$

$$\Lambda(p_{\mathrm{T}})^{\mathrm{corr}}_{\mathrm{prim}} = \Lambda(p_{\mathrm{T}})^{\mathrm{corr}}_{\mathrm{all}} \cdot \left(1.0 - \frac{\Lambda(p_{\mathrm{T}})^{\mathrm{MC}}_{\mathrm{sec}}}{\Lambda(p_{\mathrm{T}})^{\mathrm{MC}}_{\mathrm{prim}}}\right).$$

(4.9)

Unfortunately the measured p_{T} range of the Ξ^- is smaller than that of Λ. The first ends at 6 - 8 GeV/c, the latter at 12 - 16 GeV/c, depending on centrality. Therefore, the Ξ^- spectra needed to be extrapolated to higher p_{T}. Regarding the p_{T} range of the Ξ^-, the cut-off of the spectrum is located around the p_{T} region of the minimum of the charged particle R_{AA}, above which a power-law behaviour of the Pb–Pb spectra is expected due to the nearly linear rise. When the Ξ^- spectra were compared to the spectra of protons [159, 160], it was found that their ratio is flat within their uncertainties (figure 4.33). Thus, also the exponent of their power-law distributions can be expected to be very similar. The p_{T} reach of 20 GeV/c of the proton spectra qualify them as a reference for the Ξ^- extrapolation.

The protons were fitted with a combined fit function using a Tsallis-Pareto function [161, 162]

$$\frac{\mathrm{d}N^2}{\mathrm{d}p_{\mathrm{T}}\,\mathrm{d}y} = p_{\mathrm{T}} \cdot \frac{\mathrm{d}N}{\mathrm{d}y} \cdot \frac{(n-1)(n-2)}{nA \cdot (nA + (n-2)\,m)} \cdot \left(1 + \frac{m_{\mathrm{T}} - m}{n \cdot A}\right)^{-n},$$

(4.10)

where n and A are free parameters, at lower p_{T} and a power-law function,

$$\frac{\mathrm{d}N^2}{\mathrm{d}p_{\mathrm{T}}\,\mathrm{d}y} = B\left(1 + \frac{p_{\mathrm{T}}}{p_0}\right)^{-n},$$

(4.11)
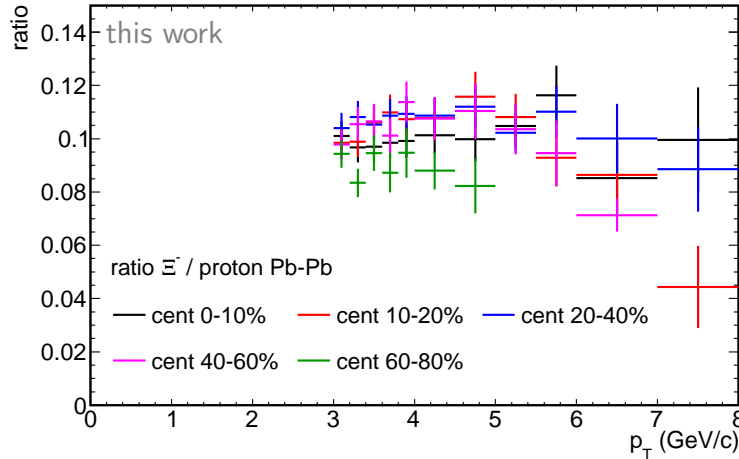
Figure 4.33: Ratio Ξ^- over protons in Pb–Pb collisions for different centralities.
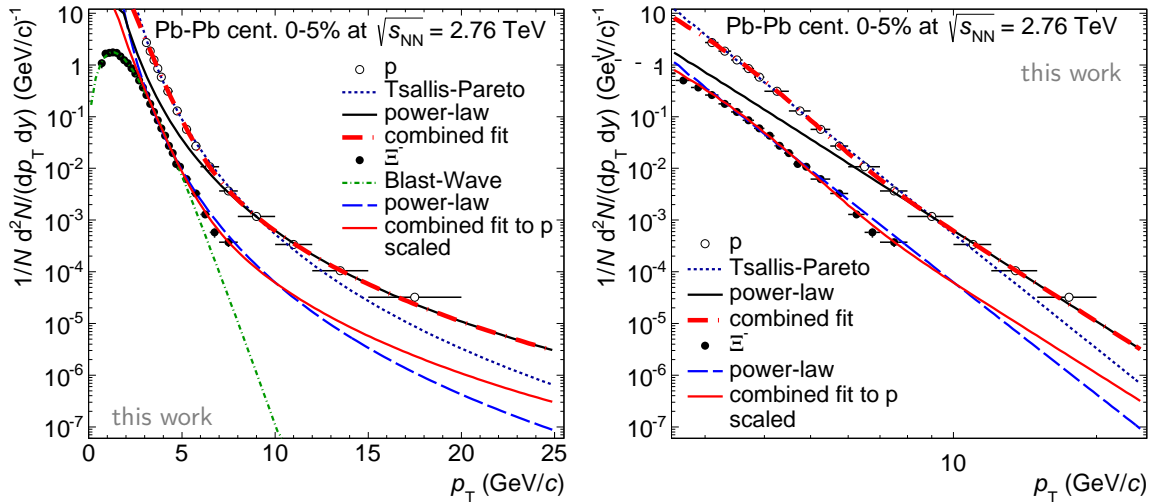
Figure 4.34: Fit of p and Ξ^- in central Pb–Pb collisions with different fit functions or with the parametrisation of the protons. Left: linear x-axis, right: logarithmic x-axis.

at higher p_T, where B, p_0 and n are free parameters. The resulting fit was down-scaled to match the Ξ^- by using a fit procedure with the scale as the only free parameter. The intermediate p_T region of the Ξ^- spectra is either described by a Tsallis function or by the parametrisation of the proton spectra. At high p_T ($p_T > 5\,\mathrm{GeV}/c$), the proton parametrization was always used. Furthermore, the Ξ^- spectra needed to be extrapolated to $p_T = 0$ and parametrized in order to obtain a finer binning in the same way as it was chosen for Λ. For the low p_T region ($p_T < 2\,\mathrm{GeV}/c$) a Blast-Wave fit (see equation 2.22) was applied. Figure 4.34 shows the Ξ^- in central Pb–Pb collisions together with a Blast-Wave fit, a power-law fit as well as with a fit with the proton parametrisation using a power-law and a Tsallis function, respectively. At high p_T, the power-law fit of the protons was chosen for the extrapolation and the power-law fit (cent 0-40%) or the Tsallis (cent 60-80%, pp) fit to the Ξ^- was used for the systematic error calculation.

Figure 4.35 displays the relative raw feed-down $\Lambda(p_T)_{\mathrm{sec}}^{\mathrm{raw}}/\Lambda(p_T)_{\mathrm{all}}^{\mathrm{raw}}$ from Ξ^- to Λ versus
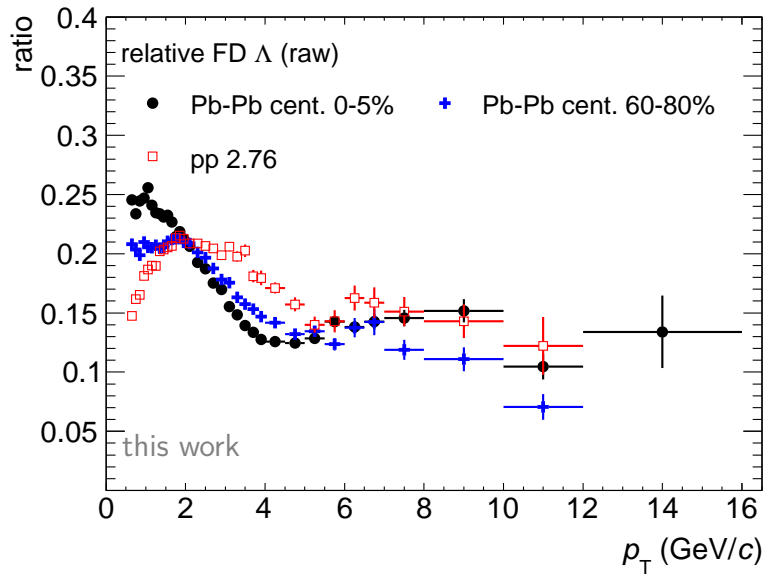
Figure 4.35: Relative feed-down for Λ in central, peripheral and pp collisions.

p_T of Λ for central and peripheral events in Pb–Pb as well as for pp (the procedure was performed for all other centralities, too). The error bars show the statistical uncertainties. For events of centrality 0 - 5% and 5 - 10%, the feed-down calculated from the Ξ^- spectra in 0 - 10% central events was up- (for cent. 0 - 5%) and down-scaled (for cent. 5 - 10%), respectively by 7.5%. This scaling results from the N_{part} scaling of the yield [30]. The maximum relative feed-down is at $p_T = 1\,\mathrm{GeV}/c$ about 25% in central events. With decreasing centrality one observes a decreasing feed-down, which is reversed at $1\,\mathrm{GeV}/c < p_T < 8\,\mathrm{GeV}/c$. At higher p_T the feed-down decreases again with decreasing centrality. The shape is a result of the similarity of the primary Λ and Ξ^- p_T shape, that is caused by their comparable mass ($1.115\,\mathrm{GeV}/c$ vs. $1.321\,\mathrm{GeV}/c$). This becomes obvious if the ratio of Λ_{sec} to Ξ^-, which is shown in figure 4.32, is compared to that of the relative feed-down. At high p_T, the ideal FD contribution does not vanish, since the boost of the Λ into the Ξ^- direction increases with p_T. Therefore, the Λ p_T gets closer to the Ξ^- p_T yielding a constant, non-zero FD contribution. Taking into account the steeper decreasing efficiency of Λ_{sec} with p_T as compared to that of the primary Λ, the measured FD indeed vanishes as soon as the efficiency ratio approaches zero. Considering the left panel of figure 4.29, this is not yet the case for the investigated p_T range, leading to a significant FD contribution of 6 to 10% at high p_T. The observation, that the last data point in central collisions suggests a rather constant behaviour at high p_T within the statistical uncertainties could be caused by the measured yield in this bin, which seems optically to be a little too low if it is compared to the spectrum in the 5-10% centrality class (see figure 4.20). This is however covered by the signal extraction uncertainties.

4.6.4 Normalization of pp spectra

The normalization of the transverse momentum spectra in pp collisions is more subtle than in Pb–Pb collisions. For the latter it is sufficient to divide by the number of events

which pass the vertex selection criterion due to a fully efficient vertex reconstruction, i.e. $N_{\text{vertex}}/N_{\text{triggered}} \approx 1$. For pp collisions, however, it is necessary to account for the events which were triggered but do not have a reconstructed vertex. Since this analysis was executed by applying a selection of the vertex position, one has to estimate those events without vertex, which would have, if a vertex was found, a vertex position within the $\pm 10\,\text{cm}$ window, $N_{\text{bin0,10cm}}$. The corresponding correction, $\text{norm}_{\text{MB,10cm}}$, to the so-called number of minimum bias events with vertex positions fulfilling the $10\,\text{cm}$ selection $N_{\text{MB,10cm}}$ is about 13.8% (values see table 4.6) and p_{T} independent. The calculation of this correction is sketched here [163]:

$$
\begin{aligned}
N_{\text{MB,10cm}} &= N_{\text{bin0,10cm}} + N_{\text{10cm}} \\
N_{\text{bin0}} &= N_{\text{triggered}} - N_{\text{vertex}} \\
N_{\text{bin0,10cm}} &= N_{\text{bin0}} \cdot \frac{N_{\text{10cm}}}{N_{\text{vertex}}} \\
\text{norm}_{\text{MB,10cm}} &= \frac{N_{\text{10cm}}}{N_{\text{MB,10cm}}} \\
\Rightarrow \text{norm}_{\text{MB,10cm}} &= \frac{N_{\text{vertex}}}{N_{\text{triggered}}} \quad .
\end{aligned}
\tag{4.12}
$$

N_{10cm} denotes the number of events with a vertex reconstructed with a position in $\pm 10\,\text{cm}$ on the z-axis. N_{bin0} are the events which are triggered but do not have a reconstructed vertex. $N_{\text{bin0,10cm}}$ is calculated from the assumption that the vertex position distribution of the not reconstructed vertices of triggered events is the same as for the reconstructed ones. This means, when normalizing the spectrum to the number of events, the latter consists of the analysed events plus the $N_{\text{bin0,10cm}}$, which is p_{T} independent. This assumption was compared to a calculation with MC information, where the MC shape of the events without vertex ($\text{n}_{\text{MCbin0}}(z)$) is normalized to the vertex distribution in data ($\text{n}_{\text{vertex}}(z)$):

$$
\begin{aligned}
\text{s}_{\text{bin0}}(z) &= \frac{\text{n}_{\text{MCbin0}}(z)}{\text{n}_{\text{MCvertex}}(z)} \cdot \text{n}_{\text{vertex}}(z) \\
\text{n}_{\text{bin0}}(z) &= N_{\text{bin0}} \cdot \frac{\text{s}_{\text{bin0}}(z)}{\int \text{s}_{\text{bin0}}(z)}
\end{aligned}
\tag{4.13}
$$

$$
N_{\text{bin0,10cm}} = \int_{-10\text{cm}}^{+10\text{cm}} \text{n}_{\text{bin0}}(z)\, \text{d}z \quad .
$$

Only a small deviation of the shape was observed which finally leads to a difference of 2% in $N_{\text{bin0,10cm}}$. On the basis of the MC information the assumption of similar vertex distribution for events with and without a reconstructed vertex is valid. The values needed for the mentioned calculations of $N_{\text{bin0,10cm}}$ are listed in table 4.6. For the data sample with SDD a value of 0.892 was obtained and for the without SDD sample the normalization is 0.881. After applying the vertex efficiency correction of 2%, the values are 0.874 for wSDD and 0.863 for nSDD. Currently the values without this correction are taken since this correction needs to be verified.

A further correction was applied in order to obtain a spectrum normalized to all kinds of inelastic reactions. The triggered collisions usually do not contain events from diffractive processes, as explained in section 3.6 (see also [153]). The corresponding

event categories	# of events wSDD (M)	# of events nSDD (M)
$N_{\text{triggered}}$	30.60	66.00
N_{vertex}	27.30	58.15
N_{10cm}	24.46	52.00
N_{bin0}	3.30	6.15
$N_{\text{bin0,10cm}}$	2.96	5.50
$N_{\text{bin0,10cm}}$ with MC LHC12b1c_wSDD	2.50	6.00
$N_{\text{bin0,10cm}}$ with MC LHC11b10a_wSDD	2.93	6.94
$N_{\text{MB,10cm}}$	27.42	57.50
$N_{\text{MB,10cm}}$ with MC LHC12b1c_wSDD	26.96	58.00
$N_{\text{MB,10cm}}$ with MC LHC11b10a_wSDD	27.39	58.94
normalisation	value	value
$\text{norm}_{\text{MB,10cm}} =$	0.892	0.881
$\text{norm}_{\text{MB,10cm, corr}} =$	0.874	0.863
$\text{norm}_{\text{MB,10cm}}$ with MC LHC12b1c_wSDD $=$	0.91	0.897
$\text{norm}_{\text{MB,10cm}}$ with MC LHC11b10a_wSDD $=$	0.893	0.882

Table 4.6: Number of events for different event classes in pp and the corresponding normalization factors to minimum bias events for the employed MC samples.

normalization value is

$$\text{norm}_{\text{INEL}} = \frac{\sigma_{\text{MBor}}}{\sigma_{\text{INEL}}} = 0.883^{+0.058}_{-0.035} \tag{4.14}$$

[153] and the final normalisation of the pp spectra is given by

$$\text{norm}_{\text{pp}} = \text{norm}_{\text{MB,10cm}} \cdot \text{norm}_{\text{INEL}} \quad . \tag{4.15}$$

4.7 Systematic Uncertainties

In this section, the systematic uncertainties on the cut selection, the signal extraction, the feed-down, the efficiency and the material budget are discussed.

For the estimation of the systematic uncertainties, the track and V^0 candidate selections were varied. In table 4.7, the difference of the these cuts from the corresponding reference cuts mentioned in section 4.3 are shown. For some variables, the changes due to the cut variation by $\pm 1\ \sigma$ of the cut variable distribution were investigated. For all other variables, the procedure of estimating the uncertainties is explained in the listing at the end of this section.

In order to remove contributions from statistical fluctuations in data influencing the BG fitting (especially at high p_{T}) and hence the extracted yield, the changes of the spectra resulting from the cut variation were studied for the raw spectra and for the efficiency separately. Since the distribution of the relative change due to the cut variation behaves rather smooth with p_{T} for the MC efficiency, the statistical fluctuations in the corresponding raw spectra distributions can be figured out by overlaying both distributions. In case of symmetrical fluctuations around the efficiency ratio or if the statistical error in the data ratio crosses the efficiency ratio, the resulting

selection criterion	V^0	Pb–Pb:		pp:	
		value or applied	$\pm$ or applied	value or applied	$\pm$ or applied
V^0 daughter track variables					
$\lvert\eta\rvert$		$<$ 0.8		$<$ 0.8	
χ^2 per cluster		$<$ 4	$+$ 1	$<$ 4	$+$ 1
TPC crossed rows	K_s^0	$>$ 70	12	$>$ 70	12
TPC crossed rows	Λ	$>$ 70	16	$>$ 70	20
TPC refit		yes	no	yes	no
found/findable	K_s^0	$>$ 0.5	0.06	$>$ 0.5	0.05
TPC cluster	Λ	$>$ 0.5	0.07	$>$ 0.5	0.06
DCA between	K_s^0	$<$ 0.23 cm	0.05 cm	$<$ 0.4 cm	0.04 cm
daughters	Λ	$<$ 0.35 cm	0.08 cm	$<$ 0.4 cm	0.07 cm
PID TPC dE/dx					
for p($\overline{\mathrm{p}}$): $n\sigma$	Λ	$<$ 3	1	$<$ 3	1
V^0 candidate variables					
$\lvert y\rvert$		$<$ 0.5	$0 < y < 0.5$	$<$ 0.5	$0 < y < 0.5$
$\lvert y\rvert$		$<$ 0.5	$-0.5 < y < 0$	$<$ 0.5	$-0.5 < y < 0$
DCA_{xy}	K_s^0	$<$ 0.4 cm	0.06 cm	$<$ 0.4 cm	0.05 cm
DCA_{xy}	Λ	$<$ 1.2 cm	0.2 cm	$<$ 1.2 cm	0.175 cm
cos(PA)	K_s^0	$>$ 0.99	$+$ 0.002	$>$ 0.99	$+$ 0.002
cos(PA)	Λ	$>$ 0.998	$+$ 0.001	$>$ 0.998	$+$0.001
cos(PA)	Λ	$>$ 0.998	$-$ 0.008	$>$ 0.998	$-$ 0.008
decay radius R_{xy}		$>$ 5 cm	$+$ 2 cm	$>$ 5 cm	$+$ 2 cm
Armenteros-Podolanski:					
$q_\perp > b \cdot \lvert\alpha\rvert$, b	K_s^0	$=$ 0.2	0.03	$=$ 0.2	0.03

Table 4.7: Selections on the V^0 candidate and its daughters with cut variations for the systematic uncertainty determination.

systematic uncertainty was neglected or a constant systematic error value of the last non-fluctuating point was used.

For each p_T bin, the systematic uncertainties due to the cut variations lowering or enlarging the yield, respectively, were added separately. Finally, the largest error of the two was taken as the symmetric uncertainty in this p_T bin.

In addition to the cut variation, the uncertainties originating from the BG fitting, yield calculation, the feed-down, efficiency correction and the material budget were estimated. The following list contains explanations of the different systematic uncertainty sources, which are not covered by the procedure of the cut variation by $\pm 1\,\sigma$:

1. **rapidity:** The analysis was performed in the forward and backward rapidity region, respectively, in order to estimate the rapidity dependence of the analysis. For K_s^0 in Pb–Pb, the variation of the spectra from the forward to backward region is about 2% in central events, for Λ and $\overline{\Lambda}$ this is about 3% in central

collision class	Λ	K_s^0
Pb–Pb cent 0-60%	3.0%	3.0%
Pb–Pb cent 60-80%	2.0%	2.0%
pp	1.5%	1.5%

Table 4.8: Systematic uncertainties due to a linear fit to the background of the invariant mass distribution of V^0 candidates instead of the standard polynomial fit of order 2 - 6.

and 1% in peripheral events below $6\,\mathrm{GeV}/c$. In pp, a difference of 1% was found for K_s^0 below $6\,\mathrm{GeV}/c$, 4% for Λ below $3\,\mathrm{GeV}/c$ and no effect for $\overline{\Lambda}$. The errors were added to the cut variation systematics.

2. $\boldsymbol{\chi^2}$ **per cluster:** The cut variation of χ^2 per cluster to < 3 was not taken into account for the systematics, because the difference of the distributions in data and MC is largest below 4. Therefore, the cut of 3 would introduce a large bias as compared to $\chi^2 = 4$ or 5, where the distributions are much more similar. Consequently, only the case for $\chi^2 < 5$ was investigated for the systematic uncertainty estimation.

3. **PID**: The cut variation for the PID was chosen to be $n\sigma = 2\sigma$ and $n\sigma = 4\sigma$. In case of the latter, the uncorrected Λ spectra with $n\sigma = 4\sigma$ were compared to the uncorrected standard spectra with $n\sigma = 3\sigma$, because in the MC efficiency correction, the PID is not applied in the present analysis. The difference between the two configurations enters in the p_T dependent error calculation. The uncertainty resulting from the selection of $n\sigma = 2\sigma$ was determined by applying the PID in data as well as in the MC efficiency calculation for the case of $n\sigma = 2\sigma$ and $n\sigma = 3\sigma$ (this is not the case for the final spectra) while using the tuned splines from data. Then the ratio of the correspondingly corrected spectra with $n\sigma = 2\sigma$ and $n\sigma = 3\sigma$ was built. From that, an error of 5% in central Pb–Pb, 3% in peripheral Pb–Pb and 2% in pp was derived. For $n\sigma = 4\sigma$, 2.0% in central, 1.2% in peripheral and 1.0% in pp was obtained on average. The individual value for each p_T bin maximally varies up to theses values.

4. **Linear background fit in tight fit range**: A linear fit between the edges of the mass window was performed up to that p_T bin, where the polynomial order is 1 by the default procedure. The resulting uncertainties were determined as a p_T-independent value, as RMS[9] of the distribution of the deviation from the standard procedure vs p_T. The values for all centralities and pp can be found in table 4.8.

5. **Signal extraction in MC treated as data**: The signal extraction procedure was also performed using $\mathrm{MC_{reco}}$, which was treated as if it was data. The corresponding p_T spectra were compared to the $\mathrm{MC_{reco}}$ spectra used for the efficiency calculation (pure distributions without background due to PDG code selection). A difference between them reveals the uncertainty of the background fitting method. The resulting uncertainties were determined as a p_T-independent value, as RMS of the distribution of the deviation from the standard procedure vs p_T.

---

[9]Root Means Squared.

collision class	Λ	K_s^0
Pb–Pb cent 0-40%	3.0% (5 - 10% $p_T > 8$ GeV/c)	2.5% (5% $p_T > 12$ GeV/c)
Pb–Pb cent 40-60%	2.5% (7% $p_T > 6$ GeV/c)	2.5% (5 - 10% $p_T > 10$ GeV/c)
Pb–Pb cent 60-80%	2.5% (7% $p_T > 6$ GeV/c)	2.5% (10% $p_T > 16$ GeV/c)
pp	2.5% (7 - 10% $p_T > 6$ GeV/c)	2.5% (7 - 14% $p_T > 9$ GeV/c)

Table 4.9: Systematic uncertainties due to signal extraction.

For detailed values including also the following uncertainties from signal extraction tests see table 4.9.

6. **Mass peak window:** The limits of the mass peak window were changed by 2‰ for Λ and 1% in case of K_s^0 in order to study the stability of the signal extraction. In this way, the mass peak window for the BG fitting was either enlarged or tightened. This relative change was chosen according to the scale and the range of the peak width and the mass window, which are around a few MeV, corresponding to per mill in case of Λ. The deviations to the standard procedure are however already covered by the previous check. Thus, they were not added to the signal extraction error.

7. **Background fitting with likelihood minimisation in adapted fit ranges**: In some high-p_T bins with low background statistics, where the likelihood fit procedure was used instead of the standard χ^2 method, the fit range was adapted to the smaller range of filled background bins. This error is added to the signal extraction error.

8. **Integral of Gauss fit function instead of bin counting**: The default procedure for the signal yield determination is the counting of bin contents in a window of 3 - 4 times the width of the mass peak depending on p_T. This method was compared for higher p_T values to the integral of a Gauss fit to the background subtracted signal for $p_T > 7$ GeV/c, where the bin content fluctuations become relevant. This error is added to the signal extraction error.

9. **Counting all bins instead of applying a mass window**: The standard method was compared to counting all bins in the full mass range. This was found to give similar results within the statistical uncertainties for K_s^0 in Pb–Pb, 17% in the last p_T bin in pp and 5% difference for Λ above $p_T = 6$ GeV/c in peripheral Pb–Pb and pp collisions. This error is added to the signal extraction error.

10. **Feed-down**: The systematic uncertainties due to the feed-down correction are dominated by the parametrization and extrapolation of the Ξ^- spectra. The main effect was observed at high p_T, where the parametrization of the protons was used. If instead of the latter, a power-law fit to the Ξ^- was performed, the feed-down corrected Λ spectrum (Λ_{FDcorr}) changed by up to 10% (figure 4.36). For peripheral events the feed-down even changes at lower p_T, since the fit range of the Blast-Wave needed to be adapted. However, the protons give at least a guidance with respect to the high p_T region and an estimate of the exponent through exhibiting a power-law pattern above 7 GeV/c. Therefore, the estimation based on the proton spectra is used for the feed-down contribution at
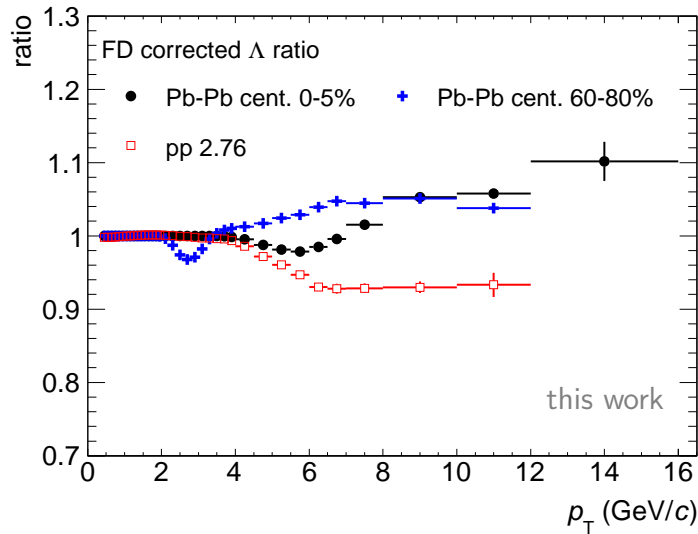
Figure 4.36: Ratio of feed-down corrected Λ spectra using a power-law fit to Ξ^- for the Ξ^- spectra extrapolation to the spectrum, where the standard procedure is applied (see text).

high p_T, and half of the difference to the Ξ^- power-law fit is taken as systematic uncertainty.

Another uncertainty on the feed-down correction results from the statistical and systematic uncertainties of the input Ξ^- spectra. Therefore, the feed-down was also calculated from Ξ^- spectra, where for one case the error (quadratic sum of the statistical and systematic error) was subtracted and for the other case added to the extrapolated and parametrized spectra. In that way, the maximal and minimal possible feed-down could be estimated.

11. **Efficiency**: The spectra were corrected by a bin-wise division of the spectrum by the efficiency, if there were no statistical fluctuations and the statistical errors were small, which was mostly the case for $p_T < 2\,\text{GeV}/c$. At larger p_T, the efficiency was parametrised in most cases in order to obtain a smooth distribution. The systematic uncertainty resulting from the bin-wise efficiency correction are the statistical errors of the efficiency. In case of the usage of the parametrisation, the largest error out of the following three sources was taken: statistical error, error from the fit and the difference of the fit function to the efficiency value.

12. **Material budget**: The systematic uncertainty due to the uncertainty on the material budget estimation was determined with the help of two MC samples, where the material budget was changed by $\pm\,7\%$ in Pb–Pb. In figure 4.37 the ratios of the efficiencies from those two samples are shown for Λ, $\overline{\Lambda}$ and K_s^0 integrated over all centralities. Despite the large statistical errors, one can conclude that the main influence of the material budget change takes place at low p_T and that it is strongest for Λ and $\overline{\Lambda}$. Using the ansatz from the multi-strange analysis in ALICE [164], it is possible to deduce from these distributions the systematic uncertainty on the spectra knowing that the uncertainty of the
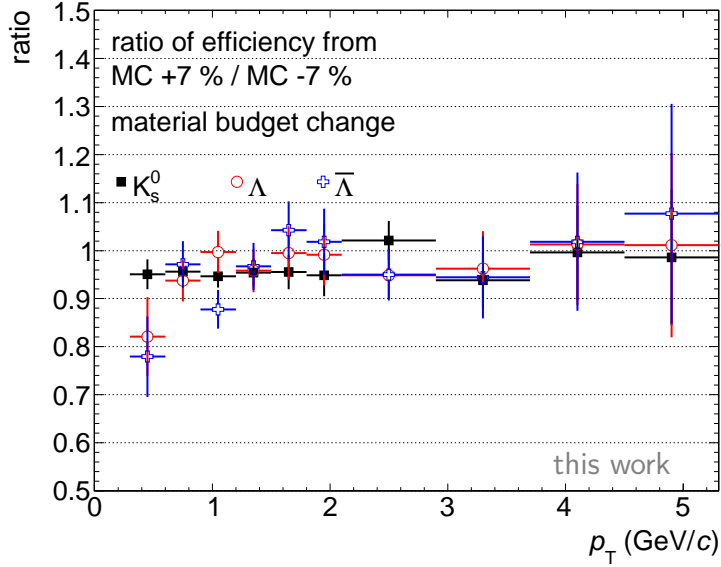
Figure 4.37: Ratio of efficiencies calculated from MC with +7% to those from MC with -7% material budget estimation. The black rectangles show K_s^0, the red open circles represent Λ and the blue hollow crosses $\overline{\Lambda}$.

material budget is about 4.86% for Pb–Pb and pp [165]. The formula for the error calculation is:

$$\text{err}_{\text{syst,material}}(p_{\text{T}}) = \frac{1.0 - \text{ratio}_{\text{eff}}(p_{\text{T}})}{2} \cdot \frac{0.0486}{0.07} \qquad (4.16)$$

with $\text{ratio}_{\text{eff}}(p_{\text{T}})$ as the ratio between the efficiencies from MC(+7%) to MC(-7%), 0.07 being the magnitude of the relative change of the material budget in the MC samples and 0.0486 as the uncertainty of the material budget estimation. The division by 2.0 is needed, since the ratio of the efficiencies was calculated for the case of +7% to -7%. Therefore, the ratio to 0% change in the material budget lies in the middle of the ratio of +7% to -7%, for example at 0.91 at around $0.5\,\text{GeV}/c$ for Λ. In order to obtain the errors for the binning used for K_s^0 and Λ, the points of the efficiency ratio were interpolated.

The corresponding errors are assumed to be centrality independent and were therefore also used for pp. For K_s^0 a constant value of 1.74% up to $p_{\text{T}} = 2\,\text{GeV}/c$ and for Λ maximal values of 6.25% and minimal of 1.04% up to $p_{\text{T}} = 1.5\,\text{GeV}/c$ were obtained. Above these p_{T} values, no influence of the material budget change on the spectra was assumed.

13. **Absorption correction:** The difference of the anti-proton absorption correction obtained in this work to the standard correction enters into the systematic uncertainty of $\overline{\Lambda}$. Furthermore, the difference of the fit used to parametrize the correction to the distribution is added to the absorption correction uncertainty.
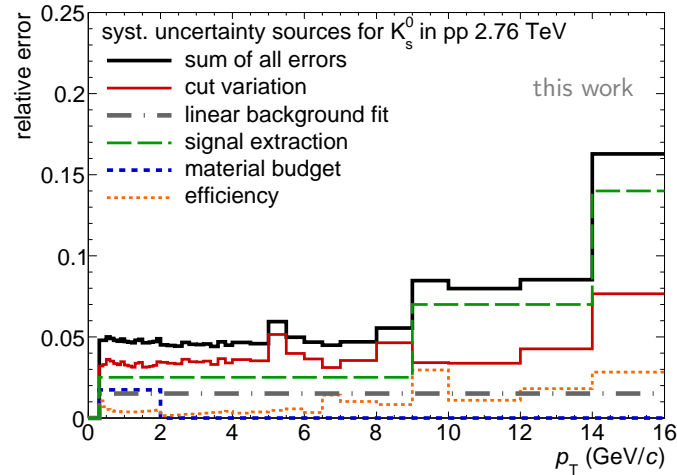
Figure 4.38: Systematic uncertainty sources for K_s^0 in pp collisions at $\sqrt{s} = 2.76\,\text{TeV}$.
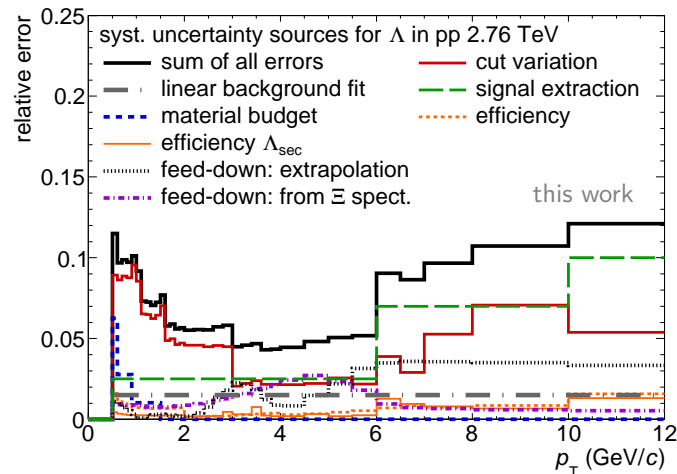
Figure 4.39: Systematic uncertainty sources for Λ in pp collisions at $\sqrt{s} = 2.76\,\text{TeV}$.

All in all, the final systematic uncertainty in each p_T bin was calculated as the quadratic sum of all the individual systematic errors. In figures 4.38, 4.39, 4.40, 4.44, 4.45, 4.46 all systematic error components are shown for K_s^0, Λ and $\overline{\Lambda}$ in pp as well as in central Pb–Pb collisions. Similar figures for the remaining centrality classes can be found in appendix B.6. Figures 4.41, 4.42, 4.43 show the total systematic uncertainties for both species in each p_T bin together with the statistical errors. The corresponding plots for Pb–Pb collisions are presented appendix B.6.2.
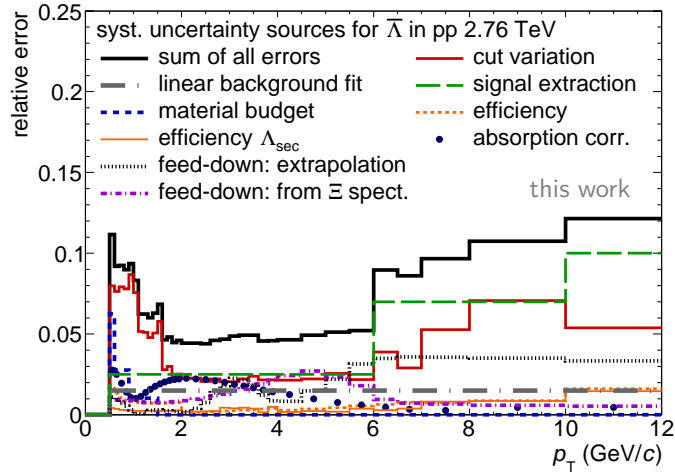
Figure 4.40: Systematic uncertainty sources for $\overline{\Lambda}$ in pp collisions at $\sqrt{s} = 2.76\,\text{TeV}$.
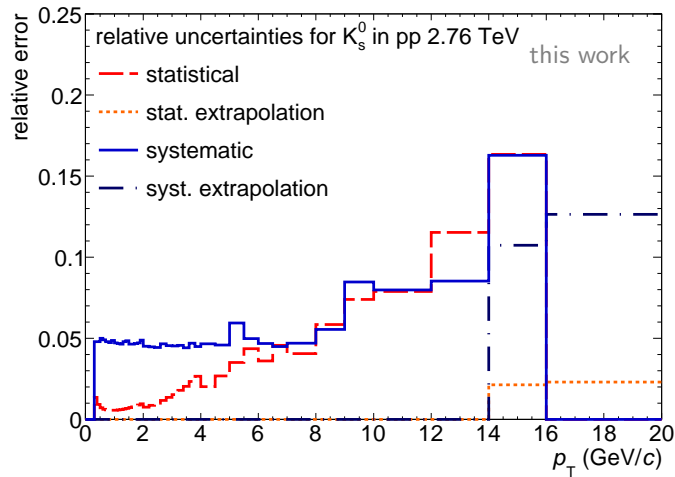
Figure 4.41: The statistical uncertainties vs. p_{T} together with the total systematic uncertainties for K_s^0 in pp collisions at $\sqrt{s} = 2.76\,\text{TeV}$. Also shown, errors assigned to the extrapolated parts of the spectra.
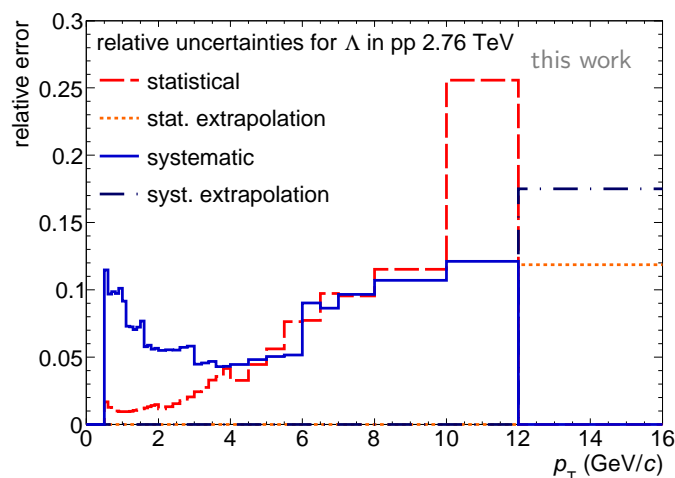
Figure 4.42: The statistical uncertainties vs. p_T together with the total systematic uncertainties for Λ in pp collisions at $\sqrt{s} = 2.76$ TeV. Also shown, errors assigned to the extrapolated parts of the spectra.

Figure 4.43: The statistical uncertainties vs. p_T together with the total systematic uncertainties for $\overline{\Lambda}$ in pp collisions at $\sqrt{s} = 2.76$ TeV. Also shown, errors assigned to the extrapolated parts of the spectra.
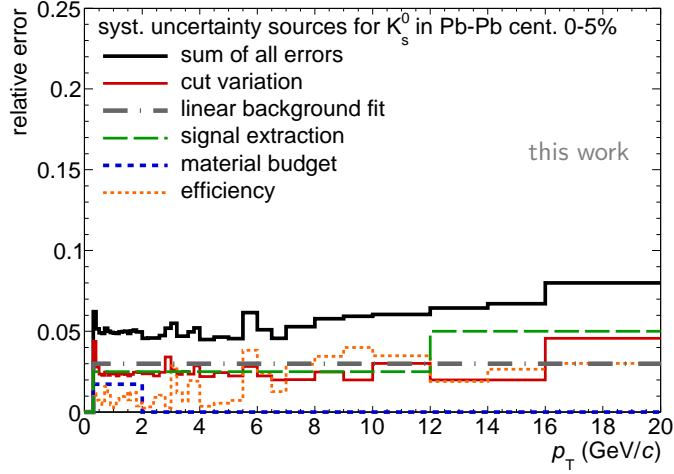
Figure 4.44: Systematic uncertainty sources for K^0_s in central Pb–Pb collisions.
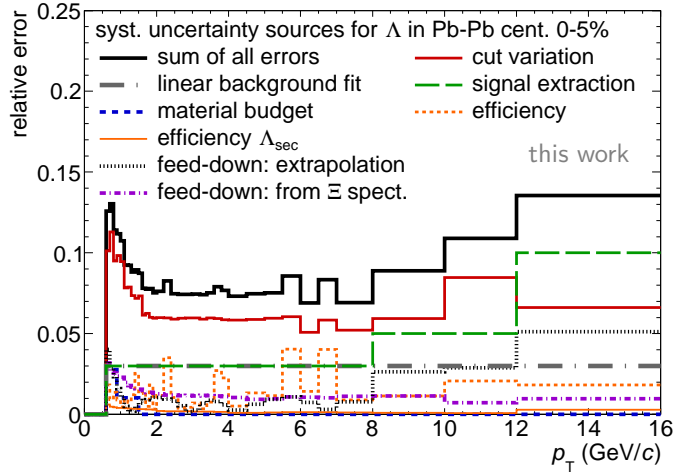
Figure 4.45: Systematic uncertainty sources for Λ in central Pb–Pb collisions.

Figure 4.46: Systematic uncertainty sources for $\overline{\Lambda}$ in central Pb–Pb collisions.

4.8 Proper particle lifetime

The proper life time ($c\tau$) distribution follows an exponential with the mean life time as the inverse decay constant. If this distribution with the correct mean life time can be extracted from data, the detector calibration was sufficient and the analysis was properly performed. In case of Pb–Pb, the mean lifetime of $\mathrm{K^0_s}$ and Λ was extracted within the offline $\mathrm{V^0}$ finder analysis in [154] and found to be consistent with the values from [13]. Since the spectra of this analysis and the offline $\mathrm{V^0}$ finder analysis agree (see section 5.1.3), it is left to this analysis to extract the mean life time for pp.

In order to measure the proper life time distribution, the values extracted from raw data according to

$$c\tau = L_\mathrm{T} \cdot \frac{m_\mathrm{lit}}{p_\mathrm{T}}, \tag{4.17}$$

with the transverse decay length L_T and the literature mass m_lit, need to be corrected for efficiency. A 3D histogram was filled with the invariant mass, p_T and $c\tau$ for data and a 2D histogram with p_T versus $c\tau$ for $\mathrm{MC_{truth}}$ and $\mathrm{MC_{reco}}$. The mass range in $\mathrm{MC_{reco}}$ was restricted to a common mass window for all p_T before filling. The 2D projection of the $\mathrm{K^0_s}$ from $\mathrm{MC_{reco}}$ was divided by the respective histogram from $\mathrm{MC_{truth}}$ in order to obtain the 2D efficiency in p_T versus $c\tau$. For each invariant mass interval in data, the corresponding 2D plane of p_T versus $c\tau$ was divided by the 2D efficiency. Afterwards, the corrected 3D histogram in data was projected on the invariant mass versus $c\tau$. The resulting 2D distribution was subsequently analysed in bins of $c\tau$ while subtracting the BG from the mass peak region (same procedure as for the p_T spectra). The corrected $c\tau$ spectrum for $\mathrm{K^0_s}$ together with an exponential fit is shown in figure 4.47. The mean life time extracted from the fit is $2.732 \pm 0.005\,\mathrm{cm}$ (fit parameter 1 in figure 4.47) which is roughly 2% larger than the literature value of $2.686\,\mathrm{cm}$ [13]. If a 1D correction in p_T was used instead of the mentioned 2D correction in p_T versus $c\tau$, the mean life time increases by 15% (open rectangles in figure 4.47).

Summary

In this chapter the analysis procedure was documented and the raw spectra of $\mathrm{K^0_s}$ and $\Lambda(\overline{\Lambda})$ were shown. The following chapter presents the corrected spectra after the application of the described corrections and normalizations. Furthermore, observables extracted from the spectra are displayed. The discussion of the results follows in chapter 6.
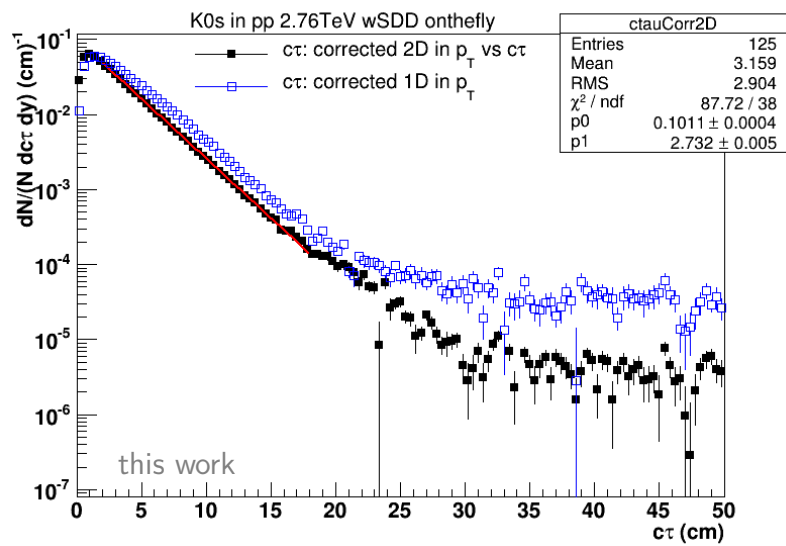
Figure 4.47: Corrected cτ distribution of K$_s^0$ in pp $\sqrt{s}$ = 2.76 TeV. The black rectangles show the case for a 2D efficiency correction, whereas the blue hollow rectangles show the case for a 1D efficiency correction. The fit with an exponential to the black rectangles is represented by the red line. The legend contains the corresponding fit values with p0 as the normalization and p1 as the mean life time.

<div style="text-align: right; font-size: 3em; font-weight: bold; color: #1a4d8f;">5</div>

Results

In this chapter, the results of K_s^0 and $\Lambda(\overline{\Lambda})$ transverse momentum spectra analysis are presented. First, the p_T spectra are shown and compared to the published results of the offline V^0 finder analysis. Afterwards, the spectra of K_s^0 are compared to the charged kaon $(K^{+,-})$ spectra results. This is followed by the discussion of the extracted yields in view of strangeness suppression in pp as well as in the context of the baryon-to-meson comparison. Finally, the nuclear modification factors of K_s^0 and $\Lambda(\overline{\Lambda})$ are presented.

5.1 Transverse momentum spectra of K_s^0 and $\Lambda(\overline{\Lambda})$

5.1.1 Results in Pb–Pb collisions

In figure 5.1, the corrected K_s^0 spectra including the systematic uncertainties are presented for all centralities in Pb–Pb. Figures 5.2 and 5.3 show the corrected Λ and $\overline{\Lambda}$ spectra, respectively.
Comparing the spectra shapes of each particle type with regard to the collision centrality, the increasing influence of the radial flow with centrality becomes visible through the growing enhancement for $p_T < 5\,\mathrm{GeV}/c$, which causes a growing mean transverse momentum. For the high-p_T region, a power-law like behaviour as in pp collisions (see section 2.1) is suggested in the double logarithmic representation. The exponent slightly decreases with centrality yielding harder spectra in central collisions.

Figure 5.4 shows the $\overline{\Lambda}$ to Λ ratio for central, mid-central and peripheral Pb–Pb collisions (other centralities in figure C.1). The systematic error of the ratio contains all systematic uncertainties of both particles and thus represents the maximal systematic uncertainty. At low p_T, where the yield is maximal, the production of particle and anti-particle is the same as it is expected at LHC energies. The ratio is compatible with unity within the uncertainties up to $p_T \approx 6\,\mathrm{GeV}/c$ for all shown collision classes, while at higher p_T, it tends to decrease with p_T. The dip at 10 - $12\,\mathrm{GeV}/c$ is however only seen in central and peripheral collisions. The $\overline{\Lambda}/\Lambda$ ratio at high p_T is subject to further studies, in particular with respect to possible instabilities of the yield extraction imposed by fluctuations of the mass peak position and width, see also figure 4.23. A separate investigation of the two magnetic field configurations
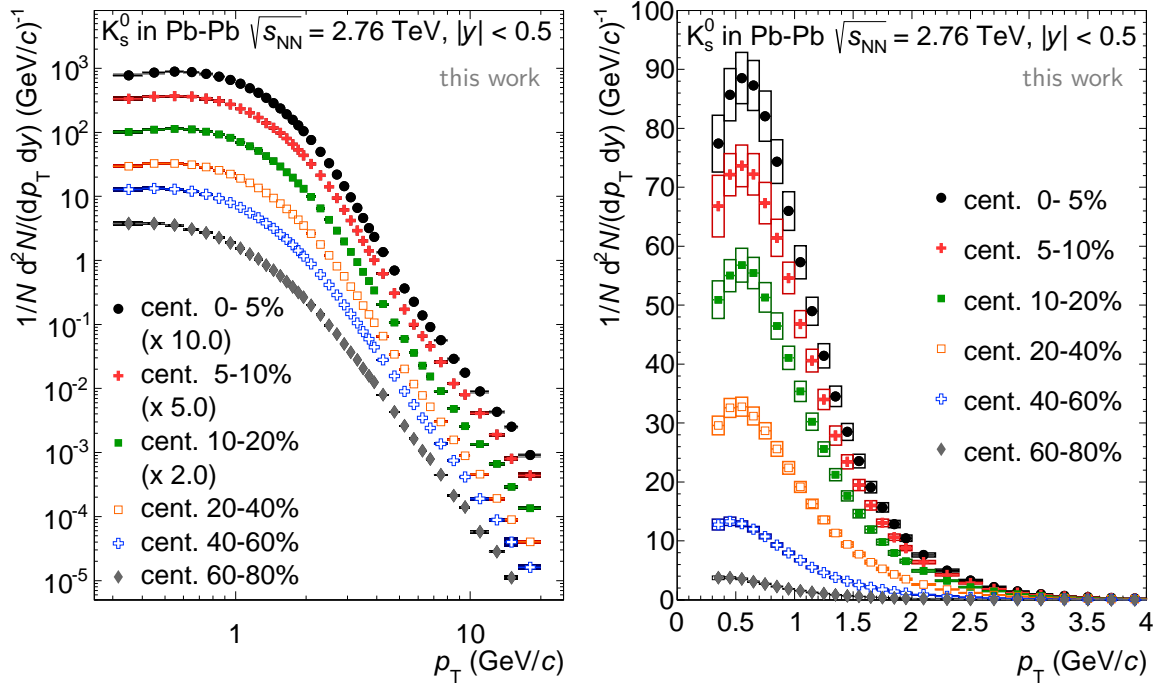
Figure 5.1: Transverse momentum spectra of K_s^0 in Pb–Pb at $\sqrt{s_{NN}} = 2.76\,\text{TeV}$ for different centralities. The boxes around the data points represent the systematic uncertainties, whereas the vertical error bars show the statistical errors. Left panel: logarithmic scale. Right panel: linear scale.
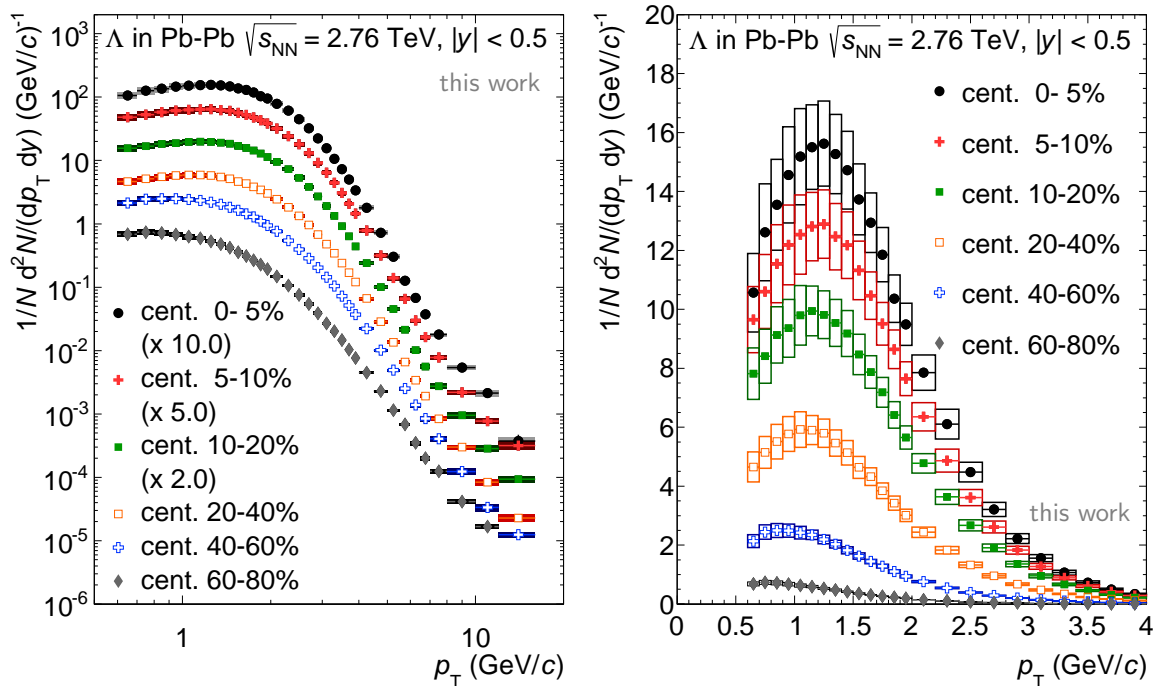
Figure 5.2: Transverse momentum spectra of Λ in Pb–Pb at $\sqrt{s_{NN}} = 2.76\,\text{TeV}$ for different centralities. The boxes around the data points represent the systematic uncertainties, whereas the vertical error bars show the statistical errors. Left panel: logarithmic scale. Right panel: linear scale.

Figure 5.3: Transverse momentum spectra of $\overline{\Lambda}$ in Pb–Pb at $\sqrt{s_{\mathrm{NN}}} = 2.76\,\mathrm{TeV}$ for different centralities. The boxes around the data points represent the systematic uncertainties, whereas the vertical error bars show the statistical errors. Left panel: logarithmic scale. Right panel: linear scale.
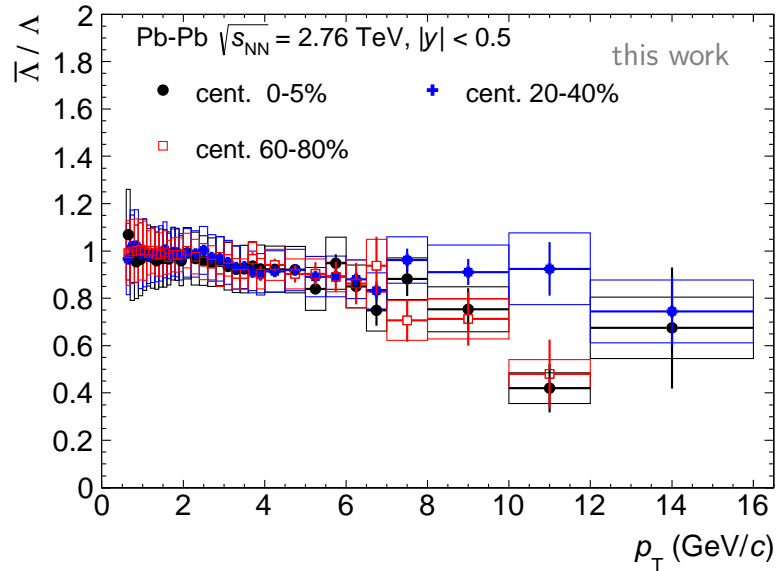
Figure 5.4: Ratio of $\overline{\Lambda}$ to Λ in central, mid-central and peripheral Pb–Pb collisions at $\sqrt{s_{\mathrm{NN}}} = 2.76$ TeV. The boxes around the data points represent the systematic uncertainties, whereas the vertical error bars show the statistical errors.

in the Pb–Pb data set could not provide information on a possible mistake of particles and anti-particles since the statistics at the considered p_{T} was too low.
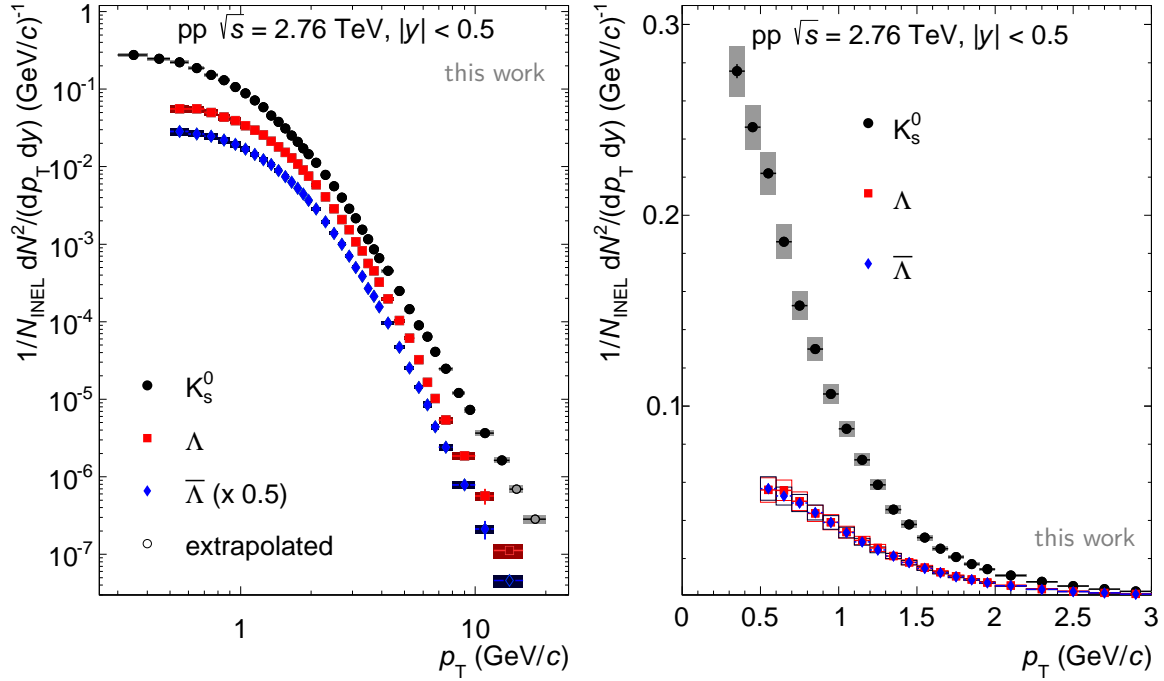
Figure 5.5: Transverse momentum spectra of K_s^0 and $\Lambda(\overline{\Lambda})$ in pp collisions at $\sqrt{s}$ = 2.76 TeV. The open symbols show the extrapolated points. The boxes around the data points represent the systematic uncertainties, whereas the vertical error bars show the statistical errors. Left panel: logarithmic scale. Right panel: linear scale.

5.1.2 Results pp

The results in pp collisions at $\sqrt{s}$ = 2.76 TeV are shown in figure 5.5. In order to obtain the same p_T range as for Pb–Pb collisions, which is needed for the R_{AA} calculation, the pp spectra were extrapolated. A power-law fit (eq. 4.11) was performed from $3 < p_T < 16\,\mathrm{GeV}/c$ for K_s^0 and from $4.5 < p_T < 12\,\mathrm{GeV}/c$ for Λ. The p_T range of the extrapolation for K_s^0 is $14 < p_T < 20\,\mathrm{GeV}/c$ and for Λ $12 < p_T < 16\,\mathrm{GeV}/c$. Although a mass peak is observed for the p_T bin 14 - 16 GeV/c of K_s^0, the bin was neglected due to the systematic uncertainty caused by the signal extraction, where a strong deviation from a Gaussian peak shape results into a too small extracted peak width. Within the statistical uncertainties though, the yield in this p_T bin from the standard signal extraction procedure compared to counting all bins in the range estimated from the previous p_T bin agree.

For the fit procedure, the statistical and systematic errors were added quadratically. The systematic uncertainty of the extrapolated data points was calculated from the following sources: First, the difference to the results from fits to the spectra, which were shifted to the upper and lower edge of the systematic errors were calculated. Second, the fit results from different starting values of the fit were evaluated. Third, the difference of the power-law function to a simple power-law ($1/p_T^n$) entered into the systematic error estimation. Concerning the statistical error, the point by point error from the fit was taken. The ratio of the data to the corresponding fit is shown in figure 5.6. Within the given fit range, the data are well described by a power-law function. The choice of a lower fit range limit for K_s^0 as compared to Λ is related to their spectra shape, which in case of K_s^0 converts to a power-law at lower p_T due to
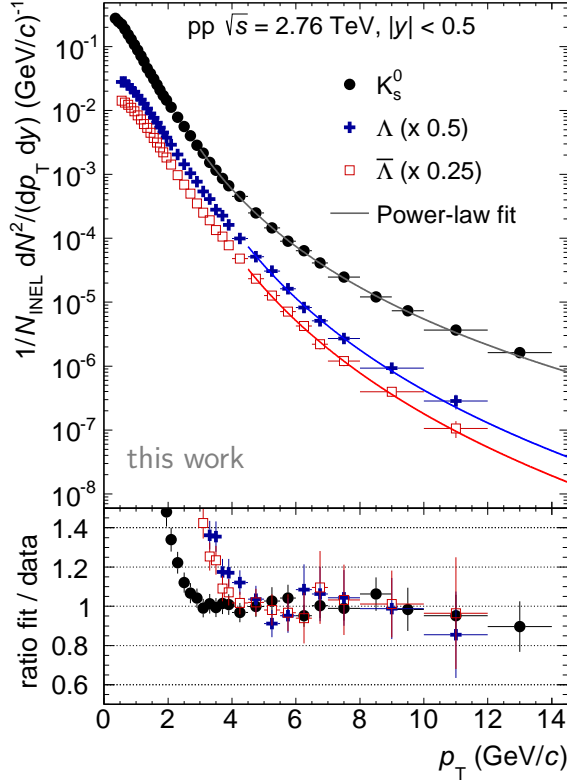
Figure 5.6: K_s^0 and $\Lambda(\overline{\Lambda})$ in pp $\sqrt{s} = 2.76\,\text{TeV}$ with power-law fits for the extrapolation. The errors represent the quadratic sum of the statistical and systematic uncertainty. Lower panel: ratio fit over data.

particle:	K_s^0	$\pm$	Λ	$\pm$	$\overline{\Lambda}$	$\pm$
exponent:	6.08	0.05	7.48	0.19	7.52	0.2

Table 5.1: Exponent of the power-law fitted to K_s^0 and $\Lambda(\overline{\Lambda})$ in pp collisions at $\sqrt{s} = 2.76\,\text{TeV}$.

its lower mass. The exponents of the power-law fit are shown in table 5.1.

In figure 5.7, the $\overline{\Lambda}/\Lambda$ ratio is shown for pp collisions. The spectra agree within systematics for the whole p_T range though a slightly decreasing trend with p_T is observed as in Pb–Pb collisions.
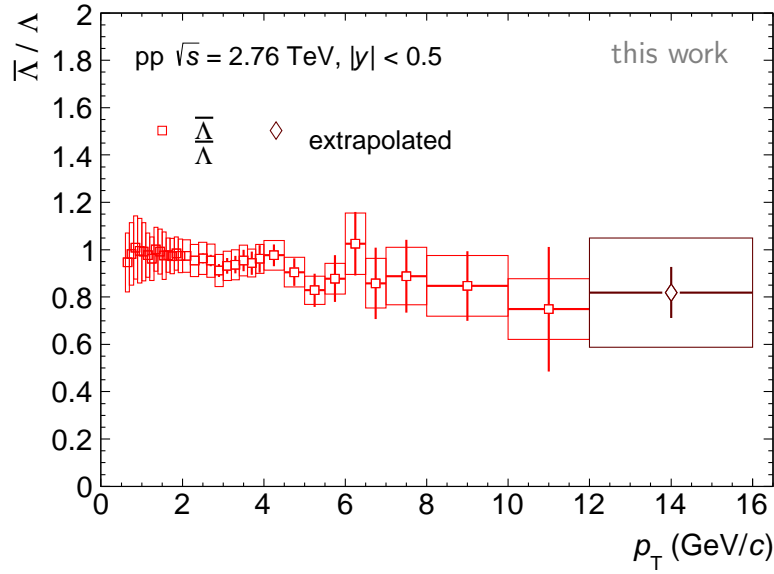
Figure 5.7: Ratio of $\overline{\Lambda}$ to Λ in pp collisions at $\sqrt{s}$ = 2.76 TeV. The boxes around the data points represent the systematic uncertainties, whereas the vertical error bars show the statistical errors.

5.1.3 Comparison to offline V^0 finder analysis

In the following, the K_s^0 and Λ spectra in Pb–Pb collisions are compared to the offline V^0 finder analysis [154] in figures 5.8, 5.9 (K_s^0) and 5.10, 5.11 (Λ). The uncertainties of both analyses are treated as independent errors.

In case of K_s^0, the results from both V^0 finders are in good agreement. However, for the centrality classes 0-20%, an enhancement of the offline K_s^0 is observed for the first two p_T bins, which exceeds the systematic uncertainties. The Λ spectra show a rather good agreement from low to intermediate p_T. At high p_T, however, the spread of the differences becomes large in central events, which is not covered by the systematics. This is supposed to be influenced by the differences in the treatment of the feed-down correction. While in this analysis the feed-down was determined for each centrality separately, a constant correction was assumed for the published spectra. The p_T spectra of $\overline{\Lambda}$ were not published within the offline V^0 finder analysis.
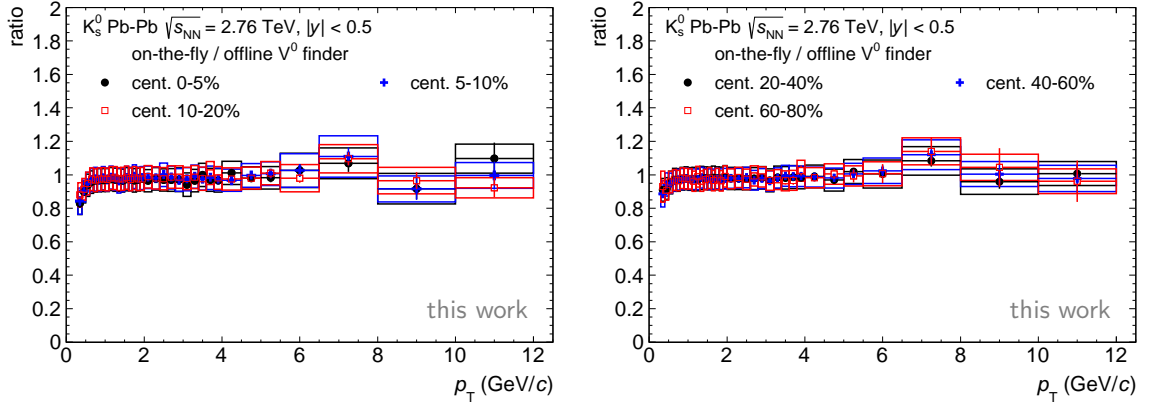
Figure 5.8: Ratio of the K_s^0 p_T spectra in Pb–Pb collisions from this analysis using the on-the-fly V^0-finder to the published K_s^0 results (offline V^0 finder) for centralities 0-5%, 5-10%, 10-20% in the left panel and for centralities 20-40%, 40-60% and 60-80% in the right panel. The boxes around the data points represent the systematic uncertainties, whereas the error bars indicate the statistical uncertainties.
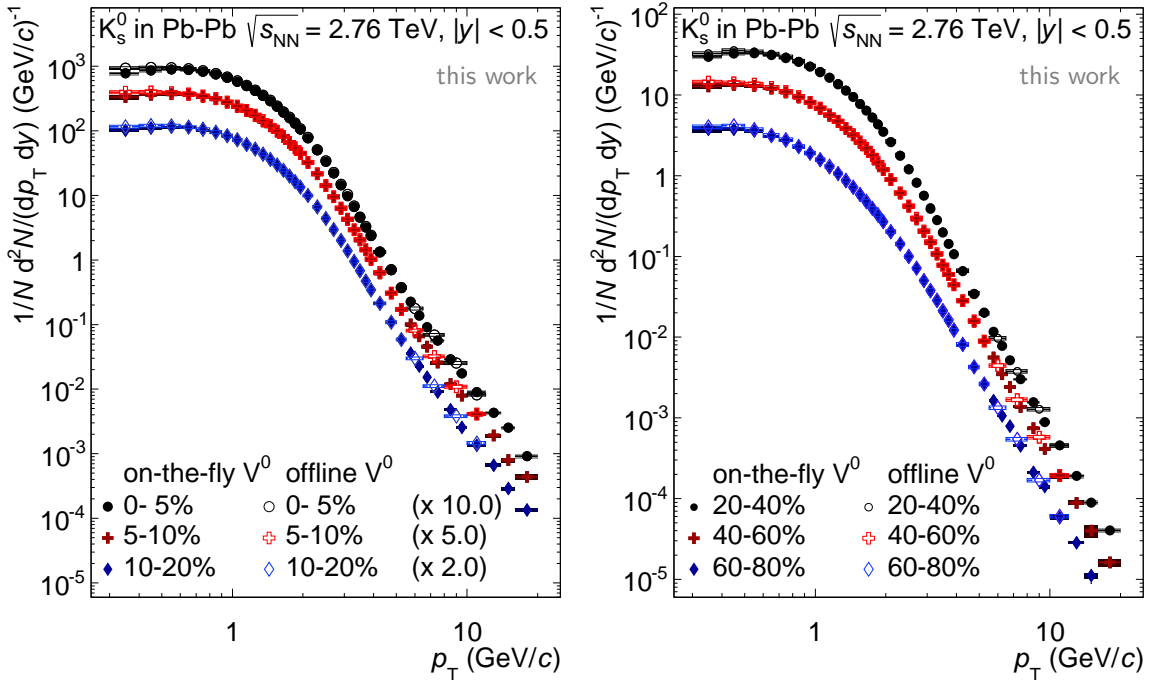
Figure 5.9: Comparison of the published K_s^0 [154] (offline V^0 finder) in Pb–Pb collisions to those from this analysis using the on-the-fly V^0 finder for centralities 0-5%, 5-10%, 10-20% in the left panel and 20-40%, 40-60% and 60-80% in the right panel. The boxes around the data points represent the systematic uncertainties, whereas the error bars indicate the statistical uncertainties.
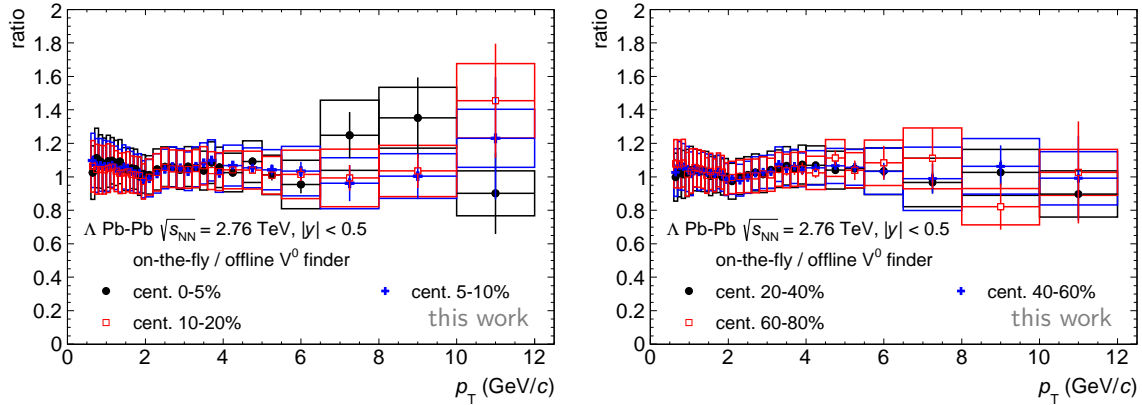
Figure 5.10: Ratio of the Λ p_T spectra in Pb–Pb collisions from this analysis using the on-the-fly V^0-finder to the published Λ results (offline V^0 finder) for centralities 0-5%, 5-10%, 10-20% in the left panel and for centralities 20-40%, 40-60% and 60-80% in the right panel. The boxes around the data points represent the systematic uncertainties, whereas the error bars indicate the statistical uncertainties.
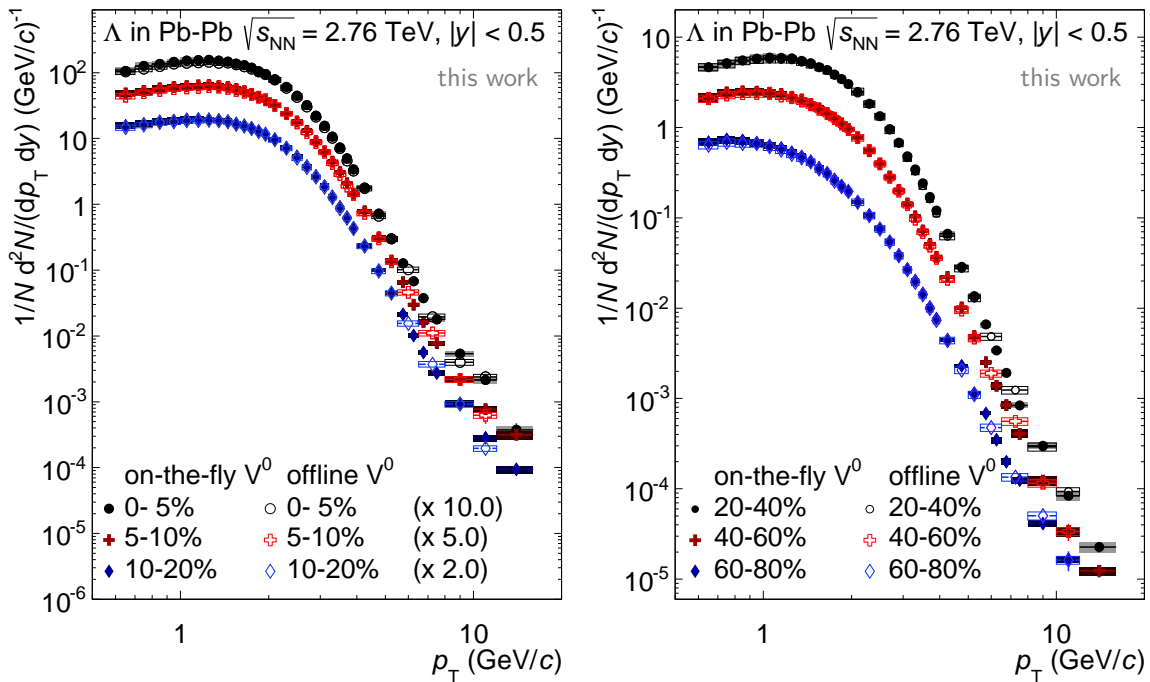
Figure 5.11: Comparison of the published Λ [154] (offline V^0 finder) in Pb–Pb collisions to those from this analysis using the on-the-fly V^0 finder for centralities 0-5%, 5-10%, 10-20% in the left panel and 20-40%, 40-60% and 60-80% in the right panel. The boxes around the data points represent the systematic uncertainties, whereas the error bars indicate the statistical uncertainties.
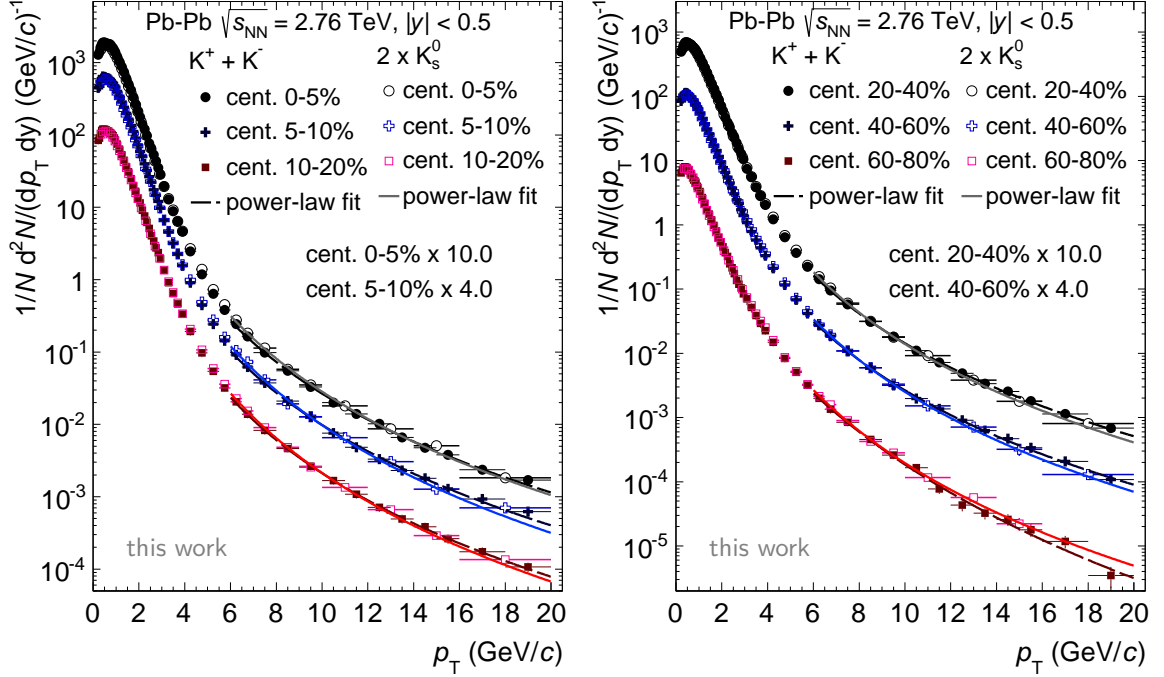
Figure 5.12: Transverse momentum spectra of K_s^0 and charged kaons in Pb–Pb collisions together with power-law fits to the data points for centralities 0 - 5%, 5 - 10%, 10 - 20% in the left panel and 20 - 40%, 40 - 60% and 60 - 80% in the right panel.

5.1.4 Comparison of K_s^0 to $K^{+,-}$

Pb–Pb collisions

Furthermore, the K_s^0 were compared to the charged kaons [159, 160] in Pb–Pb collisions. The spectra are consistent within the systematic uncertainties, which can be seen in figures 5.12 and 5.13. Although the spectra are in good agreement, small discrepancies of the order of 5% are observed at low p_T in all centrality classes as well as 10% for the highest p_T bins for the centrality classes 20 - 60%, which are however all covered by the uncertainties. Figure 5.14 shows the ratio of the power-law fits from figure 5.12 for K_s^0 as well as for the charged kaons for $p_T > 7\,\text{GeV}/c$ to the data. Above this p_T value, the data are all well described by the power-law. The fit results for K_s^0 are compared to those for the charged kaons, which can be seen in figure 5.15. This comparison reveals a common trend for all centralities except the most peripheral events: the slope of the charged kaon power-law is different to that of the K_s^0, resulting in a maximum difference of $\sim \pm\,10\%$. In peripheral Pb–Pb collisions, the larger disagreement at high p_T of the power-law fits is caused by the last two high p_T yields of the charged kaons, which pull the fit to lower values as compared to the K_s^0, since the latter has no entries in this p_T region.
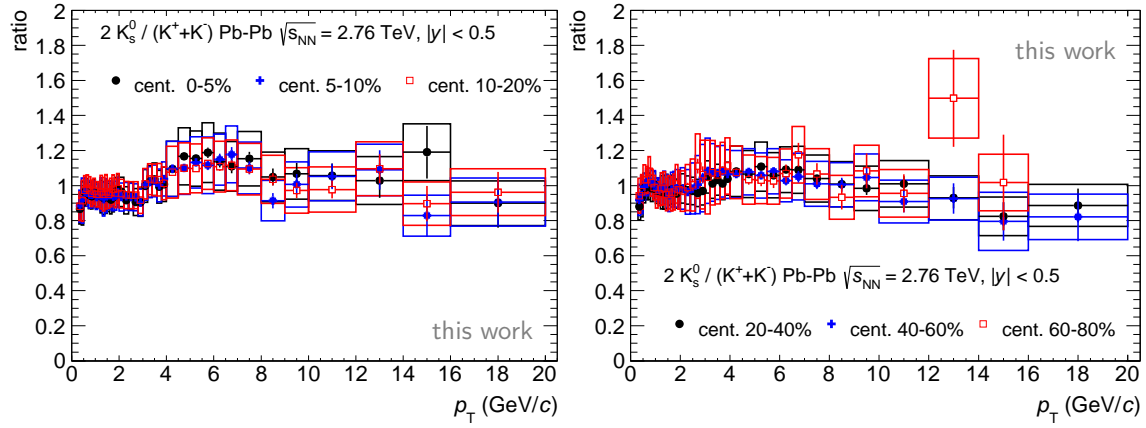
Figure 5.13: Ratio of K_s^0 to charged kaons for centralities 0 - 5%, 5 - 10%, 10 - 20% in the left panel and 20 - 40%, 40 - 60% and 60 - 80% in the right panel.
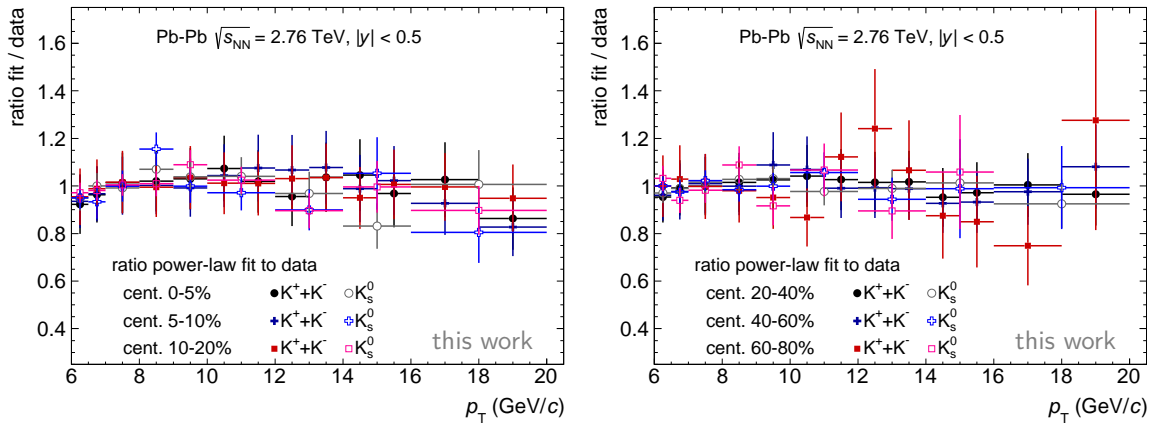
Figure 5.14: Ratio of the power-law fits to K_s^0 and to charged kaons, respectively, to the data points in Pb–Pb collisions for centralities 0 - 5%, 5 - 10%, 10 - 20% in the left panel and 20 - 40%, 40 - 60% and 60 - 80% in the right panel.
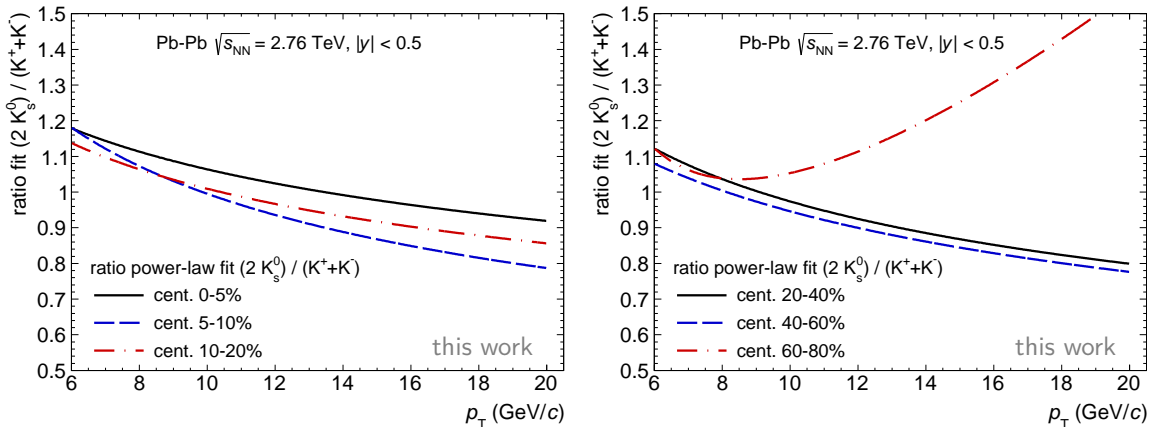
Figure 5.15: Ratio of the power-law fits of K_s^0 to those of charged kaons for centralities 0 - 5%, 5 - 10%, 10 - 20% in the left panel and 20 - 40%, 40 - 60% and 60 - 80% in the right panel.
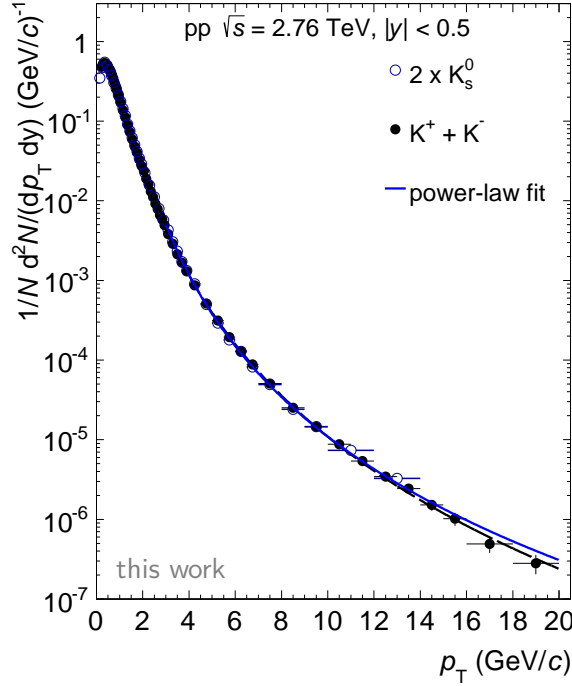
Figure 5.16: K_s^0 transverse momentum spectrum in pp collisions at $\sqrt{s}$ = 2.76 TeV together with the charged kaon results [159]. In addition, power-law fits to the spectra are shown.

pp collisions at $\sqrt{s}$ = 2.76 TeV

In pp, the K_s^0 spectrum is also in good agreement with charged kaon analysis [159], which is shown in figures 5.16 and 5.17. The value of the last p_T bin of K_s^0 at p_T = 16 - 20 GeV/c, that is a result of the extrapolation with a power-law, is however not compatible with the charged kaon yield. Figure 5.16 presents both spectra together with a power-law fit. Since the K_s^0 tend to show increasingly larger values at high p_T than the charged kaons, the exponent of the power-law is consequently smaller, resulting in larger value for the extrapolated yield. In the left panel of figure 5.18 the ratio of the fit to the data is shown. The individual fits describe the spectra well. The right panel of this figure contains the ratio of the power-law fit to the K_s^0 spectrum to that of the charged kaons, where the tension at the highest p_T bin becomes visible.

At low p_T, the systematic pattern is a result of the three different analyses contributing to the spectrum up to 3 GeV/c, employing the TPC, TOF and HMPID, respectively.
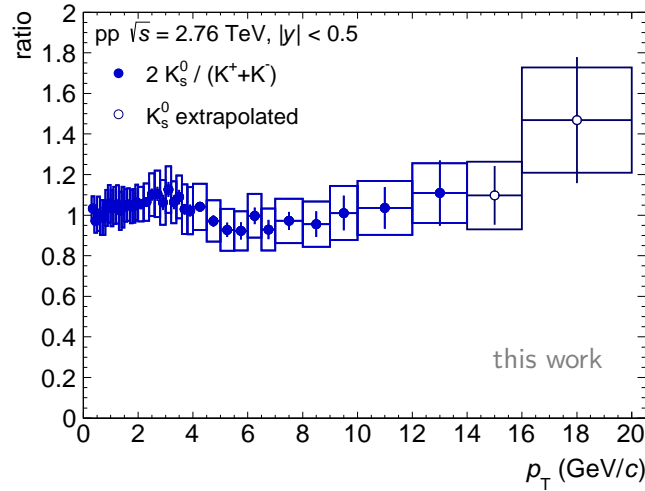
Figure 5.17: Ratio of K^0_s to the charged kaon results [159] in pp collisions at $\sqrt{s} = 2.76\,\mathrm{TeV}$.
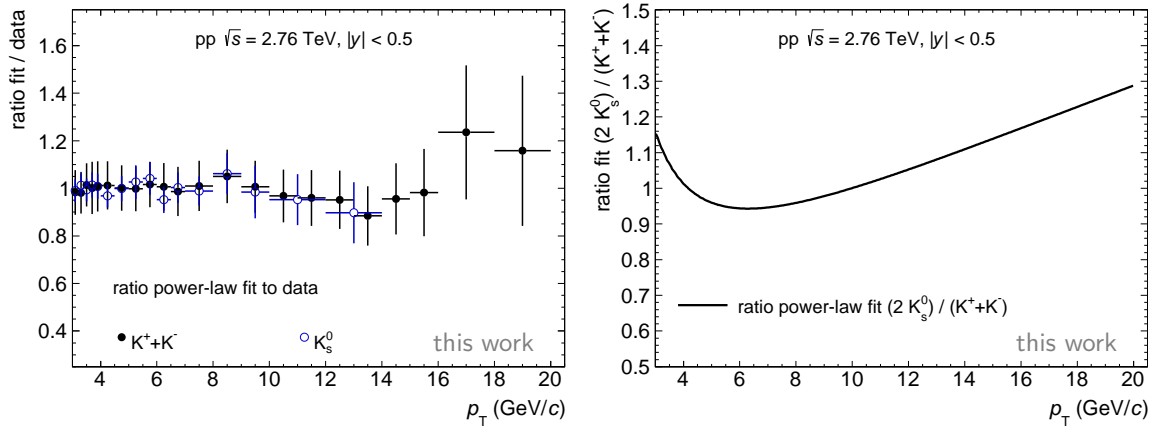
Figure 5.18: Left: Ratio of the fits from figure 5.16 to K^0_s as well as to the charged kaon [159] p_T spectra in pp at $\sqrt{s} = 2.76\,\mathrm{TeV}$ to the data. Right: Ratio of the power-law fits of K^0_s to that of the charged kaon p_T spectra.

5.1.5 Rapidity density extraction

The yield per unit rapidity $(\mathrm{d}N/\mathrm{d}y)$, i.e the rapidity density, is estimated by the integration over the p_T spectrum. Since the measurement is usually limited to finite values of p_T, an extrapolation of p_T spectra to $p_T = 0$ under the assumption of a functional form is performed. As mentioned in section 2.2, the functions commonly used for this purpose are the Blast-Wave (eq. 2.22) and the Tsallis-Pareto (eq. 4.10) function, respectively. The following figures show fits of these functions to the K^0_s and $\Lambda(\overline{\Lambda})$ p_T spectra. In case of Pb–Pb, in figures 5.19, 5.20, 5.21, mainly Blast-Wave fits were performed up to $p_T = 2.5\,\mathrm{GeV}/c$ (K^0_s) and $p_T = 3.0\,\mathrm{GeV}/c$ (Λ), respectively, since they are best described by this function. On the other hand, the Tsallis-Pareto function was used to determine the systematic uncertainty on the extrapolation. However, this function is only able to describe the spectra in fit range half as large as compared to the Blast-Wave fit. In figure 5.22, the fits for pp collisions are presented, where
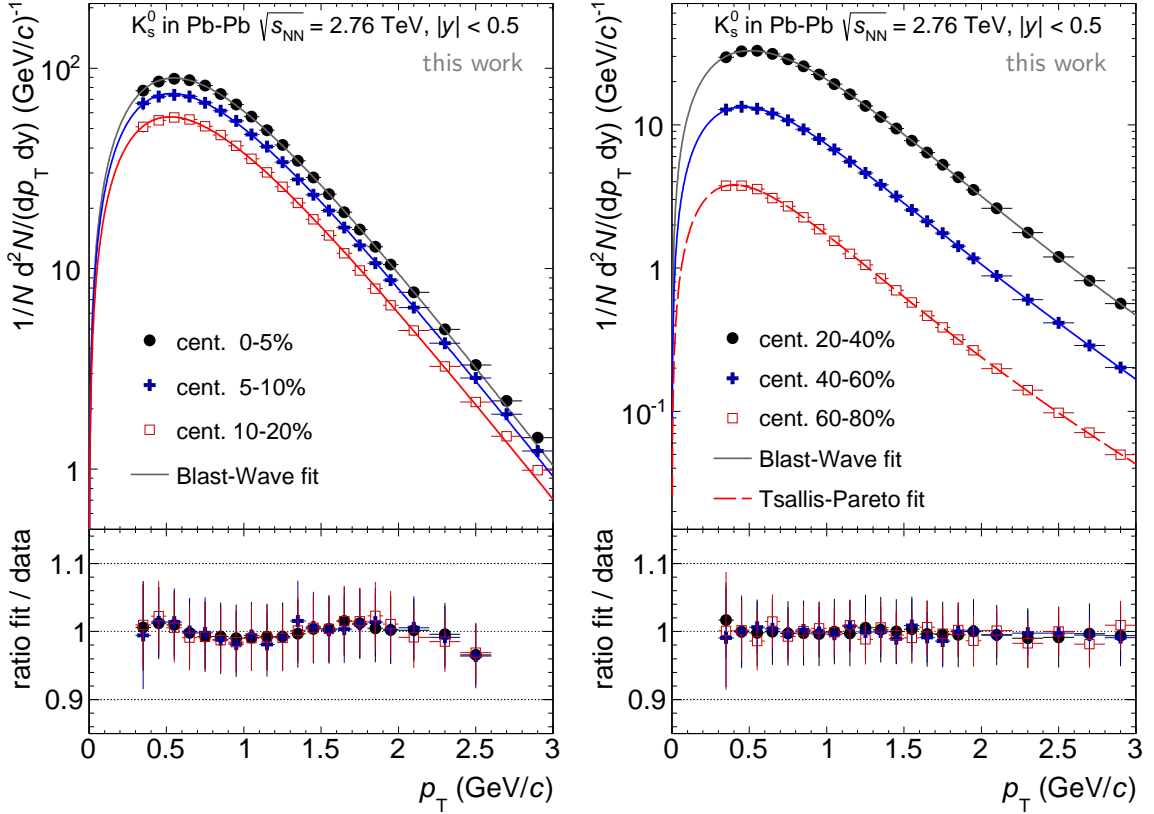
Figure 5.19: Fit to K_s^0 in Pb–Pb collisions at $\sqrt{s_{NN}}$ = 2.76 TeV. The error bars indicate the quadratic sum of the statistical and systematic uncertainties. The lower panels show the ratio of the fit to the data.

the Tsallis-Pareto function was used to extract the rapidity density. In case of pp collisions and of K_s^0 in peripheral events the quality of the Blast-Wave fit is worse than that of the Tsallis function, therefore the latter was chosen for the extraction of dN/dy. The difference to the result obtained with the Blast-Wave fit though enters in the systematic uncertainty estimation.

The resulting rapidity densities of K_s^0 and $\Lambda(\overline{\Lambda})$ are shown in figure 5.23 as a function of the average number of participants. The systematic uncertainties (boxes) include the difference to the results using the Tsallis-Pareto (Blast-Wave for pp and K_s^0 in 60-80%) parametrisation, the maximum error obtained from shifting the spectra to the upper and lower edge of the error bars (quadratic sum) as well as the uncertainty of the centrality or N_{part} determination. Table 5.2 summarises the extracted yields. A linear trend with N_{part} at $N_{\mathrm{part}} > 100$ is observed for both particles, which is also seen for charged particles [30]. The yield of Λ and $\overline{\Lambda}$ is compatible within errors and the yield of K_s^0 is about 3.5 times larger than that of Λ in all centrality classes, which is displayed in figure 5.24. Additionally, this figure contains an estimate of the yield ratio in central collisions obtained from a SHM fit to several hadrons measured by ALICE [123], where a chemical freeze-out temperature of $T_{\mathrm{ch}} = 156\,\mathrm{MeV}$ was obtained. Within the systematics, the SHM estimate agrees with the measurement.

The p_{T}-integrated particle rapidity densities can be further investigated by comparing the yields in Pb–Pb collisions to those in pp in order to study a possible (canonical) suppression in pp as well as the normalised centrality dependence to other beam
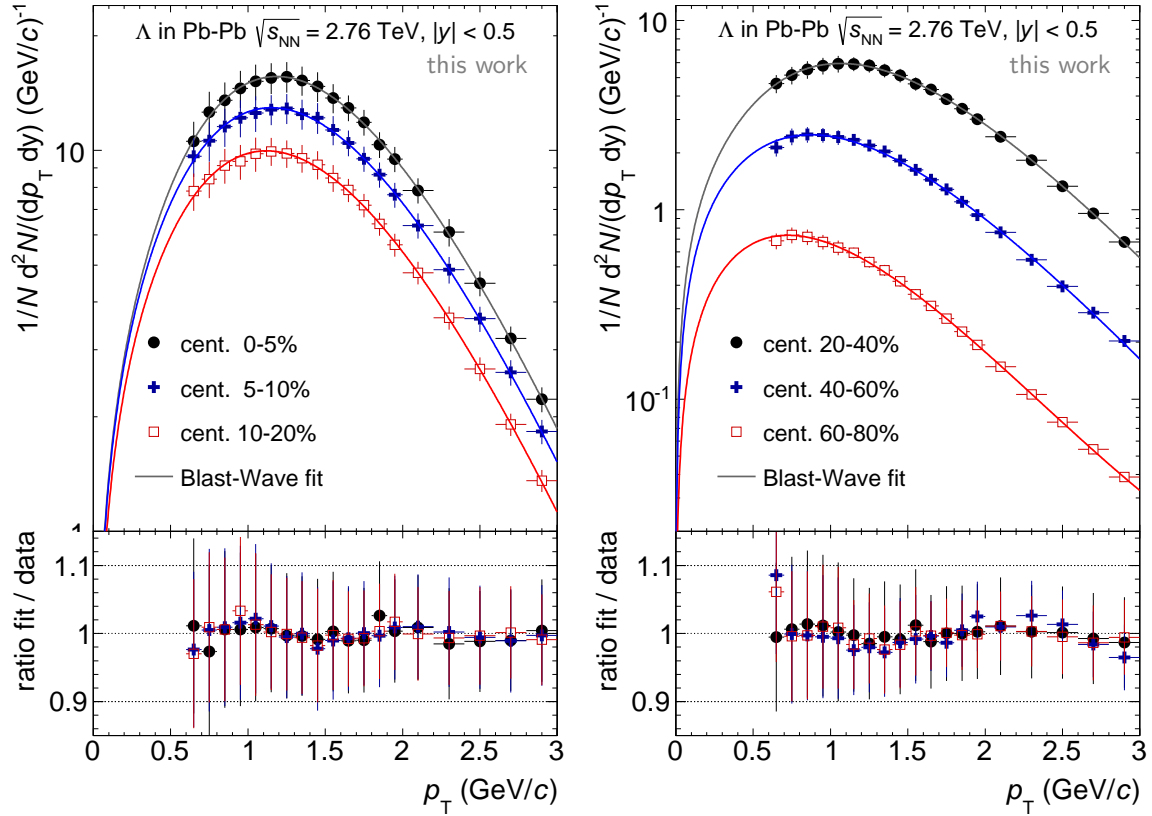
Figure 5.20: Blast-Wave fit to Λ in Pb–Pb collisions at $\sqrt{s_{NN}} = 2.76\,\text{TeV}$. The error bars indicate the quadratic sum of the statistical and systematic uncertainties. The lower panels show the ratio of the fit to the data.

energies and particle species. While the latter are shown and discussed in the last chapter, the ratio to pp collisions for K_s^0 and $\Lambda(\overline{\Lambda})$ can already be found here in figure 5.25. The K_s^0 as well as the $\Lambda(\overline{\Lambda})$ abundances in pp are suppressed by the same amount, i.e. by about a factor two (1.5) as compared to central (peripheral) collisions.

Moreover, the integration of the p_T spectra allow also the calculation of the mean transverse momentum $\langle p_T \rangle$, which serves as a variable to further characterize the soft part of the spectra. Figure 5.26 presents $\langle p_T \rangle$ of K_s^0 and $\Lambda(\overline{\Lambda})$ as a function of $dN_{ch}/d\eta$. As expected from the different particle masses, $\langle p_T \rangle$ of the heavier $\Lambda(\overline{\Lambda})$ is larger than that of the lighter K_s^0. While in central events it exceeds the K_s^0 value by nearly a factor two, which is driven by the twice larger mass of Λ, the difference decreases with decreasing centrality, approaching a factor 1.3 in pp collisions. In comparison with the protons, the mean transverse momentum of Λ is slightly larger (8%) in Pb–Pb collisions as expected from the mass difference. However, in pp this difference seems to vanish. In case of K_s^0, $\langle p_T \rangle$ exceeds the values for pions by nearly a constant factor or 1.6 at all $dN_{ch}/d\eta$.
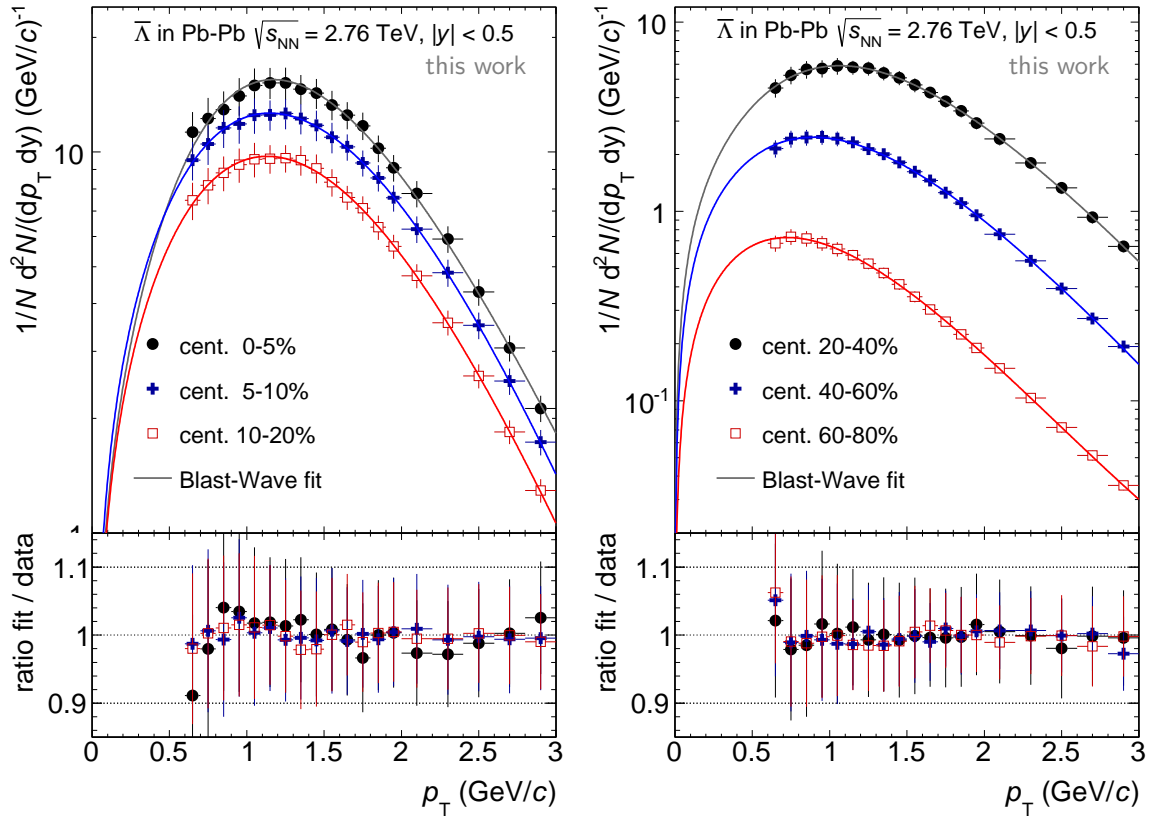
Figure 5.21: Fit to $\overline{\Lambda}$ in Pb–Pb collisions at $\sqrt{s_{\mathrm{NN}}} = 2.76\,\mathrm{TeV}$. The error bars indicate the quadratic sum of the statistical and systematic uncertainties. The lower panels show the ratio of the fit to the data.
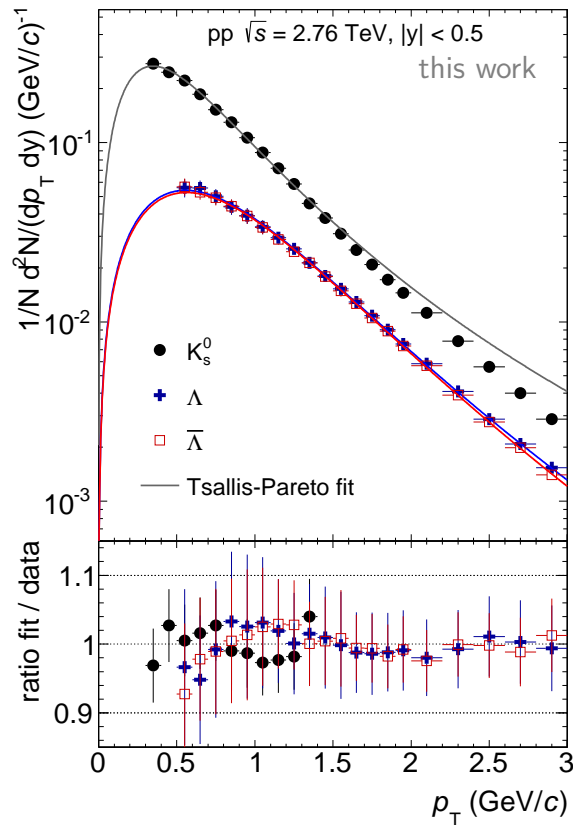
Figure 5.22: Tsallis-Pareto fit to K_s^0 and $\Lambda(\overline{\Lambda})$ in pp collisions at $\sqrt{s} = 2.76\,\text{TeV}$. The error bars indicate the quadratic sum of the statistical and systematic uncertainties. The lower panel shows the ratio of the fit to the data.
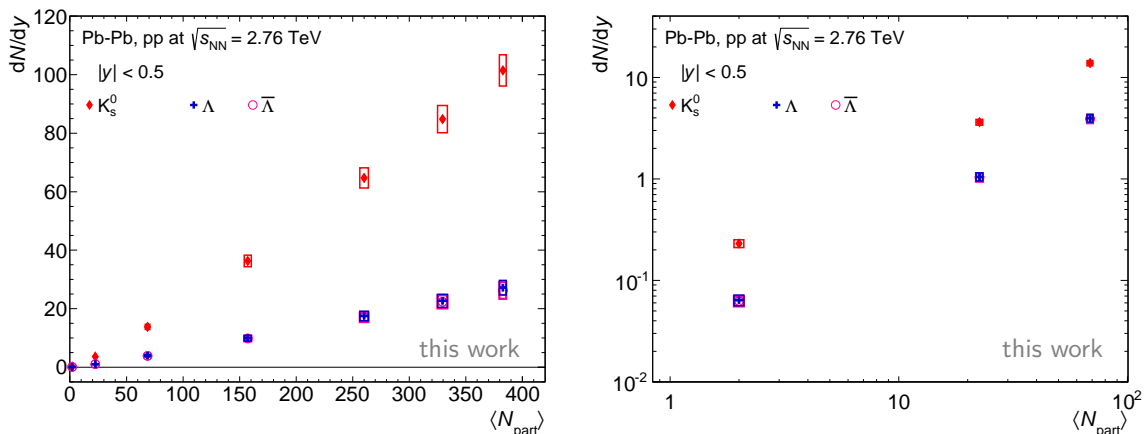
Figure 5.23: Left: Rapidity density ($\mathrm{d}N/\mathrm{d}y$) of K_s^0 and $\Lambda(\overline{\Lambda})$ in Pb–Pb collisions at $\sqrt{s_{\mathrm{NN}}} = 2.76\,\text{TeV}$ and in pp collisions at the same energy as a function of the mean number of participants $\langle N_{\mathrm{part}} \rangle$. Right: logarithmic scale of the low $\langle N_{\mathrm{part}} \rangle$ region. The boxes around the data points indicate the systematic uncertainties of the yield.

collision class	K$_s^0$			Λ			$\overline{\Lambda}$		
Pb–Pb cent.	dN/dy	$\pm$	$\pm$	dN/dy	$\pm$	$\pm$	dN/dy	$\pm$	$\pm$
0 - 5%	101.514	0.082	5.339	27.143	0.030	2.491	26.225	0.027	2.821
5 - 10%	84.835	0.080	4.664	22.701	0.026	2.268	22.322	0.024	2.256
10 - 20%	64.699	0.043	3.428	17.491	0.015	1.640	17.041	0.018	1.621
20 - 40%	36.323	0.021	1.982	9.910	0.007	0.951	9.800	0.007	0.970
40 - 60%	13.807	0.013	0.839	3.970	0.005	0.359	3.906	0.005	0.363
60 - 80%	3.621	0.007	0.237	1.047	0.002	0.097	1.037	0.002	0.098
pp	0.2305	0.0008	0.0209	0.0639	0.0002	0.0077	0.0624	0.0002	0.0071

Table 5.2: Rapidity density (dN/dy) at mid-rapidity in Pb–Pb and pp collisions at $\sqrt{s_{\mathrm{NN}}} = 2.76\,\mathrm{TeV}$. The first error represents the statistical uncertainty, the second the systematic uncertainty.
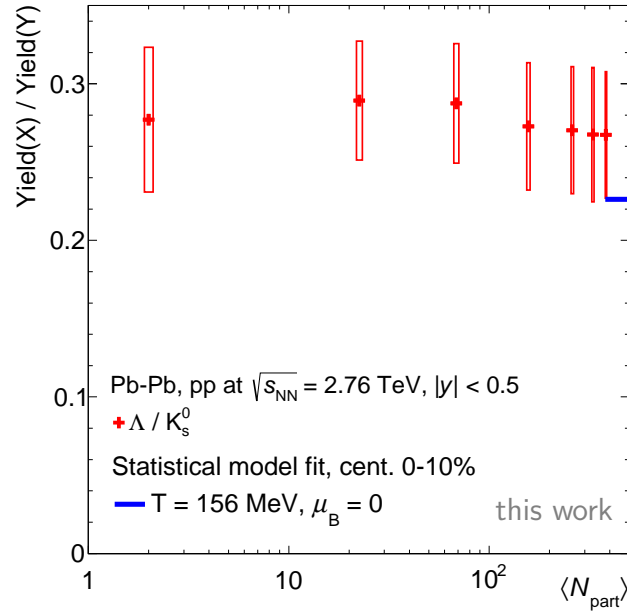
Figure 5.24: Ratio of Λ to K_s^0 rapidity density (dN/dy) in Pb–Pb collisions at $\sqrt{s_{\mathrm{NN}}} = 2.76\,\mathrm{TeV}$ and in pp collisions at the same energy as a function of the mean number of participants $\langle N_{\mathrm{part}}\rangle$. The boxes around the data points indicate the systematic uncertainties. The width of the boxes does not represent the uncertainty of $\langle N_{\mathrm{part}}\rangle$. The horizontal line show the results from a statistical model fit, where $T_{\mathrm{ch}} = 156\,\mathrm{MeV}$ [123].
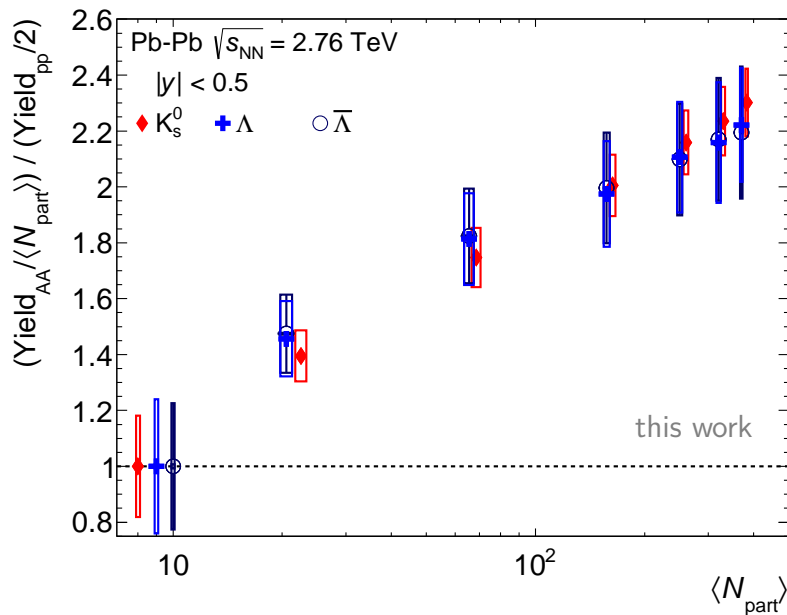
Figure 5.25: Rapidity density (dN/dy) of K_s^0 and $\Lambda(\overline{\Lambda})$ in Pb–Pb collisions at $\sqrt{s_{\mathrm{NN}}} = 2.76\,\mathrm{TeV}$ scaled to the yield in pp collisions at the same energy as a function of the mean number of participants $\langle N_{\mathrm{part}}\rangle$. The boxes around the data points indicate the systematic uncertainties. In case of Λ and $\overline{\Lambda}$, the values were shifted to the left in x-direction for better visibility.
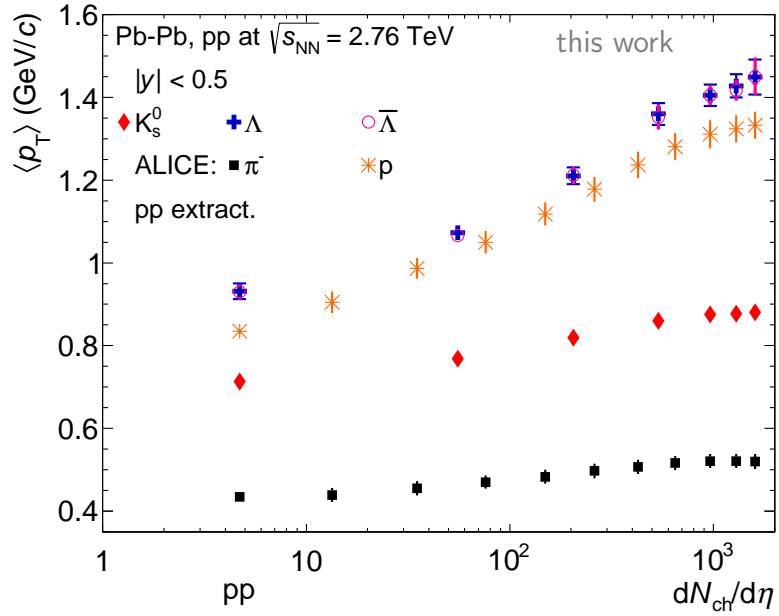
Figure 5.26: Mean transverse momentum ($\langle p_T \rangle$) of K_s^0 and Λ in Pb–Pb and pp collisions at $\sqrt{s_{NN}} = 2.76$ TeV as a function $dN_{ch}/d\eta$. The results for particles measured by ALICE in Pb–Pb were published in [107, 108] and the values for pp were extracted from [159]. The $dN_{ch}/d\eta$ values were taken from [30]. The error bars indicate the quadratic sum of the statistical and systematic uncertainties.
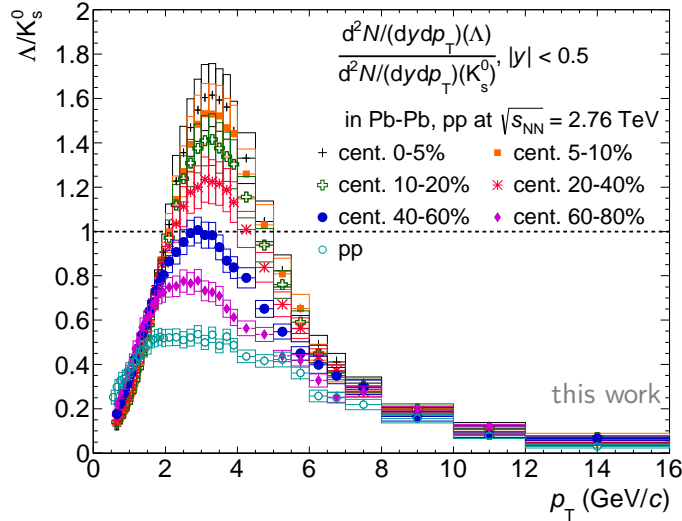
Figure 5.27: Ratio of Λ to K^0_s p_T spectra in Pb–Pb and pp collisions at $\sqrt{s} = 2.76\,\text{TeV}$.

5.2 Low-to-intermediate p_T: Baryon-to-meson ratio

In figure 5.27 the ratios of Λ to K^0_s in pp collisions as well as for all analysed centrality bins in Pb–Pb collisions is presented. At intermediate p_T (2 - 5 GeV/c), a clear enhancement of Λ to K^0_s is visible for central to mid-central collisions. This enhancement decreases the more peripheral the collisions are, until it vanishes for peripheral and pp collisions. Above $p_T = 8\,\text{GeV}/c$, all ratios exhibit the same values. This observation is similar to the baryon-to-meson enhancement in central collisions reported by RHIC experiments and by the ALICE collaboration for protons and pions.

A detailed discussion of the observed p_T spectra as well as the rapidity densities and their possible physics implications will follow in chapter 6.

5.3 High p_T: Nuclear modification factor R_{AA} of K^0_s and $\Lambda(\overline{\Lambda})$

Finally, the nuclear modification factor R_{AA} of K^0_s and Λ as a function of p_T is shown in figure 5.28. The results are presented together with the R_{AA} of charged particles [47]. The left panel shows R_{AA} for central and the right panel for peripheral collisions, respectively. The suppression of K^0_s is very similar to that of charged particles for the whole p_T range, in peripheral as well as in central collisions. In contrast, the suppression of Λ is smaller at lower p_T as it can be expected from the Λ/K^0_s ratio, where the ratio in central collisions exceeds that in pp collisions. In particular, only little nuclear modification, $R_{AA} \approx 0.9$, is observed for $p_T = 2$ - 5 GeV/c in both centrality classes. On the other hand, at high p_T, the suppression is as strong as that observed for K^0_s and thus similar to that of charged particles. The R_{AA} of K^0_s in peripheral events (right panel of figure 5.28) indicates a rather moderate but significant suppression of $R_{AA} \approx 0.6$ with almost no p_T dependence. Thus the R_{CP}, the ratio of p_T spectra in central to peripheral collisions normalised to N_{coll}, exhibits a similar pattern than that of R_{AA} for central events. The corresponding figures can be found in appendix C.2.

In figure 5.29 the R_{AA} for K^0_s and Λ are shown separately for all centralities. The low
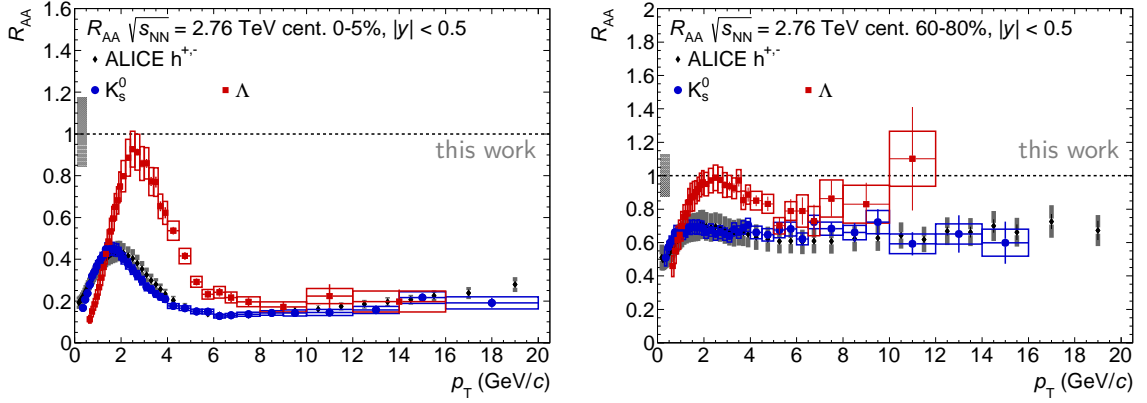
Figure 5.28: The nuclear modification factor R_{AA} of K_s^0 and Λ for central (0 – 5%, left panel) and for peripheral (60 – 80%, right panel) Pb–Pb collisions at $\sqrt{s_{NN}}$ = 2.76 TeV. In both panels the charged hadron R_{AA} measured by ALICE [47] is shown for comparison. The hollow and filled boxes around the data points indicate the systematic error. The uncertainties from the N_{coll} scaling and from the normalization in pp are indicated by the black box at unity.
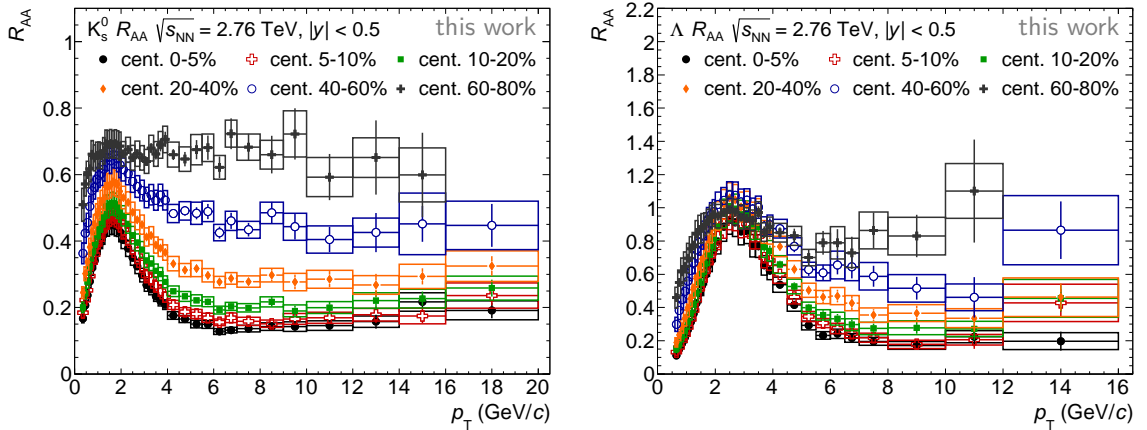
Figure 5.29: The nuclear modification factor R_{AA} of K_s^0 (left) and Λ (right) for all centralities in Pb–Pb collisions at $\sqrt{s_{NN}}$ = 2.76 TeV. The boxes around the data points indicate the systematic error.

p_T region shows a stronger decrease of the modification with centrality for K_s^0 than it is the case for the Λ. This behaviour is also already reflected in the Λ/K_s^0 ratio. The local minimum of R_{AA} around $p_T = 6$ - $8\,\text{GeV}/c$ observed for K_s^0 and the charged particles weakens with decreasing centrality. This is in agreement with the assumption of a vanishing radial flow with the collision impact parameter as mentioned in section 2.2.

Finally, the $\overline{\Lambda}$ R_{AA} is compared to that of Λ for all centralities, which is displayed in figure 5.30. Within the uncertainties, no differences are observed. However, the agreement is better at lower p_T than at the highest p_T.

Comparison to the preliminary results at Quark Matter 2011

The R_{AA} of K_s^0 and Λ is also compared to results of a preliminary analysis performed at the beginning of this thesis work, which were presented at the Quark Matter 2011
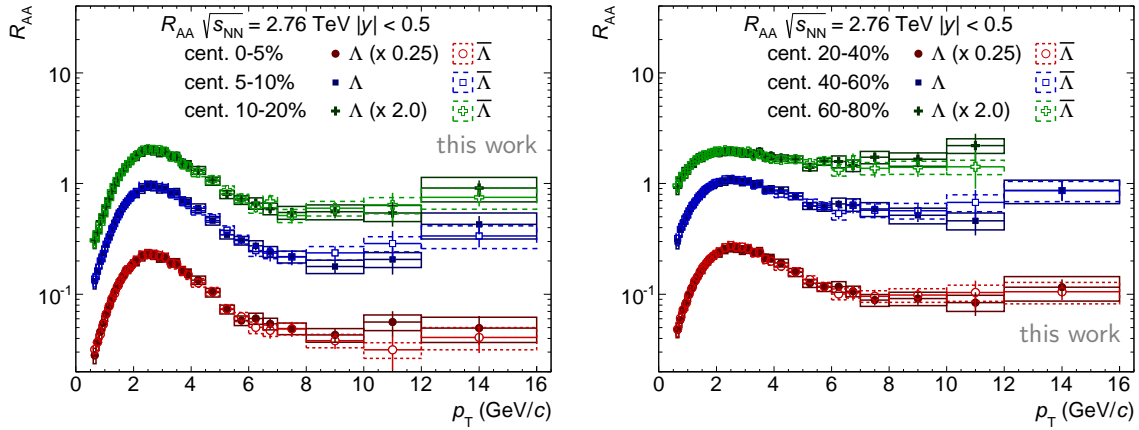
Figure 5.30: The nuclear modification factor R_{AA} of Λ and $\overline{\Lambda}$ (right) for all centralities in Pb–Pb collisions at $\sqrt{s_{NN}}$ = 2.76 TeV. The boxes around the data points indicate the systematic error.
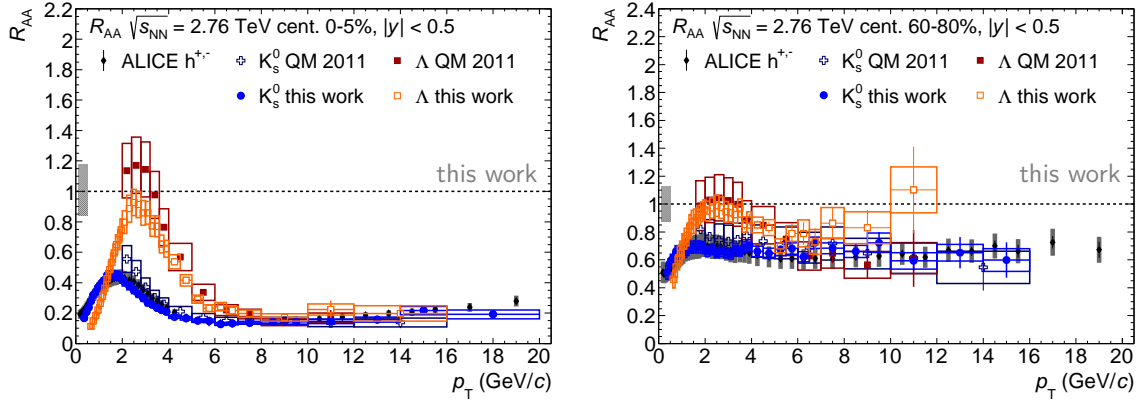
Figure 5.31: The nuclear modification factor R_{AA} of K_s^0 and Λ together with the results shown at Quark Matter (QM 2011) for central ($0-5\%$, left panel) and for peripheral ($60-80\%$, right panel) Pb–Pb collisions at $\sqrt{s_{NN}}$ = 2.76 TeV. The boxes around the data points indicate the systematic error. In both panels the charged hadron R_{AA} measured by ALICE [47] is shown for comparison. The uncertainty from the N_{coll} scaling and from the normalization in pp are indicated by the black box at unity.

conference [166], see figure 5.31. At high p_T ($p_T > 7\,\mathrm{GeV}/c$), the results from the present analysis agrees with those from the QM analysis for both Λ and K_s^0 within the statistical and systematic uncertainties. At lower p_T, the agreement is also very good in peripheral collisions. In central collisions, however, the present results are above the QM results for both Λ and K_s^0. The discrepancy is at the limit of the systematic errors. The main difference between the present and QM analysis is the treatment of the feed-down correction for Λ and the consistent usage of the data sets wSDD and nSDD in pp collisions (see section 4.5).

6

Discussion

6.1 Review of the results

This last chapter reviews the results with particular emphasis on relevant aspects in the high and low p_{T} region, respectively. Besides the comparison of the results to other particle species at the same collision energy, the energy dependence of some extracted quantities is discussed.

6.1.1 High p_{T}: Comparison of $\mathrm{K}^0_{\mathrm{s}}$ and Λ R_{AA} to other particle species

The observation of a compatible suppression of strange and non-strange hadrons at high p_{T}, as presented in the previous chapter, can be interpreted as an indication that the relevant mechanisms do not depend on the quark flavour. Figure 6.1 presents a compilation of ALICE R_{AA} results together with the results of this work for $\mathrm{K}^0_{\mathrm{s}}$ and Λ in central events (peripheral in figure C.10). This compilation and further figures in appendix C.2, were the R_{AA} for baryons (p, Λ, $\Xi^{+,-}$, $\Omega^{+,-}$) and mesons ($\pi^{+,-}$, $\mathrm{K}^0_{\mathrm{s}}$, $\mathrm{K}^{+,-}$), respectively, can be found for all centralities, underlines the flavour independence with respect to u-, d- and s-quarks. A similar modification was however also obtained for D mesons containing a c-quark. Since the c-quark is considered as a "heavy" quark due to $m_{\mathrm{c}} \gg \Lambda_{\mathrm{QCD}}$, the common modification pattern at high p_{T} seems not to be solely a feature of light-quark hadrons. Regarding the key questions raised at the beginning of this document, it has to be clarified whether this similarity in the suppression of the participles containing light- and c-quarks is caused by the same partonic energy loss and/or by the same modified fragmentation. According to [167], the observation of $R_{\mathrm{AA}}(\mathrm{light}) \approx R_{\mathrm{AA}}(\mathrm{D})$ is a "a consequence of a specific combination of the suppression and fragmentation patterns for light partons, and it does not require invoking an assumption of the same energy loss for light partons." This aspect is further discussed in the following section.

The results from the CMS collaboration for the non-prompt J/ψ R_{AA}, mainly revealing the B meson modification, however, show a smaller modification as compared to the average D meson R_{AA}. Figure 6.2 contains the integrated R_{AA} of both particles for a given high-p_{T} range versus centrality. Thus, finally, a flavour-dependent energy loss is observed, though only in the heavy-quark sector, following

$$R_{\mathrm{AA}}(\mathrm{light}) \approx R_{\mathrm{AA}}(\mathrm{D}) < R_{\mathrm{AA}}(\mathrm{B}) \quad \Rightarrow \quad \Delta E(\mathrm{u,d,s,c}) > \Delta E(\mathrm{b}). \quad (6.1)$$
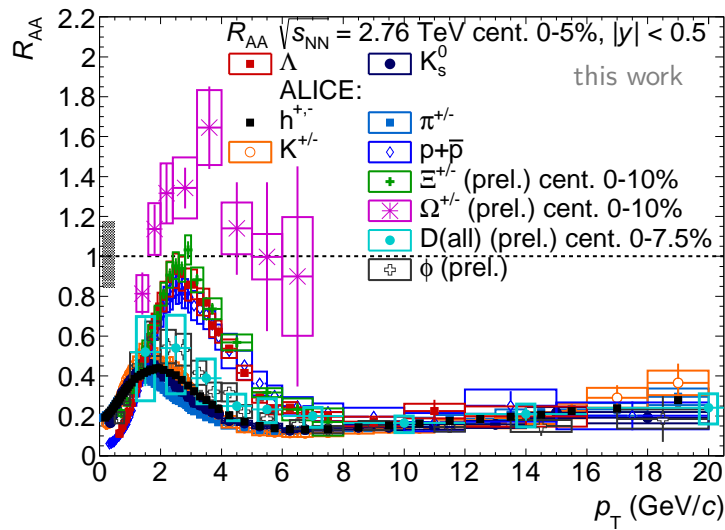
Figure 6.1: The nuclear modification factor R_{AA} of K_s^0 and Λ together with that of other hadrons measured by ALICE [47, 158, 159, 168, 169] in central $(0 - 5\%)$ Pb–Pb collisions at $\sqrt{s_{NN}} = 2.76$ TeV. The boxes around the data points represent the systematic uncertainties. The uncertainty from N_{coll} and from the normalization in pp are indicated by the grey box at unity.

The current errors, also in the presented CMS data, are still quite large and a more precise and differential measurement is needed to disentangle details of the underlying suppression mechanisms.

6.1.2 High p_T: Model calculations

While the bulk medium is successfully described by viscous hydrodynamics, transport models offer to study the low- as well as the high-p_T regions on a microscopic level [173, 174]. The R_{AA} results for K_s^0 and $\Lambda(\overline{\Lambda})$ of this work are also compared with model calculations of BAMPS, a 3+1 dimensional transport model using the Boltzmann Approach to Multi-Parton Scatterings [175], where the Boltzmann transport equations are solved numerically. Allowed collisions between the partons are $2 \rightarrow 2$ (elastic, collisional) and $2 \leftrightarrow 3$ (inelastic, radiative) processes, which are embedded in an expanding medium. The scattering cross sections are obtained from pQCD. As input for the partonic momentum spectra the distributions from PYTHIA are used, which are folded with the AKK fragmentation functions. In order to account for radiative processes, the LPM effect with a cut-off is included. The LPM cut-off imposes a constraint on the formation time of the emitted gluon that "allows only processes, where the emitted gluon is already formed before the next scattering takes place, thus, forbids all possible interfering processes"[176].

In figure 6.3, several ALICE light-quark hadron R_{AA} are shown together with the corresponding calculations from BAMPS. The measurements are well reproduced by the model for all species. Among the BAMPS results a vanishing difference between the various particles is observed, which is much smaller than the present experimental uncertainties. Moreover, no systematic uncertainties are given for the model calcu-
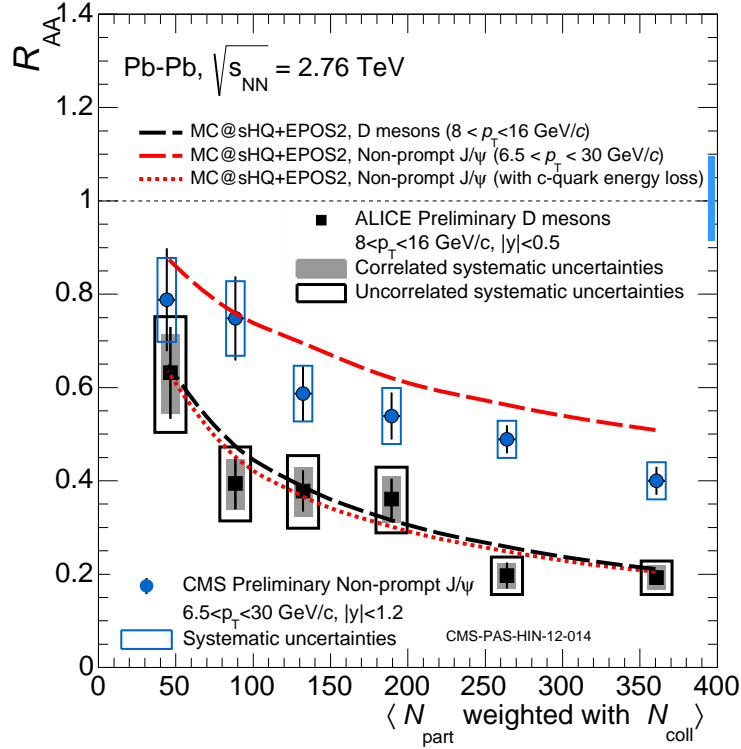
Figure 6.2: Average D meson R_{AA} versus mean N_{part} weighted with N_{coll} measured by ALICE [170]. The horizontal black error bars are the statistical uncertainties, the empty boxes the total uncorrelated systematic uncertainties and the filled boxes the correlated systematic uncertainties. The non-prompt J/ψ R_{AA} measured by CMS is shown in addition [171]. The empty boxes show the total systematic uncertainties. The normalization uncertainty plotted at unity. The lines show the calculations with the MC@sHQ + EPOS2 model [172].

lations. Thus, a common modification of the compared hadrons is observed in the measurements and from BAMPS calculations.

In order to discuss the implications of this finding, some details about the calculation of the momentum spectra are given in the following. The main equation yielding the final hadron spectra,

$$\frac{\mathrm{d}N_h^2}{\mathrm{d}p_T^h \mathrm{d}y}\left(p_T^h\right) = \sum_i \int_{z_{min}}^1 \mathrm{d}z \, \frac{\mathrm{d}N_i^2}{\mathrm{d}p_T^i \mathrm{d}y}\left(\frac{p_T^h}{z}\right) D_i^h\left(z, Q^2\right), \qquad (6.2)$$

with $z = p_T^h/p_T^i$, includes $D_i^h\left(z, Q^2\right)$, the fragmentation function for parton i fragmenting into hadron h from AKK. In this equation, no energy loss term is visible since the energy loss enters via the parton spectrum, which is modified within the BAMPS framework. Therein, u-, d- and s-quarks are classified as light quarks suffering the same energy loss. The predominant quark fragmentation contributions to the light-quark hadron formation stem from light quarks. Hence, a difference in R_{AA} for light-quark particles could only arise from the different fragmentation functions. The fragmentation process itself is not modified within BAMPS. To conclude, the BAMPS results show that the assumption of the same energy loss for u-, d- and s-quarks in combination with unmodified fragmentation functions seems to describe the meas-
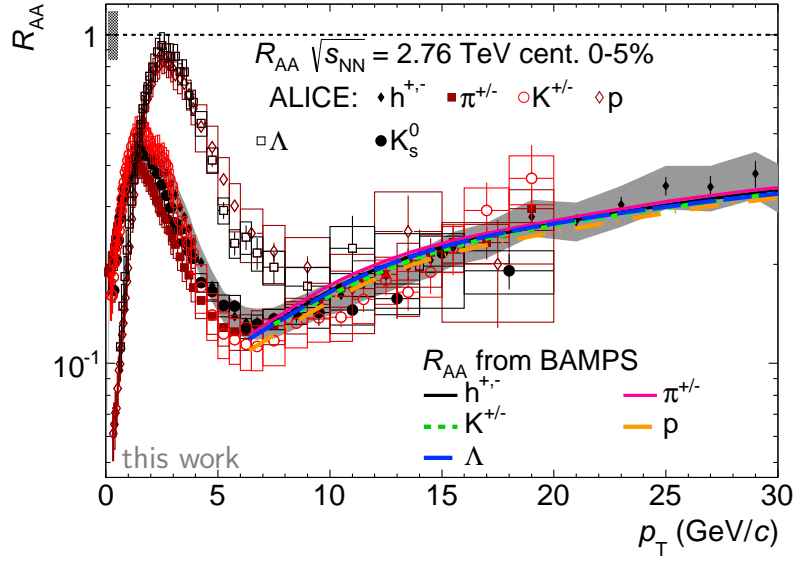
Figure 6.3: ALICE R_{AA} for different hadrons together with the results of this work for K_s^0, Λ and the corresponding model calculations with BAMPS [173, 174]. The grey band shows the systematic uncertainties of the measured charged hadron R_{AA}.

urements and that the calculated light-quark energy loss accounts for the observed suppression.

Figure 6.4 shows the probability for a hadron h with p_T^h to stem from a specific parton i with any momentum without ("initial") and after ("final") the energy loss of parton i as calculated with BAMPS employing the AKK fragmentation functions:

$$P^{i \to h}(p_T^h) = \int_{z_{\min}}^{1} \mathrm{d}z \, P^{i \to h}(z, p_T^h), \tag{6.3}$$

with

$$P^{i \to h}(z, p_T^h) = \frac{1}{\frac{\mathrm{d}N_h^2}{\mathrm{d}p_T^h \mathrm{d}y}} \frac{\mathrm{d}N_i^2}{\mathrm{d}p_T^i \mathrm{d}y}\left(\frac{p_T^h}{z}\right) D_i^h\left(z, Q^2\right), \tag{6.4}$$

which is the probability that a hadron h with p_T^h stems from a specific parton i with momentum $p_T^i = p_T^h/z$. In the unmodified case at lower p_T, all hadrons mainly stem from gluon fragmentation. At around $50\,\mathrm{GeV}/c$ however, this is only true for Λ, whereas the mesons, i.e. the kaons and the charged hadrons, are almost equally produced from quark and gluon fragmentation. In case of Λ, this balance is reached at $95\,\mathrm{GeV}/c$. Thus, the baryons (protons see appendix C.3) show a larger gluon fragmentation contribution than the mesons below these p_T. Beyond these thresholds, the quark fragmentation dominates. In the "final" case including the energy loss, the thresholds are shifted towards lower p_T by roughly 25%. The kaons distributions now differ more clearly from the charged hadron ratios. Moreover, the contribution from gluon fragmentation is reduced and the quark contribution enhanced at all p_T by roughly 10 - 15% for all particles. This shows that the fragmentation is indeed modified if the contributions from quark and gluon fragmentation to the hadron yield
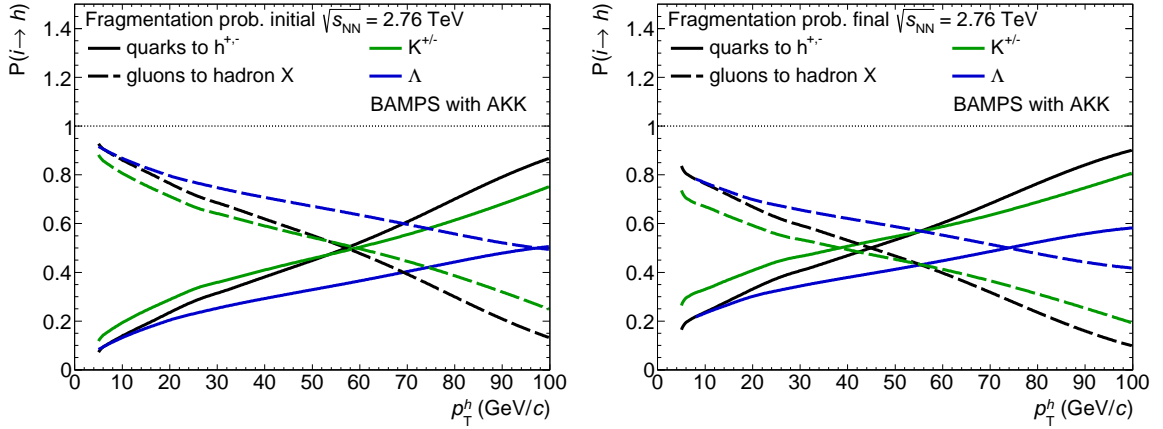
Figure 6.4: Probability, that a hadron with p_T^h stems from a specific parton i with any momentum without ("initial", left panel) and after ("final", right panel) the energy loss of parton i. These values are the basis for the R_{AA} model calculation within the BAMPS framework in [173, 174] employing the AKK fragmentation functions. The solid lines represent the case for quarks fragmenting to hadron X, whereas the dashed lines show the case for gluons [177].

are considered at a given p_T. The fragmentation process itself is however not modified in this framework.

In figure 6.5 the charged hadron R_{AA} at LHC is shown together with the results of BAMPS for charged hadrons, quarks and gluons separately. As mentioned in the introduction, the gluon energy loss in the medium is expected to be larger than that of quarks due to $C_A/C_F = 9/4$, which is clearly visible in this figure. The quark R_{AA} is compatible with the charged hadron R_{AA} above $p_T = 30\,\text{GeV}/c$. Whereas the hadrons at lower p_T are predominantly created by fragmenting gluons, for hadrons at higher p_T, the quark fragmentation contribution rises as discussed above. The main contribution of partons to the hadron yield stems on average from p_T regions 1.5 - 2 as high as the hadron p_T [173]. Therefore, the larger quark R_{AA} value at a higher p_T^q in addition with the lower gluon R_{AA} value at $p_T^g \gtrsim p_T^q$ can thus lead to the charged hadron R_{AA}, which is lower than the quark $R_{AA}(p_T^q)$ but similar as the quark R_{AA} at the hadron p_T. In brief, the p_T dependence of the hadron and the parton R_{AA} should not be directly compared.

Since mainly fragmenting gluons with a higher mean p_T than the quarks contribute to the hadron spectrum, it could be queried, if the energy loss of quarks and gluons was switched, would the R_{AA} of the different hadrons change with respect to the correspondingly charged hadron R_{AA}. A different change for baryons and mesons as well as for strange and non-strange hadrons would reflect the different quark and gluon fragmentation contributions to the hadron spectra, which is different for baryons and mesons as seen above. A simpler version of the question is: Are the light-quark-hadron R_{AA} similar by chance or is the exact combination of quark and gluon energy loss with the corresponding fragmentation functions and parton p_T spectra necessary?

In figure 6.6 the regular charged hadron R_{AA} is shown together with the R_{AA} for the case of switched partonic energy loss. Up to $50\,\text{GeV}/c$, the latter R_{AA} is larger than the regular R_{AA} as expected, since the energy loss of the gluons is now smaller and the gluons mainly contribute to this p_T region. Above this p_T, the situation is accordingly inverted. Figure 6.7 shows in the left panel the ratios of the individual
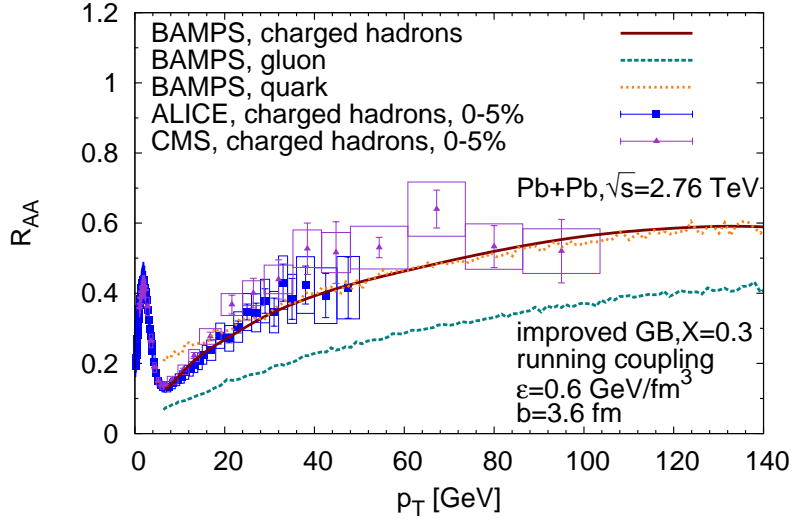
Figure 6.5: R_{AA} of charged hadrons, quarks and gluons from BAMPS for central Pb–Pb collisions at $\sqrt{s_{\mathrm{NN}}} = 2.76$ TeV together with the ALICE and CMS results [173].

hadron R_{AA} to the charged hadron R_{AA} for the standard case. In the right panel, the case for the switched energy loss of quarks and gluons is presented. Considering the Λ first, it seems that the difference to the charged hadron R_{AA} starts to increase stronger as compared to the standard case, reaching a 12% enhancement at $80\,\mathrm{GeV}/c$ as compared to 9% decrease in the standard case. Referring to the mesons, at lower p_{T}, the charged kaon R_{AA} differs by 10%, which is not the case for the regular R_{AA} calculation. This again reflects the fragmentation ratios in figure 6.4, where for the kaons a lower gluon contribution is seen in this momentum region, but which is nearly equal to that of charged hadrons at higher p_{T}. The main observation here is, however, that the spread between the kaon and the Λ distribution is increased over the whole p_{T} range in the "switched" case. Thus it seems that the observed similarity of baryon and meson R_{AA}, in particular for the present case of Λ and $\mathrm{K}_{\mathrm{s}}^{0}$, may at least partially caused by the particular combination of the different energy loss of quarks and gluons (factor 9/4) and their fragmentation into baryons and mesons. This is indicated in the naive case where the QCD colour factors of quarks and gluons are exchanged, which would indeed lead to a notable splitting of Λ and $\mathrm{K}_{\mathrm{s}}^{0}$ R_{AA}. In this sense, the experimental finding that Λ and $\mathrm{K}_{\mathrm{s}}^{0}$ are very similar may be interpreted as an indication that the common pQCD-based energy loss picture is correct. On the other hand, the overall changes caused by the exchanged partonic energy loss are close to the differences of the individual hadron R_{AA} as compared to the charged hadron R_{AA} in the natural case, which are not yet possible to resolve by measurements.

In the following, the energy loss of heavier quarks is discussed and compared to that of light quarks. Figure 6.2 shows calculations with the MC@sHQ+EPOS2 model [66, 172] in addition to the D and non-prompt J/ψ R_{AA}. This model includes collisional as well as radiative energy loss, recombination and a hydrodynamical background based on the EPOS2 model. The observed suppression of both particles is rather well reproduced by the model calculations. If the b-quark energy loss is exchanged with the c-quark energy loss for the non-prompt J/ψ R_{AA} calculation, the resulting suppression
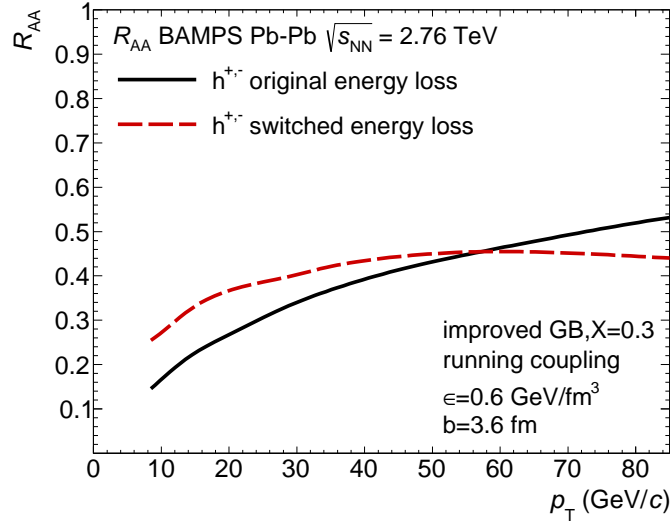
Figure 6.6: R_{AA} of charged hadrons from BAMPS for central Pb–Pb collisions at $\sqrt{s_{NN}} = 2.76$ TeV as in [173] and with a switched energy loss for gluons and quarks [177].
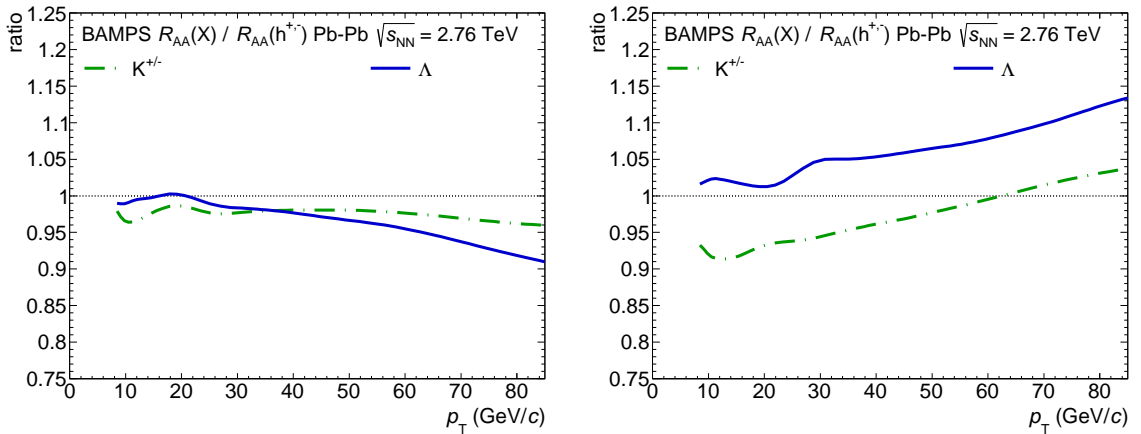
Figure 6.7: Ratio of R_{AA} for K_s^0 and Λ to the charged hadron R_{AA} as calculated with BAMPS [173] (left panel). The right panel shows the similar ratios for the case of switched energy loss for gluons and quarks [177].

resembles that of the prompt J/ψ R_{AA}, showing that mainly the differing energy loss of c- and b-quarks is causing the different modifications. In [176], the D meson and non-prompt J/ψ R_{AA} were also investigated within the BAMPS framework. In the left panel of figure 6.8, the in-medium energy loss per unit path length of light, c- and b-quarks for $2 \rightarrow 2$ (elastic) $2 \rightarrow 3$ (radiative) processes is shown. In each case, the b-quark energy loss is smaller than that of c-quarks. According to the authors, the larger mass of the b-quarks causes a larger dead-cone as compared to that due to the LPM cut-off. As a result, the radiative energy loss is reduced by roughly 40%. Also the collisional energy loss differs by about 0.25 GeV/fm between light, c- and b-quarks, respectively, showing the expected mass ordering.

Both models, the MC@sHQ+EPOS2 as well as BAMPS are able to reproduce the measured heavy-quark modification factors. The two models differ in the basic implementation of the LPM effect, in the assignment of a mass to the emitted gluons in
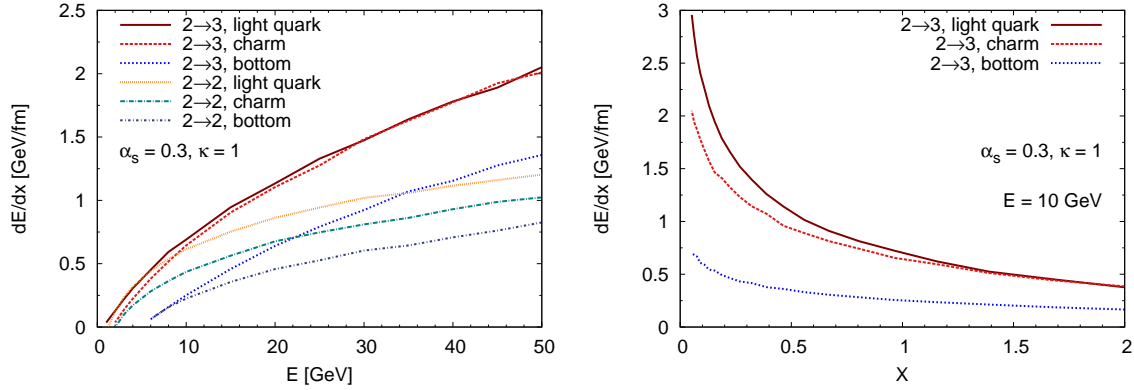
Figure 6.8: Left: Elastic and radiative energy loss per unit length of a light-quark ($M = 0$), a c-quark ($M = 1.3\,\mathrm{GeV}/c$), and a b-quark ($M = 4.6\,\mathrm{GeV}/c$) traversing a static thermal medium with temperature $T = 0.4\,\mathrm{GeV}$. Right: Dependence of the radiative energy loss of light, c-, and b-quarks with $E = 10\,\mathrm{GeV}$ on X_{LPM}, which denotes a prefactor in the LPM cut-off. Figures and captions from [176].

radiation processes as well as in the treatment of the background medium evolution, i.e. hydrodynamics. However, in both cases a phenomenological factor ("K-factor") is necessary to find agreement with the data. In MC@sHQ+EPOS2, the elastic and radiative interactions are rescaled with $K = 0.8$. In BAMPS, two scenarios were considered, one with scaled binary (elastic) collisions ($K = 3.5$) and another with elastic as well as radiative processes employing a scaled LPM effect. The latter scaling lowers "the formation time of the emitted gluon by a factor $X_{\mathrm{LPM}} = 0.2$, which effectively allows more radiative processes for $0 < X_{\mathrm{LPM}} < 1$"[1][176]. As seen in the right panel of 6.8, the influence on b-quarks is much smaller than for light and c-quarks, which start to deviate below $X_{\mathrm{LPM}} = 1$.

Within BAMPS, the treatment of the LPM effect in the R_{AA} calculation is the same for light and c-quarks. The authors found, that "small angle radiation off both charm and light quarks is suppressed [due to the implementation of the LPM cut-off] and both have a very similar radiative energy loss", leading to a similar nuclear modification factor for D mesons and charged hadrons. This statement is based on figure 6.8 (left), where the radiative as well as the collisional energy loss are depicted. While the first is similar for light and c-quarks, the latter shows a mass splitting with the lowest energy loss for the b-quark. It is argued that the calculations are in good agreement with data if both elastic and radiative processes are taken into account. However, in order to describe R_{AA} and the elliptic flow component v_2 of the D meson simultaneously, solely the scaled elastic scatterings are necessary, apparently ruling out the combined energy loss from elastic and radiative processes for the D meson. Additionally, the agreement of the R_{AA} of non-prompt J/ψ calculated with MC@sHQ+EPOS2 with the measurement is better in this case (the non-prompt J/ψ v_2 is not available yet). While the energy loss of both scenarios in BAMPS is of the same order, the transport cross section is significantly smaller in the latter. Thus, the R_{AA} results are similar but the v_2 results, mainly influenced by the transport cross sections, differ. Coalescence or recombination is presently not included in BAMPS, which could in-

---

[1]"Is important to mention that the exact value of X_{LPM} is not theoretically motivated and, thus, a free parameter"[176].
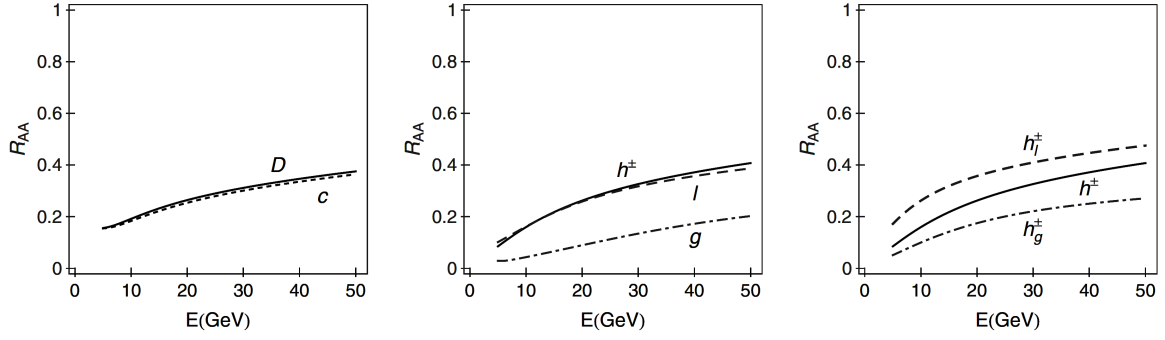
Figure 6.9: Left: Comparison of the charm-quark suppression predictions (full curve) with the D meson suppression predictions (dashed curve), as a function of momentum. Centre: Comparison of charged hadron suppression predictions (full curve) with light-quark (dashed curve) and gluon (dot-dashed curve) suppression predictions. Right: The dashed curve shows what would be the charged hadron suppression if only light quarks contributed to charged hadrons. The dot-dashed curve shows what would be the charged hadron suppression if only gluons contributed to charged hadrons, whereas the full curve shows the actual hadron suppression predictions. Figure and caption from [167].

crease the transport cross sections and thus enhance the relevance of the two-processes scenario.

To summarize, according to the authors of [176], there are two reasons why the D meson R_{AA} is compatible with that of charged hadrons: First, the LPM cut-off produces a "second dead-cone that overlays the dead-cone due to the heavy-quark mass and effectively annihilates its influence" generating a "similar suppression for light and heavy quarks." Second, the fragmentation process of the D meson, where contributions from gluon jets are suppressed due to the large c-quark mass [178], causes the D meson R_{AA} to be compatible with the c-quark R_{AA}, as seen in the left panel of figure 6.9 (from [167]). The suppression is similar to that of the charged hadrons predominantly including light-quark hadrons. The R_{AA} of light-quark hadrons stemming only from quark fragmentation is however larger than the observed charged hadron R_{AA}, as depicted in the right panel of figure 6.9. For hadrons originating solely from gluon fragmentation, the suppression is stronger and the total light-quark hadron R_{AA} lies in between the two limiting cases. Thus, the fragmentation process creating light-quark hadrons shifts their R_{AA} closer to the light-quark R_{AA}, that is compatible with the D meson and c-quark R_{AA}. Taking additionally into account the BAMPS results for the exchanged energy loss of quarks and gluons, it seems that the gluon and quark suppression together with the individual hadron fragmentation functions "combine so that, coincidentally, their "resultant" charged hadron suppression almost identically reproduces the bare light-quark suppression"[167], which seems to hold for Λ and K_s^0 as well.

6.1.3 High p_{T}: Comparison of K_s^0 and Λ R_{AA} to measurements at lower beam energies

As the formation of a QGP is expected both at RHIC and the LHC, the comparison of the results from both energies might reveal further features/subtleties of its creation
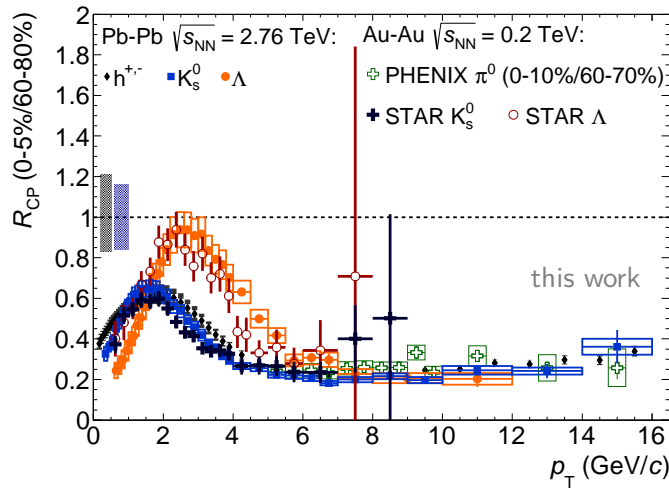
Figure 6.10: The nuclear modification factor R_{CP} of K_s^0 and Λ in Pb–Pb collisions at $\sqrt{s_{NN}}$ = 2.76 TeV in comparison to the measurement for Au–Au collisions at $\sqrt{s_{NN}}$ = 200 GeV by the STAR collaboration [179] for the same centrality intervals. In addition, the charged particle R_{CP} from ALICE [47] as well as the neutral pion R_{CP} by PHENIX [78] are shown. The uncertainty from N_{coll} and from the normalization in pp are indicated by the boxes at unity (black ALICE, blue STAR).

and its properties.

Figure 6.10 shows the comparison of the K_s^0 and Λ R_{CP} to the measurements by the STAR collaboration in Au-Au collisions at $\sqrt{s_{NN}} = 200$ GeV for central collisions. For both particles, a similar suppression is observed at RHIC and at the LHC within the uncertainties. Albeit, for Λ at the LHC, however, a slight shift of the maximum of R_{CP} to higher p_T is indicated, which could be the result of the larger radial flow and higher mean p_T observed at the LHC [107]. In addition, the neutral pion R_{CP} from PHENIX is shown, which is similar with that of charged particles at RHIC energies, but offering a larger p_T reach as well as smaller systematic uncertainties. Also in this case, the suppression is similar at both energies.

While the similarity of R_{CP} for a given particle type at RHIC and at the LHC indicates similar evolution of particle production modifications from peripheral to central collisions, a somewhat different picture emerges if modifications with respect to pp collisions, i.e. the study of R_{AA}, is considered. This is shown in figure 6.11, where R_{AA} of K_s^0 and Λ in central Pb–Pb collisions from this work are compared to results from STAR at RHIC (for peripheral collisions see figure C.11). At the LHC, the suppression of both K_s^0 and Λ is smaller by roughly a factor 2.6. In case of K_s^0, the R_{AA} approaches that of the neutral pions around 7 - 9 GeV/c, while for Λ, the p_T reach and the statistical uncertainties only a slight trend towards the pion R_{AA} is indicated. For this representation, the STAR pp reference, which is normalized to non-single diffractive events (NSD), was scaled by the ratio of cross-sections $\sigma_{NSD}/\sigma_{INEL} = 30$ mb/42 mb. Furthermore, in order to match the p_T range of the STAR Au–Au spectra, the pp references were extrapolated with a Tsallis-Pareto function from $p_T = 5$ - 8 GeV/c. The neutral pions at RHIC show only slightly less suppression than the charged particles at the LHC, why it appears to be compatible within the scaling uncer-
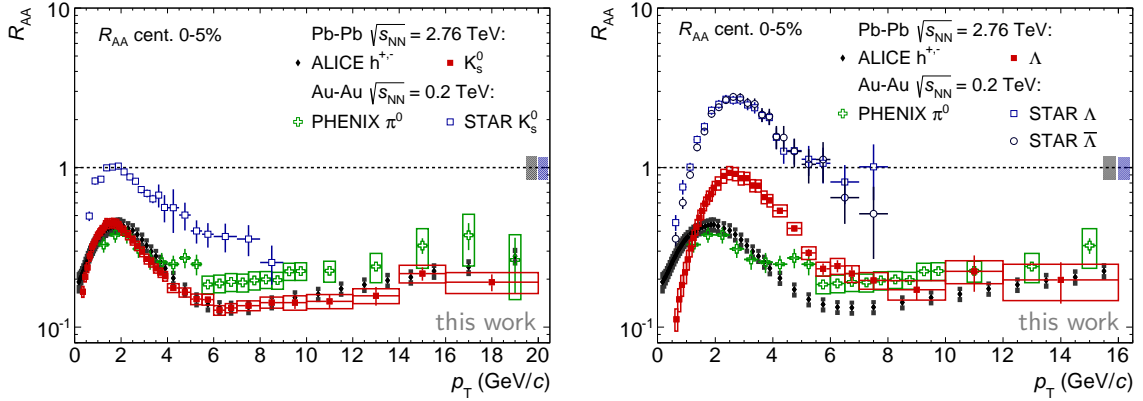
Figure 6.11: The nuclear modification factor R_{AA} of K_s^0 (left panel) and Λ (right panel) in central Pb–Pb collisions at $\sqrt{s_{NN}}$ = 2.76 TeV in comparison with the measurement in Au–Au collisions at $\sqrt{s_{NN}}$ = 200 GeV by the STAR collaboration [179, 180] for the same centrality interval. In addition, the charged particle R_{AA} from ALICE [47] as well as the neutral pion R_{AA} by PHENIX [78] are shown. The STAR pp reference was scaled by the cross-section ratio $\sigma_{NSD}/\sigma_{INEL}$ = 30 mb/42 mb. The uncertainty from N_{coll} and from the normalization in pp are indicated by the boxes at unity (black ALICE, blue STAR).

tainties. Thus, a similar high-p_T suppression could be assumed for mesons at both energies. As the STAR results are limited to the intermediate p_T region, no statement on high p_T suppression of Λ and K_s^0 with respect to pp collisions from RHIC to LHC energies is possible yet.

Taking into account that the STAR K_s^0 and Λ R_{CP} is compatible to the results of this work, the significant difference between the R_{AA} at low p_T may be driven by the pp references rather than by nuclear effects. Figure 6.12 shows the p_T spectra of Λ in central and peripheral AA as well as in pp collisions at both energies. Obviously, the spectra at the LHC are much harder than at RHIC energies. Whereas in AA collisions, the shape changes already at low p_T, in pp, the shape is similar up to $p_T \approx 1.0$ GeV/c. The vertical lines mark the maxima of the spectra. Only in central collisions, the p_T of the maximum shifts significantly from 0.9 to 1.2 GeV/c with collision energy, which could partially be related to the increased radial flow at LHC. Considering the left panel of figure 6.13, where the double-ratios of the parametrisations shown in figure 6.12 of Au–Au/pp collisions at $\sqrt{s_{NN}}$ = 200 GeV to Pb–Pb/pp collisions at $\sqrt{s_{NN}}$ = 2.76 TeV are displayed, the ratio Au–Au/pp at RHIC is larger by a factor 1.5 for central collisions than that at LHC for $1.5 < p_T < 3$ GeV/c, already without the normalisation to N_{coll}. Together with the value of the inverse N_{coll} ratio of 1.7, this yields a factor of 2.55, which corresponds to the R_{AA} enhancement at RHIC compared to that at LHC.

Regarding the p_T-depended evolution of the spectra ratios in the right panel of figure 6.13, the decreasing slope is steepest in central collisions and flattest in pp as well as in peripheral collisions, indicating a stronger modification in the shape in central collisions. At lower p_T, this could be caused by the increased radial flow, which shifts the particle production to higher p_T causing a harder spectrum. In pp, however, the particle production is increased at all p_T. While at lower p_T, the shape does not change with increasing collision energy, at higher p_T also a much harder spectrum is observed
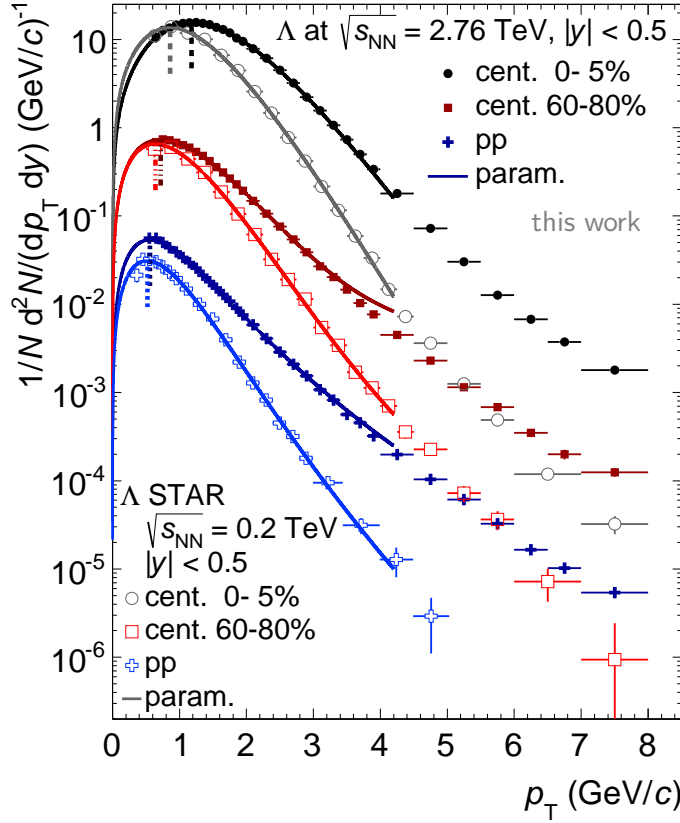
Figure 6.12: Λ transverse momentum spectra of this work in Pb–Pb and pp collisions at $\sqrt{s_{NN}} = 2.76\,\text{TeV}$ together with those measured by STAR [179, 180] in Au–Au and pp collisions at $\sqrt{s_{NN}} = 200\,\text{GeV}$. Parametrizations with a Blast-Wave (AA) and a Tsalllis-Pareto fit (pp) are shown in addition (full curves). The dashed vertical lines indicate the p_T of the the maximum of the distributions. The STAR pp spectrum was rescaled via the cross-section ratio $\sigma_{NSD}/\sigma_{INEL} = 30\,\text{mb}/42\,\text{mb}$.

at the LHC, which does not significantly affect the particle yield but influences R_{AA}. Thus, the enhanced rapidity density by a factor of two in pp collisions at the LHC is solely caused by the enhanced spectrum at low p_T, whereas in Pb–Pb, the increased rapidity density is mainly a consequence from the harder spectra. In other words, predominantly more particles with higher momenta are produced in Pb–Pb at the LHC. For R_{CP}, this change in the spectra slope eventually cancels and the change in the magnitude at each p_T is compensated by the difference in N_{coll}.

These observations seem to be the case only for K_s^0 and Λ, because the neutral pion R_{AA} is comparable at both energies. Since the mean p_T of charged kaons and protons increases by $\approx 30\%$ and that of pions by roughly 10% in central Pb–Pb collisions [107], this might be connected to the increased radial flow at LHC as well, which has a stronger effect on Λ and K_s^0 than on pions.
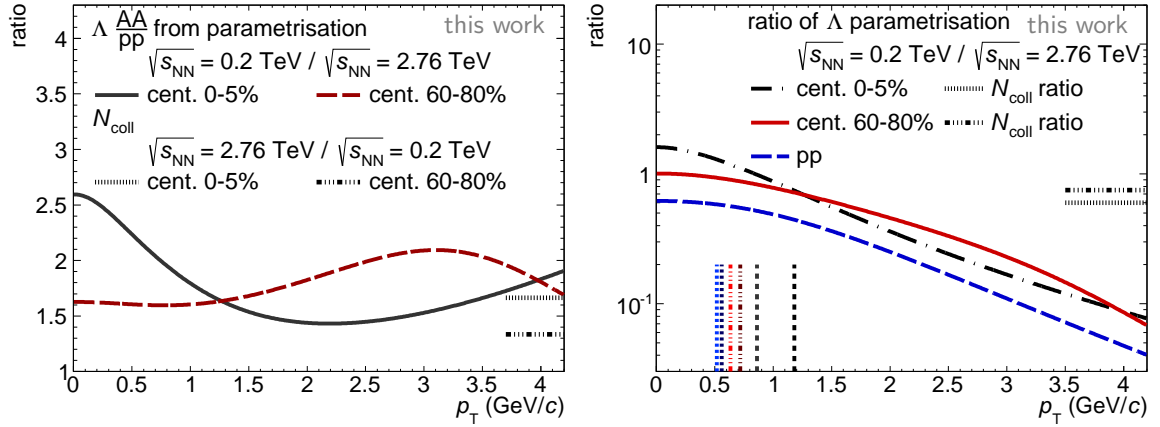
Figure 6.13: Left: Double-ratio of the parametrisations of the Λ p_{T} spectra measured by STAR (see figure 6.12) Au–Au/pp collisions at $\sqrt{s_{\mathrm{NN}}} = 200$ GeV to Pb–Pb/pp collisions at $\sqrt{s_{\mathrm{NN}}}$ = 2.76 TeV obtained for Λ in this work. The horizontal lines indicate the inverse ratios of N_{coll}. Right: Ratio of Λ p_{T} spectra parametrisations in AA and pp collisions at RHIC to those at the LHC. The ratios of N_{coll} (horizontal lines) and the p_{T} values, where the maximum of the spectra is reached, (vertical lines) are shown in addition.

6.1.4 Low-to-intermediate-to-high p_{T}: Baryon-to-meson ratio

The $\Lambda/\mathrm{K}_{\mathrm{s}}^0$ ratio in pp and Pb-Pb collisions at the LHC (see section 5.2) is compared to the measured p/π ratio and several model calculations in figure 6.14. At all centralities and pp, the peak of the p/π ratio is lower by roughly a factor 2 than that of $\Lambda/\mathrm{K}_{\mathrm{s}}^0$. On the other hand, the ratios reach the same values at $p_{\mathrm{T}} > 8\,\mathrm{GeV}/c$, where the influence of the radial flow vanishes and the power-law behaviour of the spectra sets in. In the recombination picture, the yield at intermediate p_{T} contains feed-down from higher p_{T}, where the partons suffered energy loss and a contribution from lower p_{T} due to the flow. Combining 3 instead of 2 partons, the overall p_{T} gain is larger for baryons than for mesons, enhancing the baryon yield at the considered hadron p_{T}. The calculation with a recombination model for $\Lambda/\mathrm{K}_{\mathrm{s}}^0$ as presented in figure 6.14 is able to reproduce the trend in central collisions at $p_{\mathrm{T}} = 3$ - $6\,\mathrm{GeV}/c$. The hydrodynamic model describes the data up to $p_{\mathrm{T}} = 3\,\mathrm{GeV}/c$. Finally, the EPOS calculation combining hydrodynamics with the interaction between jets and the hydrodynamically expanding medium can reproduce the data up to $p_{\mathrm{T}} = 5\,\mathrm{GeV}/c$. These considerations seem to support the recombination picture in combination with hydrodynamics at least in a limited p_{T} range.

With regard to the nuclear modification factor at lower p_{T}, a reduced suppression for Λ is observed as compared to $\mathrm{K}_{\mathrm{s}}^0$ and charged hadrons. The compilation of ALICE R_{AA} results in central collisions in figure 6.1 shows that all baryons exhibit less suppression than the mesons in this p_{T} range. Moreover, a mass hierarchy is found, which seems to hold as long as baryons and mesons are considered separately. Especially the ϕ and D meson, which both have masses larger than the proton seem to support this observation. In case of the mesons, the pion suppression is stronger as compared to that of the kaons with a four times larger mass. The baryons also exhibit a mass hierarchy above $p_{\mathrm{T}} = 2\,\mathrm{GeV}/c$, with the protons and $\Omega^{+,-}$ showing the smallest and largest R_{AA}, respectively. However, the difference between the Λ and
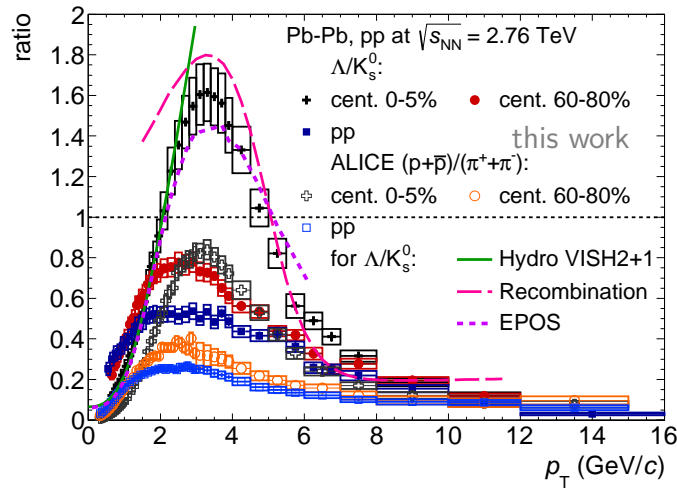
Figure 6.14: Ratio of Λ to K_s^0 p_T spectra in Pb–Pb and pp collisions at $\sqrt{s_{NN}} = 2.76\,\mathrm{TeV}$ together with the proton-to-pion-ratio measured by ALICE [159]. Calculations with a hydrodynamic model [181–183], a recombination model [184] and with EPOS [185] are shown in addition.

$\Xi^{+,-}$ R_{AA} is rather small as compared to the difference between Λ and p, although the relative mass difference is the same. Since no significant radial flow is expected in pp, the local maximum of the R_{AA} above $p_T = 1\,\mathrm{GeV}/c$ could be related to the flow in Pb–Pb as discussed above. Further figures, where the R_{AA} for all centralities of baryons (p, Λ, $\Xi^{+,-}$, $\Omega^{+,-}$) and mesons ($\pi^{+,-}$, K_s^0, $K^{+,-}$) are presented separately, can be found in appendix C.2.

In the high p_T-region, the discrimination of the jet-like part, stemming from fragmentation only, and the bulk part could shed some light on the interplay of recombination effects and the transition to pure fragmentation as the respective dominant hadron creation mechanism. Figure 6.15 shows in the left panel the proton-to-pion ratio in central collisions for the bulk contribution of the spectra and the remaining jet contribution (peak − bulk) from [186]. The latter distribution is compatible with the results obtained from PYTHIA and with the proton-to-pion ratio seen in pp collisions (see figure 6.14), representing pure fragmentation. On the other hand, the bulk ratio resembles that of the inclusive ratios. The right panel of the same figure presents the $(\Lambda+\overline{\Lambda})/K_s^0$ ratio from inclusive measurements and from hadron-jet correlations in p–Pb collisions. Above $p_T = 8\,\mathrm{GeV}/c$, the PYTHIA result and the the jet measurement reaches the values of the inclusive ratio.

To conclude this paragraph, fragmentation seems to be the dominant particle production mechanism above $p_T = 8\,\mathrm{GeV}/c$, which appears not to be modified in Pb–Pb or p–Pb collisions, since the ratios agree with those in pp and PYTHIA representing the unmodified case. Thus, the suppression seen in the R_{AA} measurement appears to be caused by partonic in-medium energy loss on the one hand and a subsequent unmodified fragmentation as the dominant particle production mechanism on the other. Having said that, the effect of a possible modification of the fragmentation could simply cancel in the baryon-to-meson ratio as it seems to be the case for the energyloss. As a reminder, the latter is expected to be the same for light-quark hadrons.
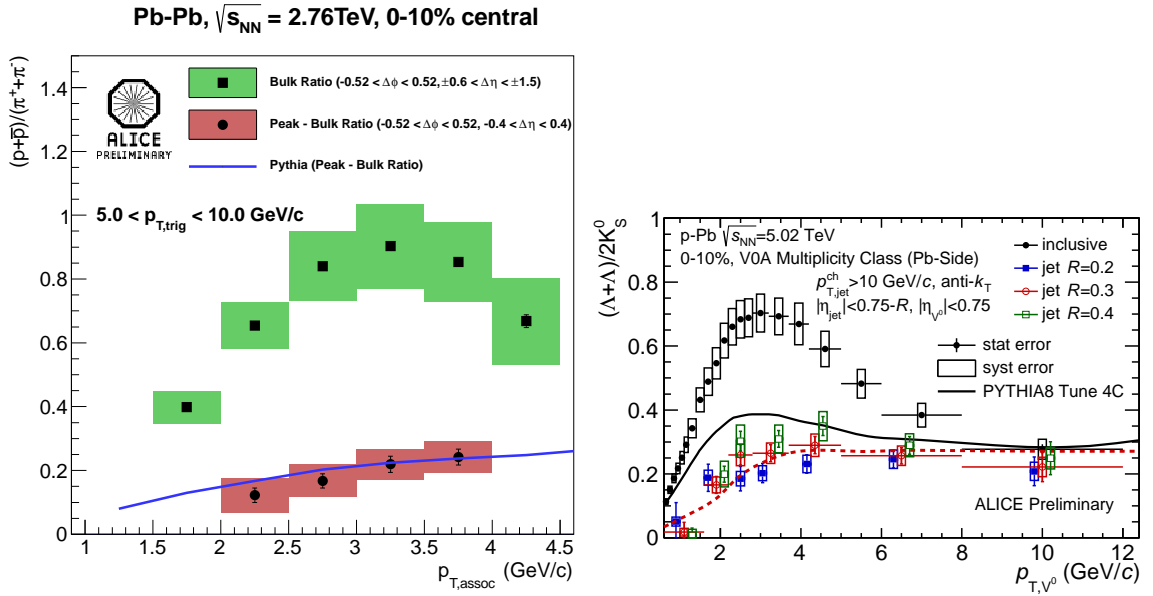
Figure 6.15: Left: Measured proton-to-pion ratio in the jet and bulk in a di-hadron correlation analysis in Pb–Pb collisions. The measurements, which are not feed-down corrected, are compared with PYTHIA results [186]. Right: $(\Lambda+\overline{\Lambda})/K_s^0$ ratio in p–Pb from inclusive measurements (black points) and from hadron-jet correlations (coloured points) in comparison with PYTHIA [187].

Hence it may be difficult to conclude on the fragmentation process modification. Indeed, the CMS collaboration measured the jet fragmentation functions in Pb–Pb and pp collisions [188]. In central collisions, only a small modification of the jet fragmentation functions is observed for the considered momentum range and a vanishing difference in the p_T spectra of the jet particles. At lower p_T, an enhancement up to 1.6 is reported for the p_T spectra of the latter, which could explain the difference between the PYTHIA result and the measurement of the $(\Lambda+\overline{\Lambda})/K_s^0$ ratio in jets at these momenta.

6.1.5 Low p_T: Rapidity densities, temperatures and strangeness suppression

In the previous chapter, the rapidity densities of K_s^0 and $\Lambda(\overline{\Lambda})$ were presented as a function of N_{part}. Since N_{part} serves as a measure of the initial system size, it can be used for the comparison of the results from different beam energies at the same collision centrality. If $dN_{ch}/d\eta$, the number of charged particles measured per pseudorapidity range is chosen instead, the centrality classes from two different beam energies are not comparable, because the particle multiplicities are different.

In the following, the relative rapidity densities of particles with different strangeness content are considered. Figure 6.16 contains such ratios measured by ALICE and from this work, respectively, for all light-quark hadrons previously addressed. In the legend of this figure, the hadron ratios with the same relative strangeness ΔS are grouped. The same symbol refers to the same ΔS and the same colour refers to the same denominator.

With regard to the centrality dependence, only the relative rapidity densities of Ξ^-
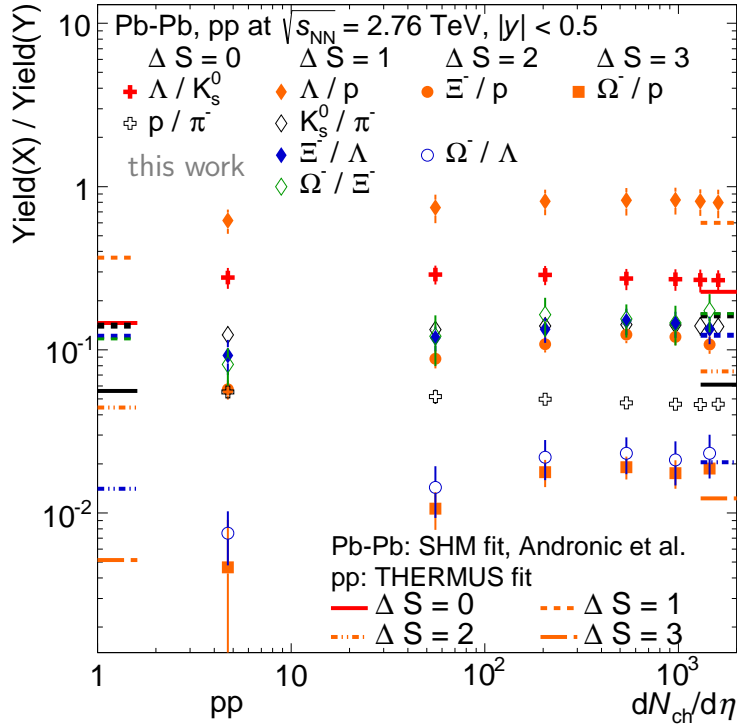
Figure 6.16: Rapidity density $(\mathrm{d}N/\mathrm{d}y)$ in Pb–Pb collisions at $\sqrt{s_{\mathrm{NN}}} = 2.76\,\mathrm{TeV}$ of particle X relative to particle Y as a function of $\mathrm{d}N_{\mathrm{ch}}/\mathrm{d}\eta$. The values of K_s^0 and Λ were taken from this work. The other results were obtained by the ALICE collaboration in [107, 108] and the pp values were extracted from [158, 159]. The ALICE $\mathrm{d}N_{\mathrm{ch}}/\mathrm{d}\eta$ values were published in [30, 189]. The error bars indicate the quadratic sum of the statistical and systematic uncertainties. The horizontal lines show the results from a statistical model fit with $T_{\mathrm{ch}} = 156\,\mathrm{MeV}$ and $\mu_{\mathrm{B}} = 0$ for central collisions (high $\mathrm{d}N_{\mathrm{ch}}/\mathrm{d}\eta$) [123] and a THERMUS [190] fit [191] with $T_{\mathrm{ch}} = 146\,\mathrm{MeV}$, $\mu_{\mathrm{B}} = 2.69\,\mathrm{MeV}$ and $\gamma_{\mathrm{s}} = 0.8$ for pp collisions (low $\mathrm{d}N_{\mathrm{ch}}/\mathrm{d}\eta$).

and Ω^- show an increase with $\mathrm{d}N_{\mathrm{ch}}/\mathrm{d}\eta$, while for the other hadron ratios no significant centrality dependence is observed, revealing that the individual rapidity densities scale with $\mathrm{d}N_{\mathrm{ch}}/\mathrm{d}\eta$ in the same manner. In addition, the particle ratios obtained from a SHM [192] fit to the particle abundances at mid-rapidity in central collisions with μ_{B} fixed to zero yielding a chemical freeze-out temperature of $156\,\mathrm{MeV}$ are depicted as horizontal lines. The line style corresponds to a certain value of $\Delta\mathrm{S}$ and the colour to that of the marker representing the corresponding measured particle ratio. Except for the ratios that contain protons, all relative rapidity densities are reproduced by the SHM within the experimental uncertainties, indicating a particle production via statistical hadronisation from a thermalised medium. Furthermore, the rapidity densities in pp collisions were fitted [191] with THERMUS [190] from which a temperature of $T_{\mathrm{ch}} = 146\,\mathrm{MeV}$, $\mu_{\mathrm{B}} = 2.69\,\mathrm{MeV}$ and $\gamma_{\mathrm{s}} = 0.8$ were obtained. The corresponding fit results for the particle ratios are indicated by the horizontal lines at around $\mathrm{d}N_{\mathrm{ch}}/\mathrm{d}\eta = 1$. Besides the ratios including Λ and Ξ^-, all other rapidity density ratios are rather well described by the fit. The extracted chemical freeze-out temperature is not much smaller in pp than in Pb–Pb. The strangeness suppression factor indicates a 20% strangeness suppression in pp as compared to Pb–Pb, where

$\gamma_{\mathrm{s}} = 1$. It has to be noted, that the $\chi^2/\mathrm{NDF} = 70.23/11$ is quite large.
Interestingly, the Ω^-/Ξ^- ratio is compatible with the Ξ^-/Λ ratio and with the $\mathrm{K}^0_{\mathrm{s}}/\pi^-$ ratio, which all have $\Delta\mathrm{S} = 1$ in common but their mass differences disagree. Thus, the relative decrease of the rapidity density from the lighter particle to the heavier particle with an additional s-quark is similar. If the baryon-to-meson ratios are considered with $\Delta\mathrm{S} = 0$, the separation of the $\Lambda/\mathrm{K}^0_{\mathrm{s}}$ ratio and the p/π^- ratio is roughly a factor 5.5. The SHM fit yields a factor 4, which leads to 5.2 if the measured "too low" proton rapidity density of 30% is taken into account. Considering the ratios with $\Delta\mathrm{S} = 2$, nearly a factor 5 is observed between the Ω^-/Λ and Ξ^-/p ratio. A factor 3.6 is expected from the SHM fit, which yields 4.7 with the 30% proton rapidity density in addition. In general, the ratios to the non-strange proton with $\Delta\mathrm{S} > 1$ are always larger by a factor 3.6 - 4 in the SHM. Whereas for the non-strange baryons only μ_{B} plays a role, for strange particles μ_{S}, i.e. the strange chemical potential, as well as μ_{B} are important. Basically, the large difference describes the energy needed to implement strangeness at all in the system.

The origin of the low proton rapidity density is not yet clarified. The statistical hadronisation models cannot reproduce the low proton rapidity density. As discussed in [122], several aspects might be considered, such as probably missing hadron states in the models, non-equilibrium effects or a flavour-dependent, sequential freeze-out causing different T_{ch} for each species. "A low value of the p/π ratio is naturally predicted by non-equilibrium models as a consequence of the lower temperature ($T_{\mathrm{ch}} \approx 140\,\mathrm{MeV}$) needed to describe the data"[122]. Such a non-equilibrium thermal model is SHARE [193–196], which is able to describe the data reasonably well. The price to pay for the inclusion of non-equilibrium effects are additional free parameters.

Historically, to estimate the strangeness enhancement in AA or the strangeness suppression in pp, respectively, the particle rapidity densities normalised to the rapidity density in pp as well as to the initial system size N_{part} have been investigated. Figure 6.17 displays such relative rapidity densities of $\mathrm{K}^0_{\mathrm{s}}$, Λ, protons, charged pions and multi-strange particles measured by ALICE in Pb–Pb at $\sqrt{s_{\mathrm{NN}}} = 2.76\,\mathrm{TeV}$ as well as by STAR and by PHENIX in Au–Au at $\sqrt{s_{\mathrm{NN}}} = 0.2\,\mathrm{TeV}$. The ratios of all particles are above unity, showing that the relative particle production is increased in AA collisions.

Focussing on $\mathrm{K}^0_{\mathrm{s}}$ and Λ at the LHC, the rapidity densities relative to pp agree and increase with N_{part}. This is also seen for RHIC energies when considering $\overline{\Lambda}$ instead of Λ, but with values that are 1.1 and 1.2 times larger. For Λ at RHIC, the N_{part} dependence is similar to that of $\overline{\Lambda}$ but exhibiting larger values. The multi-strange particles show a comparable trend with N_{part} as well for both energies though their slope is steeper than for non- and single-strange particles. However, their relative production is increased by a factor of two at RHIC. As mentioned in chapter 2, the latter observation hints to the relaxed local strangeness conservation in pp at LHC energies as compared to the 10 times lower RHIC energies causing a larger strangeness production in pp at the LHC. The results of Λ indicate that this is also the case for single-strange particles. In case of the protons, the relative production is reduced by 40% at the LHC, when considering the protons at RHIC and 30% smaller, if the anti-protons at RHIC are regarded, which is analogue to the observation for Λ. While at RHIC, the relative (anti-)proton production is comparable to the relative pion production, this is not the case at the LHC, where the protons are below the pions for non-peripheral collisions. On the other hand, the N_{part} dependence of the protons
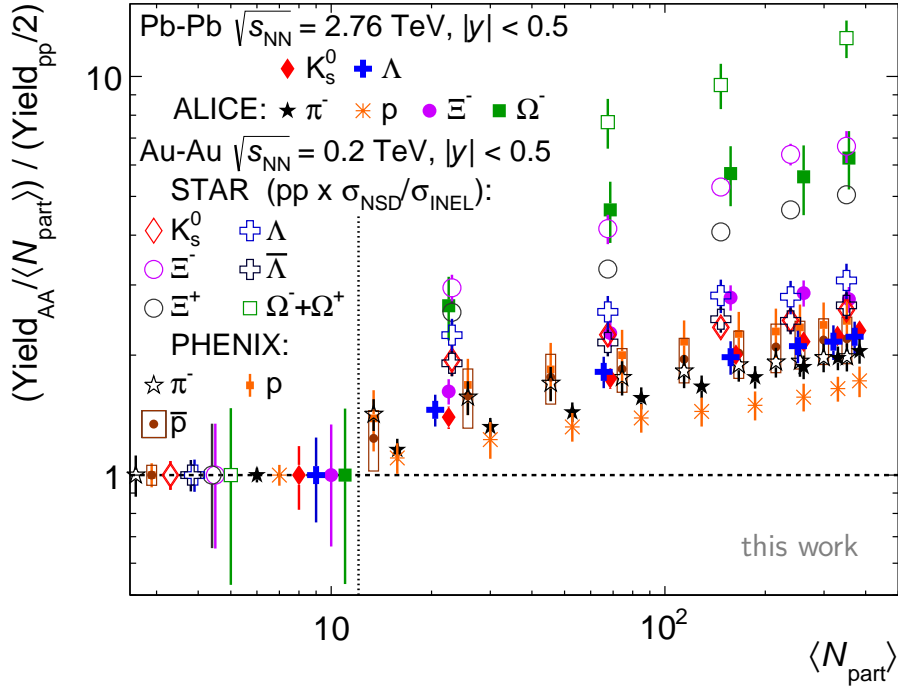
Figure 6.17: Rapidity density $(\mathrm{d}N/\mathrm{d}y)$ in Pb–Pb collisions at $\sqrt{s_{\mathrm{NN}}} = 2.76\,\mathrm{TeV}$ and Au–Au collisions at $\sqrt{s_{\mathrm{NN}}} = 0.2\,\mathrm{TeV}$ relative to pp and scaled to mean N_{part} as a function of mean N_{part}. The points for Λ were shifted to the left in x-direction for better visibility. The ALICE results were obtained from [107, 108] and the pp values were extracted from [158, 159]. The PHENIX measurements from [197, 198] and the values of STAR from [179, 199, 200]. The error bars indicate the quadratic sum of the statistical and systematic uncertainties. Since the rapidity density ratios do not contain the scaling error from the pp values, the relative scaling errors are separately shown at N_{part} values below the dashed vertical line.

is similar for STAR and ALICE. In the mesonic sector, the relative rapidity density of pions at both energies is compatible in central collisions. The same holds for $\mathrm{K_s^0}$ within uncertainties. Nonetheless it seems that the gain in collision energy in pp is mainly relevant for the baryon production as well as for the (multiple) strangeness production as mentioned earlier. Common to all relative particle rapidity densities is that they do not saturate at large N_{part}. This contradicts the so-called wounded nucleon model, where a saturation effect is expected to the geometry limiting the particle production [24]. If also binary collision scaling is additionally included, the rising $\mathrm{d}N_{\mathrm{ch}}/\mathrm{d}\eta$ distribution as function of N_{part} can be described [30]. Generally, the discussed differences in the particle production at RHIC and the LHC should be taken with care, since the scaling uncertainties of the pp measurements are large. Hence, the following considerations may convey more information.

Since the pion production relative to pp scales stronger than linearly with N_{part}, the study of pion production as a function of $\mathrm{d}N_{\mathrm{ch}}/\mathrm{d}\eta$ may reveal additional information. In particular, the pion rapidity density serves as a particle production volume estimator as demonstrated in [103], where the correlation lengths of pions are measured and from which the source volume as a function of $\mathrm{d}N_{\mathrm{ch}}/\mathrm{d}\eta$ was calculated. The
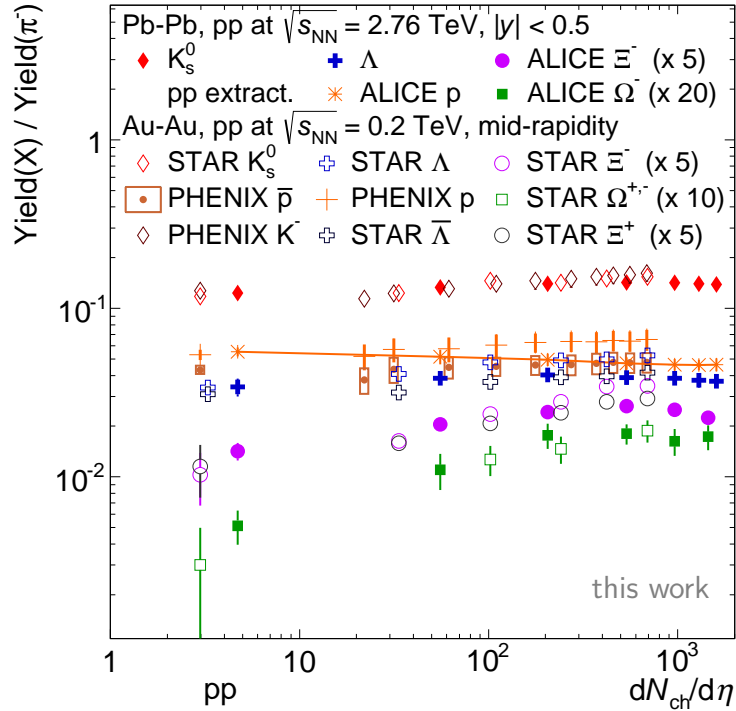
Figure 6.18: Rapidity density (dN/dy) in Pb–Pb collisions at $\sqrt{s_{NN}}$ = 2.76 TeV and Au–Au collisions at $\sqrt{s_{NN}}$ = 0.2 TeV relative to the rapidity density of π^- as a function of $dN_{ch}/d\eta$. The ALICE results were obtained from [107, 108] and the pp values were extracted from [158, 159]. For better visibility, the ALICE proton results were connect via a line. The ALICE $dN_{ch}/d\eta$ values were published in [30, 189]. The PHENIX results are taken from [197, 198, 201] and STAR results from [179, 180, 199]. The STAR pp results were rescaled by the cross-section ratio $\sigma_{NSD}/\sigma_{INEL}$ = 30 mb/42 mb. The error bars indicate the quadratic sum of the statistical and systematic uncertainties of the particle rapidity densities. In the ratios, the pion error is not included.

relative rapidity density of various particle types with respect to the pions versus $dN_{ch}/d\eta$ for ALICE and STAR is presented in figure 6.18. In case of RHIC results, the pions measured by the PHENIX collaboration were always used. This compilation demonstrates that, contrary to the ratios to pp and N_{part}, the particle production as compared to the pion abundance has a weak centrality dependence and saturates at large $dN_{ch}/d\eta$ for almost all particles at both energies, i.e. the multiplicity per volume appears to be constant. The values of Ξ^-, however, slightly decrease at the LHC in the most central collisions. According to [128], the rise of the Ξ^-/π ratio "is a result of the larger relative absorption of the Ξ^- and the larger relative production of pions". The significant centrality dependence and the drop in central collisions is explained by the authors with the concept of after-burning, i.e. deviations from chemical equilibrium. In addition the above-mentioned further aspects of particle production, inelastic multi-hadron collisions in the hadronic phase could play a significant role, which is usually not assumed in SHM. The baryon annihilation and their low regeneration is suggested as the dominant effect causing a proton and Ξ^- rapidity density reduction of up to 20%, whereas mesons are less affected. Contrary to the baryons, the pion multiplicity is even increased with centrality. The relative rapidity density modific-
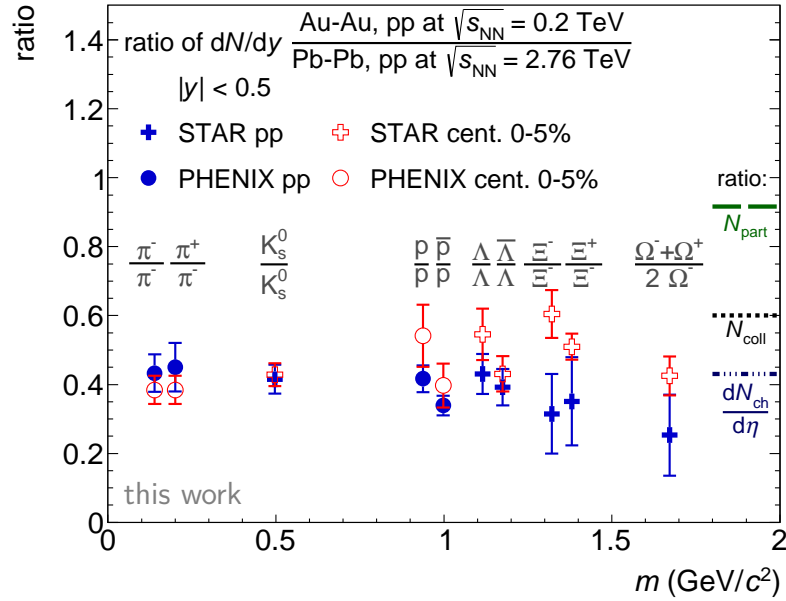
Figure 6.19: Ratio of the rapidity density ($\mathrm{d}N/\mathrm{d}y$) in central Au–Au (pp) collisions at $\sqrt{s_{\mathrm{NN}}}$ = 0.2 TeV to the rapidity density in central Pb–Pb (pp) collisions at $\sqrt{s_{\mathrm{NN}}}$ = 2.76 TeV. The ALICE results were obtained from [107, 108] and the pp values were extracted from [158, 159]. The PHENIX results are taken from [197, 198, 201] and the STAR results from [179, 180, 199]. The STAR pp results were rescaled by the cross-section ratio $\sigma_{\mathrm{NSD}}/\sigma_{\mathrm{INEL}}$ = 30mb/42mb. The anti-particle-to-particle ratios were shifted to higher masses for better visibility. The error bars indicate the quadratic sum of the statistical and systematic uncertainties of the particle rapidity densities.

ation decreases towards peripheral collisions and finally approaches unity. Thus, the chemical freeze-out seems to depend on centrality.

In pp, at $\mathrm{d}N_{\mathrm{ch}}/\mathrm{d}\eta \approx 3$ at RHIC and $\mathrm{d}N_{\mathrm{ch}}/\mathrm{d}\eta \approx 5$ at the LHC, the relative rapidity densities are comparable at both energies within the uncertainties[2], indicating a similar relative particle production at both energies. In case of the multi-strange particles, the particle production in pp may be increased at the LHC, but the current uncertainties do not allow a conclusion.

The picture would change, if the STAR results for protons and pions in pp collisions, which are 1.75 - 3.2 times larger than the PHENIX measurements, were used instead. STAR quotes the non-single diffractive particle multiplicity [180, 199], whereas PHENIX published the rapidity density normalized by the total inelastic cross-section [197], which is also the case for the ALICE measurements. Although for this figure, the STAR pp results were rescaled by the cross-section ratio $\sigma_{\mathrm{NSD}}/\sigma_{\mathrm{INEL}} = 30\,\mathrm{mb}/42\,\mathrm{mb}$, the rescaling cannot account for the remaining difference in the proton and pion rapidity densities between STAR and PHENIX. This might be connected with the fact, that in case of these particles from STAR, no feed-down from Λ was explicitly subtracted, which is in contrast to the PHENIX measurements. Therefore, only PHENIX results

---

[2]The relative rapidity densities do not include the pion rapidity density uncertainty, that is about 8-10% in Au–Au and 12% in pp at RHIC. At the LHC the values are 6 - 7% in Pb–Pb and roughly 5% in pp.

for protons and pions are used and shown here for all considered collision systems and centralities. If the rapidity density in the numerator is taken from STAR, the STAR value for $\mathrm{d}N_{\mathrm{ch}}/\mathrm{d}\eta$ was used.

In figure 6.18, the anti-protons measured by PHENIX are shown in addition, because the particle-to-anti-particle ratio is 0.7 - 0.8. This is in contrast to LHC energies, where no significant difference in the particle and anti-particle production is found [107]. Therefore, the anti-proton rapidity density represents the "true" production of protons at RHIC. The anti-protons follow the trend of the protons by ALICE, while the proton rapidity densities tend to increase with multiplicity. Although, within the uncertainties the relative proton production is comparable with that at the LHC. For $\mathrm{K}_{\mathrm{s}}^0$ and $\Omega^+ + \Omega^-$ the relative production is indeed similar in AA collisions at RHIC and LHC. In case of Λ and Ξ^-, this seems to be the case only within the uncertainties and only up to the second to last centrality class at around $\mathrm{d}N_{\mathrm{ch}}/\mathrm{d}\eta \approx 500$, where the RHIC values exceed those at LHC. On the other hand, the STAR results for $\overline{\Lambda}$ are compatible with the Λ results at the LHC. These findings can also be deduced from figure 6.19, where the rapidity densities from RHIC relative to those from the LHC for central AA and pp collisions are shown. Since the particle and anti-particle production is equal at the LHC, also the anti-particle yields at RHIC were divided by the particle yields at LHC. Within the uncertainties, the relative increased particle production appears to be the same in pp and AA. Although, in case of Ξ^- and $\Omega^{+,-}$, at the LHC, a trend to an enlarged production in pp collisions and a less increased production in Pb–Pb collisions compared to the other results may be concluded. If the AA results of these particles are considred as reference, then the production in pp is cleary enhanced. Additionally, the ratios of N_{part}, N_{coll} and $\mathrm{d}N_{\mathrm{ch}}/\mathrm{d}\eta$ at RHIC to those at the LHC are shown. Whereas N_{part} changes only slightly, the number of binary collisions is increased by 40% at the LHC and the charged particle multiplicity ratio reflects basically the relative pion rapidity density.

To summarize, the relative increase of the particle production from RHIC to the LHC is similar in pp and AA. An exception may be the multi-strange baryons, whose rapidity density seems to be stronger increased in pp, indicating a relaxed local strangeness conservation in pp at the LHC. The strange hadron production in relation to that of non-strange hadrons appears to be independent of the collision energy. Already at the highest SPS energy ($\sqrt{s_{\mathrm{NN}}} = 17.3\,\mathrm{GeV}$), a similar K^+/π^+ ratio for central AA collisions was measured [202]. In case of the Λ/π^+ ratio, only the results in pp collisions at $\sqrt{s_{\mathrm{NN}}} = 17.3\,\mathrm{GeV}$ agree with the LHC measurements, whereas the central AA results are larger by nearly a factor of two. On the other hand, considering the ratios at RHIC energies, which exceed those at LHC energies but are smaller than the SPS measurements, the relative Λ production decreases with the beam energy. With regard to the rapidity density evolution with centrality ($\mathrm{d}N_{\mathrm{ch}}/\mathrm{d}\eta$), only the multi-strange baryons exhibit a centrality dependent increase towards central collisions.

6.2 Summary

Measurements of the transverse momentum spectra of K_s^0 and $\Lambda(\overline{\Lambda})$ in Pb–Pb and pp collisions at $\sqrt{s_{NN}} = 2.76\,\mathrm{TeV}$ with ALICE were presented for $0.3 \leq p_T \leq 20\,\mathrm{GeV}/c$ and $0.6\ (0.5) \leq p_T \leq 16\,\mathrm{GeV}/c$ (pp), respectively. In addition, the particle rapidity densities at mid-rapidity and the nuclear modification factors of K_s^0 and $\Lambda(\overline{\Lambda})$ were extracted.

- **Transverse momentum spectra:** The analysis was performed in six centrality classes in Pb–Pb and in pp collisions at the same energy. The transverse momentum spectra presented in this work were measured employing the on-the-fly V^0 finder. In contrast to the offline V^0 finder, on which the published ALICE results in Pb–Pb collisions [154] are based, additional p_T bins at high p_T could be achieved within this work, increasing the p_T range by 70% (K_s^0) and 35% (Λ) from 12 to 20 and to $16\,\mathrm{GeV}/c$, respectively. Both analyses agree within the uncertainties. Furthermore, the $\overline{\Lambda}$ spectra measured in Pb–Pb and pp at $\sqrt{s_{NN}} = 2.76\,\mathrm{TeV}$ were shown for the first time. The $\overline{\Lambda}$ spectrum agrees with that of Λ for the low-to-intermediate p_T range within the uncertainties. For higher p_T, a small decreasing trend is observed for the $\overline{\Lambda}/\Lambda$ ratio, which needs to be further studied.
  Considering K_s^0, the p_T distributions were found to be compatible with those of charged kaons in Pb–Pb and pp collisions.
  With regard to lower beam energies, the p_T spectra are much harder at $\sqrt{s_{NN}} = 2.76\,\mathrm{TeV}$ than at $\sqrt{s_{NN}} = 0.2\,\mathrm{TeV}$. Whereas in Pb–Pb collisions mainly the yield at higher momenta is increased, which shifts the maximum to higher p_T and generates on average 20% larger mean p_T values, the spectra in pp are significantly enhanced at all p_T causing only a 10% increase in $\langle p_T \rangle$.

- **Rapidity densities:** The multiplicities at mid-rapidity of K_s^0 and $\Lambda(\overline{\Lambda})$ show a linear increase with N_{part}. In case of Λ and $\overline{\Lambda}$, the rapidity densities were found to be equal at the LHC. The rapidity density ratio Λ/K_s^0 remains constant with centrality including pp collisions. The calculated ratio from a SHM prediction with $T_{\mathrm{ch}} = 156\,\mathrm{MeV}$ in central Pb–Pb collisions agrees with the measurement. Regarding the strangeness production relative to non-strange matter, the results of this work show that the relative multiplicities for single-strange particles are rather constant with centrality including pp, and similar at RHIC and the LHC. In case of the particle rapidity density scaled by N_{part} and by the rapidity density in pp, a suppression of the strange and non-strange particle production in pp as compared to Pb–Pb was found for all centralities, which is also seen at RHIC energies. Comparing the strange- as well as multi-strange baryon production in pp and AA, the rapidity density in pp at $\sqrt{s} = 2.76\,\mathrm{TeV}$ seems to be stronger increased as compared to $\sqrt{s} = 0.2\,\mathrm{TeV}$ with respect to central AA collisions. However, if the anti-baryons at RHIC are regarded instead, the increase in pp collisions is only indicated for multi-strange baryons.
  The enhanced rapidity density of Λ in pp at the LHC by roughly a factor two as compared to that at RHIC is mainly determined by the overall increased Λ production, while in central Pb–Pb collisions the similar gain in $\mathrm{d}N/\mathrm{d}y$ is predominantly caused by the harder spectra, i.e. by the increased yield of higher momenta.

- **$\Lambda/\mathrm{K_s^0}$ as a function of p_T:** A baryon-to-meson ratio enhancement is observed for $\Lambda/\mathrm{K_s^0}$ in central Pb–Pb collisions as compared to peripheral and pp collisions in the intermediate p_T region. Above $p_T = 8\,\mathrm{GeV}/c$, this enhancement disappears and the $\Lambda/\mathrm{K_s^0}$ ratios become similar for all centralities and pp. A similar behaviour is also seen for p/π measured by ALICE. Already at RHIC, this phenomenon was observed for both particle ratios. Model calculations employing viscous hydrodynamics at low p_T and recombination/coalescence at intermediate p_T are successful in describing the measurements.

- **R_{AA}:** For the nuclear modification factors of $\mathrm{K_s^0}$ and Λ a strong suppression at high p_T ($p_T > 8\,\mathrm{GeV}/c$) in central collisions with respect to peripheral Pb–Pb and pp collisions is found. The nuclear modification of both particles is compatible with the modification of charged particles. Furthermore, the strange-particle suppression is similar to the charm-particle R_{AA} represented by the D mesons. Only for B mesons, a smaller modification is observed by CMS. The calculations of the transport model BAMPS for the R_{AA} of $\mathrm{K_s^0}$ and $\Lambda(\overline{\Lambda})$ are in agreement with the measurements of this work.
  Comparing the results of a simple R_{AA} description for charged particles assuming constant energy loss for central and peripheral collisions, the energy loss appears to be $\Delta E \approx 5\,\mathrm{GeV}$ for both systems, but the fraction of unaffected partons is reduced by a factor of 5 in central collisions. These fractions are compatible with those extracted for RHIC measurements at $\sqrt{s_{NN}} = 0.2\,\mathrm{TeV}$ although the energy loss is increased by nearly a factor of two at the LHC. This probably hints to a more opaque medium at the LHC, but the available I_{AA} measurements indicate the opposite. All identified hadron R_{AA} at the LHC merge and follow the charged-particle R_{AA} at $p_T = 6$ - $8\,\mathrm{GeV}/c$, where the geometrical lower bound of the hadronic R_{AA} (equation 2.18) is reached.

  At lower p_T ($p_T < 5\,\mathrm{GeV}/c$), an enhancement of the R_{AA} of Λ with respect to the R_{AA} of $\mathrm{K_s^0}$ and is observed as expected from the $\Lambda/\mathrm{K_s^0}$ ratio. The R_{AA} of $\mathrm{K_s^0}$ is compatible with that of the charged hadrons, mainly including pions, i.e. mesons. When comparing the available measurements for baryons and mesons, a mass hierarchy is seen for each species in this p_T sector, where the heavier particles are less suppressed.
  While the R_{CP} is similar at RHIC and the LHC, a significantly smaller R_{AA} of the Λ and $\mathrm{K_s^0}$ at intermediate p_T in central and peripheral events is found as compared to the STAR results, although the neutral pion R_{AA} at RHIC (analogue to the charged hadrons) is comparable to the charged-particle R_{AA} at the LHC.

6.3 Conclusions

Analysis

Within this analysis the $\mathrm{K_s^0}$ and $\Lambda(\overline{\Lambda})$ spectra in pp collisions at $\sqrt{s} = 2.76\,\mathrm{TeV}$ were obtained, which have not yet been published and thus are unique. In contrast, the Pb–Pb spectra of $\mathrm{K_s^0}$ and Λ were already released, however employing a different $\mathrm{V^0}$ finder technique. Thus, the results presented in this work serve as a complimentary consistency check of the published results. Furthermore, the $\overline{\Lambda}$ spectra in Pb–Pb were

measured within this work, which were not yet published as well. As a result, with the help of the now available pp spectra, the R_{AA} of $\mathrm{K^0_s}$ and $\Lambda(\overline{\Lambda})$ could be determined.

Particle production at lower p_{T}

The comparison of the extracted rapidity densities of $\mathrm{K^0_s}$ and $\Lambda(\overline{\Lambda})$ with the results of a statistical hadronisation model calculation considering all hadrons measured by ALICE, imply that at LHC energies the dominant particle production mainly contributing to the rapidity density is statistical hadronisation from a thermally and chemically equilibrated system. In case of the proton, however, further investigations are needed since the measured multiplicity is smaller than expected from the thermal model, indicating that additional aspects such as non-equilibrium effects probably need to be taken into account [122].

The multi-strange particle production seems to be stronger increased in pp at $\sqrt{s}$ = 2.76 TeV as compared to $\sqrt{s}$ = 0.2 TeV than in AA collisions. According to current interpretations within the SHM, this hints to a relaxed local strangeness conservation and to a transition from a canonical to a grand-canonical system at the LHC. The single-strange hadron production, i.e. the production of $\mathrm{K^0_s}$ and $\Lambda(\overline{\Lambda})$ increases equally in AA and pp collisions when going from RHIC to LHC energies, which is also true for pions and protons. Thus, the question could be raised whether pp collisions at LHC energies serve as an appropriate reference, if particle production mainly determined by low p_{T} particles is regarded, in order to study and quantify the differences of AA and pp collisions.

Model calculations employing viscous hydrodynamics at low and recombination/ coalescence at intermediate p_{T} are successful in describing the measurements in this work of the $\Lambda/\mathrm{K^0_s}$ ratio in central Pb–Pb collisions versus p_{T}. This agreement suggests that the radial flow, which affects the baryons more than the mesons, causes the observed enhancement structure on the basis of recombination mechanisms. Due to the stronger radial flow in AA collisions at the LHC as compared to RHIC, the spectra at the LHC are already harder in the low p_{T} region, although the effect of the higher collision energy is first expected at some higher p_{T}. This is visible in the pp spectra, which show a significantly harder slope above p_{T} = 2 GeV/c. In contrast to AA collisions, the amplitude of the spectra in pp collisions is strongly increased.

Particle production at high p_{T}

The measurements of the $\mathrm{K^0_s}$ and $\Lambda(\overline{\Lambda})$ R_{AA} within this work have shown that no flavour dependence of the nuclear modification in Pb–Pb as compared to pp collisions is observed in the high p_{T} region at $8 < p_{\mathrm{T}} < 20$ GeV/c within the light-quark sector. Moreover, no difference for baryons and mesons was found in this p_{T} region. This observation was possible for the first time due to the harder spectra at the LHC and the larger statistics as compared to RHIC measurements both generating a larger p_{T} reach. In combination with baryon-to-meson ratio measurements of the jet contribution to the spectra in Pb–Pb collisions and with the respective ratios in pp, it seems, that above the given p_{T}, unmodified fragmentation dominates the particle production. Comparisons with calculations of the transport model BAMPS also show, that in-medium energy loss folded with the unmodified fragmentation functions is sufficient to describe the measurements. Although within BAMPS, the energy loss of

all light quarks is assumed to be the same, there could have appeared differences in the R_{AA} from the different fragmentation functions and the different quark and gluon fragmentation contributions. However, these differences appeared to be too small to cause different modifications, which are beyond the uncertainties of the measurement. On the other hand, if the fragmentation was modified by medium interactions for the considered particles in the same manner, it is questionable if this could be visible in the studied baryon-to-meson ratios. Thus, there is a need for the measurement of identified particle fragmentation functions in Pb–Pb in order to clarify if the fragmentation process is modified or if all particles created in fragmentation stem exclusively from partons that fragmented outside the medium.

The energy loss of the heavy c-quark was calculated to be the same as for light quarks [167, 176]. The resulting suppression of charmed mesons in Pb–Pb collisions is similar to that of light-quark hadrons. Therefore, due to the agreement of the R_{AA} model calculations with the measurements of the R_{AA} of $\mathrm{K^0_s}$ and $\Lambda(\overline{\Lambda})$ from this work and with the charged-particle [47] as well as with the D meson R_{AA} [168], a compatible energy loss of u-, d-, s- and c-quarks could be concluded. The smaller modification of B mesons seen in data is currently explained by the smaller energy loss of b-quarks as a result of the stronger dead-cone effect as compared to that of c-quarks. This is surprising since the mass of the b-quark is only three times larger than the mass of the c-quark, whereas the light-quark masses are a factor 10 lighter than the c-quark and no difference is observed although the c-quark mass is already above the QCD scale of 200 MeV. The contribution of the radial and collisional energy loss needs to be precisely determined in order to better understand the mass dependence of the total in-medium energy loss. Therefore, more differential studies from the experimental and theoretical side are vital.

Résumé: The production of $\mathrm{K^0_s}$ and $\Lambda(\overline{\Lambda})$ in Pb–Pb collisions relative to pp at the LHC differs from that of hadrons solely composed of u- and d-quarks neither at lower p_{T} - regarding the rapidity density - nor at high p_{T} with respect to the nuclear modification. Furthermore, no significant difference between the respective baryons and mesons was found, especially at high p_{T}.

6.4 Outlook

Analysis

The presented $\mathrm{K^0_s}$ and $\Lambda(\overline{\Lambda})$ transverse momentum spectra, especially those in pp collisions and those for $\overline{\Lambda}$ are planned to be published. Furthermore, the additional p_{T} bins increasing the p_{T} reach of the published Λ and $\mathrm{K^0_s}$ spectra will be included there. In case of the $\overline{\Lambda}$, a few aspects remained unsolved within this work, such as the slightly decreasing trend of the $\overline{\Lambda}/\Lambda$ with p_{T}. These issues will be addressed during the publication preparation.

Physics, research

From the physics perspective, an increase in the p_{T} reach could be interesting if the fragmentation functions of baryons and mesons are considered, which were shown as ratios of gluon and quark (+ anti-quark) fragmentation in figure 6.4. An equal num-

ber of baryons and anti-baryons is produced in gluon fragmentation, which happens mainly at lower p_T, because the dominant contribution stems from fragmentation of gluons, which are located at low x. At around $p_T = 50$ - $60\,\mathrm{GeV}/c$, the contribution from gluon fragmentation is as large as that from quark fragmentation and at even higher p_T, the quark fragmentation dominates. Thus, at very high p_T, the valence quarks with large x dominate. Consequently, the baryon production could be increased over the anti-baryon production in this energy domain since the quarks likely fragment into baryons [42]. Therefore, due to the dominance of quarks, the relative gluon fragmentation contribution for anti-baryons is increased at these p_T. Since gluons suffer more energy loss than quarks and the relative contribution from gluon fragmentation is larger for anti-baryons, the suppression of anti-baryons could be stronger. The harder the fragmentation functions of the valence quarks are, the more visible this effect should be, i.e. it depends on the baryon mass. In case of pions, such an effect is not expected, since the valence quark fragmentation functions are as soft as those from gluons as well as from sea quarks and the different energy loss of quarks and gluons might not have an effect [42]. Furthermore, in this context, the measurement of fragmentation functions of identified particles via jets could help to disentangle the parton energy loss and a possibly modified fragmentation in AA collisions. For such studies, sufficient high statistics and a thorough detector calibration are vital. With the detector upgrade for the Run 3 (starting in 2020) and the now fully available Transition Radiation Detector system, which allows to trigger on high p_T particles, such measurements might be possible in future.

With regard to the charm production, the measurement of heavy-quark hadrons helps to constrain models, because high masses are much easier to implement in the calculations due to their masses being larger than Λ_{QCD}, the scaling parameter of QCD, and thus higher order terms can be neglected. From the experimental side, the precision of the corresponding measurements will be increased with the 2015-2018 data taking where the collision energy will be enhanced by nearly a factor two, which leads to an increase of the production cross section of D and B mesons by around 50 percent. Furthermore, thanks to the foreseen detector upgrade for Run 3, a more precise determination of their decay vertex can be achieved. The latter is challenging to measure due to the short lifetime of these particles translating into decay lengths of a few μm. The bottom quarks are created mainly at the beginning of the medium formation and therefore they experience the whole system evolution until the freeze-out when the detectable hadrons are formed. To measure its R_{AA} over a larger p_T range with a sufficient granularity would be a considerable step forward to the deeper understanding of the suppression and fragmentation mechanisms in the system evolution of hot and dense nuclear matter. This implies the path length dependence inside the created medium, the flavour and colour charge dependence of the energy loss of the interacting partons surrounded by the medium. From this input it could be possible to extract the medium density and to further constrain the viscosity, which would enter into the phase diagram mentioned at the beginning of this work.

Appendices

A
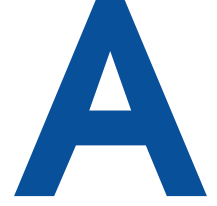
Definitions and variables

A.1 The Armenteros-Podolanski variables

The Armenteros-Podolanski [203] variables are used as a topological selection criterion for V^0 candidates. Especially Λ and K_s^0 candidates are clearly visible as ellipses in the Armenteros-Podolanski space, spanned by the asymmetry α of the decay and a daughter p_T relative to the mother momentum vector, which is named q_T. The variables are given by

$$\alpha = \frac{p_L^+ - p_L^-}{p_L^+ + p_L^-} \qquad \text{with} \qquad p_L^+ = \frac{\overrightarrow{p}^+ \cdot \overrightarrow{p}^{\,\text{mother}}}{|\overrightarrow{p}^{\,\text{mother}}|}, \tag{A.1}$$

and

$$q_T = \frac{\left| \overrightarrow{p}^- \times \overrightarrow{p}^{\,\text{mother}} \right|}{|\overrightarrow{p}^{\,\text{mother}}|}. \tag{A.2}$$

A.2 Decay kinematics

In order to translate the p_T distribution of the $\Xi^-(\Xi^+)$ into the p_T distribution of the Λ daughter, a toy MC was written on the basis of the kinematics of a two-body decay. Input to this MC was the p_T spectrum of the measured and corrected Ξ^-.
Before starting the calculations for each set of random values of the mother p_T according to the input histogram, the mother azimuthal angle and the daughter decay angles, the 4-momenta of the mother with the mass M and the daughters with the masses m_i were initialized via

$$\mathbf{P_M} = (0, 0, 0, M) \tag{A.3}$$
$$\mathbf{P_1} = (0, 0, 0, m_1) \tag{A.4}$$
$$\mathbf{P_1} = (0, 0, 0, m_1). \tag{A.5}$$

Within the centre of mass system of the mother particle:

$$e_1 = \frac{M^2 + m_1^2 - m_2^2}{2\,M} \tag{A.6}$$

$$e_2 = \frac{M^2 - m_1^2 + m_2^2}{2\,M} \tag{A.7}$$

$$p^{\mathrm{cms}} = \sqrt{e_1^2 - m_1^2} = \sqrt{e_2^2 - m_2^2} \tag{A.8}$$

and

$$p_x^{\mathrm{cms}} = p^{\mathrm{cms}} \cdot \sin(\theta) \cdot \cos(\phi) \tag{A.9}$$

$$p_y^{\mathrm{cms}} = p^{\mathrm{cms}} \cdot \sin(\theta) \cdot \sin(\phi) \tag{A.10}$$

$$p_z^{\mathrm{cms}} = p^{\mathrm{cms}} \cdot \cos(\theta) \tag{A.11}$$

$$\Rightarrow$$

$$\mathbf{P_1} = (p_x^{\mathrm{cms}}, p_y^{\mathrm{cms}}, p_z^{\mathrm{cms}}, e_1) \tag{A.12}$$

$$\mathbf{P_2} = (-p_x^{\mathrm{cms}}, -p_y^{\mathrm{cms}}, -p_z^{\mathrm{cms}}, e_2), \tag{A.13}$$

where the polar angle θ and the azimuthal angle ϕ were randomly chosen via $\theta = \arccos(2 \cdot \mathrm{rand}_1 - 1)$ and $\phi = 2\pi \cdot \mathrm{rand}_2$, respectively, with the random numbers $0 \le \mathrm{rand}_i \le 1$. The transverse momentum of the mother was given by a random value from the input histogram. While the azimuthal angle ϕ_M of the mother momentum vector was also chosen randomly in the same way as for the daughters, the polar angle θ_M was fixed to $\pi/2$, causing the longitudinal mother momentum $p_z = \cos(\theta_M)$ to be zero. This yields for the mother variables

$$E_M = \sqrt{M^2 + p_{\mathrm{T}}^2} \tag{A.14}$$

$$p_x = p_{\mathrm{T}} \cdot \cos(\phi_M) \tag{A.15}$$

$$p_y = p_{\mathrm{T}} \cdot \sin(\phi_M) \tag{A.16}$$

$$p_z = 0 \tag{A.17}$$

$$\Rightarrow$$

$$\mathbf{P_M} = (p_x, p_y, 0, M) \tag{A.18}$$

$$\beta_x = \frac{p_x}{E_M}, \quad \beta_y = \frac{p_y}{E_M}, \quad \beta_z = 0. \tag{A.19}$$

After the applying the rapidity cut of $|y| < 0.5$, the boost for each daughter Lorentz vector (A.12, A.13) was performed with the ROOT function `TLorentzVector::Boost(`β_x`,`β_y`,0)`. Finally, a 2D histogram was filled for the randomly chosen Ξ^- p_{T} and the corresponding secondary Λ p_{T}.

B
Analysis documentation

B.1 Run lists of data sets

Pb–Pb

The analysed data sample was LHC10h.pass2, which was processed in the ESD format. The following runs were investigated:

137161, 137162, 137231, 137232, 137235, 137236, 137243, 137366, 137431, 137432, 137434, 137439, 137440, 137441, 137443, 137530, 137531, 137539, 137541, 137544, 137546, 137549, 137595, 137608, 137638, 137639, 137685, 137686, 137691, 137692, 137693, 137704, 137718, 137722, 137724, 137751, 137752, 137844, 137848, 138190, 138192, 138197, 138201, 138225, 138275, 138364, 138396, 138438, 138439, 138442, 138469, 138534, 138578, 138579, 138582, 138583, 138621, 138624, 138638, 138652, 138653, 138662, 138666, 138730, 138732, 138837, 138870, 138871, 138872, 139028, 139029, 139036, 139037, 139038, 139105, 139107, 139173, 139309, 139310, 139314, 139328, 139329, 139360, 139437, 139438, 139465, 139503, 139505, 139507, 139510.

pp

The LHC11a sample was reconstructed twice, once with and once without the SDD information. The corresponding names of the data sets are LHC11a_with_SDD.pass2 (wSDD) and LHC11a_without_SDD.pass2 (nSDD). The following runs were investigated:

146746,146747, 146748, 146801, 146802, 146803, 146804, 146805, 146806, 146807, 146817, 146824, 146856, 146858, 146859, 146860.

B.2 Lists of MC samples

Pb–Pb

LHC11a10a_bis, LHC11a10b_bis and LHC11a10b_plus.

pp

LHC12b1a,b,c and LHC12b1a,b,c_wSDD. These MC samples were specially produced for this analysis. During the simulation, only events which contain at least one Λ

(LHC12b1a) or at least a $\overline{\Lambda}$ (LHC12b1b) or a K^0_s (LHC12b1c) with $p_\mathrm{T} > 2\,\mathrm{GeV}/c$ were accepted. For the low p_T region, the samples LHC11b10a (minimum bias) and LHC11b10b (injected particles) were also studied.

Material budget study

LHC10h9 with a material budget enhancement by 7% and LHC10h10 with a reduction of 7%.

B.3 Invariant mass distributions
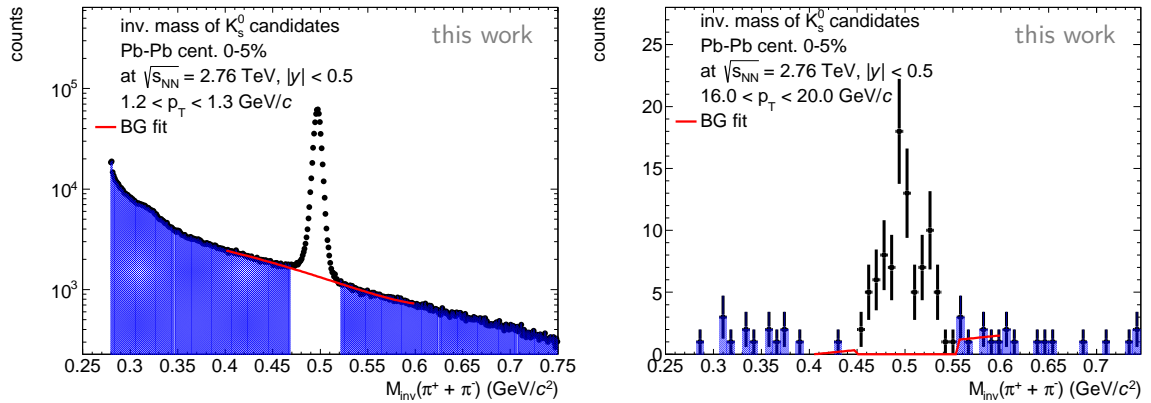
Figure B.1: Invariant mass distributions of K_s^0 candidates in central Pb–Pb collisions for two p_T bins, at lower p_T (1.2 GeV/$c < p_T < 1.3$ GeV/c) in the left panel and for the last p_T bin (16.0 GeV/$c < p_T < 20.0$ GeV/c) in the right panel. The white area underneath the peak represents the mass window which is excluded from the background fit (red line). The interrupted red line is a fit result of the likelihood fit method which was used in case of low statistics.
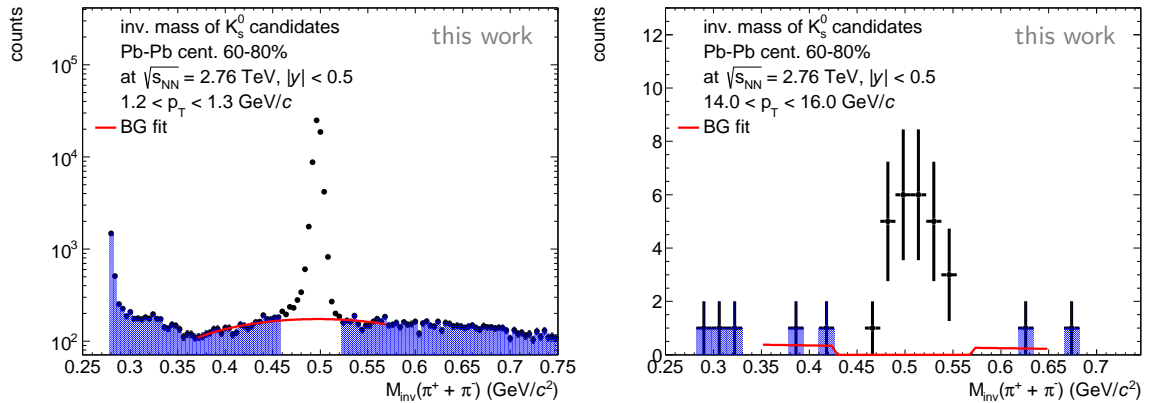
Figure B.2: Invariant mass distributions of K_s^0 candidates in peripheral Pb–Pb collisions for two p_T bins, at lower p_T (1.2 GeV/$c < p_T < 1.3$ GeV/c) in the left panel and for the last p_T bin (14.0 GeV/$c < p_T < 16.0$ GeV/c) in the right panel. The white area underneath the peak represents the mass window which is excluded from the background fit (red line). The interrupted red line is a fit result of the likelihood fit method which was used in case of low statistics.
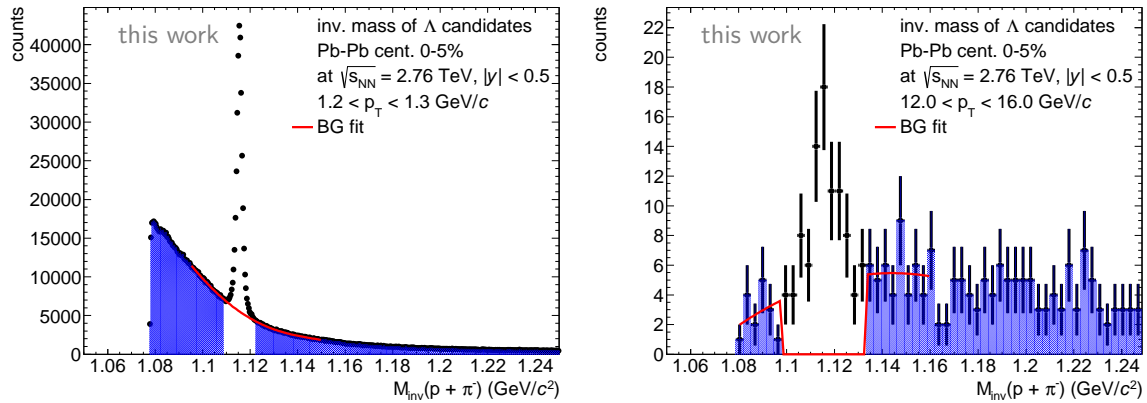
Figure B.3: Invariant mass distributions of Λ candidates in central Pb–Pb collisions for two p_T bins, at lower p_T (1.2 GeV/c < p_T < 1.3 GeV/c) in the left panel and for the last p_T bin (12.0 GeV/c < p_T < 16.0 GeV/c) in the right panel. The white area underneath the peak represents the mass window which is excluded from the background fit (red line). The interrupted red line is a fit result of the likelihood fit method which was used in case of low statistics.
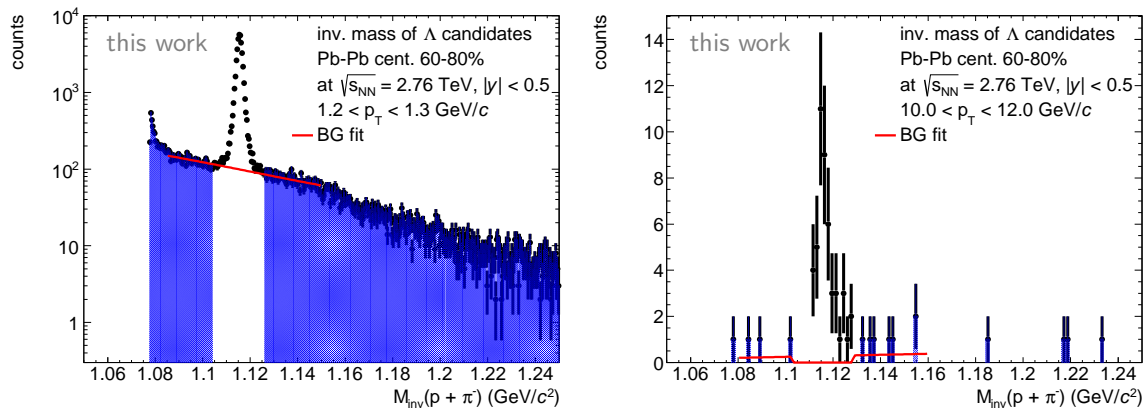
Figure B.4: Invariant mass distributions of Λ candidates in peripheral Pb–Pb collisions for two p_T bins, at lower p_T (1.2 GeV/c < p_T < 1.3 GeV/c) in the left panel and for the last p_T bin (10.0 GeV/c < p_T < 12.0 GeV/c) in the right panel. The white area underneath the peak represents the mass window which is excluded from the background fit (red line). The interrupted red line is a fit result of the likelihood fit method which was used in case of low statistics.
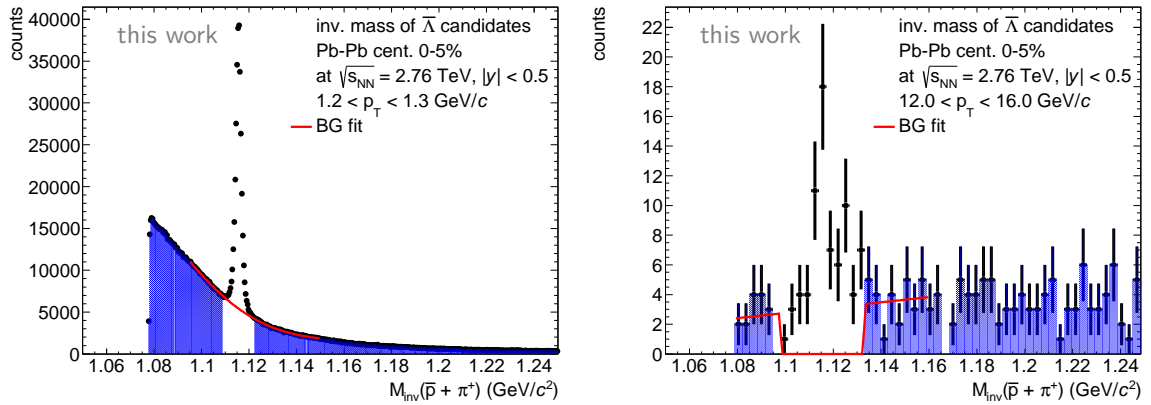
Figure B.5: Invariant mass distributions of $\overline{\Lambda}$ candidates in central Pb–Pb collisions for two p_T bins, at lower p_T (1.2 GeV/c < p_T < 1.3 GeV/c) in the left panel and for the last p_T bin (12.0 GeV/c < p_T < 16.0 GeV/c) in the right panel. The white area underneath the peak represents the mass window which is excluded from the background fit (red line). The interrupted red line is a fit result of the likelihood fit method which was used in case of low statistics.
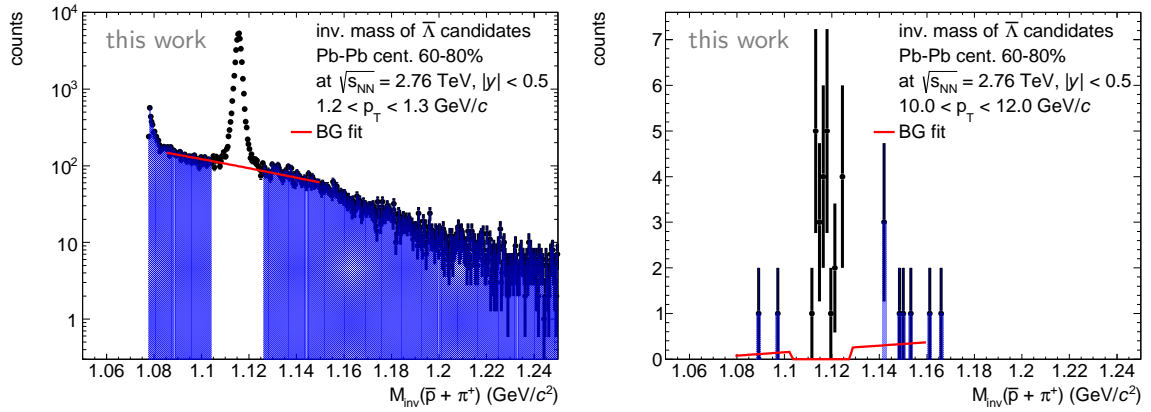
Figure B.6: Invariant mass distributions of $\overline{\Lambda}$ candidates in peripheral Pb–Pb collisions for two p_T bins, at lower p_T (1.2 GeV/c < p_T < 1.3 GeV/c) in the left panel and for the last p_T bin (10.0 GeV/c < p_T < 12.0 GeV/c) in the right panel. The white area underneath the peak represents the mass window which is excluded from the background fit (red line). The interrupted red line is a fit result of the likelihood fit method which was used in case of low statistics.
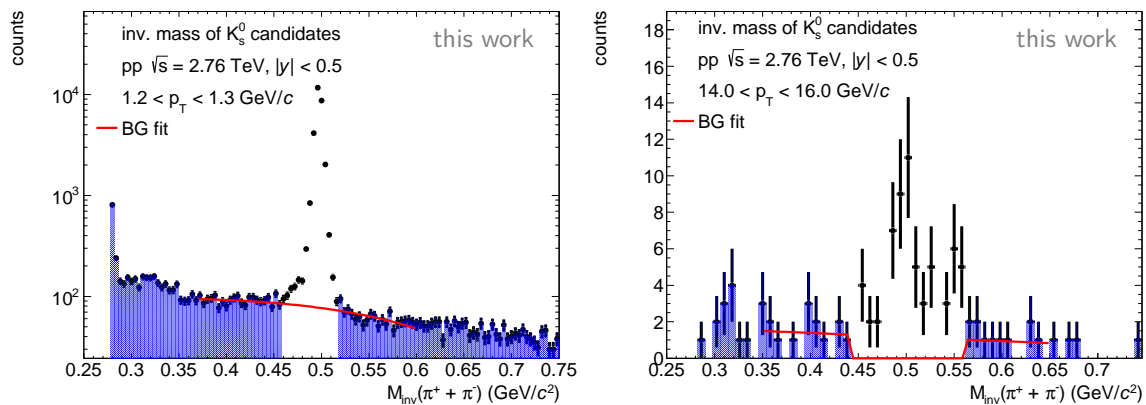
Figure B.7: Invariant mass distributions of K_s^0 candidates in pp collisions for two p_T bins, at lower p_T (1.2 GeV/c < p_T < 1.3 GeV/c) in the left panel and for the last p_T bin (14.0 GeV/c < p_T < 16.0 GeV/c) in the right panel. The white area underneath the peak represents the mass window which is excluded from the background fit (red line). The interrupted red line is a fit result of the likelihood fit method which was used in case of low statistics.
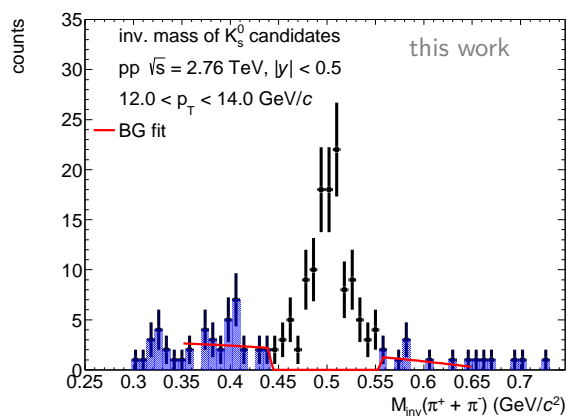
Figure B.8: Invariant mass distributions of K_s^0 candidates in pp collisions for the last p_T bin used at 12.0 GeV/c < p_T < 14.0 GeV/c. The white area underneath the peak represents the mass window which is excluded from the background fit (red line). The interrupted red line is a fit result of the likelihood fit method which was used in case of low statistics.
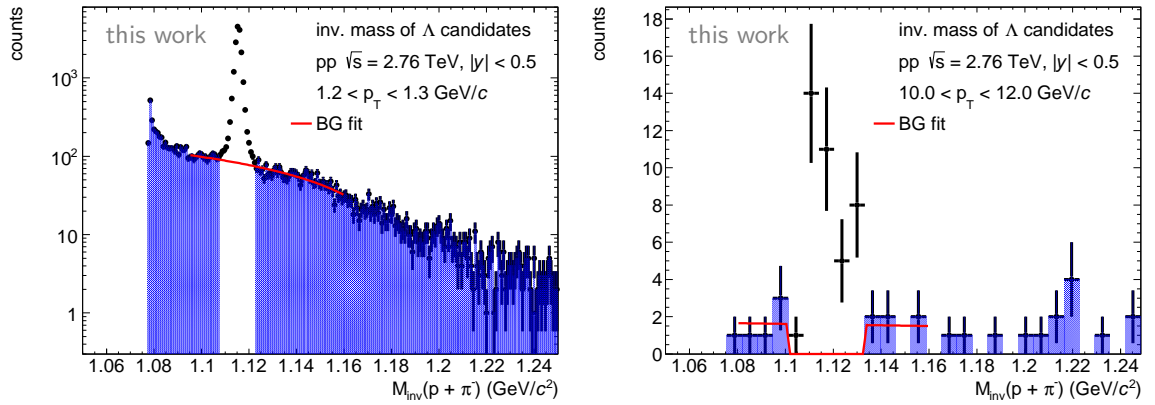
Figure B.9: Invariant mass distributions of Λ candidates in pp collisions for two p_{T} bins, at lower p_{T} (1.2 GeV/c < p_{T} < 1.3 GeV/c) in the left panel and for the last p_{T} bin (10.0 GeV/c < p_{T} < 12.0 GeV/c) in the right panel. The white area underneath the peak represents the mass window which is excluded from the background fit (red line). The interrupted red line is a fit result of the likelihood fit method which was used in case of low statistics.
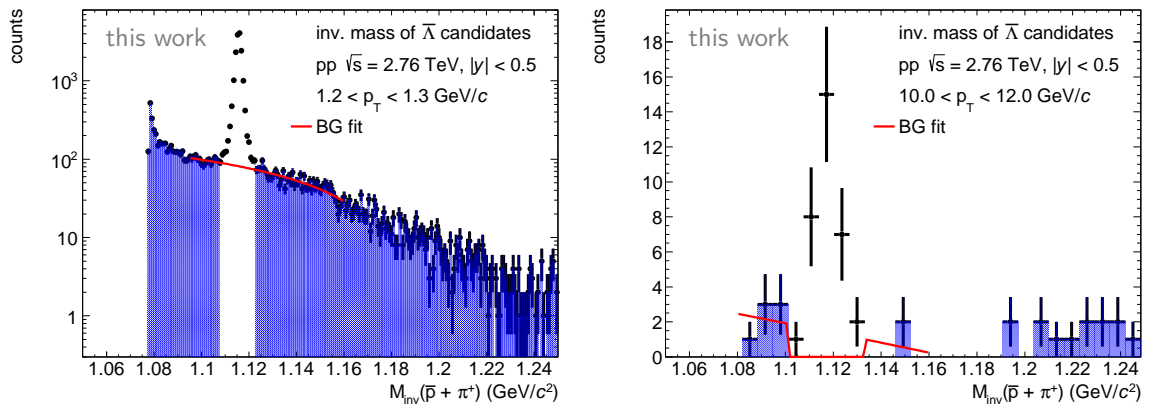
Figure B.10: Invariant mass distributions of $\overline{\Lambda}$ candidates in pp collisions for two p_{T} bins, at lower p_{T} (1.2 GeV/c < p_{T} < 1.3 GeV/c) in the left panel and for the last p_{T} bin (10.0 GeV/c < p_{T} < 12.0 GeV/c) in the right panel. The white area underneath the peak represents the mass window which is excluded from the background fit (red line). The interrupted red line is a fit result of the likelihood fit method which was used in case of low statistics.

Peak windows
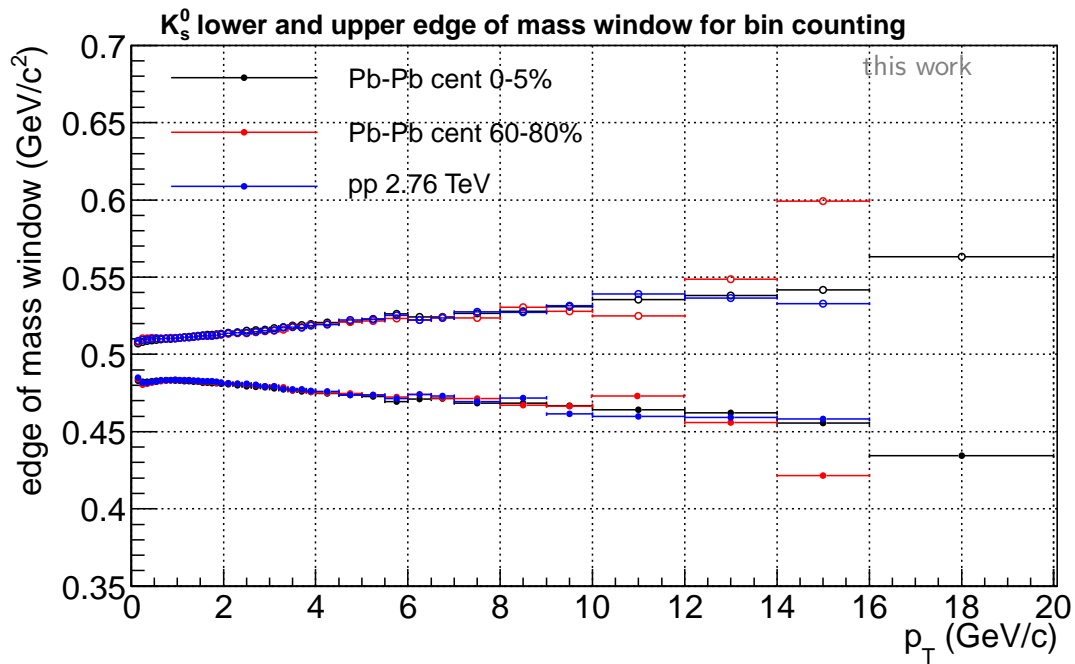
Figure B.11: The edges of the mass window used for the bin counting of the signal extraction for K_s^0.
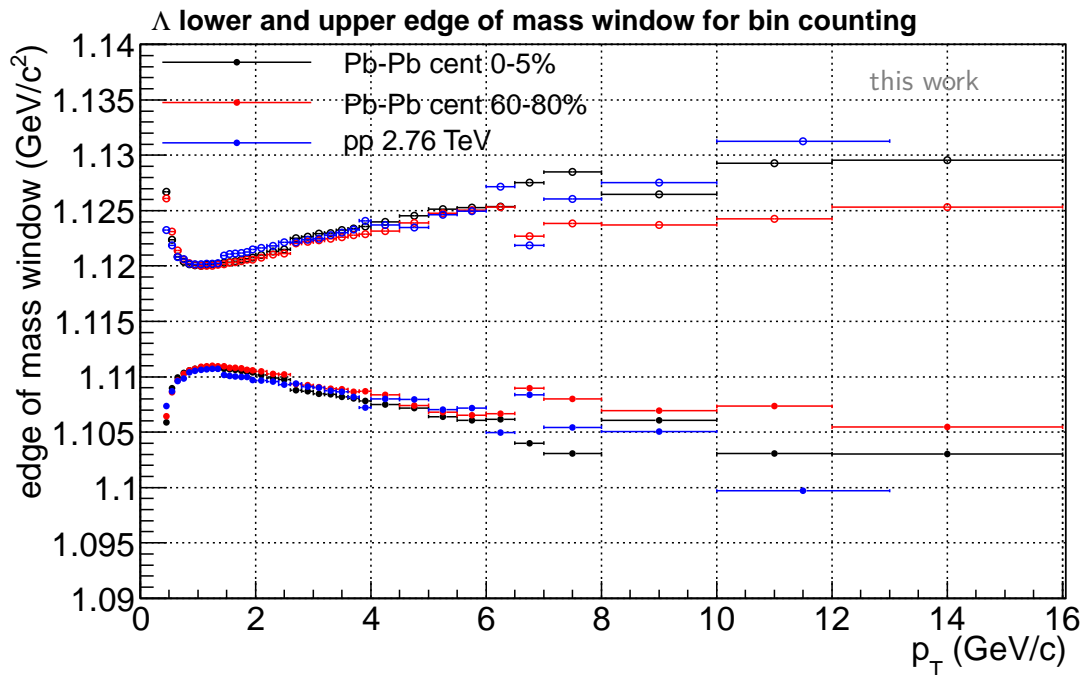
Figure B.12: The edges of the mass window used for the bin counting of the signal extraction for Λ.

Masses and peak widths
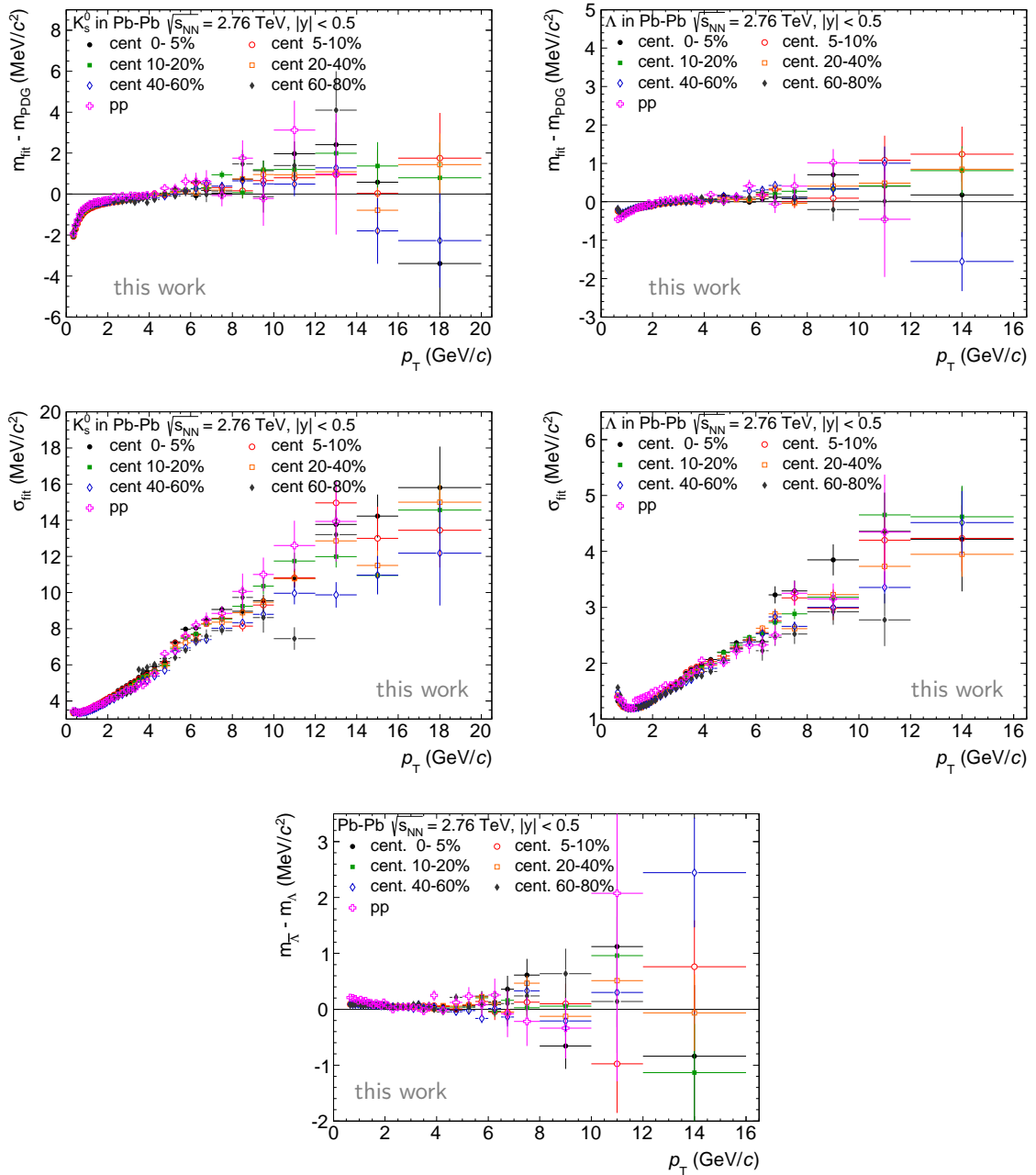
Figure B.13: Top: Difference of the mass obtained from Gaussian fit to the K_s^0 (left) and Λ (right) invariant mass peak after BG subtraction to the literature mass documented in [13]. Middle: Peak width obtained from Gaussian fit to the K_s^0 (left) and Λ (right) invariant mass peak after BG subtraction. Bottom: Difference of the mass obtained from a Gaussian fit to the invariant mass peak of $\overline{\Lambda}$ and Λ after BG subtraction.

B.4 Figures of MC to data comparison

K_s^0 Pb–Pb
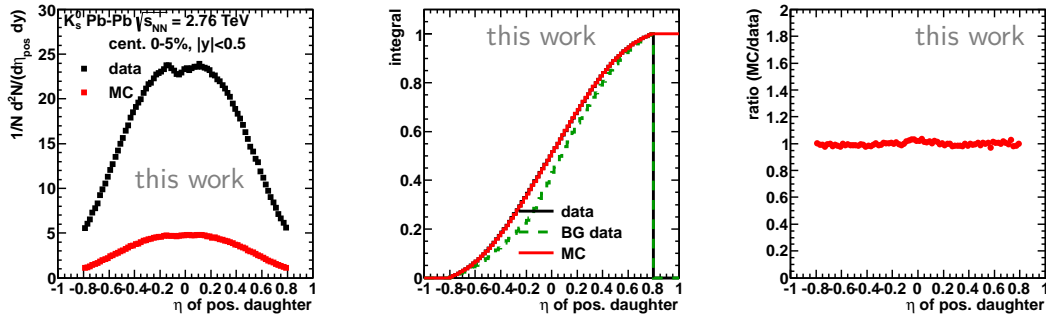
Figure B.14: Comparison of the pseudo-rapidity of positive K_s^0 daughters in data with that in MC rescaled with the data p_T distribution in central Pb–Pb collisions. The ratio of MC and data is normalized to the ratio of the distribution integrals.
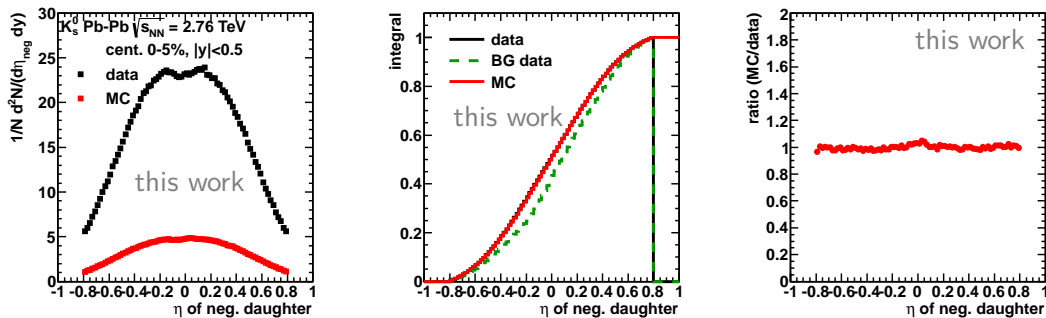
Figure B.15: Comparison of the pseudo-rapidity of negative K_s^0 daughters in data with that in MC rescaled with the data p_T distribution in central Pb–Pb collisions. The ratio of MC and data is normalized to the ratio of the distribution integrals.
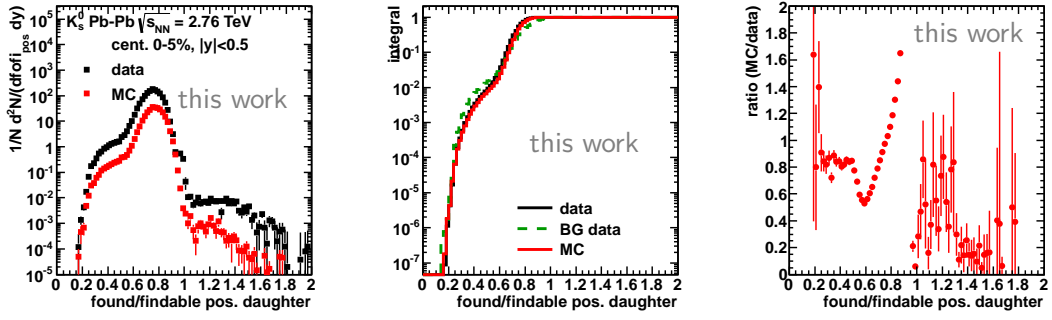
Figure B.16: Comparison of the ratio found/findable cluster in the TPC for the positive K_s^0 daughter in data with that in MC rescaled with the data p_T distribution in central Pb–Pb collisions. The ratio of MC and data is normalized to the ratio of the distribution integrals.
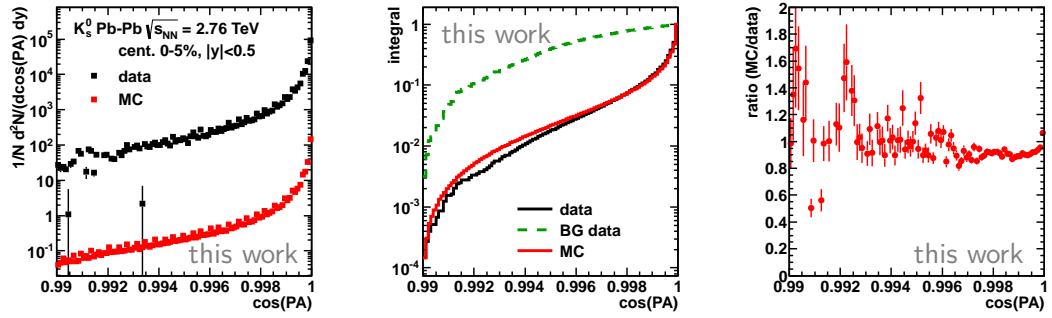
Figure B.17: Comparison of the cosine of pointing angle of K_s^0 in data with that in MC rescaled with the data p_T distribution in central Pb–Pb collisions. The ratio of MC and data is normalized to the ratio of the distribution integrals.
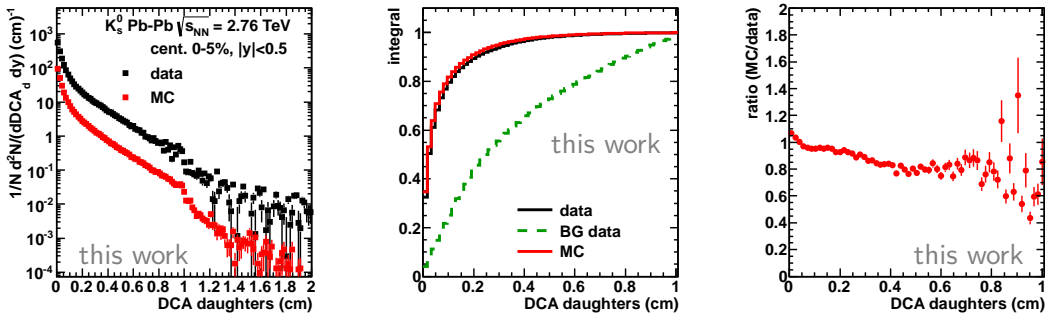
Figure B.18: Comparison of the DCA between the daughters of K_s^0 in data with that in MC rescaled with the data p_T distribution in central Pb–Pb collisions. The ratio of MC and data is normalized to the ratio of the distribution integrals.
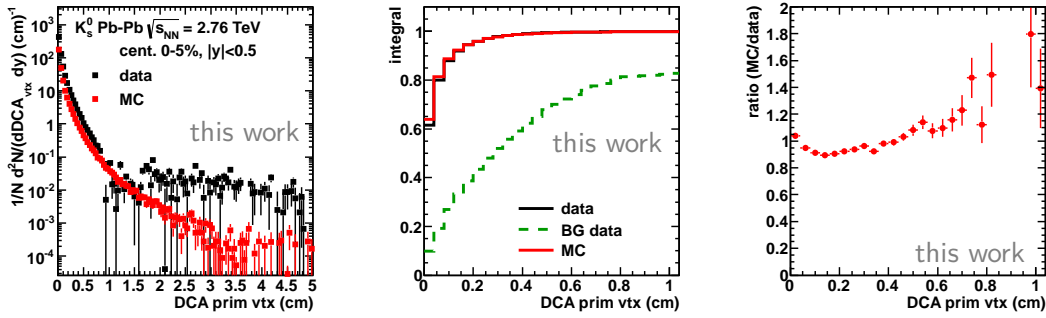
Figure B.19: Comparison of the DCA of the K_s^0 to the primary vertex in data with that in MC rescaled with the data p_T distribution in central Pb–Pb collisions. The ratio of MC and data is normalized to the ratio of the distribution integrals.
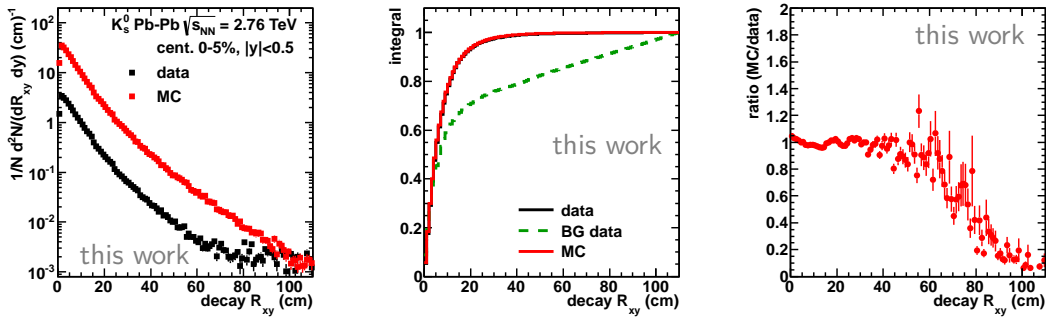
Figure B.20: Comparison of the 2D decay radius of K_s^0 in data with that in MC rescaled with the data p_T distribution in central Pb–Pb collisions. The ratio of MC and data is normalized to the ratio of the distribution integrals.
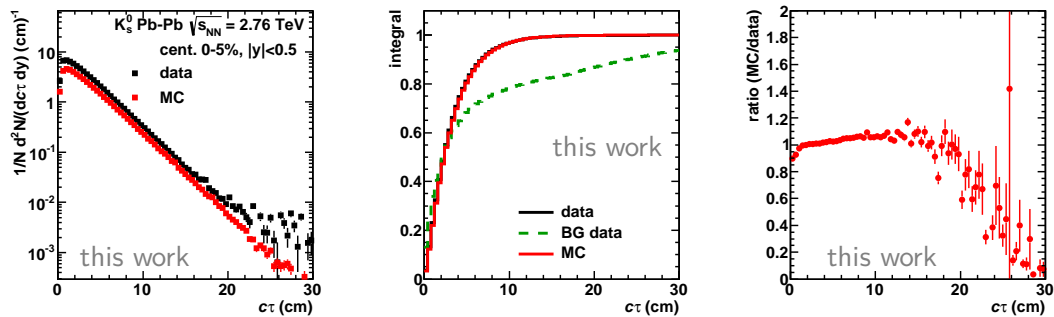
Figure B.21: Comparison of the proper decay length ($c\tau$) of K_s^0 in data with that in MC rescaled with the data p_T distribution in central Pb–Pb collisions. The ratio of MC and data is normalized to the ratio of the distribution integrals.

K_s^0 pp
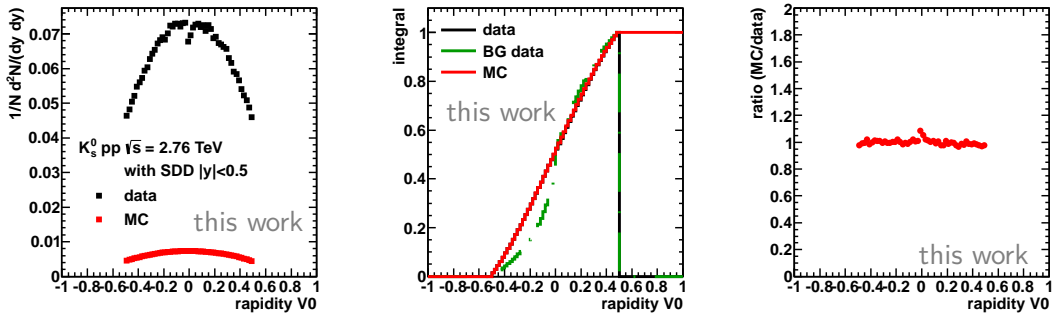
Figure B.22: Comparison of the rapidity of K_s^0 in data with that in MC rescaled with the data p_T distribution in pp collisions. The ratio of MC and data is normalized to the ratio of the distribution integrals.
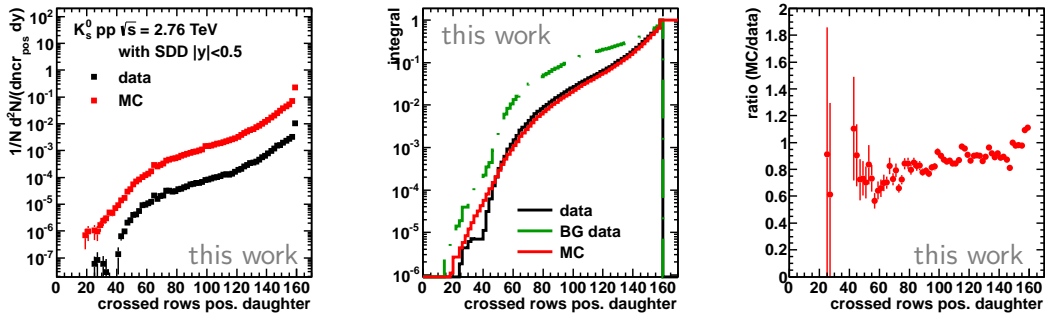
Figure B.23: Comparison of the number of crossed rows in the TPC for the positive K_s^0 daughter in data with that in MC rescaled with the data p_T distribution in pp. The ratio of MC and data is normalized to the ratio of the distribution integrals.
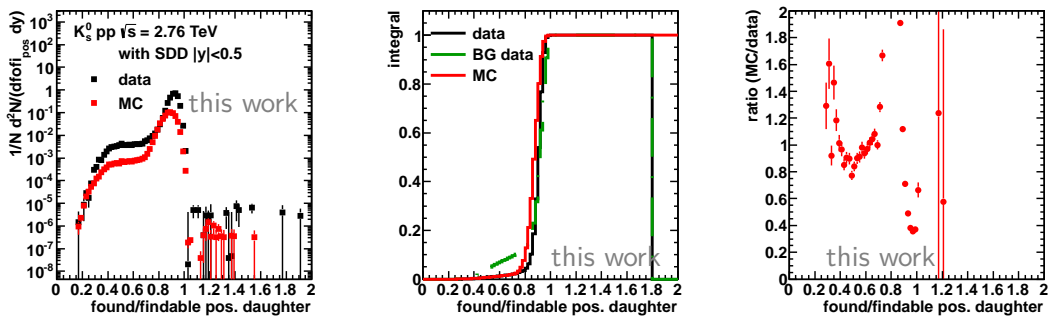
Figure B.24: Comparison of the ratio found/findable clusters in the TPC for the positive K_s^0 daughter in data with that in MC rescaled with the data p_T distribution in pp. The ratio of MC and data is normalized to the ratio of the distribution integrals.
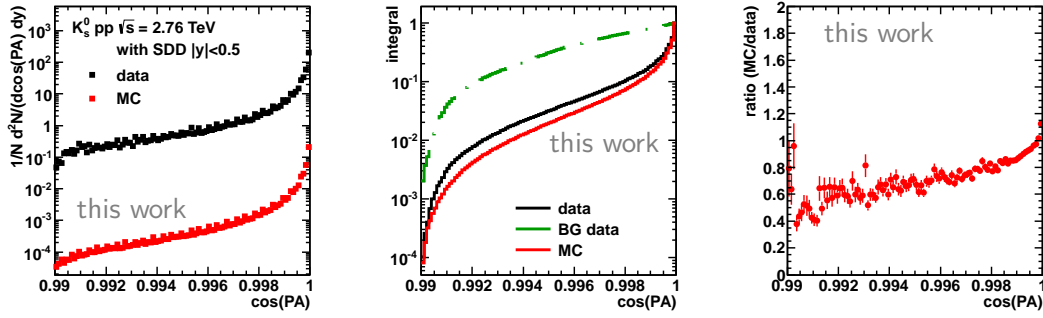
Figure B.25: Comparison of the cosine of pointing angle of K_s^0 in data with that in MC rescaled with the data p_T distribution in pp. The ratio of MC and data is normalized to the ratio of the distribution integrals.
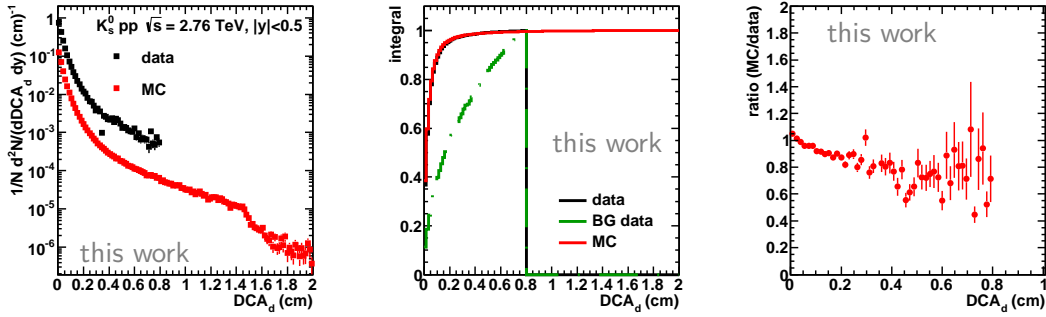
Figure B.26: Comparison of the DCA between the K_s^0 daughters in data with that in MC rescaled with the data p_T distribution in pp. The ratio of MC and data is normalized to the ratio of the distribution integrals.
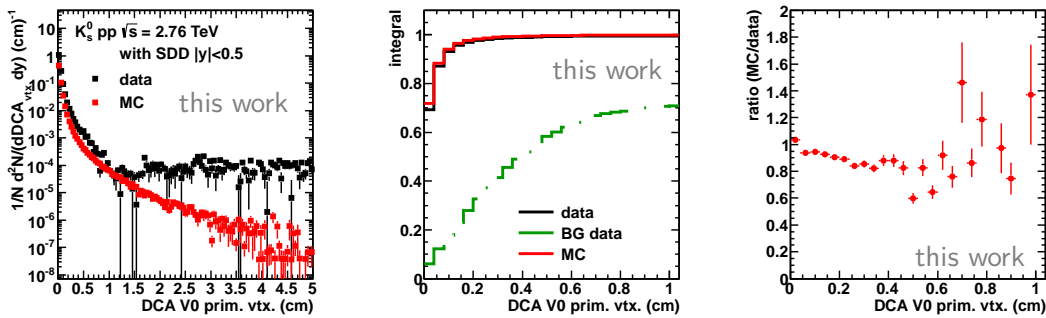
Figure B.27: Comparison of the DCA of K_s^0 to the primary vertex in data with that in MC rescaled with the data p_T distribution in pp. The ratio of MC and data is normalized to the ratio of the distribution integrals.
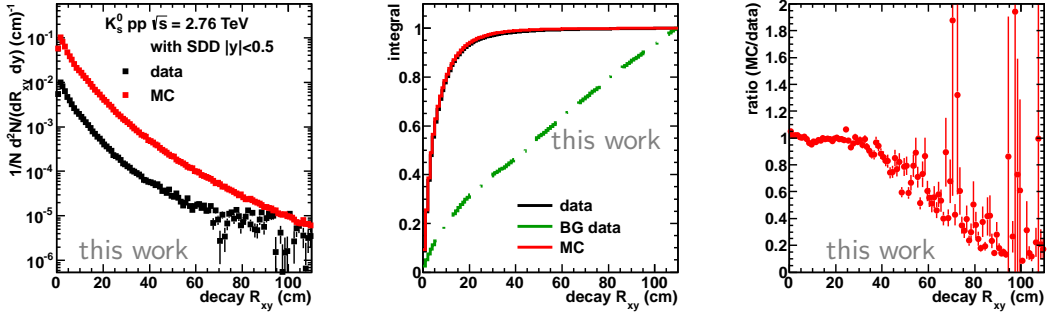
Figure B.28: Comparison of the 2D decay radius of K_s^0 in data with that in MC rescaled with the data p_T distribution in pp. The ratio of MC and data is normalized to the ratio of the distribution integrals.
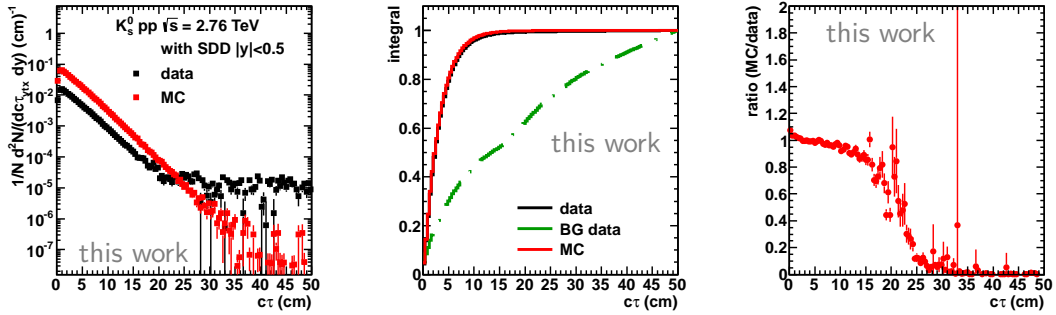
Figure B.29: Comparison of the lifetime of K_s^0 in data with that in MC rescaled with the data p_T distribution in pp. The ratio of MC and data is normalized to the ratio of the distribution integrals.
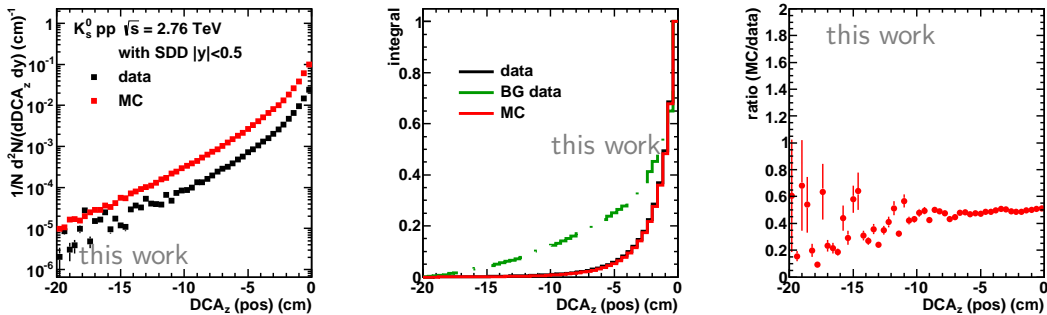
Figure B.30: Comparison of the z-component of the DCA of the positive K_s^0 daughter in data with that in MC rescaled with the data p_T distribution in pp. The ratio of MC and data is normalized to the ratio of the distribution integrals.

Λ Pb–Pb
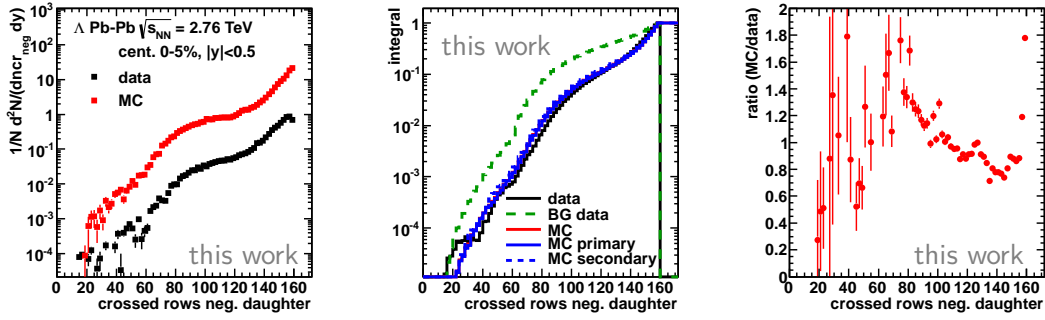
Figure B.31: Comparison of the number of crossed rows in the TPC for the negative Λ daughter in data with that in MC rescaled with the data p_T distribution in central Pb–Pb collisions. The ratio of MC and data is normalized to the ratio of the distribution integrals.
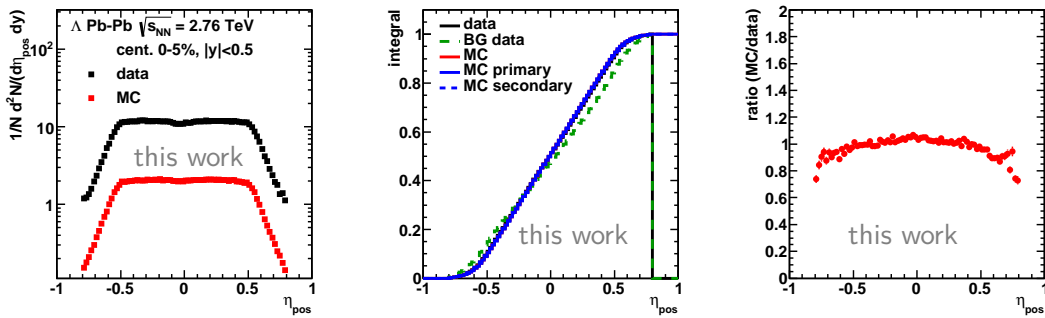
Figure B.32: Comparison of pseudo-rapidity of the positive Λ daughter in data with that in MC rescaled with the data p_T distribution in central Pb–Pb collisions. The ratio of MC and data is normalized to the ratio of the distribution integrals.
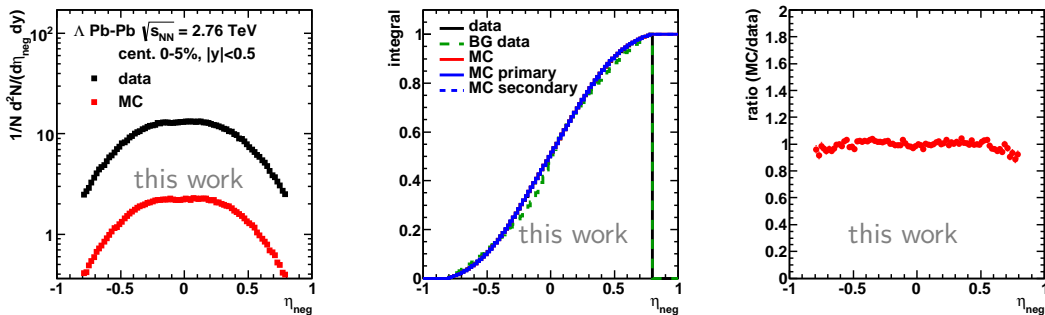
Figure B.33: Comparison of pseudo-rapidity of the negative Λ daughter in data with that in MC rescaled with the data p_T distribution in central Pb–Pb collisions. The ratio of MC and data is normalized to the ratio of the distribution integrals.
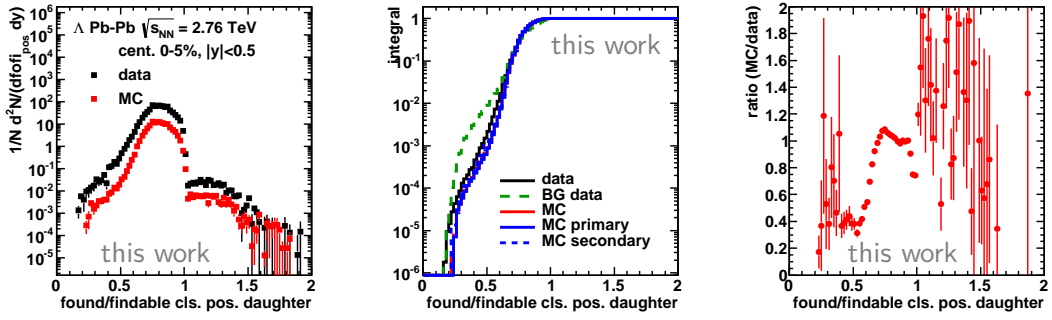
Figure B.34: Comparison of the ratio found/findable clusters in the TPC for the positive Λ daughter in data with that in MC rescaled with the data p_T distribution in central Pb–Pb collisions. The ratio of MC and data is normalized to the ratio of the distribution integrals.
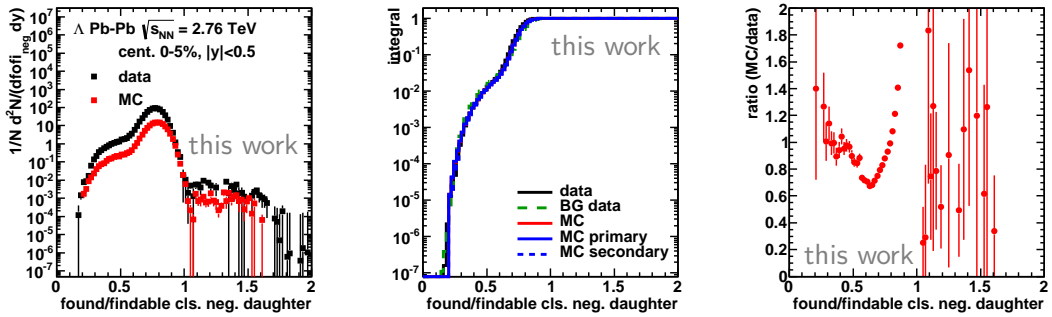
Figure B.35: Comparison of the ratio found/findable clusters in the TPC for the negative Λ daughter in data with that in MC rescaled with the data p_T distribution in central Pb–Pb collisions. The ratio of MC and data is normalized to the ratio of the distribution integrals.
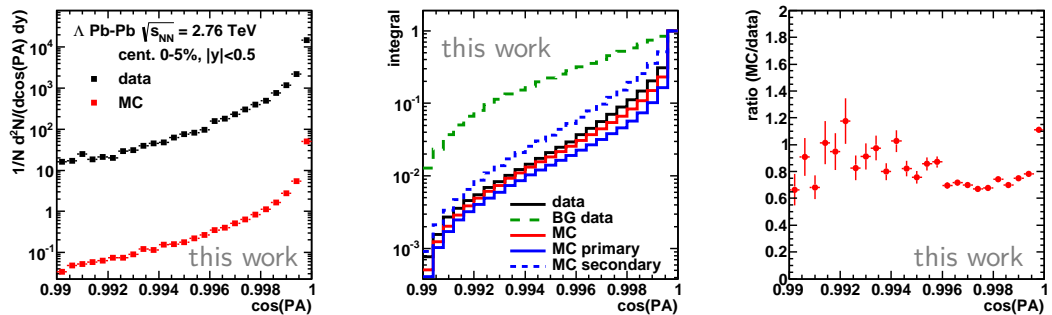
Figure B.36: Comparison of the cosine of pointing angle of Λ in data with that in MC rescaled with the data p_T distribution in central Pb–Pb collisions. The ratio of MC and data is normalized to the ratio of the distribution integrals.
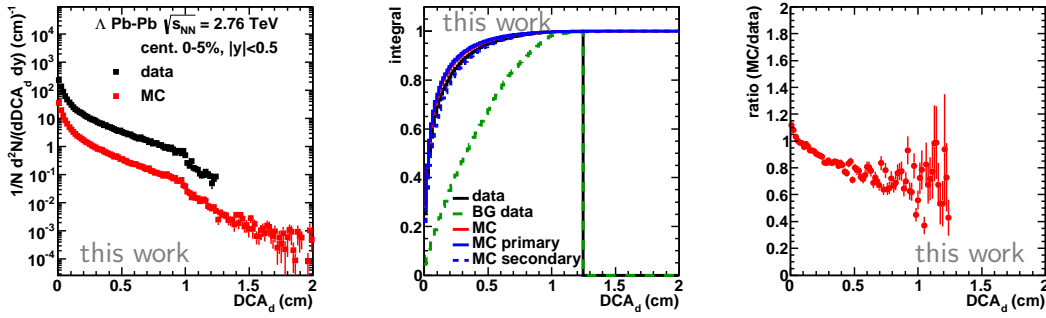
Figure B.37: Comparison of the DCA between the daughters of Λ in data with that in MC rescaled with the data p_T distribution in central Pb–Pb collisions. The ratio of MC and data is normalized to the ratio of the distribution integrals.
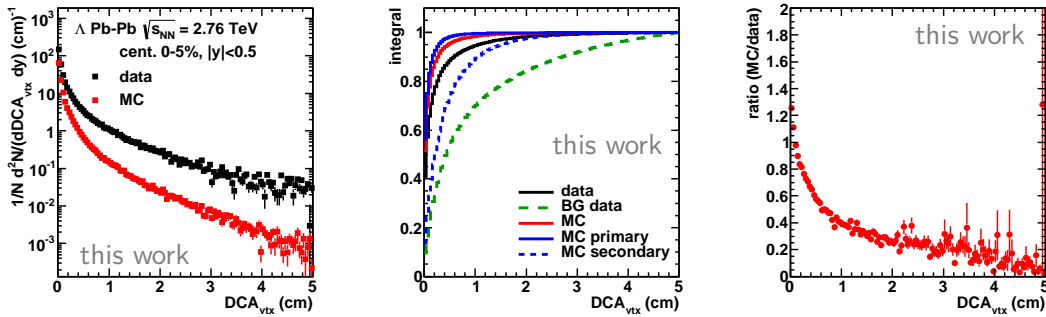
Figure B.38: Comparison of the DCA of the Λ to the primary vertex in data with that in MC rescaled with the data p_T distribution in central Pb–Pb collisions. The ratio of MC and data is normalized to the ratio of the distribution integrals.
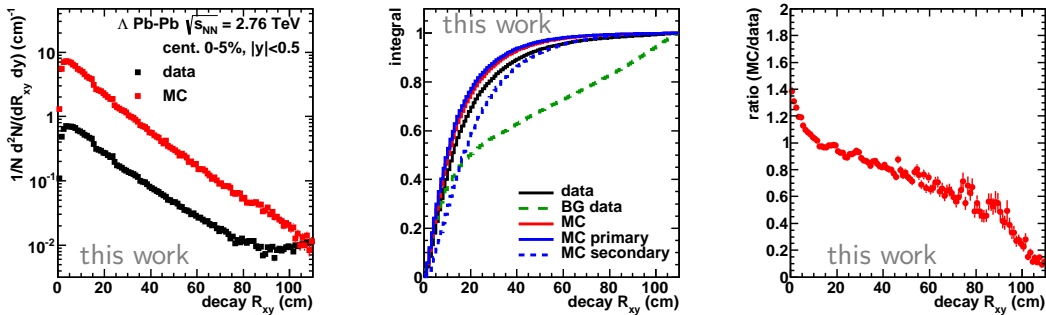
Figure B.39: Comparison of the 2D decay radius of Λ in data with that in MC rescaled with the data p_T distribution in central Pb–Pb collisions. The ratio of MC and data is normalized to the ratio of the distribution integrals.
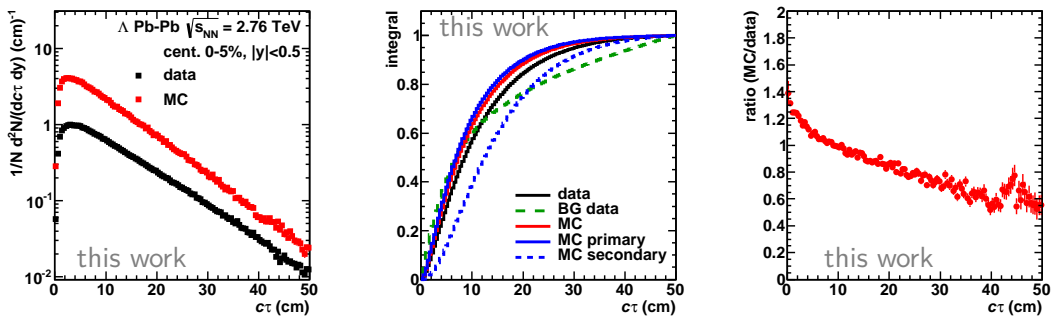
Figure B.40: Comparison of the proper lifetime $c\tau$ of Λ in data with that in MC rescaled with the data p_T distribution in central Pb–Pb collisions. The ratio of MC and data is normalized to the ratio of the distribution integrals.

Λ pp
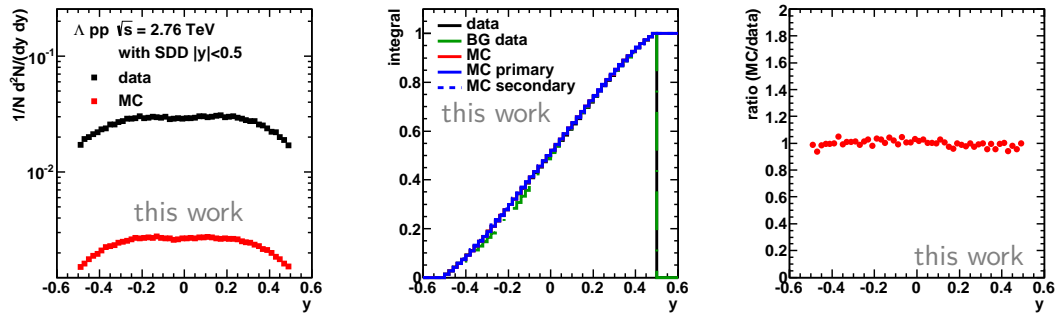
Figure B.41: Comparison of the rapidity of Λ in data with that in MC rescaled with the data p_T distribution in pp collisions. The ratio of MC and data is normalized to the ratio of the distribution integrals.
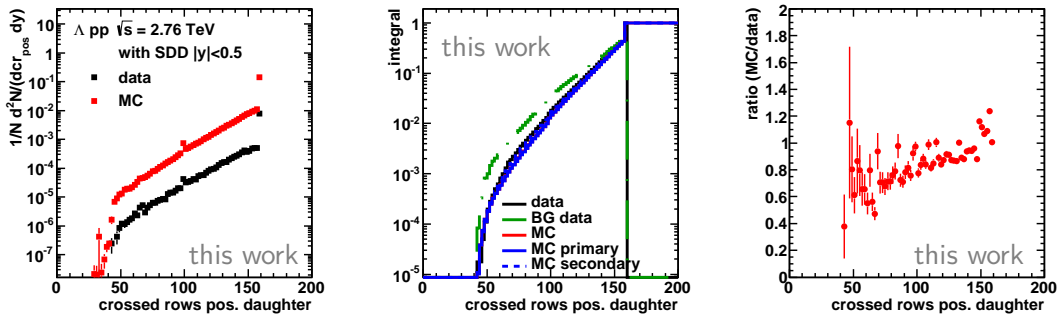
Figure B.42: Comparison of the number of crossed rows in the TPC for the positive Λ daughter in data with that in MC rescaled with the data p_T distribution in pp collisions. The ratio of MC and data is normalized to the ratio of the distribution integrals.
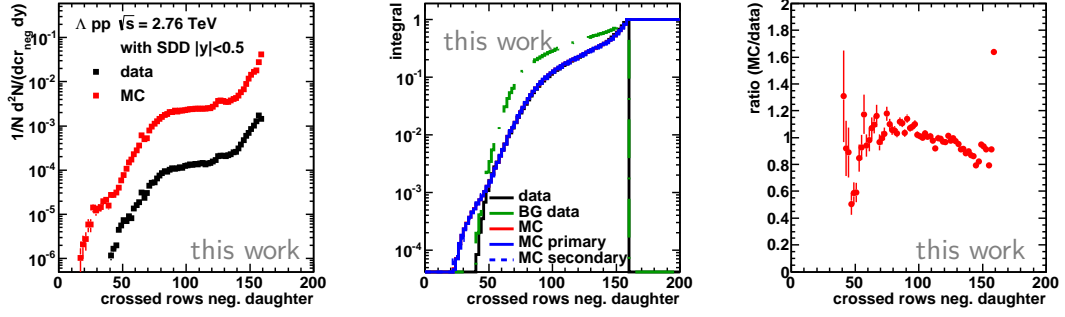
Figure B.43: Comparison of the number of crossed rows in the TPC for the negative Λ daughter in data with that in MC rescaled with the data p_T distribution in pp collisions. The ratio of MC and data is normalized to the ratio of the distribution integrals.
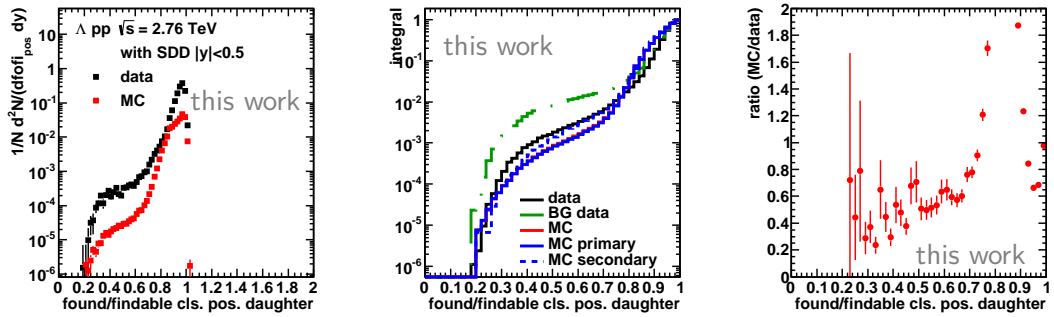
Figure B.44: Comparison of the ratio of found/findable clusters in the TPC for the positive Λ daughter in data with that in MC rescaled with the data p_T distribution in pp collisions. The ratio of MC and data is normalized to the ratio of the distribution integrals.
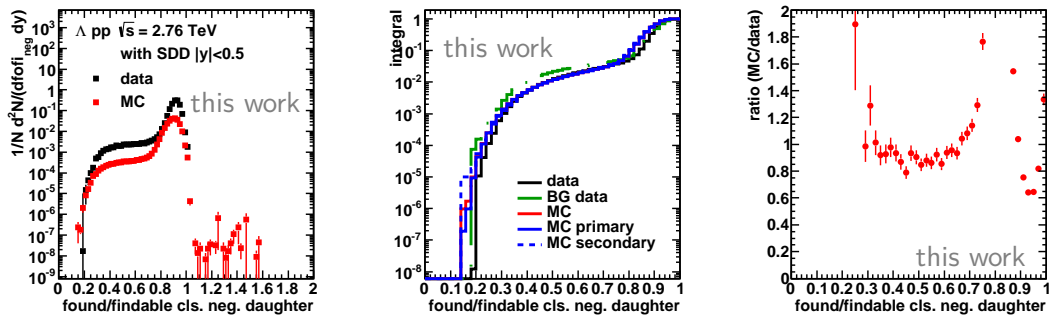
Figure B.45: Comparison of the ratio of found/findable clusters in the TPC for the negative Λ daughter in data with that in MC rescaled with the data p_T distribution in pp collisions. The ratio of MC and data is normalized to the ratio of the distribution integrals.
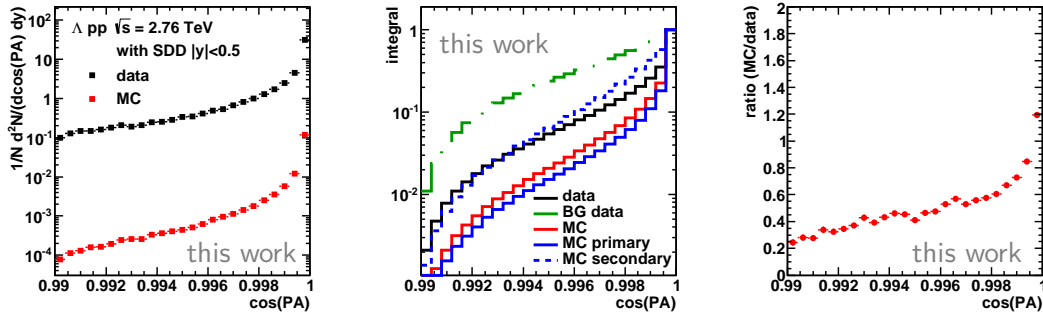
Figure B.46: Comparison of the cosine of pointing angle of Λ in data with that in MC rescaled with the data p_T distribution in pp collisions. The ratio of MC and data is normalized to the ratio of the distribution integrals.
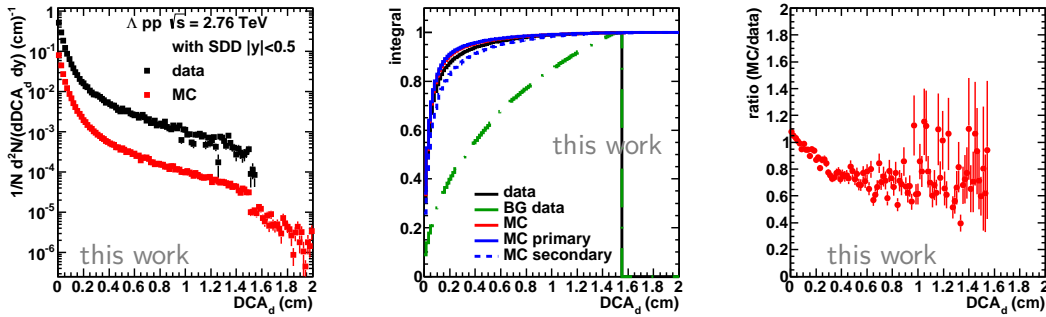
Figure B.47: Comparison of the DCA between the Λ daughters in data with that in MC rescaled with the data p_T distribution in pp collisions. The ratio of MC and data is normalized to the ratio of the distribution integrals.
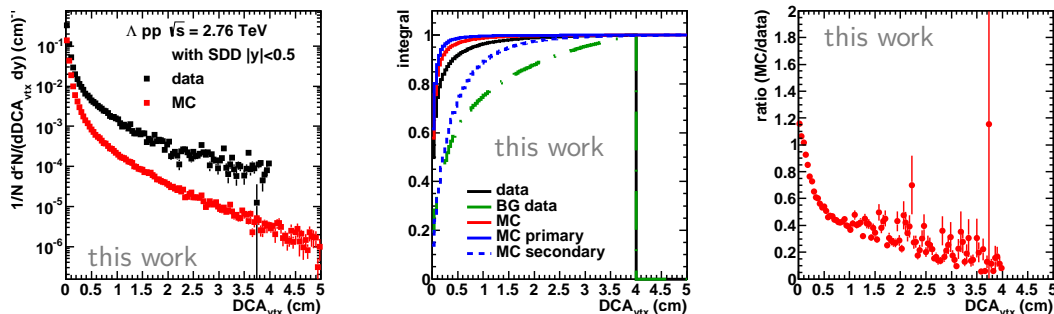
Figure B.48: Comparison of the DCA of Λ to the primary vertex in data with that in MC rescaled with the data p_T distribution in pp collisions. The ratio of MC and data is normalized to the ratio of the distribution integrals.
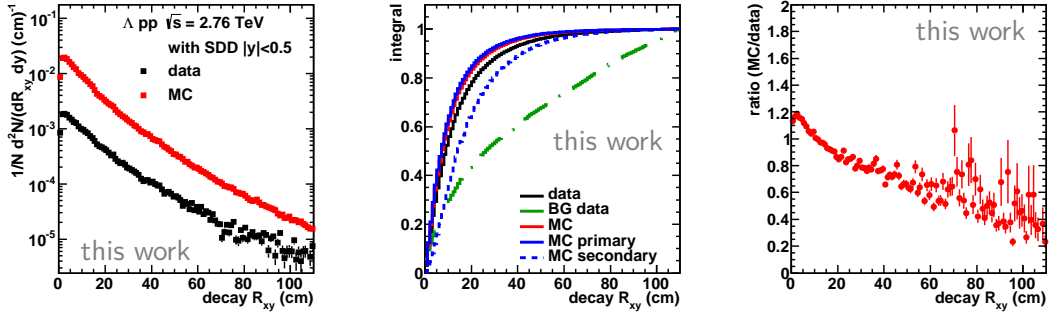
Figure B.49: Comparison of the 2D decay radius Λ in data with that in MC rescaled with the data p_T distribution in pp collisions. The ratio of MC and data is normalized to the ratio of the distribution integrals.
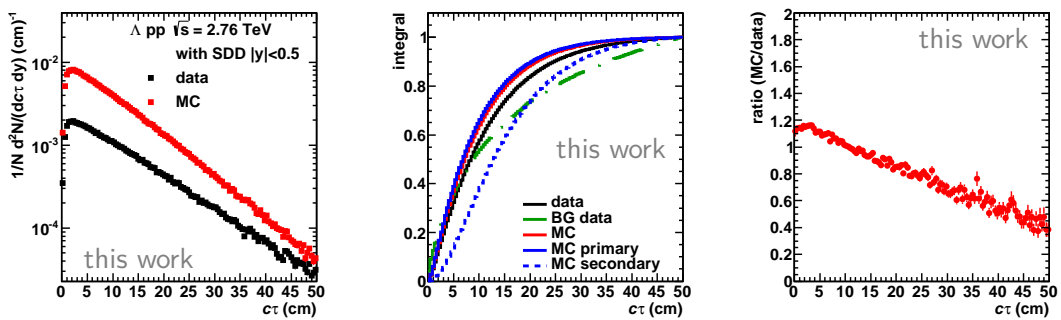
Figure B.50: Comparison of the lifetime of Λ in data with that in MC rescaled with the data p_T distribution in pp collisions. The ratio of MC and data is normalized to the ratio of the distribution integrals.

B.5 Figures cut studies

B.5.1 Λ Pb–Pb
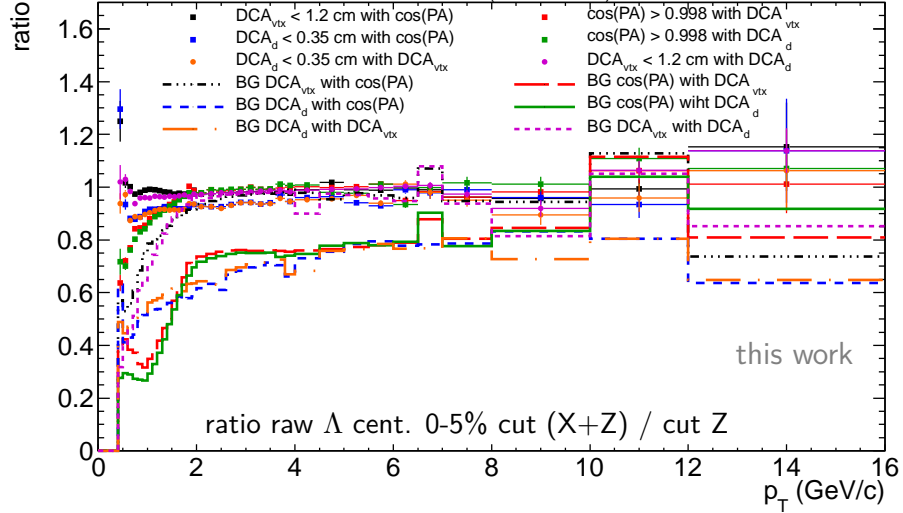
Figure B.51: Ratio of raw Λ spectra in central Pb–Pb collisions with the cut X indicated in the legend plus cut Z applied over those spectra without cut X but with cut Z applied.
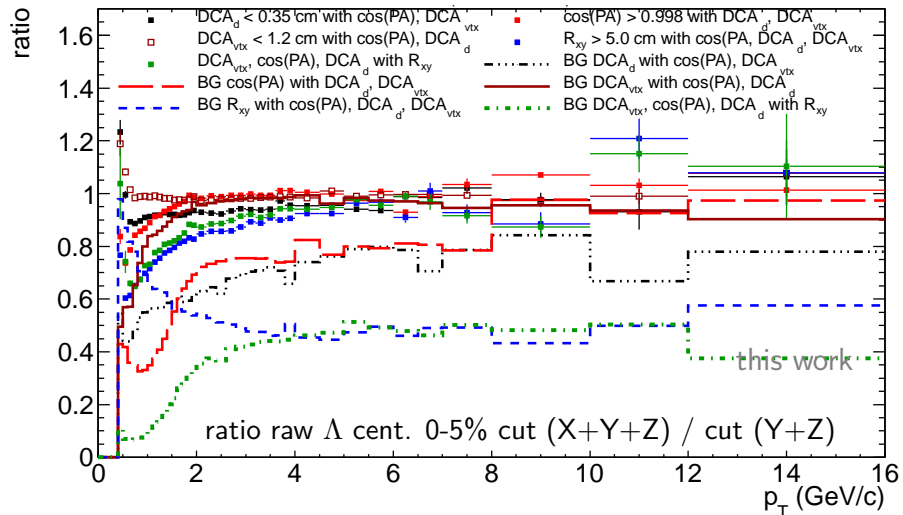
Figure B.52: Ratio of raw Λ spectra in central Pb–Pb collisions with the cut X indicated in the legend applied plus cuts Y+Z over those spectra without cut X but with cuts Y and Z applied.

B.6 Statistical and systematic uncertainties

B.6.1 Systematic uncertainties
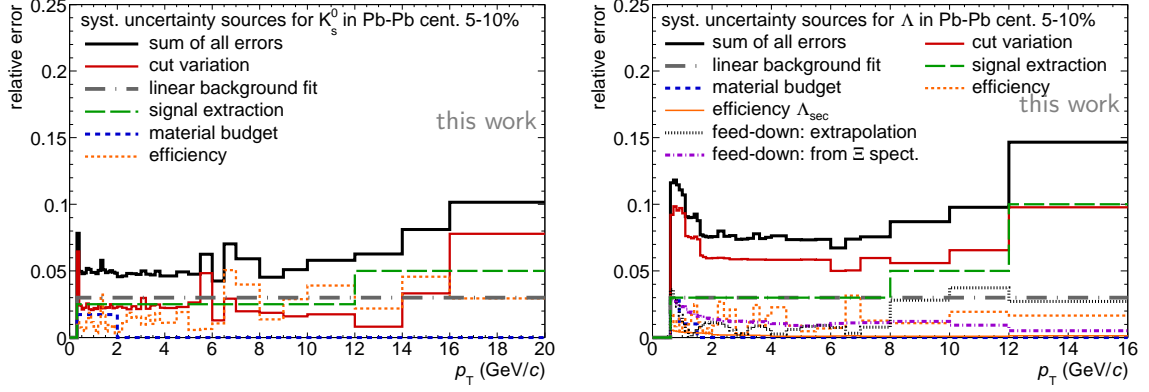
Figure B.53: Systematic uncertainty sources for K_s^0 (left) and Λ (right) in Pb–Pb collisions with centrality 5 - 10%.
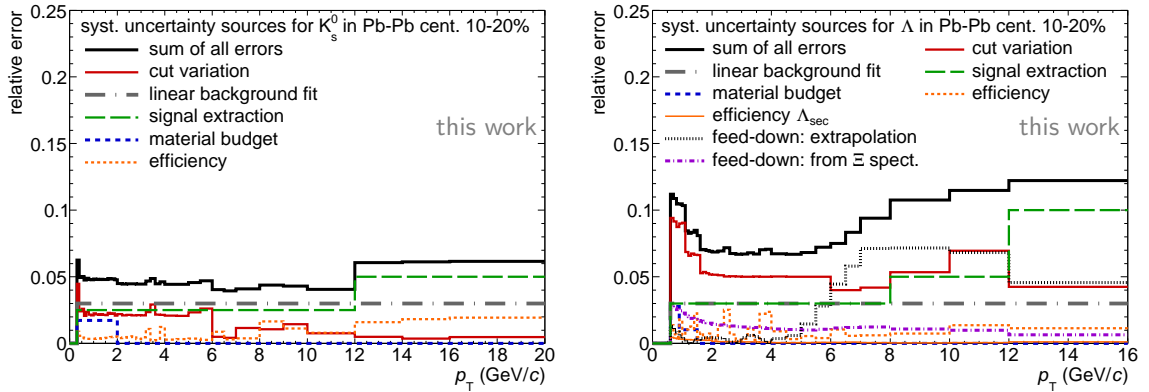
Figure B.54: Systematic uncertainty sources for K_s^0 (left) and Λ (right) in Pb–Pb collisions with centrality 10 - 20%.
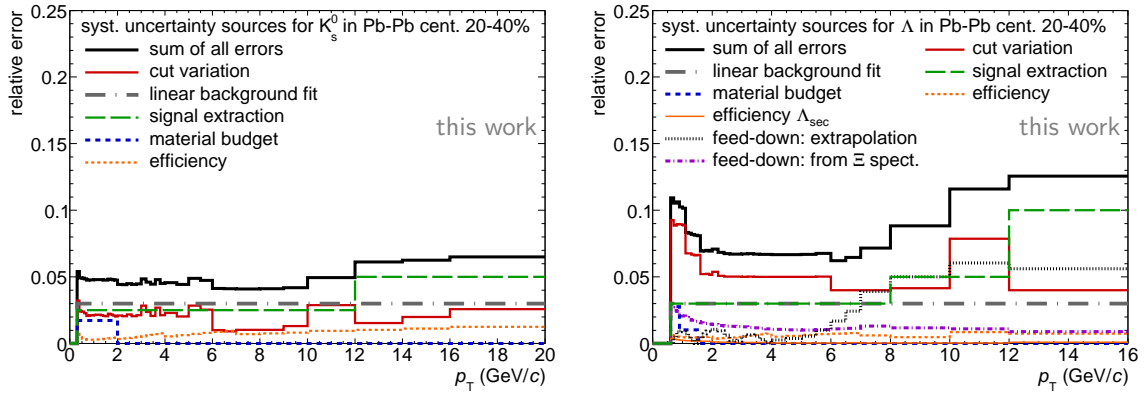
Figure B.55: Systematic uncertainty sources for K_s^0 (left) and Λ (right) Pb–Pb collisions with centrality 20 - 40%.
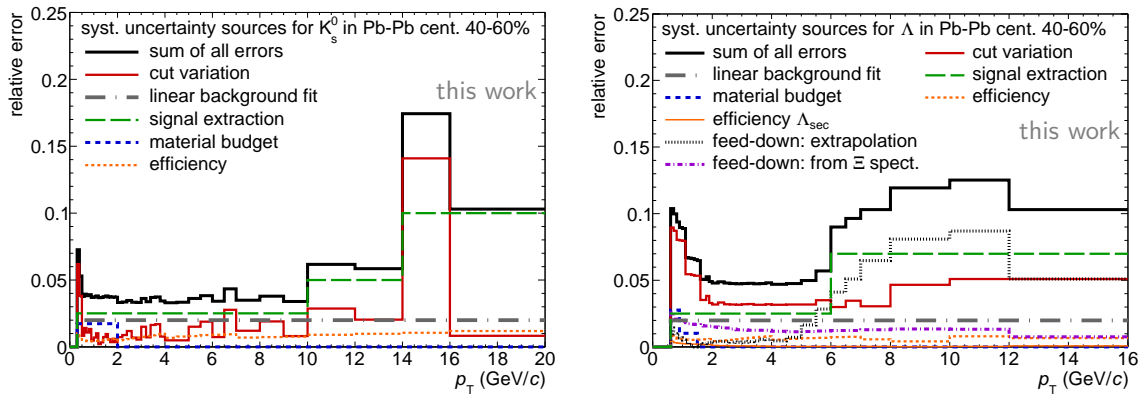
Figure B.56: Systematic uncertainty sources for K_s^0 (left) and Λ (right) in Pb–Pb collisions with centrality 40 - 60%.
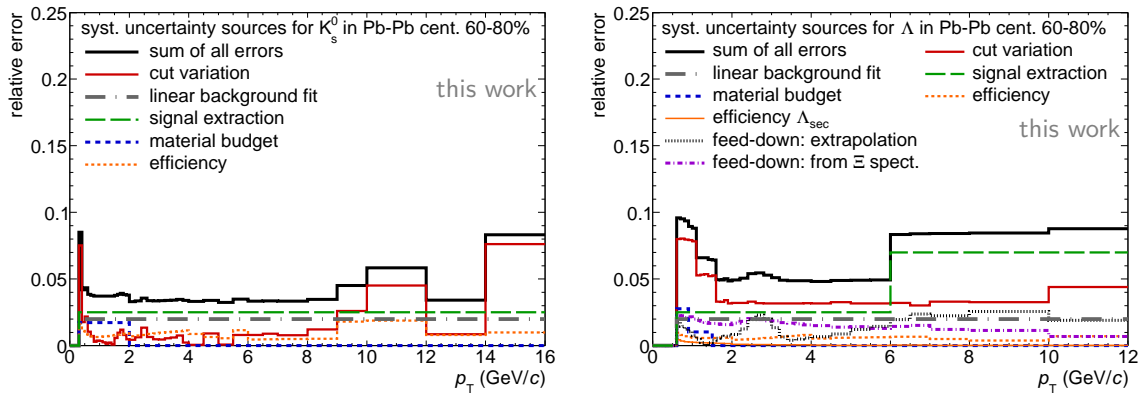
Figure B.57: Systematic uncertainty sources for K_s^0 (left) and Λ (right) in Pb–Pb collisions with centrality 60 - 80%.
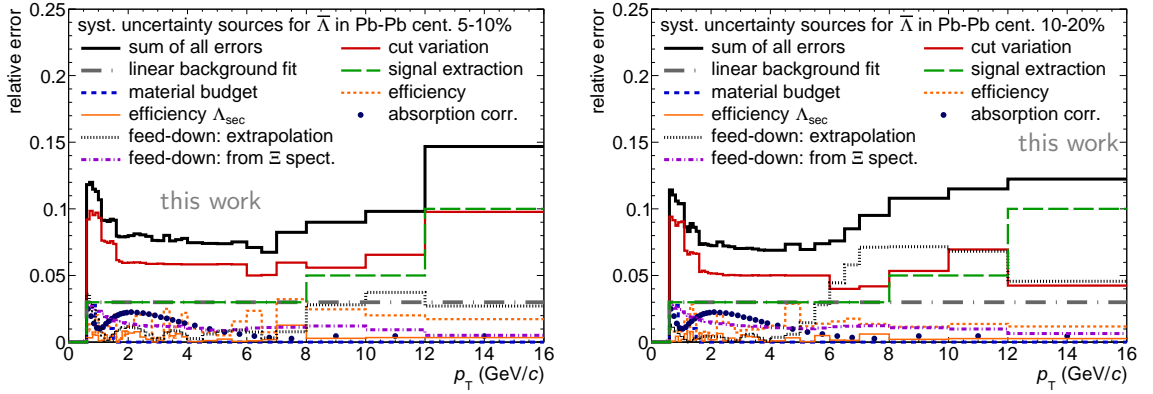
Figure B.58: Systematic uncertainty sources for $\overline{\Lambda}$ in Pb–Pb collisions with centrality 5 - 10% (left) and 10 - 20% (right).
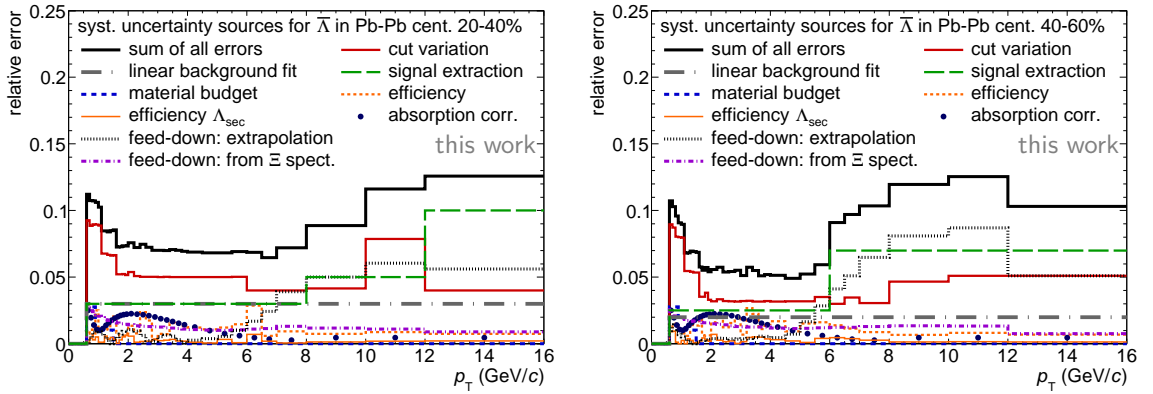
Figure B.59: Systematic uncertainty sources for $\overline{\Lambda}$ in Pb–Pb collisions with centrality 20 - 40% (left) and 40 - 60% (right).
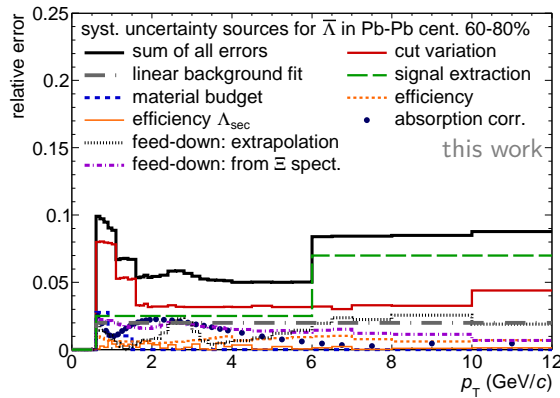
Figure B.60: Systematic uncertainty sources for $\overline{\Lambda}$ in peripheral Pb–Pb collisions.

B.6.2 Statistical uncertainties
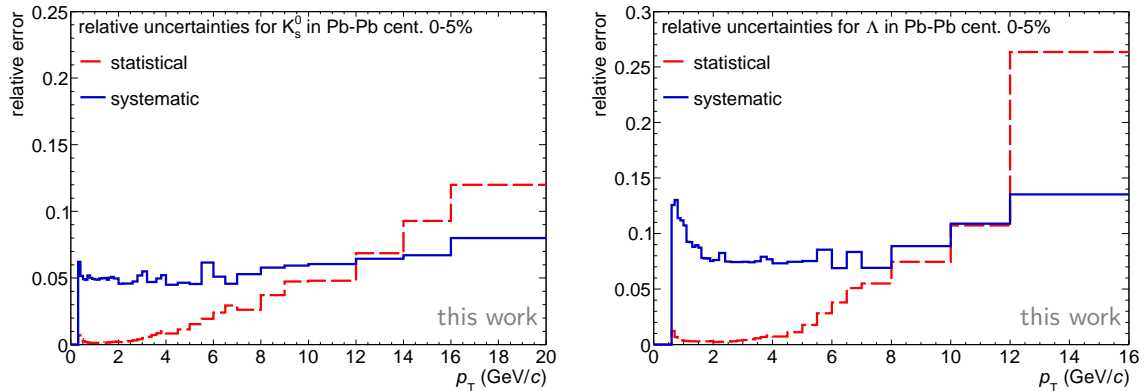
Figure B.61: The statistical uncertainties vs. p_T together with the total systematic uncertainties for K_s^0 (left) and Λ (right) in Pb–Pb collisions with centrality 0 - 5%.
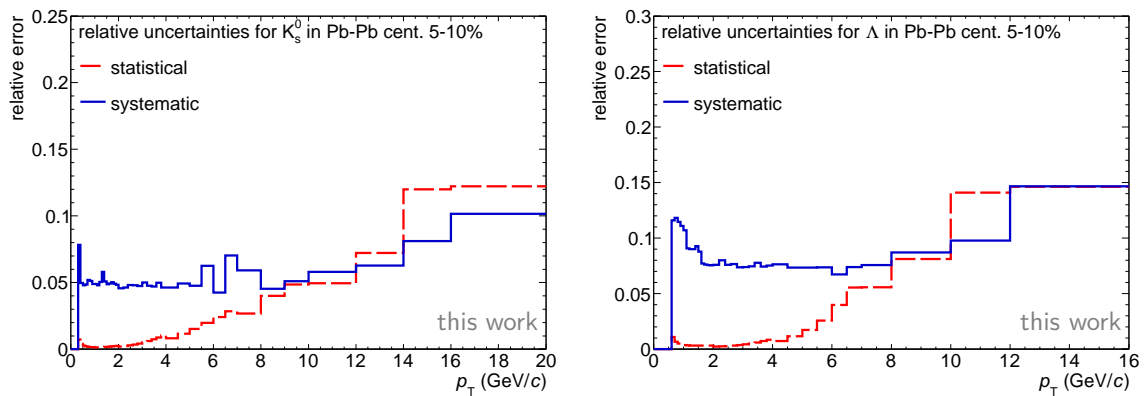
Figure B.62: The statistical uncertainties vs. p_T together with the total systematic uncertainties for K_s^0 (left) and Λ (right) in Pb–Pb collisions with centrality 5 - 10%.
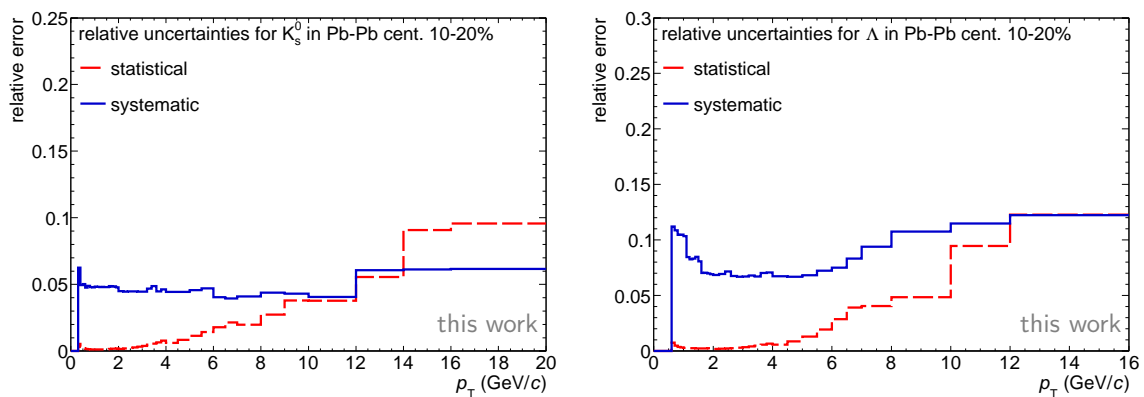
Figure B.63: The statistical uncertainties vs. p_T together with the total systematic uncertainties for K_s^0 (left) and Λ (right) in Pb–Pb collisions with centrality 10 - 20%.
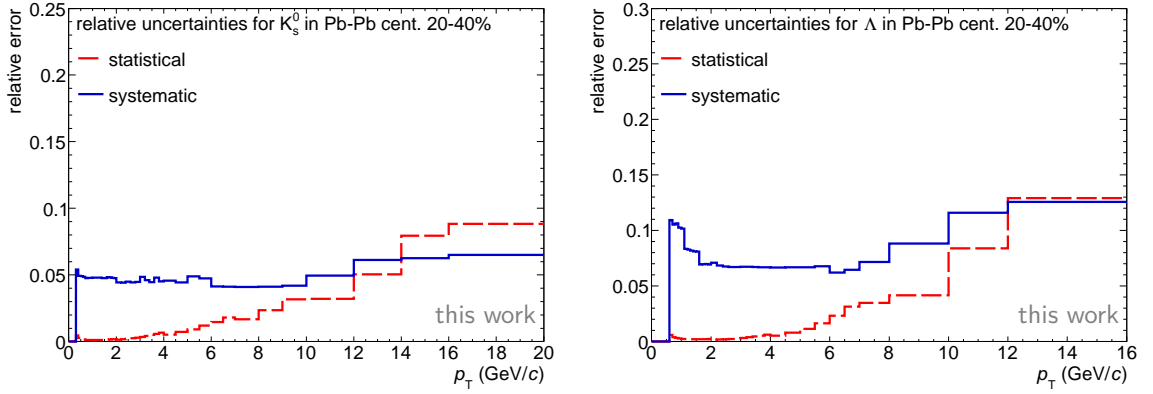
Figure B.64: The statistical uncertainties vs. p_T together with the total systematic uncertainties for K_s^0 (left) and Λ (right) Pb–Pb collisions with centrality 20 - 40%.
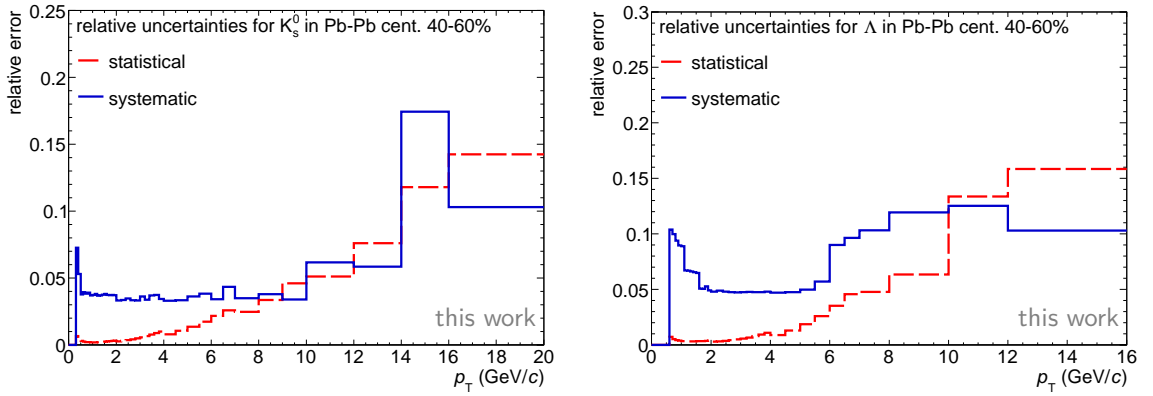
Figure B.65: The statistical uncertainties vs. p_T together with the total systematic uncertainties for K_s^0 (left) and Λ (right) in Pb–Pb collisions with centrality 40 - 60%.
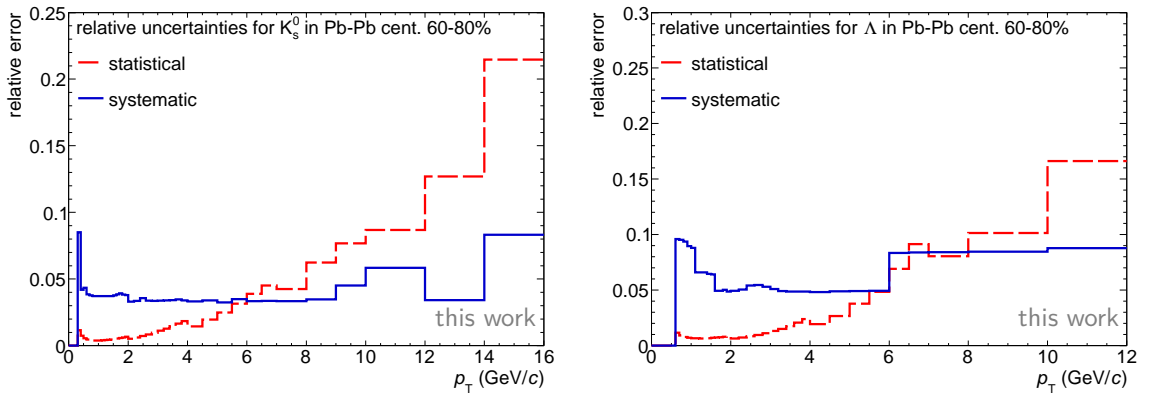
Figure B.66: The statistical uncertainties vs. p_T together with the total systematic uncertainties for K_s^0 (left) and Λ (right) in Pb–Pb collisions with centrality 60 - 80%.
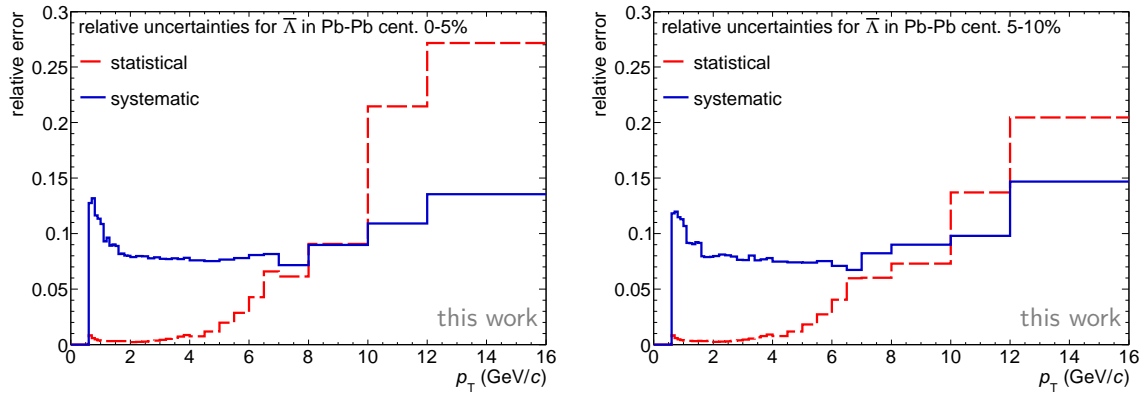
Figure B.67: The statistical uncertainties vs. p_T together with the total systematic uncertainties for $\overline{\Lambda}$ in Pb–Pb collisions with centrality 0 - 5% (left) and 5 - 10% (right).
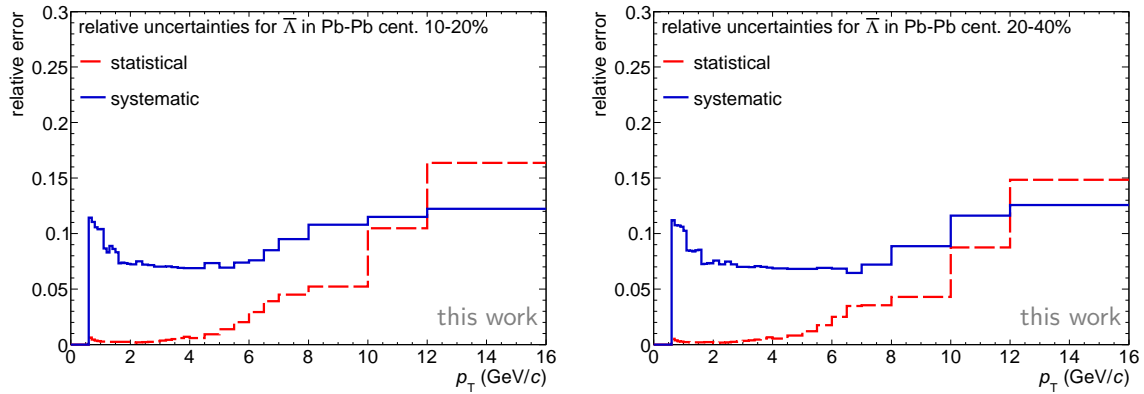
Figure B.68: The statistical uncertainties vs. p_T together with the total systematic uncertainties for $\overline{\Lambda}$ in Pb–Pb collisions with centrality 10 - 20% (left) and 20 - 40% (right).
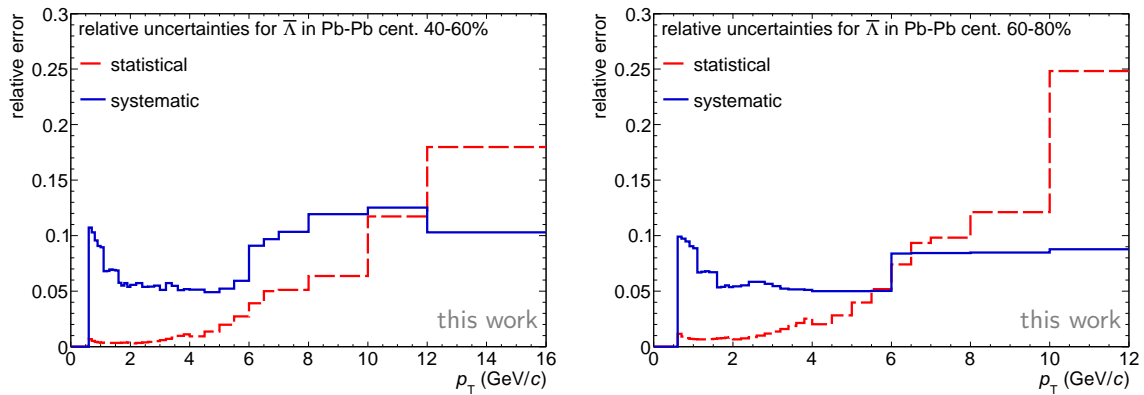
Figure B.69: The statistical uncertainties vs. p_T together with the total systematic uncertainties for $\overline{\Lambda}$ in Pb–Pb collisions with centrality 40 - 60% (left) and 60 - 80% (right).

C Additional figures

C.1 $\overline{\Lambda}/\Lambda$ ratio: additional centralities
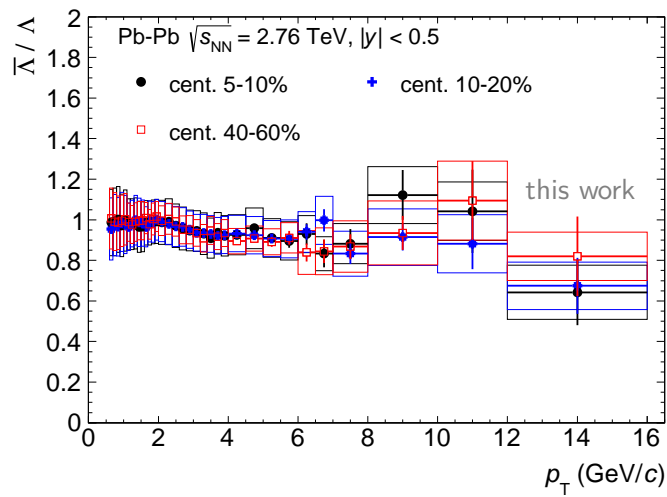
Figure C.1: Ratio of $\overline{\Lambda}$ to Λ in mid-central Pb–Pb collisions at $\sqrt{s_{\mathrm{NN}}}$ = 2.76 TeV. The boxes around the data points represent the systematic uncertainties, whereas the vertical error bars show the statistical errors.

C.2 R_{CP} and R_{AA}
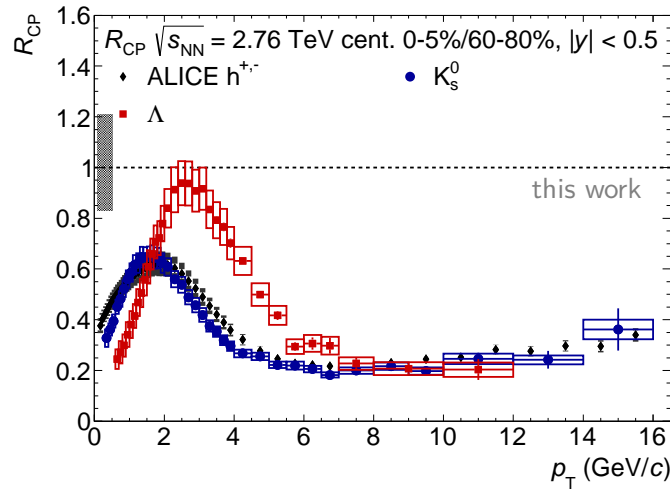
Figure C.2: The nuclear modification factor R_{CP} of Λ and $\mathrm{K}^0_{\mathrm{s}}$ together with that of charged particles measured by ALICE for central $(0-5\%)$ and peripheral $(60-80\%)$ Pb–Pb collisions at $\sqrt{s_{\mathrm{NN}}} = 2.76\,\mathrm{TeV}$ [47]. The boxes around the data points indicate the systematic error.
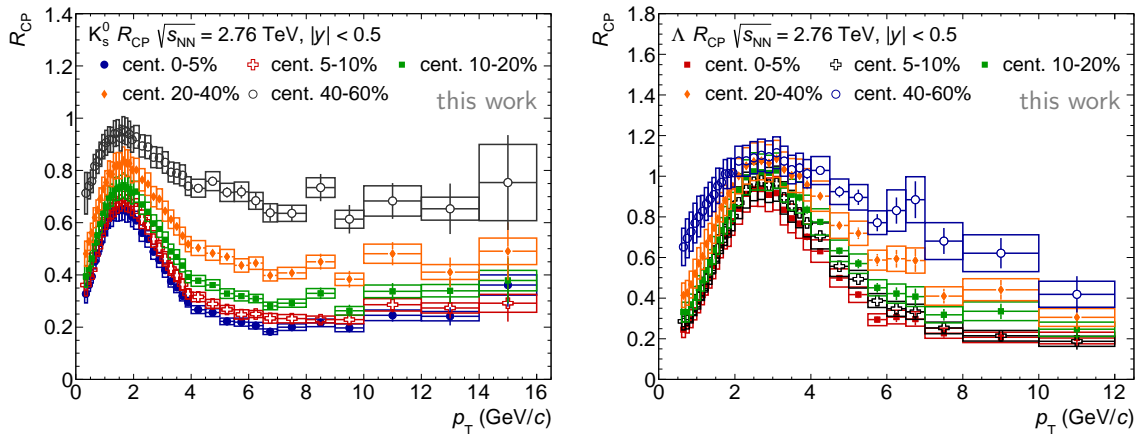
Figure C.3: The nuclear modification factor R_{CP} of $\mathrm{K}^0_{\mathrm{s}}$ (left) and Λ (right) for all centralities to peripheral $(60-80\%)$ Pb–Pb collisions at $\sqrt{s_{\mathrm{NN}}} = 2.76\,\mathrm{TeV}$. The boxes around the data points indicate the systematic error.
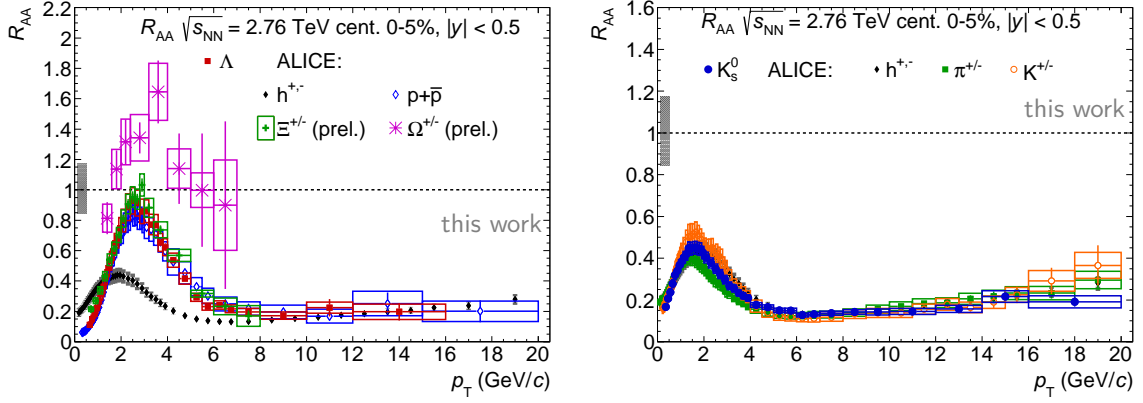
Figure C.4: R_{AA} compilation for baryons (left) and mesons (right) in central Pb–Pb collisions [47, 158–160]. The Ξ and Ω R_{AA} was measured for 0 - 10% centrality. The uncertainty from N_{coll} and from the normalization in pp are indicated by the black box at unity.
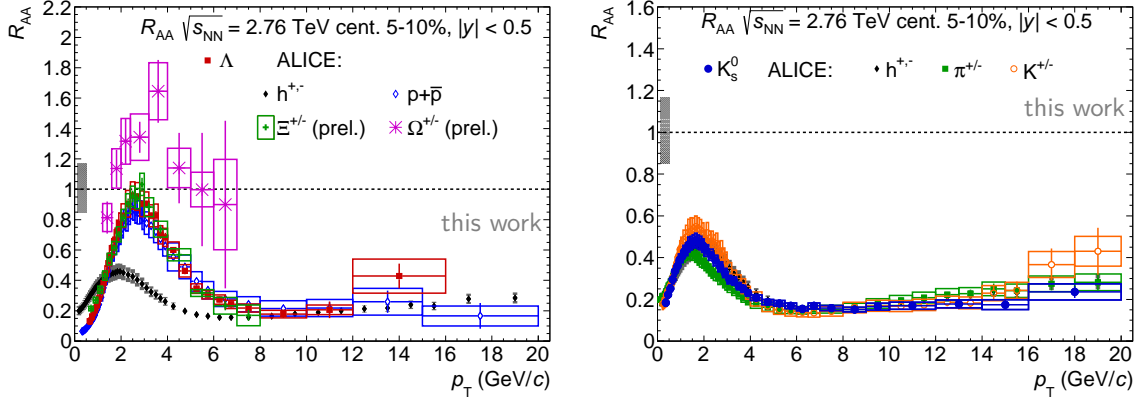
Figure C.5: R_{AA} compilation for baryons (left) and mesons (right) in Pb–Pb collisions of 5 - 10% centrality [47, 158–160]. The Ξ and Ω R_{AA} was measured for 0 - 10% centrality. The uncertainty from N_{coll} and from the normalization in pp are indicated by the black box at unity.
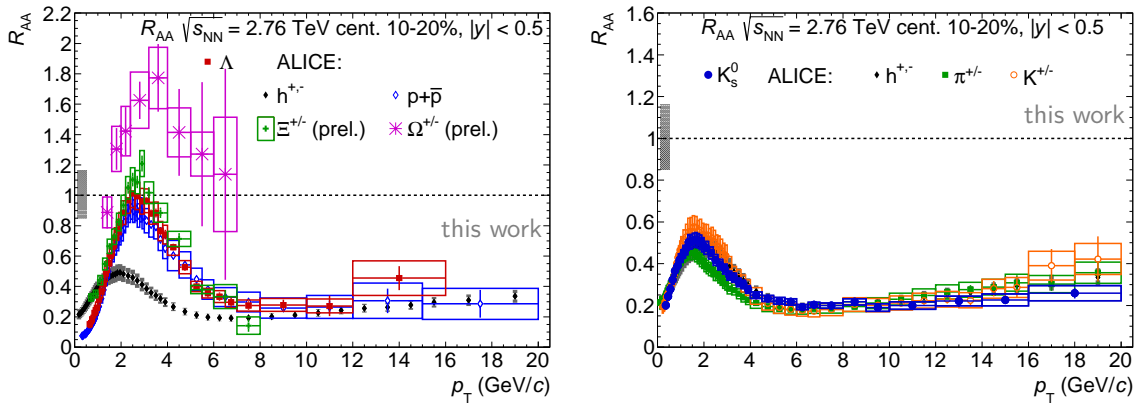
Figure C.6: R_{AA} compilation for baryons (left) and mesons (right) in Pb–Pb collisions of 10 - 20% centrality [47, 158–160]. The uncertainty from N_{coll} and from the normalization in pp are indicated by the black box at unity.
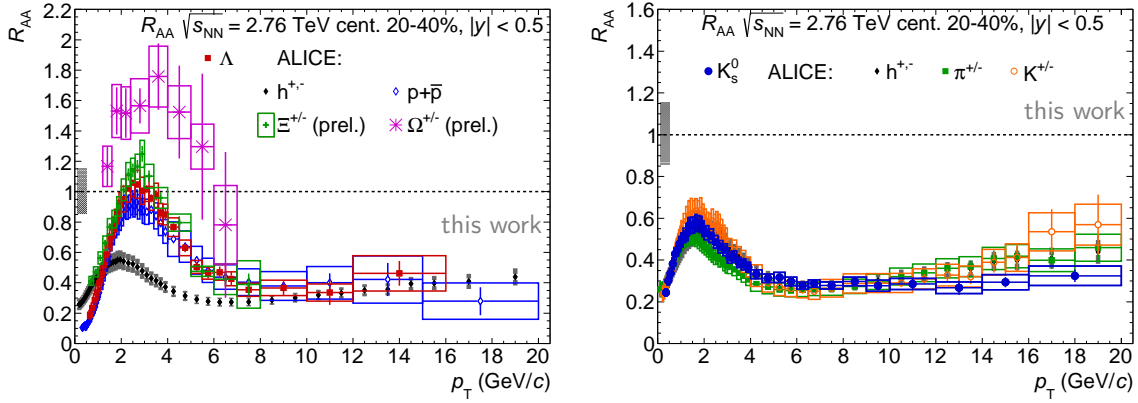
Figure C.7: R_{AA} compilation for baryons (left) and mesons (right) in Pb–Pb collisions of 20 - 40% centrality [47, 158–160]. The uncertainty from N_{coll} and from the normalization in pp are indicated by the black box at unity.
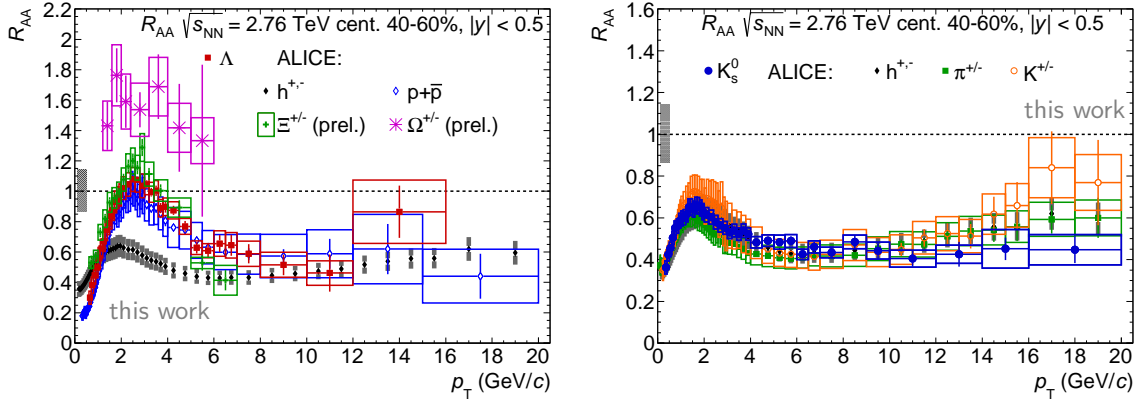
Figure C.8: R_{AA} compilation for baryons (left) and mesons (right) in Pb–Pb collisions of 40 - 60% centrality [47, 158–160]. The uncertainty from N_{coll} and from the normalization in pp are indicated by the black box at unity.
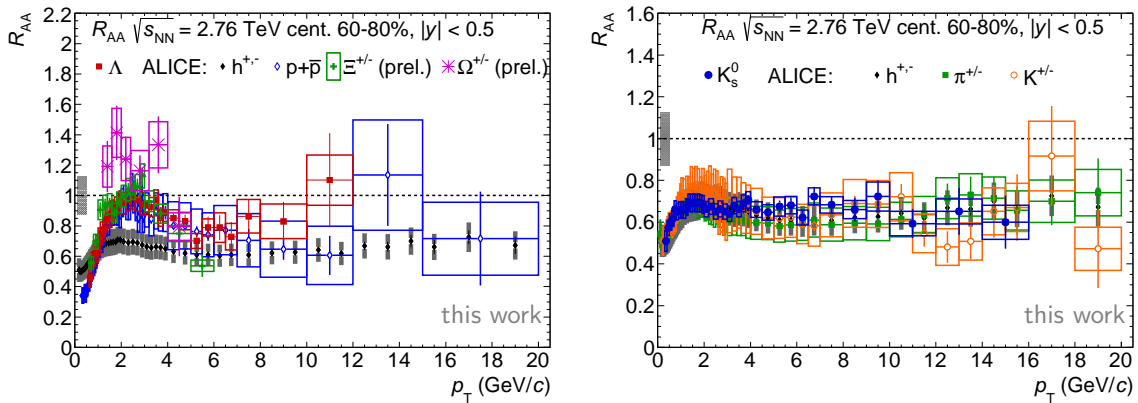
Figure C.9: R_{AA} compilation for baryons (left) and mesons (right) in Pb–Pb collisions of 60 - 80% centrality [47, 158–160]. The uncertainty from N_{coll} and from the normalization in pp are indicated by the black box at unity.
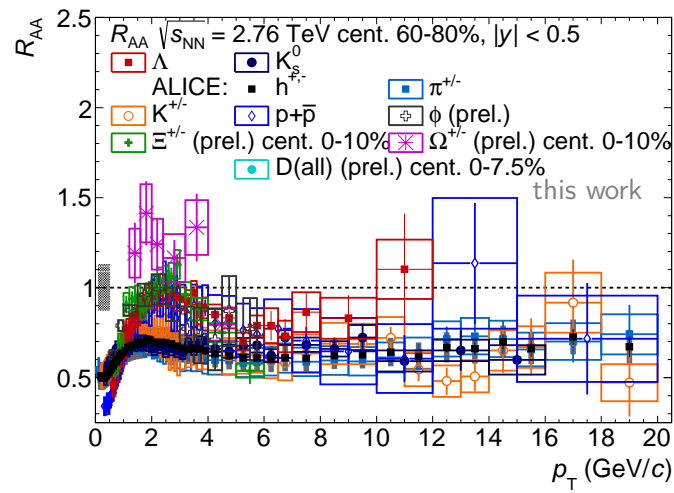
Figure C.10: The nuclear modification factor R_{AA} of K_s^0 and Λ together with that of other hadrons by ALICE [47, 158–160, 168, 169] for peripheral (60 – 80%) Pb–Pb collisions at $\sqrt{s_{NN}} = 2.76$ TeV. The uncertainty from N_{coll} and from the normalization in pp are indicated by the black box at unity.

R_{AA} with RHIC results
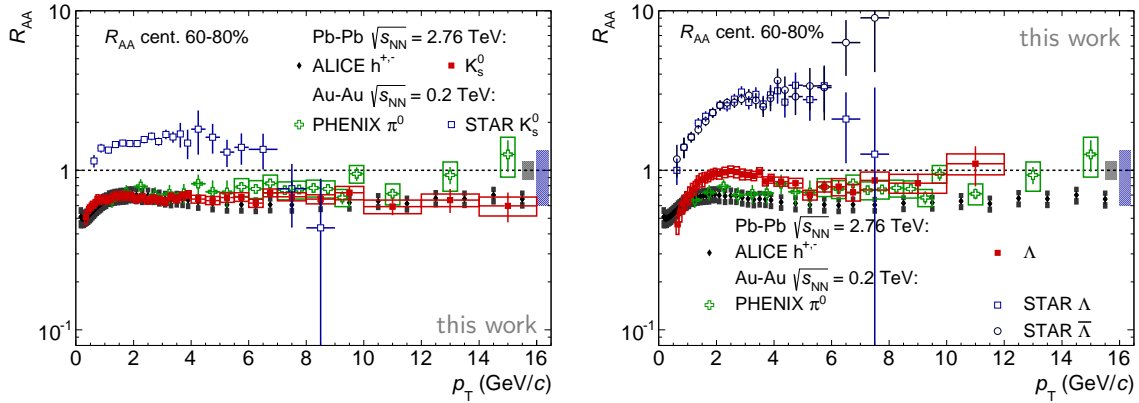
Figure C.11: The nuclear modification factor R_{AA} of $\mathrm{K_s^0}$ (left panel) and Λ (right panel) in peripheral Pb–Pb collisions in comparison with the measurement in Au–Au collisions at $\sqrt{s_{\mathrm{NN}}} = 200\,\mathrm{GeV}$ by the STAR collaboration [179, 180] for the same centrality interval. In addition, the charged particle R_{AA} from ALICE [47] as well as the neutral pion R_{AA} by PHENIX [78] are shown. The STAR pp reference, which is normalized to non-single diffractive events (NSD), was scaled by the cross-section ratio $\sigma_{\mathrm{NSD}}/\sigma_{\mathrm{INEL}} = 30\mathrm{mb}/42\mathrm{mb}$. The uncertainty from N_{coll} and from the normalization in pp are indicated by the boxes at unity (black ALICE, blue STAR).

C.3 BAMPS figures
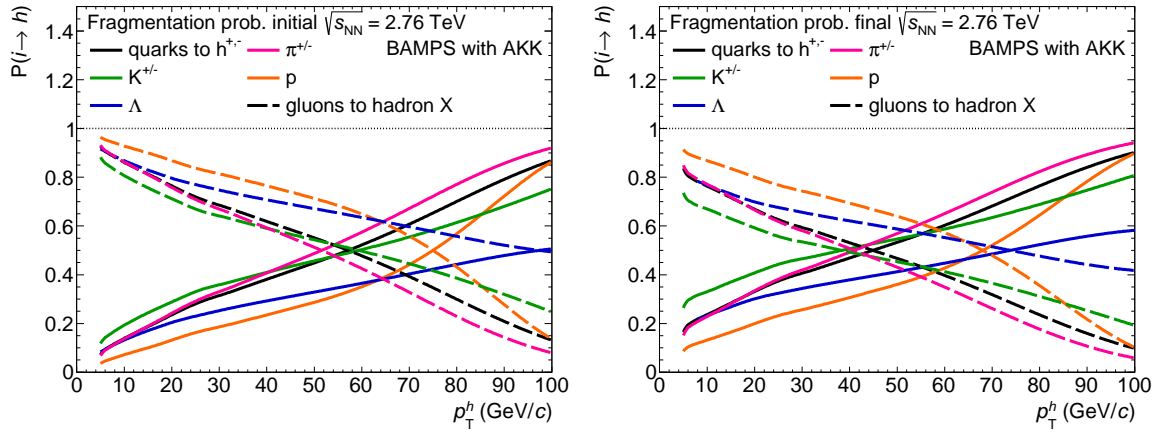
Figure C.12: Probability, that a hadron with p_T^h stems from a specific parton i with any momentum without ("initial", left panel) and after ("final", right panel) the energy loss of parton i. These values are the basis for the R_{AA} model calculation within the BAMPS framework in [173, 174] employing the AKK fragmentation functions. The solid lines represent the case for quarks fragmenting to hadron X, whereas the dashed lines show the case for gluons [177].

List of Figures

List of Tables

Bibliography

[1] L. EVANS, P. BRYANT, "LHC Machine", **JINST 3 (2008), p. S08001**,
URL: http://stacks.iop.org/1748-0221/3/i=08/a=S08001.

[2] G. AAD et al., "Observation of a new particle in the search for the Standard Model Higgs boson with the ATLAS detector at the LHC", **Phys. Lett. B 716 (2012), p. 1**,
DOI: 10.1016/j.physletb.2012.08.020.

[3] S. CHATRCHYAN et al., "Observation of a new boson at a mass of 125 GeV with the CMS experiment at the LHC", **Phys. Lett. B 716 (2012), p. 30**,
DOI: 10.1016/j.physletb.2012.08.021.

[4] "The Higgs Boson", **Science 338.6114 (2012), p. 1558**,
DOI: 10.1126/science.1232005.

[5] A. A. ALVES et al., "The LHCb Detector at the LHC", **J. Instrum. 3 (2008)**, **p. S08005**,
URL: http://stacks.iop.org/1748-0221/3/i=08/a=S08005.

[6] T. H. KOHSUKE YAGI, Y. MIAKE, "Quark-Gluon Plasma", Cambridge University Press, 2005.

[7] "NASA",
URL: http://map.gsfc.nasa.gov/media/060915.

[8] A. ADAMS et al., "Strongly correlated quantum fluids: ultracold quantum gases, quantum chromodynamic plasmas and holographic duality", **New Journal of Physics 14 (2012), p. 115009**,
DOI: 10.1088/1367-2630/14/11/115009.

[9] "Hot and Dense QCD Matter - A Community White Paper on the Future of Relativistic Heavy-Ion Physics in the US",
URL: http://www.bnl.gov/npp/docs/Bass_RHI_WP_final.pdf.

[10] H. D. PERKINS, "Introduction to High Energy Physics", 4th edition, Cambridge Universtity Press, 2000.

[11] F. ABE et al., "Observation of Top Quark Production in $\overline{p}p$ Collisions with the Collider Detector at Fermilab", **Phys. Rev. Lett. 74 (1995), p. 2626**,
DOI: 10.1103/PhysRevLett.74.2626.

[12] S. ABACHI et al., "Observation of the Top Quark", **Phys. Rev. Lett. 74 (1995), p. 2632**,
DOI: 10.1103/PhysRevLett.74.2632.

[13] K. OLIVE et al., "Review of Particle Physics", **Chin. Phys. C 38 (2014)**, **p. 090001**,
URL: http://pdg.lbl.gov/.

[14] K. OLIVE et al., "Neutrino mass, mixing, and oscillations", **Chin. Phys. C 38** (**2014**), **p. 090001**,
URL: `http://pdg.lbl.gov/2014/reviews/rpp2014-rev-neutrino-mixing.pdf`.

[15] H. FRITZSCH, M. GELL-MANN, "Current algebra: Quarks and what else?", - Proceedings of the 16th International Conference On High-Energy Physics, ed. by J. JACKSON, A. ROBERTS, **2**, Batavia, Illinois, USA, **1972**, **p. 135**,
URL: `http://www.slac.stanford.edu/econf/C720906/`.

[16] H. FRITZSCH, M. GELL-MANN, H. LEUTWYLER, "Advantages of the color octet gluon picture", **Phys. Lett. B 47** (**1973**), **p. 365**,
DOI: `10.1016/0370-2693(73)90625-4`.

[17] E. EICHTEN et al., "Spectrum of Charmed Quark-Antiquark Bound States", **Phys. Rev. Lett. 34** (**1975**), **p. 369**,
DOI: `10.1103/PhysRevLett.34.369`.

[18] S. BETHKE, "The 2009 World Average of alpha(s)", **Eur. Phys. J. C 64** (**2009**), **p. 689**,
DOI: `10.1140/epjc/s10052-009-1173-1`.

[19] H. D. POLITZER, "Asymptotic freedom: An approach to strong interactions", **Physics Reports 14** (**1974**), **p. 129**,
DOI: `10.1016/0370-1573(74)90014-3`.

[20] H. D. POLITZER, "Reliable Perturbative Results for Strong Interactions?", **Phys. Rev. Lett. 30** (**1973**), **p. 1346**,
DOI: `10.1103/PhysRevLett.30.1346`.

[21] D. J. GROSS, F. WILCZEK, "Ultraviolet Behavior of Non-Abelian Gauge Theories", **Phys. Rev. Lett. 30** (**1973**), **p. 1343**,
DOI: `10.1103/PhysRevLett.30.1343`.

[22] K. G. WILSON, "Confinement of quarks", **Phys. Rev. D 10** (**1974**), **p. 2445**,
DOI: `10.1103/PhysRevD.10.2445`.

[23] F. A. WILCZEK, "Asymptotic freedom: from paradox to paradigm", Nobel Lecture, 2004.

[24] J. RAK, M. J. TANNENBAUM, "High p_T physics in the heavy ion era", Cambridge University Press, 2013.

[25] J. SCHAFFNER-BIELICH, "Signals of the QCD Phase Transition in the Heavens", **POS CPOD2007** (**2007**), **p. 062**, arXiv: `0709.1043 [astro-ph]`.

[26] K. FUKUSHIMA, T. HATSUDA, "The phase diagram of dense QCD", **Rept. Prog. Phys. 74** (**2011**), **p. 014001**,
DOI: `10.1088/0034-4885/74/1/014001`.

[27] S. BORSANYI et al., "Full result for the QCD equation of state with 2+1 flavors", **Phys. Lett. B 730** (**2014**), **p. 99**,
DOI: `10.1016/j.physletb.2014.01.007`.

[28] J. D. BJORKEN, "Highly Relativistic Nucleus-Nucleus Collisions: The Central Rapidity Region", **Phys. Rev. D 27** (**1983**), **p. 140**,
DOI: `10.1103/PhysRevD.27.140`.

[29] S. Chatrchyan et al., "Measurement of the pseudorapidity and centrality dependence of the transverse energy density in Pb–Pb collisions at $\sqrt{s_{\mathrm{NN}}} = 2.76$ TeV", **Phys. Rev. Lett. 109 (2012), p. 152303**,
DOI: 10.1103/PhysRevLett.109.152303.

[30] K. Aamodt et al., "Centrality Dependence of the Charged-Particle Multiplicity Density at Midrapidity in Pb–Pb Collisions at $\sqrt{s_{\mathrm{NN}}} = 2.76$ TeV", **Phys. Rev. Lett. 106 (2011), p. 032301**,
DOI: 10.1103/PhysRevLett.106.032301.

[31] B. Abelev et al., "Centrality determination of Pb–Pb collisions at $\sqrt{s_{\mathrm{NN}}} = 2.76$ TeV with ALICE", **Phys. Rev. C 88 (2013), p. 044909**,
DOI: 10.1103/PhysRevC.88.044909.

[32] A. Bazavov et al., "The chiral and deconfinement aspects of the QCD transition", **Phys. Rev. D 85 (2012), p. 054503**,
DOI: 10.1103/PhysRevD.85.054503.

[33] Y. Aoki et al., "The Order of the quantum chromodynamics transition predicted by the standard model of particle physics", **Nature 443 (2006), p. 675**,
DOI: 10.1038/nature05120.

[34] K. M. Burke et al., "Extracting jet transport coefficient from jet quenching at RHIC and LHC", **Phys. Rev. C 90 (2014), p. 014909**,
DOI: 10.1103/PhysRevC.90.014909.

[35] M. Gyulassy, L. McLerran, "New forms of QCD matter discovered at RHIC", **Nucl. Phys. A 750 (2005), p. 30**,
DOI: 10.1016/j.nuclphysa.2004.10.034.

[36] P. Ehrenfest, "Phasenumwandlungen im ueblichen und erweiterten Sinn, classifiziert nach den entsprechenden Singularitaeten des thermodynamischen Potentiales", **Proceedings Royal Acad., Amsterdam 36 (1933), p. 153**,
URL: http://www.dwc.knaw.nl/DL/publications/PU00016385.pdf.

[37] B. Müller, "Investigation of Hot QCD Matter: Theoretical Aspects" (**2013**),
arXiv: 1309.7616 [nucl-th].

[38] N. Metropolis, S. Ulam, "The Monte Carlo Method", **Journal of the American Statistical Association 44 (1949), p. 335**,
URL: http://home.gwu.edu/~stroud/classics/MetropolisUlam49.pdf.

[39] M. H. Seymour, M. Marx, "Monte Carlo Event Generators" (**2013**), arXiv: 1304.6677 [hep-ph].

[40] R. Stock, "Relativistic Heavy Ion Physics: Introduction", ed. by R. Stock, vol. 23, Springer Materials - Landolt-Börnstein - Group I Elementary Particles, Nuclei and Atoms, Springer-Verlag, 2010,
DOI: 10.1007/978-3-642-01539-7_1.

[41] CERN-press-office, "New State of Matter created at CERN",
URL: http://press.web.cern.ch/press-releases/2000/02/new-state-matter-created-cern.

[42] X.-N. Wang, "Effects of jet quenching on high p_{T} hadron spectra in high-energy nuclear collisions", **Phys. Rev. C 58 (1998), p. 2321**,
DOI: 10.1103/PhysRevC.58.2321.

[43]   A. ANDRONIC, "An overview of the experimental study of quark-gluon matter in high-energy nucleus-nucleus collisions", **Int. J. Mod. Phys. A29 (2014)**, **p. 1430047**,
DOI: 10.1142/S0217751X14300476.

[44]   B. BACK et al., "Centrality Dependence of Charged Hadron Transverse Momentum Spectra in Au–Au Collisions from $\sqrt{s_{NN}}$ = 62.4 to 200 GeV", **Phys. Rev. Lett. 94 (2005)**, **p. 082304**,
DOI: 10.1103/PhysRevLett.94.082304.

[45]   J. D. BJORKEN, "Energy Loss of Energetic Partons in Quark - Gluon Plasma: Possible Extinction of High p(t) Jets in Hadron - Hadron Collisions", **FERMILAB-PUB-82-059-THY (1982)**.

[46]   M. GYULASSY, M. PLUMER, "Jet quenching in dense matter", **Phys. Lett. B 243 (1990)**, **p. 432**,
DOI: 10.1016/0370-2693(90)91409-5.

[47]   B. ABELEV et al., "Centrality dependence of charged particle production at large transverse momentum in Pb–Pb collisions at $\sqrt{s_{NN}}$ = 2.76 TeV", **Phys. Lett. B 720 (2013)**, **p. 52**,
DOI: 10.1016/j.physletb.2013.01.051.

[48]   G. I. VERES, "Overview of results on jets from the CMS Collaboration", **Nucl. Phys. A 904-905 (2013)**, **p. 146c**,
DOI: 10.1016/j.nuclphysa.2013.01.056.

[49]   T. RENK, "Towards jet tomography: γ-hadron correlations", **Phys. Rev. C 74 (2006)**, **p. 034906**,
DOI: 10.1103/PhysRevC.74.034906.

[50]   R. P. FEYNMAN, "Very High-Energy Collisions of Hadrons", **Phys. Rev. Lett. 23 (1969)**, **p. 1415**,
DOI: 10.1103/PhysRevLett.23.1415.

[51]   R. P. FEYNMAN, "Photon–hadron interactions", WA Benjamin, Inc., Reading, MA, 1972.

[52]   J. D. BJORKEN, "Can We Measure Parton-Parton Cross Sections?", **Phys. Rev. D 8 (1973)**, **p. 4098**,
DOI: 10.1103/PhysRevD.8.4098.

[53]   J. F. OWENS, "Large-momentum-transfer production of direct photons, jets, and particles", **Rev. Mod. Phys. 59 (1987)**, **p. 465**,
DOI: 10.1103/RevModPhys.59.465.

[54]   I. J. AITCHISON, A. J. HEY, "Gauge theories in particle physics", 4th ed., vol. 2, CRC Press, 2012.

[55]   Y. L. DOKSHITZER, "Calculation of the Structure Functions for Deep Inelastic Scattering and e+–e- Annihilation by Perturbation Theory in Quantum Chromodynamics." **Sov. Phys. JETP 46 (1977)**, **p. 641**.

[56]   V. GRIBOV, L. LIPATOV, "Deep inelastic e–p scattering in perturbation theory", **Sov. J. Nucl. Phys. 15 (1972)**, **p. 438**.

[57]   L. LIPATOV, "The parton model and perturbation theory", **Sov. J. Nucl. Phys. 20 (1975)**, **p. 94**.

[58] G. Altarelli, G. Parisi, "Asymptotic Freedom in Parton Language", **Nucl. Phys. B 126 (1977), p. 298**, DOI: 10.1016/0550-3213(77)90384-4.

[59] S. M. Berman, J. D. Bjorken, J. B. Kogut, "Inclusive Processes at High Transverse Momentum", **Phys. Rev. D 4 (1971), p. 3388**, DOI: 10.1103/PhysRevD.4.3388.

[60] B. B. Abelev et al., "Energy Dependence of the Transverse Momentum Distributions of Charged Particles in pp Collisions Measured by ALICE", **Eur. Phys. J. C 73 (2013), p. 2662**, DOI: 10.1140/epjc/s10052-013-2662-9.

[61] K. J. Eskola, H. Paukkunen, C. A. Salgado, "Nuclear PDFs at NLO - status report and review of the EPS09 results", **Nucl. Phys. A 855 (2011), p. 150**, DOI: 10.1016/j.nuclphysa.2011.02.032.

[62] K. J. Eskola, H. Paukkunen, C. A. Salgado, "EPS09 - A new generation of NLO and LO nuclear parton distribution functions", **JHEP 2009 (2009), p. 065**, URL: http://stacks.iop.org/1126-6708/2009/i=04/a=065.

[63] S. Albino, B. Kniehl, G. Kramer, "AKK Update: Improvements from New Theoretical Input and Experimental Data", **Nucl. Phys. B 803 (2008), p. 42**, DOI: 10.1016/j.nuclphysb.2008.05.017.

[64] D. d'Enterria, "Relativistic Heavy Ion Physics: 6.4 Jet Quenching", ed. by R. Stock, vol. 23, Springer Materials - Landolt-Börnstein - Group I Elementary Particles, Nuclei and Atoms, Springer-Verlag, 2010, DOI: 10.1007/978-3-642-01539-7_16.

[65] Y. Dokshitzer, D. Kharzeev, "Heavy-quark colorimetry of QCD matter", **Phys. Lett. B 519 (2001), p. 199**, DOI: 10.1016/S0370-2693(01)01130-3.

[66] M. Nahrgang et al., "Azimuthal correlations of heavy quarks in Pb–Pb collisions at $\sqrt{s} = 2.76$ TeV at the CERN Large Hadron Collider", **Phys. Rev. C 90 (2014), p. 024907**, DOI: 10.1103/PhysRevC.90.024907.

[67] B. Zakharov, "Fully quantum treatment of the Landau-Pomeranchuk-Migdal effect in QED and QCD", **JETP Lett. 63 (1996), p. 952**, DOI: 10.1134/1.567126.

[68] S. Wicks et al., "Elastic, inelastic, and path length fluctuations in jet tomography", **Nucl. Phys. A 784 (2007), p. 426**, DOI: 10.1016/j.nuclphysa.2006.12.048.

[69] T. Renk, "Constraining the Physics of Jet Quenching", **Phys. Rev. C 85 (2012), p. 044903**, DOI: 10.1103/PhysRevC.85.044903.

[70] T. Renk, "Physics probed by the p_T dependence of the nuclear suppression factor", **Phys. Rev. C 88 (2013), p. 014905**, DOI: 10.1103/PhysRevC.88.014905.

[71]   K. AAMODT et al., "Particle-yield modification in jet-like azimuthal di-hadron correlations in Pb–Pb collisions at $\sqrt{s_{NN}} = 2.76$ TeV", **Phys.Rev.Lett. 108** (**2012**), **p. 092301**,
DOI: 10.1103/PhysRevLett.108.092301.

[72]   B. ABELEV et al., "Studying Parton Energy Loss in Heavy-Ion Collisions via Direct-Photon and Charged-Particle Azimuthal Correlations", **Phys. Rev. C 82** (**2010**), **p. 034909**,
DOI: 10.1103/PhysRevC.82.034909.

[73]   A. ADARE et al., "Trends in Yield and Azimuthal Shape Modification in Di-hadron Correlations in Relativistic Heavy Ion Collisions", **Phys. Rev. Lett. 104** (**2010**), **p. 252301**,
DOI: 10.1103/PhysRevLett.104.252301.

[74]   B. BETZ, M. GYULASSY, "Examining a reduced jet-medium coupling in Pb–Pb collisions at the Large Hadron Collider", **Phys. Rev. C 86** (**2012**), **p. 024903**,
DOI: 10.1103/PhysRevC.86.024903.

[75]   M. van LEEUWEN, "Lectures at Helmholtz Graduate School, 28 Feb-5 March, Manigod, France", 2011,
URL: http://www.phys.uu.nl/~leeuw179/#helmholtz_lect.

[76]   S.S. ADLER et al., "Detailed study of high-p_T neutral pion suppression and azimuthal anisotropy in Au–Au collisions at $\sqrt{s_{NN}} = 200$ GeV", **Phys. Rev. C 76** (**2007**), **p. 034904**,
DOI: 10.1103/PhysRevC.76.034904.

[77]   B. ABELEV et al., "Measurement of the inclusive differential jet cross section in pp collisions at $\sqrt{s} = 2.76$ TeV", **Phys. Lett. B 722** (**2013**), **p. 262**,
DOI: 10.1016/j.physletb.2013.04.026.

[78]   A. ADARE et al., "Neutral pion production with respect to centrality and reaction plane in Au–Au collisions at $\sqrt{s_{NN}} = 200$ GeV", **Phys. Rev. C 87** (**2013**), **p. 034911**,
DOI: 10.1103/PhysRevC.87.034911.

[79]   K. AAMODT et al., "Suppression of charged particle production at large transverse momentum in central Pb–Pb collisions at $\sqrt{s_{NN}} = 2.76$ TeV", **Phys. Lett. B 696** (**2011**), **p. 30**,
DOI: 10.1016/j.physletb.2010.12.020.

[80]   D. KHARZEEV, "Parton energy loss at strong coupling and the universal bound", **Eur. Phys. J. C 61** (**2009**), **p. 675**,
DOI: 10.1140/epjc/s10052-008-0860-7.

[81]   S. CHATRCHYAN et al., "Study of high-pT charged particle suppression in Pb–Pb compared to pp collisions at $\sqrt{s_{NN}} = 2.76$ TeV", **Eur. Phys. J. C72** (**2012**), **p. 1945**,
DOI: 10.1140/epjc/s10052-012-1945-x.

[82]   T. RENK et al., "Systematics of the charged-hadron p_T spectrum and the nuclear suppression factor in heavy-ion collisions from $\sqrt{s_{NN}} = 200$ GeV to $\sqrt{s_{NN}} = 2.76$ TeV", **Phys. Rev. C 84** (**2011**), **p. 014906**,
DOI: 10.1103/PhysRevC.84.014906.

[83] M. Gyulassy, P. Levai, I. Vitev, "Jet quenching in thin quark gluon plasmas. 1. Formalism", **Nucl. Phys. B 571 (2000), p. 197**,
DOI: 10.1016/S0550-3213(99)00713-0.

[84] M. Gyulassy, P. Levai, I. Vitev, "Reaction operator approach to nonAbelian energy loss", **Nucl. Phys B. 594 (2001), p. 371**,
DOI: 10.1016/S0550-3213(00)00652-0.

[85] C. A. Salgado, U. A. Wiedemann, "Calculating quenching weights", **Phys. Rev. D 68 (2003), p. 014008**,
DOI: 10.1103/PhysRevD.68.014008.

[86] P. B. Arnold, G. D. Moore, L. G. Yaffe, "Photon and gluon emission in relativistic plasmas", **JHEP 0206 (2002), p. 030**,
DOI: 10.1088/1126-6708/2002/06/030.

[87] X.-N. Wang, X.-f. Guo, "Multiple parton scattering in nuclei: Parton energy loss", **Nucl. Phys. A 696 (2001), p. 788**,
DOI: 10.1016/S0375-9474(01)01130-7.

[88] X.-F. Chen et al., "Suppression of high-p_T hadrons in Pb–Pb collisions at energies available at the CERN Large Hadron Collider", **Phys. Rev. C 84 (2011), p. 034902**,
DOI: 10.1103/PhysRevC.84.034902.

[89] A. Majumder, B. Müller, "Hadron Mass Spectrum from Lattice QCD", **Phys. Rev. Lett. 105 (2010), p. 252002**,
DOI: 10.1103/PhysRevLett.105.252002.

[90] T. Renk, "Path-length dependence of energy loss within in-medium showers", **Phys. Rev. C 83 (2011), p. 024908**,
DOI: 10.1103/PhysRevC.83.024908.

[91] W. Horowitz, M. Gyulassy, "Heavy quark jet tomography of Pb–Pb at LHC: AdS/CFT drag or pQCD energy loss?", **Phys. Lett. B 666 (2008), p. 320**,
DOI: 10.1016/j.physletb.2008.04.065.

[92] T. Renk, "Charm energy loss and D-D correlations from a shower picture", **Phys. Rev. C 89 (2014), p. 054906**,
DOI: 10.1103/PhysRevC.89.054906.

[93] A. Majumder, M. Van Leeuwen, "The Theory and Phenomenology of Perturbative QCD Based Jet Quenching", **Prog. Part. Nucl. Phys. A 66 (2011), p. 41**,
DOI: 10.1016/j.ppnp.2010.09.001.

[94] T. Matsui, H. Satz, "J/ψ Suppression by Quark-Gluon Plasma Formation", **Phys. Lett. B 178 (1986), p. 416**,
DOI: 10.1016/0370-2693(86)91404-8.

[95] B. A. Kniehl, G. Kramer, B. Potter, "Testing the universality of fragmentation functions", **Nucl. Phys. B 597 (2001), p. 337**,
DOI: 10.1016/S0550-3213(00)00744-6.

[96] T. Renk, K. J. Eskola, "Proton-antiproton suppression in 200A GeV Au–Au collisions", **Phys. Rev. C 76 (2007), p. 027901**,
DOI: 10.1103/PhysRevC.76.027901.

[97] J. Aichelin, P. B. Gossiaux, T. Gousset, "Gluon radiation by heavy quarks at intermediate energies", **Phys. Rev. D 89** (**2014**), **p. 074018**,
DOI: 10.1103/PhysRevD.89.074018.

[98] E. Schnedermann, J. Sollfrank, U. Heinz, "Thermal phenomenology of hadrons from 200A GeV S+S collisions", **Phys. Rev. C 48** (**1993**), **p. 2462**,
DOI: 10.1103/PhysRevC.48.2462.

[99] S. S. Adler et al., "Production of ϕ mesons at midrapidity in $\sqrt{s_{\mathrm{NN}}} = 200\,\mathrm{GeV}$", **Phys. Rev. C 72** (**2005**), **p. 014903**,
DOI: 10.1103/PhysRevC.72.014903.

[100] S. Voloshin, Y. Zhang, "Flow study in relativistic nuclear collisions by Fourier expansion of Azimuthal particle distributions", **Z. Phys. C 70** (**1996**), **p. 665**,
DOI: 10.1007/s002880050141.

[101] J.-Y. Ollitrault, "Anisotropy as a signature of transverse collective flow", **Phys. Rev. D 46** (**1992**), **p. 229**,
DOI: 10.1103/PhysRevD.46.229.

[102] C. Gale et al., "Event-by-event anisotropic flow in heavy-ion collisions from combined Yang-Mills and viscous fluid dynamics", **Phys. Rev. Lett. 110** (**2013**), **p. 012302**,
DOI: 10.1103/PhysRevLett.110.012302.

[103] K. Aamodt et al., "Two-pion Bose-Einstein correlations in central Pb–Pb collisions at $\sqrt{s_{\mathrm{NN}}} = 2.76\,\mathrm{TeV}$", **Phys. Lett. B 696** (**2011**), **p. 328**,
DOI: 10.1016/j.physletb.2010.12.053.

[104] V. Khachatryan et al., "Observation of Long-Range Near-Side Angular Correlations in Proton-Proton Collisions at the LHC", **JHEP 1009** (**2010**), **p. 091**,
DOI: 10.1007/JHEP09(2010)091.

[105] T. Pierog et al., "EPOS LHC : test of collective hadronization with LHC data" (**2013**), arXiv: 1306.0121 [hep-ph].

[106] K. Werner et al., "Analysing radial flow features in p-Pb and p-p collisions at several TeV by studying identified particle production in EPOS3", **Phys. Rev. C 89** (**2014**), **p. 064903**,
DOI: 10.1103/PhysRevC.89.064903.

[107] B. Abelev et al., "Centrality dependence of π, K, p production in Pb–Pb collisions at $\sqrt{s_{\mathrm{NN}}} = 2.76\,\mathrm{TeV}$", **Phys. Rev. C 88** (**2013**), **p. 044910**,
DOI: 10.1103/PhysRevC.88.044910.

[108] B. Abelev et al., "Multi-strange baryon production at mid-rapidity in Pb–Pb collisions at $\sqrt{s_{\mathrm{NN}}} = 2.76\,\mathrm{TeV}$", **Phys. Let. B 728** (**2014**), **p. 216**,
DOI: 10.1016/j.physletb.2013.11.048.

[109] M. Nahrgang et al., "Elliptic and triangular flow of heavy flavor in heavy-ion collisions" (**2014**), arXiv: 1410.5396 [hep-ph].

[110] P. Kovtun, D. T. Son, A. O. Starinets, "Viscosity in strongly interacting quantum field theories from black hole physics", **Phys. Rev. Lett. 94** (**2005**), **p. 111601**,
DOI: 10.1103/PhysRevLett.94.111601.

[111] B. SCHENKE, S. JEON, C. GALE, "Elliptic and triangular flow in event-by-event (3+1)D viscous hydrodynamics", **Phys.Rev.Lett. 106** (**2011**), **p. 042301**,
DOI: 10.1103/PhysRevLett.106.042301.

[112] H. SONG et al., "200 A GeV Au–Au collisions serve a nearly perfect quark-gluon liquid", **Phys. Rev. Lett. 106** (**2011**), **p. 192301**,
DOI: 10.1103/PhysRevLett.106.192301.

[113] P. BOZEK, I. WYSKIEL-PIEKARSKA, "Particle spectra in Pb–Pb collisions at $\sqrt{s_{NN}} = 2.76$ TeV", **Phys. Rev. C 85** (**2012**), **p. 064915**,
DOI: 10.1103/PhysRevC.85.064915.

[114] I. A. KARPENKO, Y. M. SINYUKOV, K. WERNER, "Uniform description of bulk observables in the hydrokinetic model of AA collisions at the BNL Relativistic Heavy Ion Collider and the CERN Large Hadron Collider", **Phys. Rev. C 87** (**2013**), **p. 024914**,
DOI: 10.1103/PhysRevC.87.024914.

[115] R. J. FRIES et al., "Hadronization in Heavy-Ion Collisions: Recombination and Fragmentation of Partons", **Phys. Rev. Lett. 90** (**2003**), **p. 202303**,
DOI: 10.1103/PhysRevLett.90.202303.

[116] B. B. ABELEV et al., "Elliptic flow of identified hadrons in Pb–Pb collisions at $\sqrt{s_{NN}} = 2.76$ TeV" (**2014**), arXiv: 1405.4632 [nucl-ex].

[117] S. ADLER et al., "Scaling properties of proton and anti-proton production in $\sqrt{s_{NN}} = 200$ GeV Au–Au collisions", **Phys. Rev. Lett. 91** (**2003**), **p. 172301**,
DOI: 10.1103/PhysRevLett.91.172301.

[118] B. ABELEV et al., "Energy dependence of pi+−, p and anti-p transverse momentum spectra for Au–Au collisions at $\sqrt{s_{NN}} = 62.4$ and 200 GeV", **Phys. Lett. B 655** (**2007**), **p. 104**,
DOI: 10.1016/j.physletb.2007.06.035.

[119] J. SCHUKRAFT, "Heavy Ion Physics at the LHC: What's new ? What's next ?" (**2013**), arXiv: 1311.1429 [hep-ex].

[120] U. W. HEINZ, "Concepts of heavy ion physics" (**2004**), **p. 165–238**, arXiv: hep-ph/0407360 [hep-ph].

[121] P. BRAUN-MUNZINGER, K. REDLICH, J. STACHEL, "Particle production in heavy ion collisions" (**2003**), arXiv: nucl-th/0304013 [nucl-th].

[122] M. FLORIS, "Hadron yields and the phase diagram of strongly interacting matter", **Nucl. Phys. A 931** (**2014**), **p. 103**,
DOI: 10.1016/j.nuclphysa.2014.09.002.

[123] P. BRAUN-MUNZINGER et al., "Confronting LHC data with the statistical hadronization model", **J. Phys. Conf. Ser. 509** (**2014**), **p. 012019**,
DOI: 10.1088/1742-6596/509/1/012019.

[124] J. CLEYMANS et al., "Statistical model predictions for particle ratios at $\sqrt{s_{NN}} = 5.5$ TeV", **Phys. Rev. C 74** (**2006**), **p. 034903**,
DOI: 10.1103/PhysRevC.74.034903.

[125] F. BECATTINI, R. FRIES, "The QCD confinement transition: Hadron formation", **Landolt-Bornstein 23** (**2010**), **p. 208**,
DOI: 10.1007/978-3-642-01539-7_8.

[126] R. HAGEDORN, "CERN lectures Thermodynamics of strong interactions", CERN publications, European Organisation for Nuclear Research, 1970 - 1971.

[127] F. BECATTINI, "An Introduction to the Statistical Hadronization Model" (**2009**), arXiv: 0901.3643 [hep-ph].

[128] F. BECATTINI et al., "Centrality dependence of hadronization and chemical freeze-out conditions in heavy ion collisions at $\sqrt{s_{NN}}$ = 2.76 TeV", **Phys. Rev. C 90** (5 **2014**), **p. 054907**,
DOI: 10.1103/PhysRevC.90.054907.

[129] K. AAMODT et al., "The ALICE experiment at the CERN LHC", **JINST 3** (**2008**), **p. S08002**,
URL: http://stacks.iop.org/1748-0221/3/i=08/a=S08002.

[130] F. MARCASTEL, "CERN's Accelerator Complex", CERN Graphic Design service, 2013.

[131] B. ABELEV et al., "Performance of the ALICE Experiment at the CERN LHC", **Int. J. Mod. Phys. A 29** (**2014**), **p. 1430044**,
DOI: 10.1142/S0217751X14300440.

[132] H. BETHE, "Theory of the passage of fast corpuscular rays through matter", **Annalen Phys. 5** (**1930**), **p. 325**.

[133] E. ABBAS et al., "Performance of the ALICE VZERO system", **JINST 8** (**2013**), **p. P10016**,
DOI: 10.1088/1748-0221/8/10/P10016.

[134] K. OYAMA, "Reference cross section measurements with ALICE in pp and Pb–Pb collisions at LHC" (**2013**), arXiv: 1305.7044 [nucl-ex].

[135] C. W. FABJAN et al., "ALICE Technical Design Report on Trigger, Data Acquisition, High Level Trigger and Control System", **CERN-LHCC-2003-062,** (**2004**),
URL: http://cds.cern.ch/record/684651.

[136] I. FOSTER, "What is the Grid? A Three Point Checklist." **GRIDtoday 1** (**2002**), **p. 32**.

[137] I. FOSTER, C. KESSELMAN, S. TUECKE, "The Anatomy of the Grid: Enabling Scalable Virtual Organizations", **International J. Supercomputer Applications 15** (**2001**), **p. 3**.

[138] I. FOSTER, "Globus Toolkit Version 4: Software for Service-Oriented Systems", **Springer-Verlag LNCS 3779**[**7**] (**2006**), **p. 2**.

[139] "gLite - Lightweight Middleware for Grid Computing",
URL: http://glite.cern.ch.

[140] "A European Grid Technology",
URL: http://www.unicore.eu.

[141] P. SAIZ et al., "AliEn–ALICE environment on the GRID", **Nucl. Inst. & Meth. in Phys. Res. A 502** (**2003**), Proceedings of the VIII International Workshop on Advanced Computing and Analysis Techniques in Physics Research, **p. 437**,
DOI: 10.1016/S0168-9002(03)00462-5.

[142] R. BRUN, F. RADEMAKERS, "ROOT - An Object Oriented Data Analysis Framework", **Nucl. Inst. & Meth. in Phys. Res. A 389 (1997)**, **p. 81**, URL: http://root.cern.ch/.

[143] "ALICE Offline Pages", URL: http://aliceinfo.cern.ch/Offline.

[144] X.-N. WANG, M. GYULASSY, "HIJING: A Monte Carlo model for multiple jet production in pp, p A, and A A collisions", **Phys. Rev. D 44 (1991)**, **p. 3501**, DOI: 10.1103/PhysRevD.44.3501.

[145] T. SJOSTRAND, S. MRENNA, P. Z. SKANDS, "A Brief Introduction to PYTHIA 8.1", **Comput.Phys.Commun. 178 (2008)**, **p. 852**, DOI: 10.1016/j.cpc.2008.01.036.

[146] R. ENGEL, J. RANFT, "Hadronic photon-photon interactions at high-energies", **Phys. Rev. D 54 (1996)**, **p. 4244**, DOI: 10.1103/PhysRevD.54.4244.

[147] S. ROESLER, R. ENGEL, J. RANFT, "The Monte Carlo event generator DPMJET-III" (**2000**), **p. 1033**, arXiv: hep-ph/0012252 [hep-ph].

[148] K. WERNER, "The hadronic interaction model {EPOS}", **Nuclear Physics B - Proceedings Supplements 175 (2008)**, **p. 81**, DOI: 10.1016/j.nuclphysbps.2007.10.012.

[149] R. BRUN, F. CARMINATI, S. GIANI, "GEANT 3 detector description and simulation tool", **CERNW5013 (1993)**.

[150] B. ALESSANDRO et al., "ALICE: Physics Performance Report, Volume II", **Journal of Physics G: Nuclear and Particle Physics 32 (2006)**, **p. 1295**, DOI: 10.1088/0954-3899/32/10/001.

[151] R. J. GLAUBER, "Cross Sections in Deuterium at High Energies", **Phys. Rev. 100 (1955)**, **p. 242**, DOI: 10.1103/PhysRev.100.242.

[152] M. GAGLIARDI, "Measurement of reference cross sections in pp and Pb–Pb collisions at the LHC in van der Meer scans with the ALICE detector", **AIP Conf. Proc. 1422 (2012)**, **p. 110**, DOI: 10.1063/1.3692205.

[153] B. ABELEV et al., "Measurement of inelastic, single- and double-diffraction cross sections in proton–proton collisions at the LHC with ALICE", **Eur. Phys. J. C 73 (2013)**, **p. 2456**, DOI: 10.1140/epjc/s10052-013-2456-0.

[154] B. ABELEV et al., "K^0_s and Λ production in Pb–Pb collisions at $\sqrt{s_{NN}} = 2.76$ TeV", **Phys. Rev. Lett. 111 (2013)**, **p. 222301**, DOI: 10.1103/PhysRevLett.111.222301.

[155] "ALICE internal analysis note", URL: https://aliceinfo.cern.ch/Notes/node/48.

[156] F. A. R. FERRARI A., S. J., "FLUKA: a multi-particle transport code", **CERN 2005-10 (2005), INFN/TC_05/11, SLAC-R-773 (2005)**.

[157] B. ABELEV et al., "Multi-strange baryon production at mid-rapidity in Pb–Pb collisions at $\sqrt{s_{NN}} = 2.76$ TeV", **Phys. Lett. B728 (2014)**, **p. 216**,
DOI: 10.1016/j.physletb.2013.11.048.

[158] D. COLELLA, "Multi-strange baryon production in Pb–Pb and pp collisions at $\sqrt{s_{NN}} = 2.76$ TeV with the ALICE experiment at the LHC", **J. Phys. Conf. Ser. 509 (2014)**, **p. 012090**,
DOI: 10.1088/1742-6596/509/1/012090.

[159] B. B. ABELEV et al., "Production of charged pions, kaons and protons at large transverse momenta in pp and Pb–Pb collisions at $\sqrt{s_{NN}} = 2.76$ TeV", **Phys. Lett. B 736 (2014)**, **p. 196**,
DOI: 10.1016/j.physletb.2014.07.011.

[160] J. ADAM et al., "Centrality dependence of the nuclear modification factor of charged pions, kaons, and protons in Pb–Pb collisions at $\sqrt{s_{NN}} = 2.76$ TeV" (**2015**), arXiv: 1506.07287 [nucl-ex].

[161] C. TSALLIS, "Possible Generalization of Boltzmann-Gibbs Statistics", **J. Statist.Phys. 52 (1988)**, **p. 479**,
DOI: 10.1007/BF01016429.

[162] S. CHATRCHYAN et al., "Study of the production of charged pions, kaons, and protons in p-Pb collisions at $\sqrt{s_{NN}} =5.02$ TeV", **Eur. Phys. J. C 74 (2012)**, **p. 2847**,
DOI: doi:10.1140/epjc/s10052-014-2847-x.

[163] M. KNICHEL, ALICE internal,
URL: https://indico.cern.ch/getFile.py/access?contribId=19\&resId=1\&materialId=slides\&confId=197058.

[164] "ALICE internal analysis note",
URL: https://aliceinfo.cern.ch/Notes/node/47.

[165] "ALICE internal analysis note",
URL: https://aliceinfo.cern.ch/Notes/node/217.

[166] S. SCHUCHMANN, "High p_T suppression of Λ and K^0_s in Pb–Pb collisions at $\sqrt{s_{NN}} = 2.76$ TeV with ALICE", **J. Phys. G 38 (2011)**, **p. 124080**,
DOI: 10.1088/0954-3899/38/12/124080.

[167] M. DJORDJEVIC, "Heavy flavor puzzle at LHC: a serendipitous interplay of jet suppression and fragmentation", **Phys. Rev. Lett. 112**.4 **(2014)**, **p. 042302**,
DOI: 10.1103/PhysRevLett.112.042302.

[168] A. GRELLI, "D meson nuclear modification factors in Pb–Pb collisions at $\sqrt{s_{NN}} = 2.76$ TeV with the ALICE detector", **Nucl. Phys. A 904 (2013)**, **p. 635c**,
DOI: 10.1016/j.nuclphysa.2013.02.096.

[169] F. BELLINI, "Hadronic resonance production measured by ALICE at the LHC", **Nucl. Phys. A 931 (2014)**, **p. 846**,
DOI: http://dx.doi.org/10.1016/j.nuclphysa.2014.08.031.

[170] E. BRUNA, "D-meson nuclear modification factor and v$_2$ in Pb–Pb collisions at the LHC", **J.Phys.Conf.Ser. 509 (2014)**, **p. 012080**,
DOI: 10.1088/1742-6596/509/1/012080.

[171] "CMS-PAS-HIN-12-014".

[172] P. B. Gossiaux et al., "Gluon radiation by heavy quarks at intermediate energies and consequences for the mass hierarchy of energy loss", **Nucl. Phys. A 931 (2014)**, **p. 581**,
DOI: 10.1016/j.nuclphysa.2014.08.096.

[173] J. Uphoff et al., "Elliptic flow and nuclear modification factor in ultra-relativistic heavy-ion collisions within a partonic transport model" (**2014**),
arXiv: 1401.1364 [hep-ph].

[174] F. Senzel et al., "Elliptic flow and nuclear modification factor within a partonic transport model", **Nuclear Physics A 931 (2014)**, **p. 937**,
DOI: 10.1016/j.nuclphysa.2014.08.099.

[175] Z. Xu, C. Greiner, "Thermalization of gluons in ultrarelativistic heavy ion collisions by including three-body interactions in a parton cascade", **Phys. Rev. C 71 (2005)**, **p. 064901**,
DOI: 10.1103/PhysRevC.71.064901.

[176] J. Uphoff et al., "Elastic and radiative heavy quark interactions in ultra-relativistic heavy-ion collisions" (**2014**), arXiv: 1408.2964 [hep-ph].

[177] F. Senzel, private communication.

[178] K. Cheung, "Recent progress on perturbative QCD fragmentation functions" (**1995**), arXiv: hep-ph/9505365 [hep-ph].

[179] G. Agakishiev et al., "Strangeness Enhancement in Cu–Cu and Au–Au Collisions at $\sqrt{s_{\mathrm{NN}}} = 200$ GeV", **Phys. Rev. Lett. 108 (2012)**, **p. 072301**,
DOI: 10.1103/PhysRevLett.108.072301.

[180] B. I. Abelev et al., "Strange particle production in pp collisions at $\sqrt{s} = 200$ GeV", **Phys. Rev. C 75 (2007)**, **p. 064901**,
DOI: 10.1103/PhysRevC.75.064901.

[181] H. Song, U. Heinz, "Causal viscous hydrodynamics in $2 + 1$ dimensions for relativistic heavy-ion collisions", **Phys. Rev. C 77 (2008)**, **p. 064901**,
DOI: 10.1103/PhysRevC.77.064901.

[182] H. Song, U. Heinz, "Multiplicity scaling in ideal and viscous hydrodynamics", **Phys. Rev. C 78 (2008)**, **p. 024902**,
DOI: 10.1103/PhysRevC.78.024902.

[183] H. Song, U. Heinz, "Suppression of elliptic flow in a minimally viscous quark gluon plasma", **Phys. Lett. B 658 (2008)**, **p. 279**,
DOI: http://dx.doi.org/10.1016/j.physletb.2007.11.019.

[184] H. Song, S. A. Bass, U. Heinz, "Elliptic flow in 200 A GeV Au–Au collisions and 2.76 A TeV Pb–Pb collisions: insights from viscous hydrodynamics + hadron cascade hybrid model", **Phys. Rev. C 83 (2011)**, **p. 054912**,
DOI: 10.1103/PhysRevC.83.054912,10.1103/PhysRevC.87.019902.

[185] K. Werner, "Lambda-to-Kaon Ratio Enhancement in Heavy Ion Collisions at Several TeV", **Phys. Rev. Lett. 109 (2012)**, **p. 102301**,
DOI: 10.1103/PhysRevLett.109.102301.

[186] M. VELDHOEN, "p/π Ratio in Di-Hadron Correlations", **Nucl. Phys. A 910 (2013)**, **p. 306**,
DOI: 10.1016/j.nuclphysa.2012.12.103.

[187] X. ZHANG, "K_s^0 and Λ Production in Charged Particle Jets in p–Pb Collisions at $\sqrt{s_{NN}} = 5.02$ TeV with ALICE", **Nucl. Phys. A 931 (2014)**, **p. 444**,
DOI: 10.1016/j.nuclphysa.2014.08.102.

[188] S. CHATRCHYAN et al., "Measurement of jet fragmentation in Pb–Pb and pp collisions at $\sqrt{s_{NN}} = 2.76$ TeV", **Phys. Rev. C 90 (2014)**, **p. 024908**,
DOI: 10.1103/PhysRevC.90.024908.

[189] K. AAMODT et al., "Charged-particle multiplicity measurement in proton-proton collisions at $\sqrt{s} = 7$ TeV with ALICE at LHC", **Eur.Phys.J. C68 (2010)**, **p. 345–354**,
DOI: 10.1140/epjc/s10052-010-1350-2.

[190] S. WHEATON, J. CLEYMANS, M. HAUER, "THERMUS: A Thermal model package for ROOT", **Comput.Phys.Commun. 180 (2009)**, **p. 84**,
DOI: 10.1016/j.cpc.2008.08.001.

[191] B. DÖNIGUS, private communication.

[192] A. ANDRONIC, P. BRAUN-MUNZINGER, J. STACHEL, "Thermal hadron production in relativistic nuclear collisions: The Hadron mass spectrum, the horn, and the QCD phase transition", **Phys. Lett. B 673 (2009)**, **p. 142**,
DOI: 10.1016/j.physletb.2009.02.014.

[193] M. PETRÁN et al., "Hadron production and quark-gluon plasma hadronization in Pb-Pb collisions at $\sqrt{s_{NN}} = 2.76$ TeV", **Phys. Rev. C C88**.3 **(2013)**, **p. 034907**,
DOI: 10.1103/PhysRevC.88.034907.

[194] M. PETRÁN et al., "SHARE with CHARM", **Comput. Phys. Commun. 185 (2014)**, **p. 2056**,
DOI: 10.1016/j.cpc.2014.02.026.

[195] G. TORRIERI et al., "SHAREv2: Fluctuations and a comprehensive treatment of decay feed-down", **Comput.Phys.Commun. 175 (2006)**, **p. 635**,
DOI: 10.1016/j.cpc.2006.07.010.

[196] G. TORRIERI et al., "SHARE: Statistical hadronization with resonances", **Comput.Phys.Commun. 167 (2005)**, **p. 229**,
DOI: 10.1016/j.cpc.2005.01.004.

[197] A. ADARE et al., "Identified charged hadron production in pp collisions at $\sqrt{s} = 200$ and 62.4 GeV", **Phys. Rev. C 83 (2011)**, **p. 064903**,
DOI: 10.1103/PhysRevC.83.064903.

[198] S. ADLER et al., "Identified charged particle spectra and yields in Au–Au collisions at $\sqrt{s_{NN}} = 200$ GeV", **Phys. Rev. C 69 (2004)**, **p. 034909**,
DOI: 10.1103/PhysRevC.69.034909.

[199] B. ABELEV et al., "Systematic Measurements of Identified Particle Spectra in pp, d–Au and Au–Au Collisions from STAR", **Phys. Rev. C 79 (2009)**, **p. 034909**,
DOI: 10.1103/PhysRevC.79.034909.

[200] J. ADAMS et al., "Scaling Properties of Hyperon Production in Au–Au Collisions at $\sqrt{s_{\mathrm{NN}}} = 200$ GeV", **Phys. Rev. Lett. 98 (2007), p. 062301**,
DOI: `10.1103/PhysRevLett.98.062301`.

[201] S. ADLER et al., "Systematic studies of the centrality and $\sqrt{s_{\mathrm{NN}}}$ dependence of the $\mathrm{dE(T)}/\mathrm{d}\eta$ and $\mathrm{d}N_{ch}/\mathrm{d}\eta$ in heavy-ion collisions at mid-rapidity",
Phys. Rev. C 71 (2005), p. 034908,
DOI: `10.1103/PhysRevC.71.049901`.

[202] C. ALT et al., "System-size dependence of strangeness production in nucleus-nucleus collisions at $\sqrt{s_{\mathrm{NN}}} = 17.3$ GeV", **Phys. Rev. Lett. 94 (2005), p. 052301**,
DOI: `10.1103/PhysRevLett.94.052301`.

[203] J. PODOLANSKI, R. ARMENTEROS, "Analysis of V-events", **Philosophical Magazine 45 (1953), p. 13**.

Acknowledgements